Structures and luminescence properties of some new rare-earth aluminates and gallates obtained by non-equilibrium synthesis

Xue Fang

UNIVERSITÉ D'ORLÉANS

ÉCOLE DOCTORALE ÉNERGIE MATÉRIAUX SCIENCES DE LA TERRE ET DE L'UNIVERS

CEMHTI-CNRS

THÈSE présentée par :

Xue FANG

soutenue le : **03 Octobre 2023**

pour obtenir le grade de : **Docteur de l'Université d'Orléans**

Discipline/ Spécialité : Chimie

Structures and luminescence properties of some new rare-earth aluminates and gallates obtained by non-equilibrium synthesis

THÈSE dirigée par :

M. Mathieu Allix	Directeur de Recherche, CEMHTI CNRS
M. Michael J. Pitcher	Chargé de Recherche, CEMHTI CNRS

RAPPORTEURS :

Mme. Abigail MCLAUGHLIN	Professeure, University of Aberdeen
M. Romain GAUTIER	Chargé de recherche, IMN CNRS

JURY :

Mme. Abigail MCLAUGHLIN	Professeure, University of Aberdeen
M. Romain GAUTIER	Chargé de recherche, IMN CNRS
M. Marcelo NALIN	Professeur, Universidade Estadual Paulista
Mme. Julia PAYNE (Présidente)	Lecturer,University of St Andrews
M. Mathieu Allix	Directeur de Recherche, CEMHTI CNRS
M. Michael J. Pitcher	Chargé de Recherche, CEMHTI CNRS

Acknowledgment

It is with immense gratitude and heartfelt appreciation that I extend my acknowledgments to all those who have contributed to the completion of this thesis. This three years PhD journey has been a profound and transformative experience, and I am grateful thank the support, guidance, and inspiration that I have received along the way.

I owe my deepest gratitude to my supervisor Mathieu Allix and Michael Pitcher, whose unwavering dedication, insightful guidance, and scholarly expertise have been pivotal in shaping the direction of this research. Your mentorship has not only enhanced my understanding of the new materials but has also fostered my strong passion for exploring new materials. Your constant encouragement and patient guidance have been instrumental in shaping the outcome of this thesis.

I thank the fellows at CEMHTI for generously sharing their expertise and collaborating with me throughout this journey. I extend my heartfelt gratitude to Emanuel Véron for his invaluable assistance in conducting XRD and SEM measurements, which significantly contributed to the advancement of this research. Cécile Genevois' expertise in STEM measurement and meticulous analysis of STEM results have been instrumental, and I am truly appreciative of her responsive guidance to my inquiries. I am also indebted to Didier Zanghi for his expert support in EXAFS measurement and meticulous analysis of results. My sincere thanks are extended to Vincent Sarou-Kanian for his expertise in conducting NMR measurement and skillful data fitting. Many thanks to Sandra for her help in DSC measurement. Additionally, I wish to express my gratitude to Ana Isabel Becerro and Victor Castaing (CSIC, Seville, Spain) for their dedicated efforts in performing luminescence experiments and conducting thorough data analysis, all while graciously addressing my questions and uncertainties. I would be remiss not to extend my appreciation to Matthew S. Dyer (University of Liverpool, Liverpool, UK) for his critical role in performing structural simulations that significantly informed the analysis of the EXAFS results. The microprobe measurement conducted at BRGM-CNRS in Orleans is greatly acknowledged. I wish to extend my acknowledgment to the assistance provided by the Argonne Laboratory (USA), where the synchrotron X-ray powder diffraction (SPD) measurements were conducted. My

gratitude goes to Synchrotron Soleil for the contribution under Dr. Emiliano Fonda (SAMBA beamline, SOLEIL) in conducting the EXAFS measurements.

To my fellow doctoral candidates, colleagues, and laboratory companions, your camaraderie, intellectual exchanges, and unwavering support have been a constant source of inspiration. I express my gratitude to Weiwei Cao, Haytem Bazzaoui, Renaud Valois, Euan Duncan, and Jan Baborak for your invaluable assistance and camaraderie. II will deeply miss the enjoyable moments and shared experiences we had together.

I extend my deepest gratitude to my family and friends, whose unwavering support, patience, and encouragement have been my foundation throughout this endeavor. Your belief in my abilities, understanding during challenging times, and boundless love have been a driving force behind my perseverance and determination

I extend my appreciation to CEMHTI-CNRS for providing me with the resources, facilities, and opportunities that have facilitated the completion of this research. Finally, a grand thank you to CSC for providing funding to support the completion of my PhD studies.

I am filled with gratitude for this three-year journey. This experience has not only enriched my academic path but also allowed me to rediscover myself and has provided a renewed perspective on shaping my future.

Scientific production and communication

Publications:

1. **Highly non-stoichiometric YAG ceramics with modified luminescence properties**.

   *Cao, W, Becerro, A. I., Castaing, V, **Fang, X**, Florian, P, Fayon, F, Zanghi, D, Veron, E, Zandonà, A, Genevois, C, Pitcher, M J, Allix, M. (2023). Advanced Functional Materials, 33(14), 2213418. https://doi.org/10.1002/adfm.202213418*

2. **Structure and luminescence properties of the highly nonstoichiometric gadolinium aluminate garnets $Gd_{3+x}Al_{5-x}O_{12}$ ($0 \leq x < 0.60$)**

   ***Xue Fang**, Ana Isabel Becerro, Victor Castaing, Weiwei Cao, Emmanuel Veron, Didier Zanghi, Matthew S. Dyer, Cécile Genevois, Michael J. Pitcher* and Mathieu Allix* (manuscript in preparation)*

3. **Discovery of novel solid solution phosphors via phase transition associated with the substitution of Al by Si in $Lu_4Al_2O_9$.**

   ***Xue Fang**, Ana Isabel Becerro, Victor Castaing, Emmanuel Veron, Vincent Sarou-Kanian, Frank Fayon, Michael J. Pitcher* and Mathieu Allix* (manuscript in preparation)*

Communication:

Communication (International Conferences)

1. **Structure and multiple RE^{3+} luminescence sites of highly nonstoichiometric gadolinium aluminium garnet (GAG) (Oral)**

   ***Xue Fang**, Ana Isabel Becerro, Victor Castaing, Weiwei Cao, Emmanuel Veron, Didier Zanghi, Matthew S. Dyer, Cécile Genevois, Michael J. Pitcher and Mathieu Allix. The XVIIIth Conference of the European Ceramic Society (EcerS). 2nd July 2023, Lyon, France.*

2. **Structure and multiple RE^{3+} luminescence sites of highly nonstoichiometric gadolinium aluminium garnet (GAG) (Oral)**

   ***Xue Fang**, Ana Isabel Becerro, Victor Castaing, Weiwei Cao, Emmanuel Veron, Didier Zanghi,*

Matthew S. Dyer, Cécile Genevois, Michael J. Pitcher and Mathieu Allix. International Workshop Advanced Ceramics 09 (IWAC9). 26th September 2023, Limoges, France.

3. **Structure and multiple RE^{3+} luminescence sites of highly nonstoichiometric gadolinium aluminium garnet (GAG) synthesized by crystallization from glass. (Oral)**

   ***Xue Fang**, Ana Isabel Becerro, Victor Castaing, Weiwei Cao, Emmanuel Veron, Didier Zanghi, Matthew S. Dyer, Cécile Genevois, Michael J. Pitcher and Mathieu Allix. The French Union for Science and Glass Technology in conjunction with the 96th Annual Meeting of the German Society of Glass Technology (USTV-DGG). 22th May 2023, Orleans, France.*

4. **Phase transformation in the novel phosphor hosts $Lu_4Al_2O_9$, $Lu_{4-x/3}Al_{2-x}Si_xO_9$ ($0 \leq x \leq 1.25$) and $Lu_{4-x}Mg_xAl_{2-x}Si_xO_9$ ($0 \leq x \leq 1.5$). (Poster)**

   ***Xue Fang**, Emmanuel Veron, Vincent Sarou-Kanian, Michael J. Pitcher and Mathieu Allix. 17th European Power Diffraction Conference (EPDIC 17). 31th May 2022, Sibenik, Croatia.*

5. **Phase transformation in the novel phosphor hosts $Lu_4Al_2O_9$, $Lu_{4-x/3}Al_{2-x}Si_xO_9$ ($0 \leq x \leq 1.25$) and $Lu_{4-x}Mg_xAl_{2-x}Si_xO_9$ ($0 \leq x \leq 1.5$). (Poster)**

   ***Xue Fang**, Emmanuel Veron, Vincent Sarou-Kanian, Michael J. Pitcher and Mathieu Allix. 7th European Crystallographic School (ECS 7).11th July 2022, Lisbon, Portugal.*

Communication (Local)

6. **Structure and multiple RE^{3+} luminescence sites of highly nonstoichiometric gadolinium aluminium garnet (GAG).(Oral)**

   ***Xue Fang**, Ana Isabel Becerro, Victor Castaing, Weiwei Cao, Emmanuel Veron, Didier Zanghi, Matthew S. Dyer, Cécile Genevois, Michael J. Pitcher and Mathieu Allix. Journées Jeunes Chercheurs (J2C).24th May 2023. Orleans, France.*

7. **New highly-nonstoichiometric garnets $A_{3+x}B_{5-x}O_{12}$. (Poster)**

   ***Xue Fang**, Michael J. Pitcher and Mathieu Allix**. Journées Jeunes Chercheurs. 24th May 2021. Orleans, France.*

Abstract

The synthesis, characterization and performance exploration of new materials are crucial to the development of functional materials. In this thesis, the non-equilibrium synthetic methods crystallization from the glass and crystallization from the under-cooled melt have been considered to develop new materials. Here the ADL laser heating equipment was used to achieve the high temperature, fast and controlled cooling rate synthesis conditions required for glass synthesis and crystallization from the melt. Garnet, perovskite and monoclinic phases from the RE_2O_3-$(Al/Ga)_2O_3$ system are widely used in the field of optics. Here, the structure and luminescence properties of highly non-stoichiometric $Gd_{3+x}Al_{5-x}O_{12}$ garnet, monoclinic $Lu_4Al_2O_9$ and a new solid solution phosphor substituted by Si in $Lu_4Al_2O_9$ are reported.

The previous non-stoichiometric YAG work reported that extreme non-stoichiometry in garnet $Y_{3+x}Al_{5-x}O_{12}$ ($0 \leq x \leq 0.4$) is an effective way to achieve emission wavelength modification, which is due to that rare earth ions located at two different crystallographic sites, and the associated local structural distortions. Rare earth ions of different sizes show different distribution preferences in non-stoichiometric YAG garnets, with large REs (e.g. Ce^{3+}) preferring to occupy an 8-coordinate site, and small REs (e.g. Yb^{3+}) preferring a 6-coordinate site. Here we report a series of non-stoichiometric GAG synthesized by crystallization from glass method. It was confirmed that up to 30 % of six-coordinated Al is disorderly replaced by Gd^{3+} in $Gd_{3.6}Al_{4.6}O_{12}$, which allows the smaller radius dopant ions RE^{3+} (Tb^{3+}, Er^{3+}, Tm^{3+}, Yb^{3+}) to prefer to occupy the AlO_6 site, forming six-coordinated REO_6. Two crystallographic luminescence sites with (1) inequivalent AO_8 sites around with different BO_6 neighbours configurations and (2) BO_6 sites are created in ns-GAG, which is responsible for modifying the luminescent properties.

In addition, in the garnet-based material GAGG, a variation in the ratio of Ga/Al has been shown to alter the conduction band shift to control the depth of the electron trap and thus achieve better persistent luminescence performance. Theoretically, adjusting the ratio of A/B ions (non-stoichiometric ratio) can not only adjust the emission colour but also shift the CB band and thus the depth of the electron trap. Here, a series of $Gd_{3+x}(Al_{0.4}Ga_{0.6})_{5-x}O_{12}$

materials have been synthesized using crystallisation from glass, and a series of studies on the persistent luminescence properties of GAGG and GGG-based material show that the excess Gd occupies the Al/Ga sites in the non-stoichiometric GAGG. This not only affects the crystal field of the Ce^{3+} ions resulting in the red-shift of the emission wavelengths but also affects the decay lifetime of the persistent luminescence.

Furthermore, here single-phase $Lu_4Al_2O_9$ (LuAM) and the solid-solution compound $Lu_{4-\alpha}Al_{2-x}Si_xO_{9+\delta}$ ($x = \alpha/3 + \delta/2$, $x = 0.5, 1$) (LuASO) were synthesised for the first time using direct crystallisation from the under-cooled melt. The substitution of Si^{4+} for Al^{3+} resulted in an elevation of crystal structure symmetry, transitioning from a monoclinic $P2_1/c$ phase to an orthorhombic *Pbnm* phase. The LuASO phase was determined to contain a locally ordered arrangement of complex $(Al,Si)O_4$ and AlO_5 polyhedral chains, as opposed to the parent phase which contains isolated AlO_4 tetrahedra, and charges are balanced by cation vacancies and oxide interstitials characterized using a combination of averaged and localized structural probes (powder crystallography and NMR). Different behaviors of photoluminescence response to the structural variation were verified between LuAM and LuASO. Novel solid solution phosphors were discovered, including the yellow LuAM: Ce^{3+} phosphor with blue excitation and blue LuASO: Ce^{3+} phosphor with UV excitation. In addition, the Eu^{3+} occupied different local symmetry sites in the two different hosts, leading to a more reddish emission colour in LuASO. The investigation of up conversion LuAM: Er^{3+}/Yb^{3+} and LuASO: Er^{3+}/Yb^{3+} revealed that changes in symmetry caused a shift in emission color from orange to yellow. These findings suggest that cation substitution can induce alterations in crystal symmetry and the introduction of defects and polyhedral distortion, which can affect the local environment of the dopant consequently affecting luminescence performance.

List of abbreviations and symbols

Synthesis methods and characterization techniques:

ADL: Aerodynamic levitation
SSR: Solid state reaction
PXRD: Powder X-ray diffraction
VT-XRD: Variable temperature X-ray diffraction
SPD: synchrotron powder diffraction
EXAFS: Extended X-ray absorption fine structure
SEM: Scanning electron microscopy and microprobe
EDS: Energy dispersive spectrometer
BSE: Backscattered electron
STEM：Scanning transmission electron microscopy
HAADF：High angle angular dark field
DSC: Differential scanning calorimetry
DFT: Density functional theory ，
PLE: Photoluminescence exitation
PL: Photoluminescence
CB：Conduct bond

Compounds:

YAG: $Y_3Al_5O_{12}$
ns-YAG: Nonstoichiomtric $Y_{3+x}Al_{5-x}O_{12}$ ($0 < x \leq 0.4$)
GAG: $Gd_3Al_5O_{12}$
ns-GAG: Nonstoichiomtric $Gd_{3+x}Al_{5-x}O_{12}$ ($0 < x \leq 0.6$)
GGG: $Gd_3Ga_5O_{12}$
ns-GGG: Nonstoichiomtric $Gd_{3+x}Ga_{5-x}O_{12}$ ($0 < x \leq 0.6$)
GAGG: $Gd_3Al_2Ga_3O_{12}$
ns-GAGG: Nonstoichiomtric $Gd_{3+x}(Al_{0.4}Ga_{0.6})_5O_{12}$ ($0 < x \leq 0.6$)
GAP: $GdAlO_3$ perovskite
YAP: $YAlO_3$ perovskite
YAM: $Y_4Al_2O_9$ monoclinic
YAH: $YAlO_3$ hexagonal
LuAM: $Lu_4Al_2O_9$ monoclinic
LuASO: $Lu_{4-\alpha}Al_{2-x}Si_xO_{9+\delta}$ ($0 < x \leq 1$) orthorhombic solid solution

Table of Contents

General introduction

With the rapid development of technology, there is an increasing global demand for ceramic materials in various fields such as energy, electronics, biology, medicine, environment, aerospace, and architecture. The development of ceramics entails exploring new compositions, structures, and processing techniques to meet the performance requirements of different applications[1]. The solid state reaction method is a commonly employed method for ceramic synthesis due to its simplicity, universality and cost-effectiveness. However, it usually requires high sintering temperatures, which may lead to grain growth, phase separation of impurity phase formation[2]. Non-equilibrium synthesis methods can control material composition and structure by adjusting reaction conditions and kinetic pathways, thereby producing amorphous, metastable, and nanostructured materials, which are difficult to obtain by solid-state reaction synthesis.

The ADL combined with laser heating is a device available in CEMHTI to achieve the non-equilibrium synthesis methods of crystallization from melt or from glass, which are effective method for the synthesis of new metastable compounds. The device uses gas to levitate the sample while the laser heats the sample through its melting point. It can reach temperatures over 2500 ^{o}C, and then by abruptly cutting off the laser power, the melt can be cooled quickly without touching the container[3]. The melt, which can be highly corrosive, does not suffer contamination from the container, and the absence of a container interface suppresses heterogeneous surface crystallization on cooling, favouring glass formation. The above methods have been successfully used to synthesize several new ceramic materials that are not possible to synthesise by traditional solid-state reaction methods, and these materials have potential applications in optics, energy storage and other fields[4-7].

The RE_2O_3-$(Al/Ga)_2O_3$ system (RE = yttrium Y), gadolinium (Gd) and lutetium (Lu)) is an important ceramic material system with a wide range of applications in many fields such as electronics, catalysts, magnetism and optics [8-12]. For example, $RE_3Al_5O_{12}$ garnet materials from RE_2O_3-Al_2O_3 system are excellent host materials for optical applications[13-14], while in the RE_2O_3-Al_2O_3 system, GGG, and GGM exhibit excellent magnetic properties[12-15], while

$RE_4Ga_2O_9$ materials have significant oxygen ion and proton conductivity[16]. However, there are many compounds in these systems that have not been reported or synthesized, so the array of unknown compounds in this system is a great treasure trove for exploring new optical, magnetic, and other potentially functional materials. My PhD work will focus on exploring the synthesis of new compounds from this system using ADL, their structural analysis and potential performance studies to discover new functional ceramics. The main work will be presented in three chapters.

Chapter 1:

Our group has recently made a surprising discovery - the synthesis of highly non-stoichiometric YAG ceramics $Y_{3+x}Al_{5-x}O_{12}$ in the composition range $0 \le x \le 0.40$ using the ADL technique crystallized from melt and glass methods, demonstrating the dramatic effect of non-stoichiometric on the emission color of the Er^{3+}-doped upconversion system[4]. In the non-stoichiometric YAG, up to 20% of the octahedrally-coordinated Al^{3+} is replaced by excess Y, which allows the small RE^{3+}(Er^{3+}, Yb^{3+}) to be distributed in two crystallographic sites. The emission color of the up-conversion phosphor $Y_{3.2}Al_{4.8}O_{12}$: Er^{3+}/Yb^{3+} is green instead of the red color of the stoichiometric YAG host, due to the distribution of Er^{3+} on the inequivalent dodecahedral and new octahedral sites. In contrast, the color of non-stoichiometric YAG: Ce^{3+} phosphor is almost unaffected by the non-stoichiometric because the larger ionic radius of Ce^{3+} prevents it from occupying the smaller octahedral sites in ns-YAG. In addition to non-stoichiometric YAG, non-stoichiometric GAG and GGG ($Gd_{3.2}Al_{4.8}O_{12}$ and $Gd_{3.2}Ga_{4.8}O_{12}$) were also shown to be accessible by ADL and deserve further exploration for their synthesis in non-stoichiometric solid solutions and their applications in optics. Whereas in the case of non-stoichiometric GAG, GGG the radius of Gd^{3+} (0.94 Å) is much larger than that of Y^{3+} (0.9 Å), the excess Gd occupying the octahedral sites may provide more space to accommodate the larger size of rare-earth dopants. These results prompted us to investigate the non-stoichiometric solid solution range of different garnets, distribution preference of different sizes dopants in two crystallographic sites in the new highly non-stoichiometric GAG and GGG, as well as the effect of the new REO_6 sites on the luminescence properties. These unknown questions will be the first work.

Chapter 2:

Compounds with garnet structure are not only excellent host materials for up-conversion and down-conversion, but also well-known host materials for persistent luminescence[17]. And garnet-based materials are of interest because of their special structure, especially the larger dodecahedral sites, which are ideal for lanthanide ions [$Ln^{2+/3+}$], and the smaller octahedral and tetrahedral sites, which are dimensionally suitable for Cr^{3+} ions, which allow various doping strategies to be used to obtain different crystal fields and to tune the electron trap depth[17-18]. In garnet-based materials, the energy levels of the traps formed by Cr^{3+} remain constant, so the depth of the electron traps can be controlled by varying the conduction band shift. For example, studies on YAGG and GAGG doped Ce^{3+}/Cr^{3+} persistent luminescent materials found that longer persistent luminescence could be obtained by adjusting the ratio of Ga/Al comparing GAG and GGG based materials[19-21]. Theoretically, adjusting the ratio of A/B ions (stoichiometric) can also shift the CB band and thus adjust the depth of electron traps. In addition, the interference with the A crystal field environment caused by the substitution of A ions for B sites may lead to a change in the emission wavelength. We noted that unlike GAG garnet, the Ga^{3+} is larger than Al^{3+}, which may be more favorable for Gd^{3+} to occupy the B site. Therefore, modification of the A/B ratio in non-stoichiometric garnet may achieve tuning of the color and electron trap depth of persistent luminescent materials, resulting in persistent luminescent materials with longer persistence and desirable emission wavelengths. This will be my second work.

Chapter 3:

In Feng's report on $(Lu/Mg)_3(Al/Si)_5O_{12}$, they found the presence of an unknown secondary phase of $(LuMg)_4(AlSi)_2O_9$, which was determined by EDS[22]. The $Lu_8Al_3SiO_{18}$ compound was synthesized using ADL and its PXRD pattern shows that the space group can be assigned as $P2_1/c$. A literature survey of $Lu_4Al_2O_9$ as well as $Lu_4(Al/Si)_2O_9$ solid solutions revealed that in the RE_2O_3-Al_2O_3 system, in addition to the $REAlO_3$ perovskite, $RE_3Al_5O_{12}$ garnet, $RE_4Al_2O_9$ (where RE = La, Nd, Ce, Eu, Gd, Tb, Dy, Ho, Er, Yb, Lu and Y) can be produced when $RE_2O_3 : Al_2O_3 = 2 : 1$[23]. However, structural information on $Lu_4Al_2O_9$ has been missing because $Lu_4Al_2O_9$ is stable only at temperatures of 1650-2000°C and decomposes on cooling[24]. Only in 2020, a single crystal $Lu_4Al_2O_9$ was synthesized to determine the detailed

crystallographic parameters[25]. Other members of the $RE_4Al_2O_9$ family, $Y_4Al_2O_9$ and $Gd_4Al_2O_9$ have been extensively studied as host materials for optical applications[26-28]. Therefore, the synthesis of $Lu_4Al_2O_9$ and the exploration of its optical properties are promising and meaningful. In the RE_2O_3-Al_2O_3-SiO_2 system, the ternary solid solutions $Nd_4Al_{2(1-x)}Si_{2x}O_{9+x}$ and $Gd_4Al_{2(1-x)}Si_{2x}O_{9+x}$ (x = 0 - ~ 0.4) based on the pseudo-binary phase $RE_4Al_2O_9$ have been determined by SEM-EDX, however, no pure phases have been synthesized so far, and no detailed structural analysis and subsequent investigations[29-32]. We can know that in the case of the well-known $A_3B_2C_3O_{12}$ garnet structural host material, various substitution methods, such as cation/anion, cation pair and chemical unit substitution, are usually used to modulate the crystal field or covalent interactions to explore new colored phosphor materials[33-34]. The replacement of Al^{3+} with Si^{4+} in $Lu_4Al_2O_9$, which may introduce Lu vacancies or additional oxygen to form $Lu_{4-\alpha}(Al/Si)_2O_{9+\delta}$ solid solution. And in this unknown solid solution, local defects caused by the introduction of Lu vacancies or distortion of polyhedra may have an impact on the luminescence properties. Therefore in this chapter, $Lu_4Al_2O_9$ and solid solution compounds of $Lu_{4-\alpha}(Al/Si)_2O_{9+\delta}$ ($0 \le x \le 1$, $x = \alpha/3 + \delta/2$,) were synthesised by ADL. A comprehensive structural study of the new compound $Lu_{4-\alpha}(Al/Si)_2O_{9+\delta}$ will to carried out. The correspondence between the crystal structures and luminescence properties of $Lu_4Al_2O_9$ and $Lu_{4-\alpha}(Al/Si)_2O_{9+\delta}$ solid solutions will be elucidated, which is of great importance for the design, modification and application of a range of $RE_4Al_2O_9$ host materials.

References

[1] C.N.R. Rao, Journal of Materials Chemistry C. ***1999****, 9, 1-14.*

[2] A.O. Tunmise, P.U. Okoye, G. Chen et al., Journal of Industrial and Engineering Chemistry. ***2020****, 85, 34-65.*

[3] C.J. Benmore, J.K.R. Weber, Advances in Physics: X. ***2017****, 2, 717-736.*

[4] W.W Cao, A. Isabel Becerro, V. Castaing, et al., Advanced Functional Materials. ***2023****, 33, 2213418.*

[5] M. Allix, S. Alahrache, F. Fayon et al., Advanced Materials. ***2012****, 24, 5570-5575.*

[6] J. Fan, V. Sarou-Kanian, X. Yang et al., Chemistry of Materials. ***2020****, 32, 9016-9025.*

[7] C. Genevois, H. Bazzaoui, M. Boyer et al., Inorg Chem. ***2021****, 60, 12339-12354.*

[8] P. Haritha, I.R. Martín, K. Linganna et al., Journal of Applied Physics. ***2014****, 116, 174308.*

[9] X. Li, X. Zhao, C. Wang et al., Journal of Luminescence. ***2022****, 248, 118932.*

[10] G. Okada, M. Akatsuka, H. Kimura et al., Sensors and Materials. ***2018****, 30, 1547.*

[11] N.D. Andryushin, M.S. PavlovskiyV.I. Zinenko, Ferroelectrics. ***2020****, 567, 28-36.*

[12] X.Q. Yin, Y.L. Zhong, Y.M. Cao et al., Journal of Applied Crystallography. ***2021****, 54, 1641-1646.*

[13] M. Moszynski, T. Ludziejewski, D. Wolski, et al., Nuclear Instruments and Methods in Physics Research A. ***1994****, 345, 461-467.*

[14] M. Nikl, A. Yoshikawa, K. Kamada et al., Progress in Crystal Growth and Characterization of Materials. ***2013****, 59, 47-72.*

[15] J.A.M. Paddison, H. Jacobsen, O. A. Petrenko et al., Science. ***2015****, 350, 179-181.*

[16] S. Tajima, J. Lee, A. Suzumura et al., Journal of the European Ceramic Society. ***2021****, 41, 4516-4527.*

[17] J. Xu, J. Ueda. S. Tanabe, Journal of Materials Chemistry C. ***2016****, 4, 4380-4386.*

[18] J. Ueda, Bulletin of the Chemical Society of Japan. ***2021****, 94, 2807-2821.*

[19] J.Ueda, K.Kuroishi, S. Tanabe, Applied Physics Letters. ***2014****, 104,*

[20] J. Xu, J. Ueda, S. Tanabe, Optical Materials Express. ***2015****, 5, 963.*

[21] J. Xu, J. Ueda, S. Tanabe, Journal of the American Ceramic Society. ***2017****, 100, 4033-4044.*

[22] S. Feng, Y. Guo, M. Allix et al., Cell Reports Physical Science. ***2022****, 3, 101044.*

[23] A.G. Petrosyan, V.F. Popova, V.V. Gusarov et al., Journal of Crystal Growth. ***2006****, 293, 74-77.*

[24] A.G. Petrosyan, V.F. Popova, V.L. Ugolkov et al., Journal of Crystal Growth. ***2013****, 377, 178-183.*

[25] R. SimuraH. Yamane, Acta Crystallogr E Crystallogr Commun. ***2020****, 76, 752-755.*

[26] W. You, F. Lai, H. JiangJ. Liao, Physica B: Condensed Matter. ***2012****, 407, 1094-1098.*

[27] A. Das, S. Saha, K. Panigrahi et al., CrystEngComm. ***2018****, 20, 2540-2552.*

[28] Y.S. Lian, Y. Wang, J.F. Li et al., Vacuum. ***2020****, 173, 109165.*

[29] J.P. Coutures, E. Antic, P. Caro, Materials Research Bulletin. ***1967****, 11, 699-706.*

[30] U. Kolitsch, H.J. Scifert, F. Aldinger, Journal of Phase Equilibria. ***1998****, 19, 426.*

[31] U. Kolitsch, H.J. Seifert, T. Ludwig et al., Journal of Materials Research. ***1999****, 14, 447–455.*

[32] U. Kolitsch, H.J. Seifert, F. Aldinger, Journal of Alloys and Compounds. ***1999****, 257, 104-114.*

[33] H.P. Ji, L. Wang, S. Maxim et al., Journal of Materials Chemistry C. ***2016****, 4, 2359-2366.*

[34] Z. Ming, J. Qiao, M.S. Molokeev et al., Inorganic Chemistry. ***2020****, 59, 1405-1413.*

Chapter I: State of the art

1.1 Introduction

The investigation of new inorganic oxides holds significant importance is in the field of materials science and engineering important. The core activity of research into new materials synthesised through design or discovered for the first time lies in understanding their structure, physical and chemical properties, as well as exploring and expanding their potential functions. Chemical synthesis methods of materials play a crucial role in the design and discovery of new materials. Traditionally, the exploration of innovative metal oxide materials involved studying the structural and compositional phase space at or near thermodynamic equilibrium, taking advantage of the universal application of solid-state ceramic reaction methods. Non-equilibrium synthesis methods such as rapid solidification of the melt[1], chemical vapour deposition[2], sol-gel[3], pulsed laser deposition[4] synthesis allow for the control of material components and structure by modulating reaction conditions and kinetic pathways to produce amorphous, metastable and nanostructured materials that are difficult to obtain by solid state reaction synthesis. The aerodynamic levitation (ADL) combined with laser heating is a device available in CEMHTI to achieve the non-equilibrium synthesis methods of crystallization from melt or from glass. The method has been applied successfully in synthesizing a diverse range of new compounds with potential functional applications in our group. (**see 1.2 Out of equilibrium synthesis methods**)

Much of the recent research of new materials in our group is based on the synthesis of RE_2O_3-$(Al/Ga)_2O_3$, an important ceramic material system because the compounds in this system have a wide range of applications in many fields such as electronics, catalysts, magnetism and optics. (**see 1.3 Functional compound in RE_2O_3-Ga/Al_2O_3 (RE = Y, Gd, Lu) system**). However, many compounds in this system remain unreported or unexplored, making it meaningful to attempt the synthesis of new materials, investigate their structures, and explore their potential as functional materials. In these systems, we have made notable discoveries regarding non-stoichiometric YAG garnets, which have unexpected effects on luminescence properties **(see 1.4 Non-stoichiometric garnet**). Additionally, new solid solution compounds $Lu_4(Al/Si)_2O_9$ have been identified in the work on $(Lu/Mg)_3(Al/Si)_5O_{12}$ garnets, which hold potential as luminescent materials. (**see 1.5 Monoclinic $Lu_4Al_2O_9$ and**

SiO_2 solubility). Therefore, this chapter is focused on presenting the non-equilibrium methods of crystallization from glass and from melt as well as ADL combined with laser heating devices. Furthermore, new compounds recently synthesized using ADL in our group are introduced. Finally, an overview of the background pertaining to the two main system compounds studied throughout the PhD, non-stoichiometric garnet and $Lu_4(Al/Si)_2O_9$ compounds, were provided. (**see 1.5 Brief conclusion**)

1.2 Out of equilibrium synthesis methods

The arrangement and bonding of atoms in solids are influenced by a number of factors, such as the size of the atoms, their chemical properties (ease of gaining and losing electrons), the type of chemical bonding between them, etc. Different materials can often be distinguished by their unique atom arrangements. The growth of materials essentially involves the combination of atoms in specific ways, and the final arrangement is governed by both thermodynamic and kinetic considerations[5-6]. In processes controlled by growth kinetics and occurring far from thermodynamic equilibrium, special kinetic pathways can be used to create new materials that are metastable under ambient temperature and pressure.[7]

1.2.1 Crystallization from glass

Crystallisation from glass is the process of re-arranging the amorphous atomic structural state of a glass system from a random short-range ordered network to a long-range ordered periodic crystalline structure. Crystallisation involves two essential processes: nucleation and crystal growth. Upon heating the glass above its glass transition temperature (T_g), it transitions from a rigid amorphous state to a more fluid-like state, promoting increased molecular mobility and enabling atomic rearrangement and diffusion. At this critical T_g point, nucleation sites form within the glass, providing the foundation for subsequent crystal growth. Once nucleation occurs, the surrounding atoms or molecules in the glass matrix align themselves into a structured lattice, resulting in the growth of crystals with a periodic and ordered arrangement[8].

When a material undergoes vitrification or amorphisation to form a glass, its atoms or molecules are frozen in a disordered, non-crystalline structure which is closely related to the structure of the parent super-cooled liquid[9], which is a non-equilibrium state (a liquid below the equilibrium melting temperature). This disordered arrangement prevents the material from reaching its thermodynamic equilibrium state. The amorphous structure of the glass provides a higher energy state where, during heating, the atoms or molecules have the opportunity to rearrange into a lower energy crystalline configuration including the metastable phase. The non-equilibrium nature of the glassy state results in higher kinetic barriers to crystallisation compared to the corresponding equilibrium crystalline phase, slowing down the transformation process and allowing the metastable compound to stabilise. By exploiting the nonequilibrium nature of the glassy state, crystallisation from glass provides a favourable route for the formation of metastable compounds.[10-11]

Glass is usually produced by melting high purity raw materials and then cooling them rapidly. During the formation of glass from the melt, the atoms are rearranged as the temperature decreases and the viscosity increases[12]. When the liquid is cooled rapidly, the arrangement of the atomic-scale structure into an ordered state (i.e. crystallisation) is hindered by the rapid increase in viscosity[13]. As a result, the atoms in the liquid are frozen due to the high viscosity and can no longer rearrange themselves into an equilibrium crystal structure[14]. The time-temperature-transition diagram illustrated in ***Fig 1.1*** reveals that when the melt is rapidly cooled from T_m to below T_g, without passing through the critical nucleation temperature (T_n), the system does not have sufficient time to arrange its crystallisation and instead form a glass [15].

The key to achieving glass formation during the cooling of the liquid lies in effectively avoiding nucleation and crystallization. Therefore, in order to obtain a pure glass, the liquid must be cooled at a sufficiently high cooling rate. This minimum cooling rate required for glass formation is referred to as the critical cooling rate (R_c). For different materials the undercooled liquid can be classified as “strong” or “fragile”, depending on its viscosity and the rate at which the relaxation time changes close to the glass transition temperature. For strong liquids such as SiO_2, the viscosity exhibits almost Arrhenius behavior and only subtle changes in structure are observed over a very wide temperature range. In contrast, fragile

liquids require rapid cooling rates to achieve critical cooling conditions for glass formation due to the rapid change in viscosity (see ***Fig 1.2*** R_c1) [16]. Thus, it is known that a wide variety of glasses formed from fragile liquids can be obtained by using extremely fast cooling rates and need not be limited to typical glasses formed from strong liquids, such as silicate glasses.

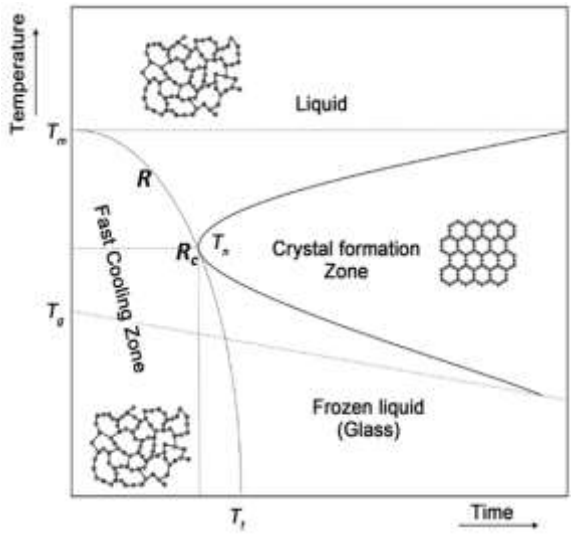

Fig 1.1[15] *Time-Temperature-Transformation (TTT) diagram. Crystallization occurs at T_n between T_m and T_g, and it can be avoided when the liquid is chilled with the cooling rate $R \geq R_c$. (T_m is melt temperature, T_g is glass transition temperature, T_t is the minimum time, which is required to start crystallization, occurs at a critical nucleation temperature T_n)*

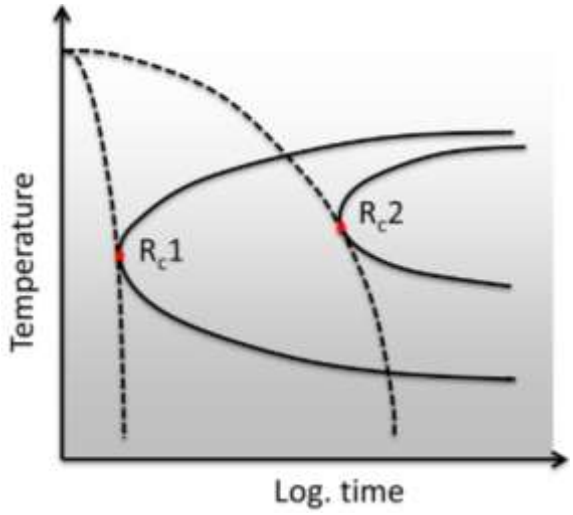

Fig 1.2[16] *Time – temperature - transformation diagram illustrates the critical cooling rate for a fragile liquid (Rc1) and a strong liquid (Rc2).*

1.2.2 Crystallization from melt

Crystallization from glass is a reliable method for obtaining new metastable compounds. However, not all compounds can form glasses even with rapid cooling rates. And in such cases, direct crystallisation from the under-cooled melt is another effective alternative to synthesise metastable compounds. This method involves heating a mixture compounds to a high temperature, causing them to melt and form a homogeneous liquid, and then cooling the liquid under controlled conditions to induce crystallisation to form the desired crystal structure. The process of crystallization from the melt consists of two main stages (*see* ***Fig 1.3***): nucleation and growth. As the liquid cools rapidly below its melting point, it undergoes undercooling (liquid cool below its real freezing point before solidification begins as shown by curve AB). Under appropriate cooling conditions, nucleation takes place, resulting in the formation of small nuclei within the undercooled liquid (at point B). The nucleus serves as the starting point for crystal growth, which is caused by the addition of atoms or molecules from the surrounding liquid (crystallization starts at point C and ends at point D). The growth process involves the rearrangement of atoms or molecules to form a periodic lattice structure, leading to the formation of larger crystal. The cooling rate and thermodynamic conditions during solidification play a key role in determining the crystal structure, morphology and properties of the resulting material [17-18]. ***Fig 1.3*** shows the cooling curve for crystallisation from the melt.[18]

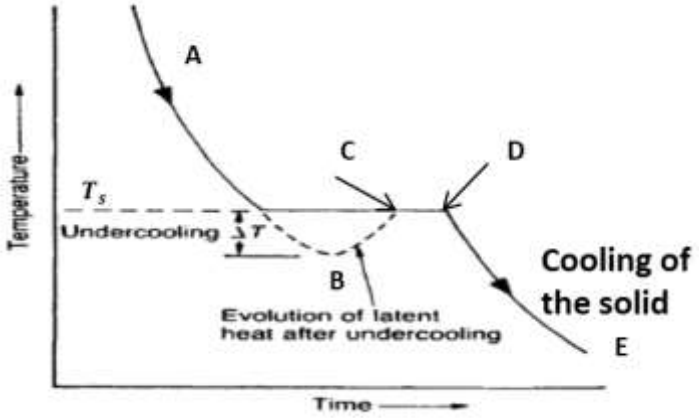

Fig 1.3[18] *Cooling curve for crystallisation from the melt.(T_s is solidification temperature, nucleation at B point, crystallisation starts at C point and ends at D point)*

The synthetic methods of crystallization from the melt offer several important advantages. One of these advantages is the ability to achieve high purity and homogeneity in the resulting crystalline material. The homogeneity of the melt plays a crucial role in promoting uniform nucleation and growth, leading to a material that exhibits consistent composition and properties throughout its volume. By definition, the metastable phase is not the most thermodynamically stable state for that composition. However, through rapid cooling during melt synthesis crystallization, this metastable phase can be kinetically trapped or stabilized. By precisely controlling the composition and cooling rate, it becomes possible to obtain materials with specific crystal structures and metastable material.

1.2.3 Aerodynamic levitation (ADL)

The above discussion highlights the crucial role of high temperatures for melting high melting point oxides and the importance of rapid and controlled cooling processes for both glass formation and crystallization from the melt. The conventional approach for glass formation and melt crystallization at the laboratory scale involves placing the raw starting materials in a crucible, melting it at a high temperature, and subsequently quenching the melt by transferring it onto a lower temperature metal plate or crucible. During this process, the crucible and the melt are in contact, even if there is a small amount of heterogeneous nucleation centres, which can easily lead to rapid crystallisation.

Aerodynamic levitation combined with laser heating is an effective technique for achieving crystallisation from melt and glass synthesis in our laboratory, as laser heating can reach temperatures above 2500°C to melt refractory oxides and allows for a rapid cooling process by controlling the type of levitation gas. More importantly, the contactless nozzle-melt interface inhibits heterogeneous crystallization and liquid phase crystallization[19]. The basic schematic of aerodynamic levitation equipment is shown in ***Fig 1.4***. The typical operation process is as follows: placing the fragment of pelletised solid raw material on a gas flow nozzle in a chamber and adjusting the gas flow appropriately to allow it to be levitated. Two laser beams are then focused on the sample, with their power adjusted gradually to induce melting. Once the sample is completely melted and stable

without touching the nozzle, the melt will rapidly cool by abruptly cutting off the laser to form glass or crystalline beads. The whole process can be observed through the camera, and the temperature of the sample can be recorded in real time by the temperature detector (optical pyrometer).

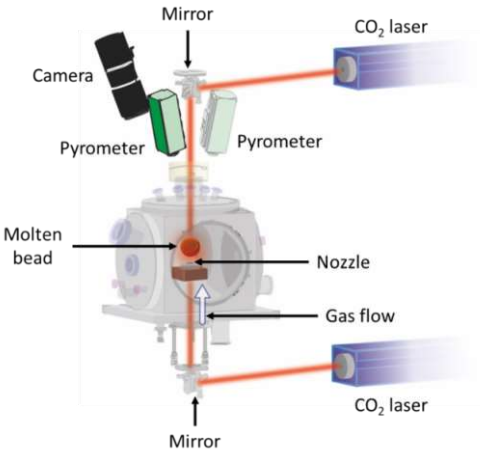

Fig 1.4 *The diagram of ADL combined with laser heating setup at CEMHTI.*

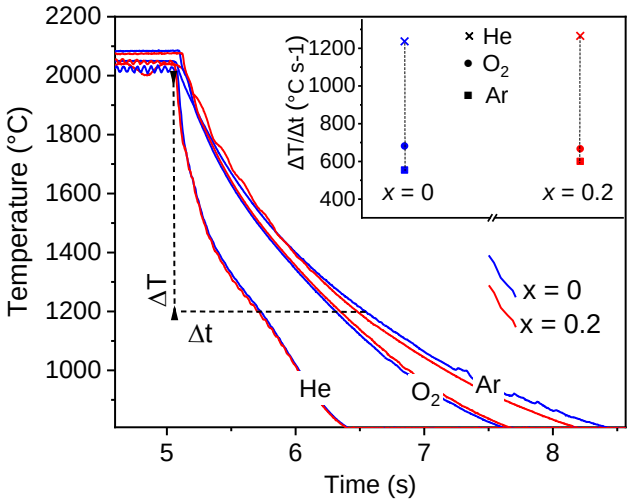

Fig 1.5[20] *Cooling curves of the glassy $Y_3Al_5O_{12}$ (blue curves) and $Y_{3.2}Al_{4.8}O_{12}$ (red curves), with samples of mass 9 mg levitated in argon, oxygen or helium, showing the effect of gas density on the cooling rate.*

Rapid and controlled cooling rates are essential for the formation of glass or for crystallisation directly from the melt. In our research focusing on nonstoichiometric YAG, we have found that the levitation gas and the melt mass have a significant influence on the cooling rate. ***Fig 1.5*** illustrates the cooling curves obtained using different levitation gases,

showing that oxygen promotes faster cooling compared to argon, and helium gas demonstrates the highest cooling rate[20]. To achieve an optimal cooling rate and maintain a stable gas flow, a gas mixture can be employed for precise control.

In addition, the mass of the melt also plays a significant role in determining the cooling rate. ***Fig 1.6*** depicts the cooling curves for three distinct masses of the melt using argon gas, revealing that smaller melt exhibit a faster cooling rate. Upon closer examination, it becomes evident that the crystallization behavior of the melt is influenced by the precise control of the cooling rate, leading to different temperatures of undercooled liquid. (see **Fig 1.6a** inset) Melts with the same composition crystallized as a mixture of perovskite $YAlO_3$ and corundum Al_2O_3 in undercooled liquids with high temperature and as single garnet phase in undercooled liquids with lower temperature. (see ***Fig 1.6b*** and ***c***). Thus, the meticulous regulation of the cooling rate to attain an appropriate temperature for the subcooled liquid is crucial for synthesizing specific phases.

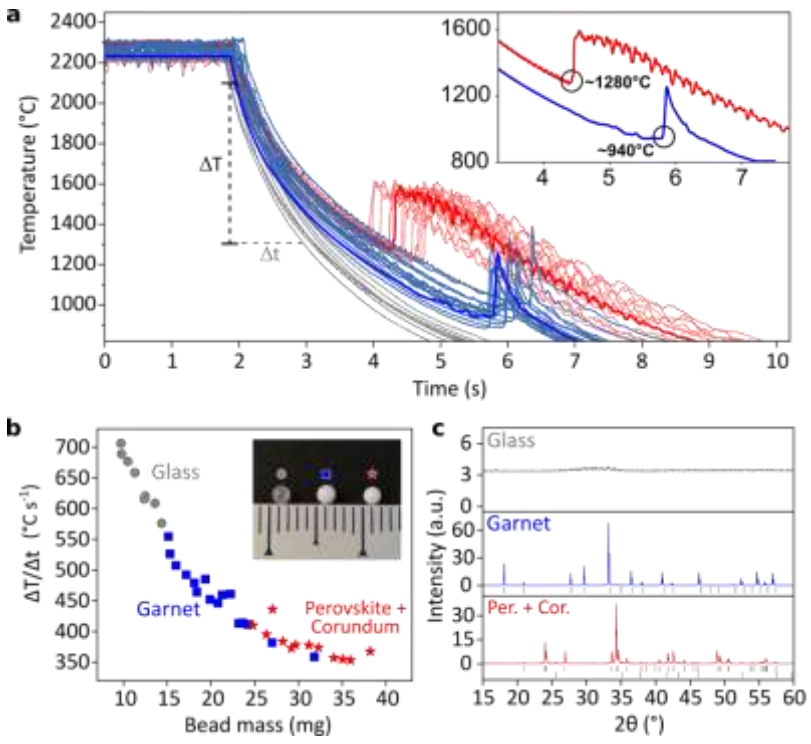

Fig 1.6[20] (a) *Cooling curves recorded in-situ for 36 quenched melts $Y_{3.2}Al_{4.8}O_{12}$, colour coded to show melts that formed glass (grey), garnet (blue) and mixed phase perovskite/corundum (red). The inset shows a direct comparison of crystallized from low temperature and high temperature undercooled liquid.* ***(b)*** *Cooling rates of three type sample with different mass.* ***(c)*** *PXRD patterns of the resulting samples.*

Furthermore, Shete et al.[21] conducted a study demonstrating the significant impact of crystallization in undercooled liquids at varying temperatures or cooling rates on the microstructure of the resulting crystals. ***Fig 1.7a*** and ***b*** illustrate the morphology of samples obtained through the crystallization of undercooled liquids at different temperatures and employing different cooling rates, respectively, using the ADL technique.

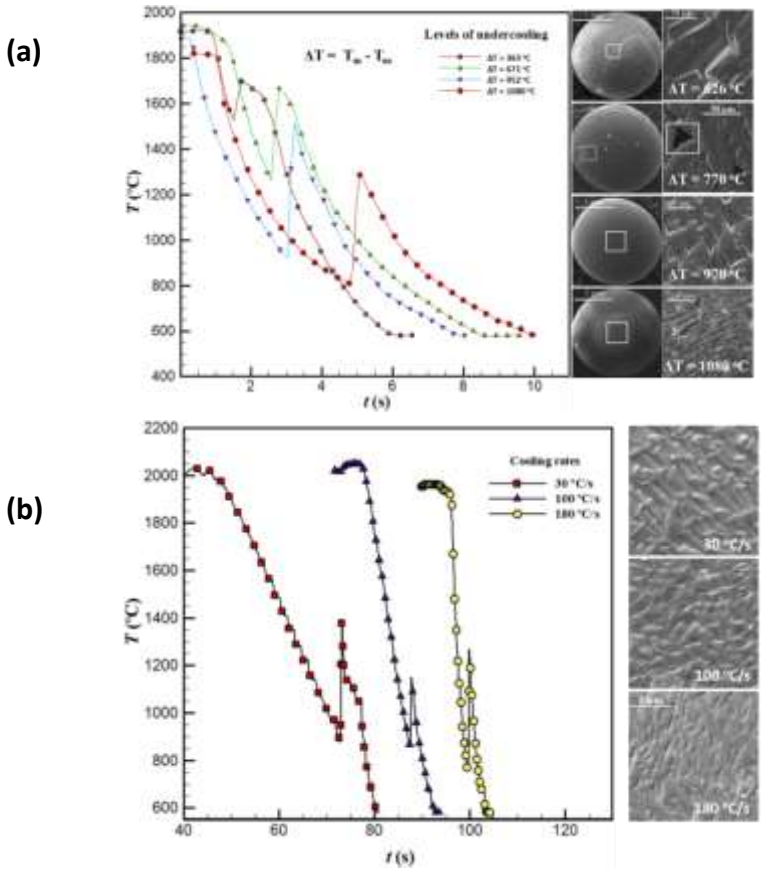

Fig 1.7[21] *Forsterite (Mg_2SiO_4).* ***(a)*** *Cooling curves for different levels of undercooling (left) and SEM images of a solidified spherule for different level undercooling, enlarged view of square box (right)* ***(b)*** *Cooling curves for experiments conducted at different cooling rates and SEM images.*

Based on the above description, it is evident that the ADL combined with laser heating serves as a highly efficient technique for achieving crystallization from the melt and producing glass. By controlling factors such as the gas type or melt mass, diverse cooling rates can be attained, thereby influencing the crystallization behavior and morphology of the resulting material. This method proves to be an exceptionally effective synthetic tool for synthesizing novel metastable compounds that are inaccessible through solid state reaction methods.

1.2.4 Synthesis of new compounds by aerodynamic levitation

In recent years our group has developed a number of new metastable and transparent ceramic materials using synthetic methods from crystallisation from glass and melt, which have shown excellent properties in optical and oxygen ion conductor applications.

$BaAl_4O_7$ compound in BaO-Al_2O_3 system could not be synthesised by conventional solid phase methods, but transparent polycrystalline $BaAl_4O_7$ ceramics were successfully synthesised using crystallisation from glass by ADL (see ***Fig 1.8a***). It is noteworthy that the previously unreported composition crystallized into different orthogonal polycrystalline forms, namely α-$BaAl_4O_7$ and β-$BaAl_4O_7$ (see ***Fig 1.8b***), by varying the annealing temperature [22]. Both crystalline phases exhibit a high degree of transparency and hold promise for various optical applications. The synthesis of this polycrystalline ceramic provides a new route for the synthesis of novel metastable compounds and offers potential applications for a range of transparent compounds in the optical field. Subsequently, $BaGa_4O_7$ gallate with substitution of gallium for aluminum glass compositions and related polycrystalline ceramics were prepared by ADL[23].

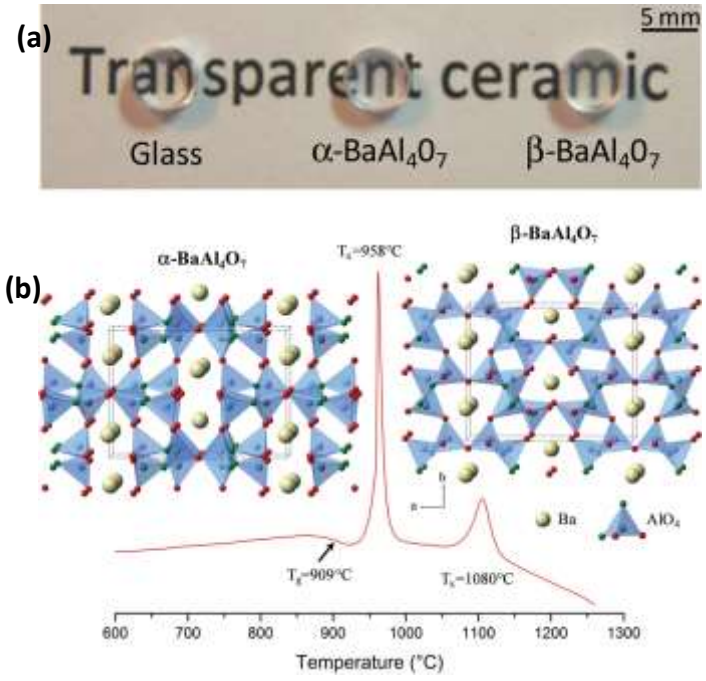

Fig 1.8[22] ***(a)*** *α-polymorph and β-polymorph polished transparent ceramics.* ***(b)*** *Crystal structures of the α- and β-$BaAl_4O_7$ polymorph and differential scanning calorimetry measurement of the $BaAl_4O_7$ glass.*

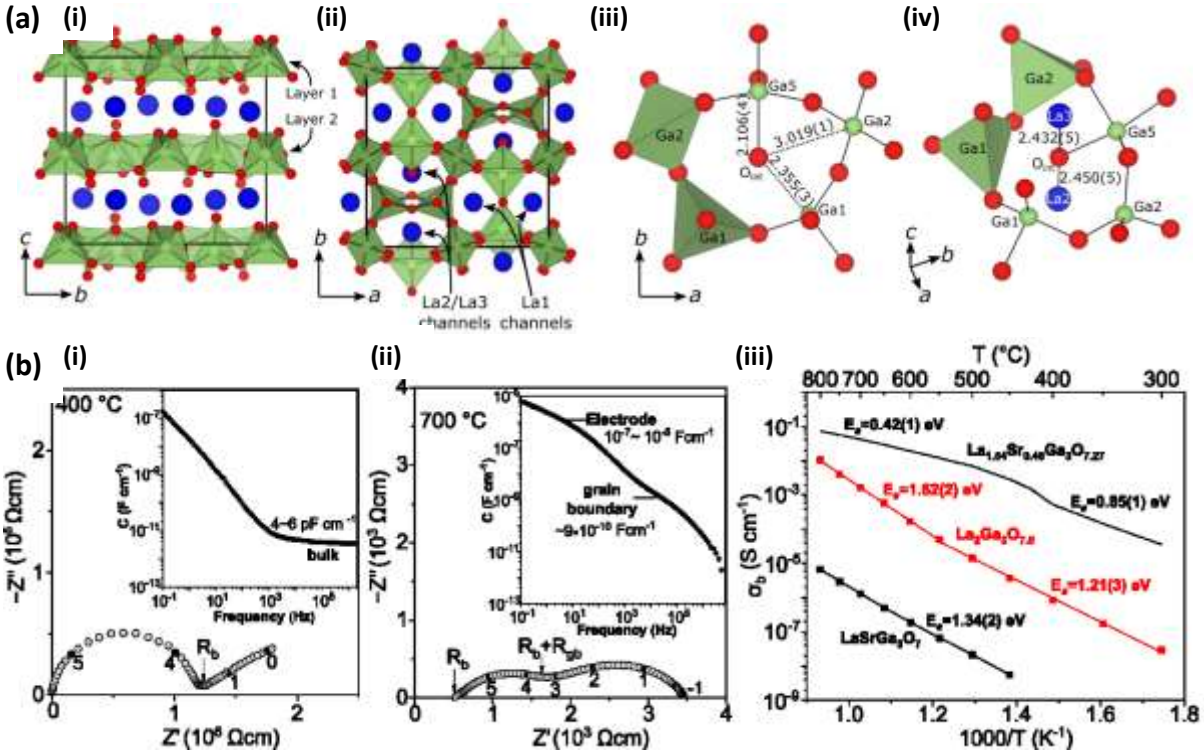

Fig 1.9[24] ***(a)*** *Crystal structure of $La_2Ga_3O_{7.5}$ in Ima2 along the (i) a- and (ii) c-axes and (iii and iv) local coordination environment of the interstitial oxide at the centres of the pentagonal rings.* ***(b)*** *Complex impedance plots at (i) 400 °C and (ii) 700 °C of the $La_2Ga_3O_{7.5}$ ceramic, and (iii) Arrhenius plot of the bulk conductivities for $La_2Ga_3O_{7.5}$ (red points) in comparison with those of $LaSrGa_3O_7$ (black points) and $La_{1.54}Sr_{0.46}Ga_3O_{7.25}$.*

The $La_{1+x}AE_{1-x}Ga_3O_{7+x/2}$ melilite group (AE = Ca, Sr, Ba and $0 \leq x \leq 0.64$) are excellent interstitial oxygen ion conductors owing to the ability of layered tetrahedral $[Ga_3O_{7+x/2}]$ network to accommodate and transport interstitial oxide ions[25]. An increase in the concentration of interstitial oxygen ions ($x \geq 0.65$) has the potential to enhance the ionic conductivity of this system. However, solid solution with only $x \leq 0.64$ can be achieved by the conventional solid state reaction method. Our group reported that a fully substituted $La_2Ga_3O_{7.5}$ (x = 1) melilite ceramic was obtained directly by crystallization from the melt (crystal structure see ***Fig 1.9a***) and this super- substituted ceramic exhibits stability at 830 ^{o}C and an ionic conductivity three orders of magnitude higher than that of a comparable $LaSrGa_3O_7$ ceramic (see ***Fig 1.9b***). These results suggest that synthetic methods based on melt crystallization can extend the range of solid solution compositions, leading to the development of new solid oxide ionic electrolytes with high concentrations of interstitial

oxide charge carriers[24]. Interestingly, this compound can also be made by a sol-gel method which illustrates that metastable materials isolated by ADL methods may also be accessible by other more widespread techniques[26].

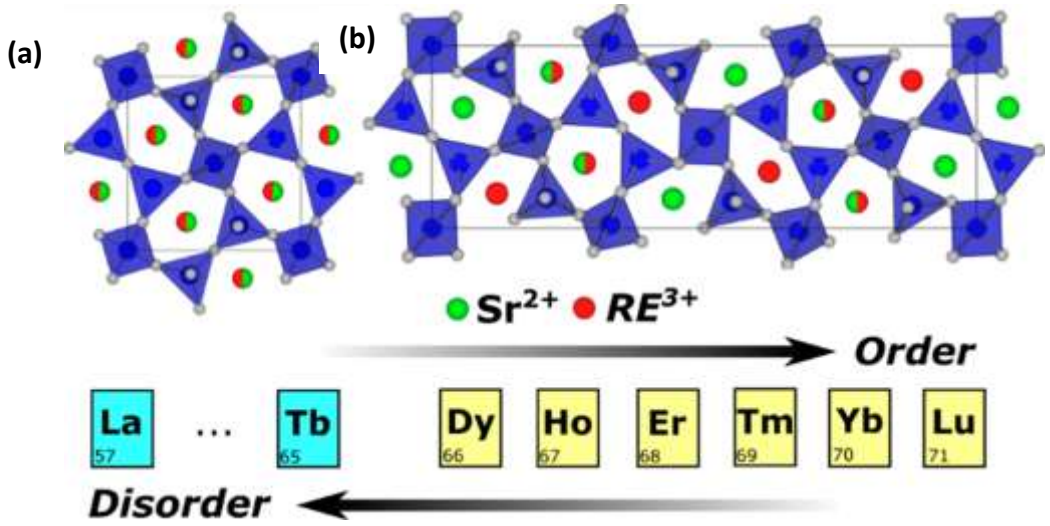

Fig 1.10[27] *Crystal structure of $SrREGa_3O_7$* ***(a)*** *(RE = La to Tb) in $P\bar{4}21m$ and* ***(b)*** *(RE = Dy to Lu) in 3 × 1 × 1 orthorhombic ($P2_12_12$) superstructure.*

The melilite $SrREGa_3O_7$ with the largest RE cation, i.e., RE = La to Tb and Y, possesses excellent luminescence properties and can easily be synthesized by conventional methods. However, the structure and properties of RE compounds with small ionic radii have not been investigated due to the difficult synthesis using solid-state reaction methods. Instead, a range of $SrREGa_3O_7$ (RE = Dy - Lu) metastable compounds have been shown to be obtained by crystallisation from glass using ADL. It is interesting to note that, in contrast to the conventional tetragonal ($P\bar{4}21m$) melilite structure which consists of mixed Sr/RE cationic sites, these compositions can form a 3 × 1 × 1 orthorhombic ($P2_12_12$) superstructure (see **Fig 1.10**). A series of structural studies have shown that proper control of the synthesis conditions by glass crystallisation can lead to the formation of the desired polymorphs, whether ordered or disordered. In addition, this cation ordering/disordering has been studied for its effect on RE luminescence spectral properties.[27]

In recent years, there has been a growing recognition that a wide range of materials, including non-silicate glasses, polymers, metals, and various non-oxide inorganic compositions, can form glasses. Contemporary theories on glass formation have reevaluated

the notion of substances as glass-forming agents and have acknowledged that any material can indeed transform into glass if it is cooled at a sufficiently rapid rate, preventing the restructuring of its atomic arrangement into the periodic structure necessary for crystallization. Consequently, the focus lies not on whether a material can form glass, but rather on determining methods to achieve accelerated cooling rates that impede crystallization[8]. With its notable advantages of achieving of high temperatures, rapid cooling rates, and absence of container contact, ADL combined with laser heating enables the fabrication of glasses that are unattainable through conventional melting methods. This includes systems with exceptionally high melting points and systems that necessitate swift critical cooling rates for glass formation. These glass systems often lack traditional glass-forming components like Si, B, Al and Ge, but they play an important role in optics, mechanical properties. Aluminate/galliumate glasses have been investigated for a wide range of applications, such as calcium aluminate glasses for near-infrared windows, optical storage and high strength optical fibres[28]. Our group has reported on a range of new rare earth aluminates/galliumates[20], barium aluminates/galliumates[22] and strontium aluminates/ galliumates[29] ceramic materials obtained by crystallization from glass, all of which have potential applications. In addition, the niobate system[30], titanate system[31] and tungstate system[32] have all been reported to be susceptible to glass formation by ADL methods. It is worth exploring the possibility that some new structures of metastable compounds may exist in these systems that have not been discovered.

From the above reports, it is clear that the using of crystallization from melt and glass by ADL is a very effective synthetic method for the synthesis of new metastable compounds as well as for the expansion of solid solution zones. In addition to above reports, this method successfully synthesised new highly non-stoichiometric YAG solid solutions[20] (see 1.4 Highly non-stoichiometric garnet). The synthesis of non-stoichiometric ratio garnet structures in this work was developed based on this report.

1.3 Functional compounds in RE_2O_3-Ga/Al_2O_3 (RE = Y, Gd, Lu) system

The RE_2O_3-Al/Ga_2O_3 system (RE = yttrium (Y), gadolinium (Gd), and lutetium (Lu)) is a

significant ceramic material system that has a wide range of applications in many fields such as electronics, catalysts, magnetic and optics due to its good thermal, chemical stability, and mechanical properties[33-34]. In the RE_2O_3-Al_2O_3 system, four different phases, namely perovskite $REAlO_3$ (REAP), hexagonal perovskite $REAlO_3$ (REAH), $RE_3Al_5O_{12}$ garnet (REAG) and monoclinic $RE_4Al_2O_9$ (REAM) have been reported with excellent optical properties, making them highly appropriate for various optics applications [35-37]. For instance, YAG:Ce^{3+} is employed as a yellow phosphor in LEDs[38], while LuAG:Ce^{3+}, YAM:Ce^{3+} exhibit scintillation performance[39-40], and YAP:Nd^{3+} is considered a potential laser materials[41]. In the RE_2O_3-Ga_2O_3 system, five compounds have been reported, including perovskite $REGaO_3$ (REGP), hexagonal $REGaO_3$ (REGH), $RE_3Ga_5O_{12}$ garnet (REGG), monoclinic $RE_4Ga_2O_9$ (REGM) and orthorhombic RE_3GaO_6 (REGO) [42-44]. Among these materials, apart from excellent optical materials such as YGG: Yb^{3+} laser material[45], YGH:Nd^{3+} infrared-red material[46] LuGG:Dy^{3+} white phosphor[47], GGG[48] , GGM[49] materials exhibit superb magnetic properties, while $RE_4Ga_2O_9$ material has remarkable oxygen ion and proton conductivity[50-51]. A range of compounds presented in this system is a great treasure trove for exploring new optical, magnetic and other potential functions materials.

In recent years, our group and cooperating groups found interesting non-stoichiometric YAG garnet and $(Lu/Mg)_4(Al/Si)_2O_9$ new compounds in these systems. Based on these two works, my PhD work focused on RE_2O_3-Al/Ga_2O_3 two systems.

1.4 Non-stoichiometric garnets

As an example, the generally accepted phase diagram of the Y_2O_3-Al_2O_3 binary system in ***Fig 1.11*** indicates that $Y_3Al_5O_{12}$, $YAlO_3$, and $Y_4Al_2O_9$ are a constant ratio compounds (line phases)[52]. However, in the study of the coefficient of thermal expansion of YAG garnet crystals in 1969, Geller observed an increase of the lattice in the Y-rich YAG due to the excess Y^{3+} occupying the octahedral Al lattice[53]. This phenomenon, known as anti-site defects, was found to affect the spectra of rare-earth doped phosphor[54], leading to further synthesis and structural studies of non-stoichiometric garnets have never ceased. However, restricted solid solution intervals have hindered investigations into their structural and optical properties in

recent decades[55]. $REAlO_3$ (REAP) is an excellent scintillator material. The cation antisite disordered has been determined to be energetically favourable in LuAP:Ce^{3+} and YAP:Ce^{3+} and it slowing delay the decay of the luminescence process[56]. Such antisite defects, in which the Y ion occupies the position of Al and vice versa, are one of the most common types of defects in YAP crystals, usually arising during high temperature crystallisation from the melt at temperatures above 2000°C, and have a significant impact on optical properties, although these types of antisite defects are difficult to detect by structural or morphological studies[56-57]. Therefore, the study of the extension of non-stoichiometric solid solutions of compounds in the RE_2O_3-Ga/Al_2O_3 (RE = Y, Gd, Lu) system and such anti-site defects is of great interest in determining how they affect the optical properties.

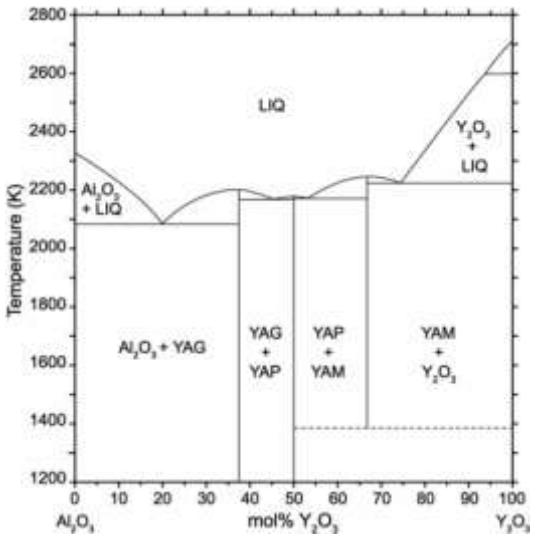

Fig 1.11[52] *Phase diagram of Al_2O_3-Y_2O_3.(YAP is $YAlO_3$ perovskite, YAG is $Y_3Al_5O_{12}$ garnet, and YAM is $Y_4Al_2O_9$ monoclinice phase)*

1.4.1 Garnet overview

Since the first synthesis of synthetic garnets, numerous new types of garnets have been designed, synthesized and applied in various fields[58]. Synthetic garnets are basically composed of rare earth oxides (RE_2O_3) and metal oxides (M_2O_3), of which the most representative synthetic garnet crystals are $Y_3Al_5O_{12}$ (YAG)[59], $Y_3Fe_5O_{12}$ (YIG)[60], $Gd_3Ga_5O_{12}$ (GGG)[61], $Gd_3Al_5O_{12}$ (GAG)[62], $Gd_3Fe_5O_{12}$ (GIG)[63], $Lu_3Al_5O_{12}$ (LuAG)[64] etc. There are also lithium-stuffed garnets, such as $Li_7La_3Zr_2O_{12}$ that have been extensively studied as solid-state

electrolytes for lithium ion batteries[65]. The crystal structure diagram of YAG garnet is shown in ***Fig 1.12***. The space group of garnet is *Ia*-3*d* with cubic symmetry with a = 12.002 Å. The chemical formula for garnet is usually written as $A_3[B]_2[C]_3O_{12}$, where A is the dodecahedral site with a coordination number of eight, while B and C are the octahedrally and tetrahedrally coordinated sites, respectively[66]. The possible ions at the A, B, C, sites are list in the ***Table 1.1***. Due to its unique structure, garnet structured compounds play a pivotal role in various fields, especially in optics. YAG: Ce^{3+} is the phosphors for LED[38], YAG: Nd^{3+} is excellent solid laser materials[67]. In addition, YIG and GIG are ferrimagnetic ceramics that are widely applied in passive microwave devices [68-69]. Recently, YIG and GIG have also been reported as lithium and oxygen ion conductors [70-71], in addition to belonging to a class of magnetic oxides with specific magnetic and magneto-optical properties.[72]

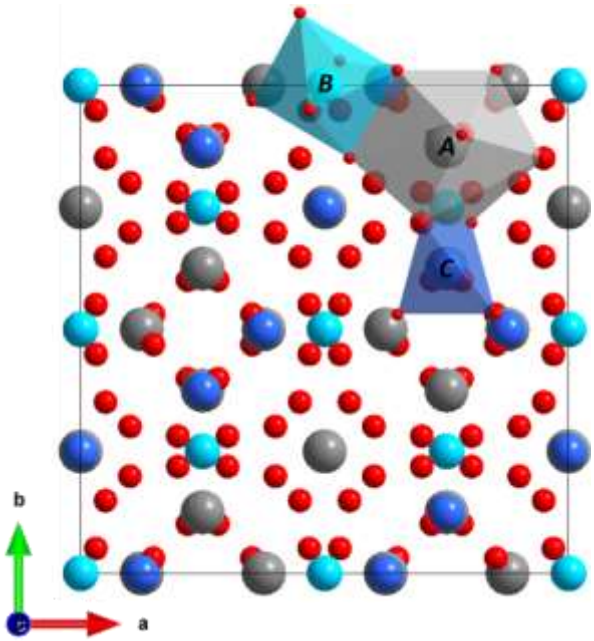

Fig 1.12 *Crystal structure of $A_3[B]_2(C)_3O_{12}$ garnet along c axe.*

Table 1.1 *Atom occupying at site A, B, C.*

Site	Coordination number	Coordinating polyhedron	Occupying Ion
A	8	Dodecahedron	Y, Lu, Gd, Ce, Pr, Nd, Yb, Tm, Ho
B	6	Octahedron	Al, Ga, Cr, Sc, Mn, Mg
C	4	Tetrahedron	Al, Ga, Si

The modulation of different emission colors and optimization of luminescence efficiency in garnet optical material can be achieved not only by adjusting the dopant type and concentration, but also flexible substitution of cations, which stem from the dodecahedra that can accommodate rare earth ions (e.g. Y^{3+}, Lu^{3+}, Gd^{3+}, Ce^{3+}, Tb^{3+}, Eu^{3+}, Yb^{3+}, Tm^{3+}) and BO_6/CO_4 polyhedra that can be replaced by metal ions (e.g. *B* = Al^{3+}, Ga^{3+}, Si^{4+}, Ge^{4+}, *C* = Al^{3+}, Ga^{3+}, Sc^{3+}, Sb^{3+}….)[73-75]. Generally, (1) replacing single cations in A sites with larger trivalent cation(Gd), (2) adjustment the ratio B/C of cation, and (3) chemical unit substitution of Mg^{2+}-Si^{4+} for Al^{3+}-Al^{3+}, which effectively produce new color or improve luminescent properties by directly or indirectly altering the luminescent ion environment are commonly used substitution strategies. The substitution of the A, B, C site, or the adjustment of the B/C site ratio, essentially interferes with the local crystal environment of the three sites and thus affects the transition behaviour of the luminescent ion. Theoretically, for non-stoichiometric compositions the adjustment of the A/B ion ratio might affect the crystal environment at the A and B sites and thus the spectral behaviour.

1.4.2 Development of non-stoichiometric garnets.

Research into non-stoichiometric garnet has continued since the discovery of the "anti-site defect" in garnet in 1972[53]. Studies by Ashuro[54] and Voronko[76] et al. showed that the partial substitution of Y^{3+} into the Al^{3+} site in YAG (16a) resulted in a local distortion of the octahedral environment, affecting the environment of the 24d lattice in the dodecahedron and influencing the spectral properties of the rare earth ions in the garnet host. The extremely low defect concentrations these compositions difficult to study experimentally. Patel et al. reported that the non-stoichiometric YAG with only 2 mol% excess on the Y-rich side and 0.2 mol% excess on the Al-rich side synthesized using the solid phase method and also predicted the defect structure associated with this deviation using atomistic simulations, which indicates that it is difficult to achieve high non-stoichiometric ratios of garnet using the solid phase method and component deviations in YAG are more likely to occur on the Y-rich side rather than the Al-rich side[55]. Meanwhile, computational simulations of non-stoichiometry in synthetic $A_3B_5O_{12}$ garnet by Milanese show that the

non-stoichiometry in garnet is dominated by the formation of A_B anti-site defects and the corresponding energy decreases with decreasing size of the A cation[77]. However, the synthesis of nonstoichiometric garnets has been an intractable problem, thus limiting the further exploration and application [78-81]. In studying phase separation, crystallisation and polyamorphism in Y_2O_3-Al_2O_3 systems, Skinner[82] used ADL with laser heating to synthesize YAG compositions containing glassy and crystalline YAG inclusions (see ***Fig 1.13a***). This method has been applied to successfully obtain transparent YAG-Al_2O_3 ceramics[83] as well as YAG glass with 15% crystalline phase[84]. Additionally, RE_2O_3-rich glass composition from RE_2O_3-Al_2O_3 system has been shown to be obtained by ADL methods (see ***Fig 1.13b***), but unfortunately has not been studied in depth[85]. This information tells us that some non-stoichiometric rare earth aluminate compositions can be obtained as glasses by ADL, with the possibility of obtaining highly non-stoichiometric garnet by low temperature induced crystallization from glass.

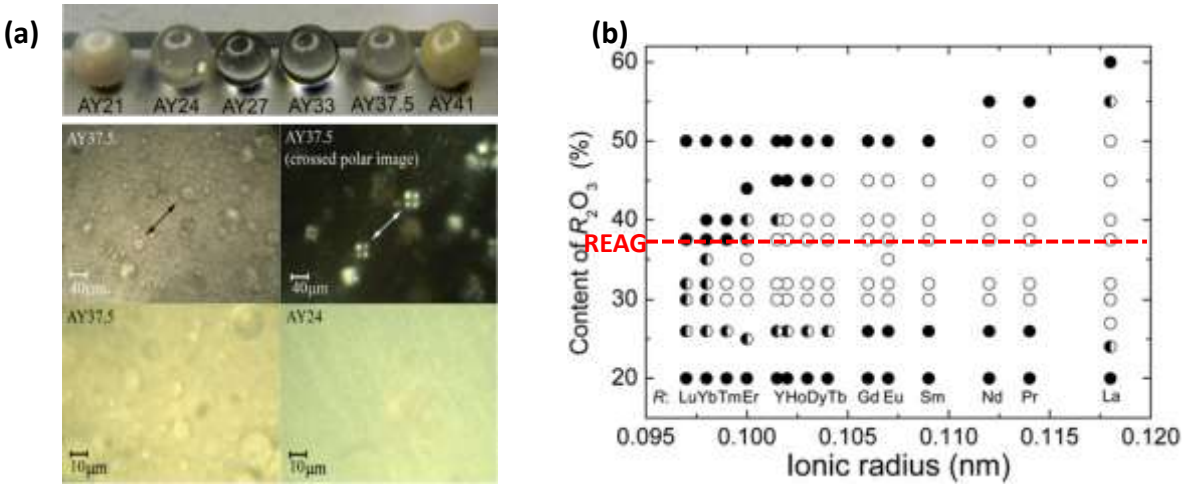

Fig 1.13 (a) *Photographs of 2.3 - 2.5 mm diameter solid samples of $(Y_2O_3)_x(Al_2O_3)_{1-x}$ ($0.24 \leq x \leq 0.32$) produced by the ADL in upper, optical images of sections of the spheres labelled AY37.5 in lower.[82]* ***(b)*** *Glass forming region of composition in the RE_2O_3–Al_2O_3 system synthesized by ADL at 600-800$^oCs^{-1}$ cooling rate.(Open circles, half-filled circles, and closed circles represent glass, partially crystallized, and crystallized, respectively. Red dotted line is garnet for composition [85])*

Our group has recently synthesized highly non-stoichiometric YAG ceramics $Y_{3+x}Al_{5-x}O_{12}$ with an compositional range $0 \leq x \leq 0.40$ using crystallization from melt and glass methods by ADL techniques[86], demonstrating that non-stoichiometric dramatic impact on

the emission colour[20] (see ***Fig 1.14***). In the preparation of a series of YAG we found that the type of levitation gas and masses of samples affected the cooling rate and crystallisation behaviour of the melt (detailed description in ADL section). The SPD refinement of a series of YAG samples showed a clear structural trend with a strong linear increase in unit cell volume in the range of $0 \leq x \leq 0.40$, consistent with the formation of solid solution (see ***Fig 1.14a*** upper). In addition we find that excess Y occupies the B site of Al and that the Y in B site increases linearly with increasing Y content and the solid solution limit is x = 0.4 (see ***Fig 1.14a*** lower) TEM, and $^{89}Y/^{27}Al$ MAS-NMR and EXAFS have also been used to characterise octahedral Y^{3+} local environment. These results suggest that six-coordination Al^{3+} at octahedral *B* site can be occupied by Y^{3+} in non-stoichiometric YAG (see ***Fig 1.14b***). The variable temperature data show the thermal decomposition behaviour of the non-stoichiometric YAG, which starts to decompose at 1350 ℃ and eventually decomposes into stoichiometric YAG, YAP and YAM. Interestingly, we found that the dominant emission colour of the up-conversion phosphor $Y_{3.2}Al_{4.8}O_{12}$: Er^{3+}/Yb^{3+} is green instead of red in stoichiometric YAG matrix due to the Er^{3+} being distributed on the inequivalent AO_8 and new BO_6 sites ns-YAG, altering its luminescence properties (see **Fig 1.14c**). By contrast, the colour of the ns-YAG:Ce^{3+} phosphor to $Y_{3.2}Al_{4.8}O_{12}$: Er^{3+}/Yb^{3+} is hardly affected by non-stoichiometric since the larger ionic radius of Ce^{3+} only occupies the larger dodecahedral sites in ns-YAG (see **Fig 1.14d**). From this we believe that the distribution preferences in the non-stoichiometric YAG of the different sizes of rare earth are different. In addition to ns-YAG, non-stoichiometric $Gd_{3.2}Al_{4.8}O_{12}$ and $Gd_{3.2}Ga_{4.8}O_{12}$ have been shown to be accessible by ADL and deserve further exploration for their synthesis in non-stoichiometric solid solutions and their applications in optics. The synthesis of highly non-stoichiometric YAG opens up new avenues for the synthesis and application exploration of other high non-stoichiometric garnets. It is important to conduct in-depth studies on the synthesis and properties of a series of high non-stoichiometric garnet represented by YAG. And from the YAG study we have raised new questions. The ionic radius of Gd^{3+} is larger than Y^{3+}, so how much Gd can occupy the Al site (solid solution range)? The B site is occupied by the larger Gd^{3+}, does it provide more space for the larger RE^{3+} ion to occupy the B site? Do different ions differ in their sensitivity to luminescent behaviour in a new coordination environment? These

questions will be addressed in my PhD work.

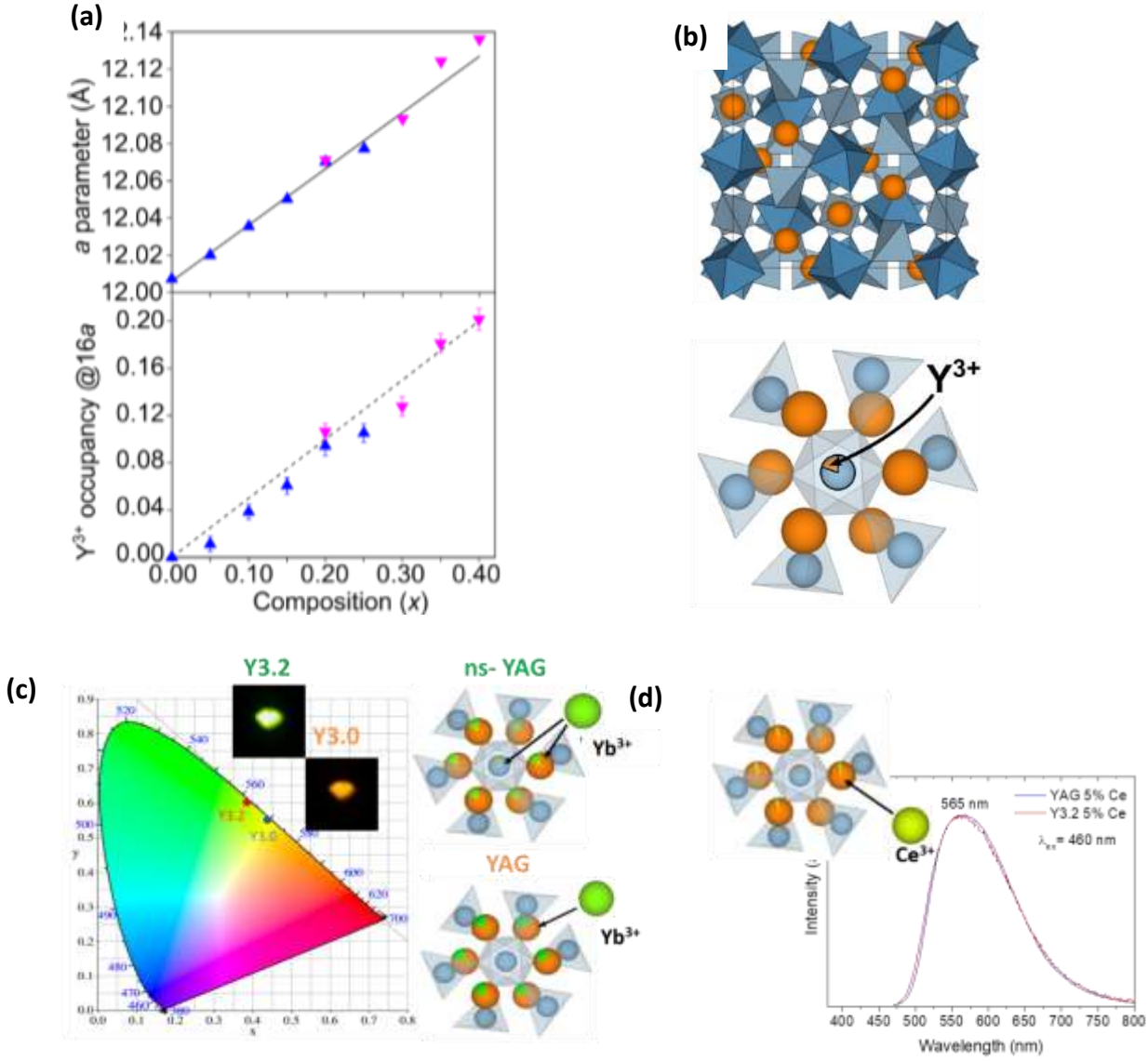

Fig 1.14[20] ***(a)*** *Refined lattice parameter a of $Y_{3+x}Al_{5-x}O_{12}$ (x = 0 - 0.4) (solid line upper), and refined occupancy of the B site by Y with nominal occupancy overlaid (dashed line lower).* ***(b)*** *The structure of $Y_{3.4}Al_{4.6}O_{12}$ along (100) (upper), and a fragment projected along (111) showing the three different cation environments A, B and C (lower) (orange atoms =Y^{3+}; dark blue octahedra = AlO_6; light blue tetrahedra = AlO_4).* ***(c)*** *CIE chromaticity coordinates and photographs of $Y_{3+x}Al_{5-x}O_{12}$:2%Er^{3+}/20%Yb^{3+} (x = 0, 0.2) taken under 980 nm laser irradiation in the dark.* ***(d)*** *Down-conversion emission spectra of $Y_{3+x}Al_{5-x}O_{12}$:5%Ce^{3+} (x = 0, 0.2) after 460nm excitation. The insets show structural fragments representing the Rietveld-refined locations of the dopant ions in each case.*

1.4.3 Previous studies of GAG, GGG, and GAGG-based optical materials.

As a well-known garnet compound, YAG has been extensively researched and applied in phosphors for fluorescent lamps, field emission displays (FED) and white LEDs owing to its excellent chemical stability, radiation stability, high creep resistance, and optical isotropy[87]. Compared with YAG, however, GAG and GGG has its own unique ascendancy in optical applications. GAG compounds interest lies in (1) the presence of Gd^{3+} which can act as a new activator (intrinsic $^8S_{7/2} \rightarrow {}^6I_J$ transition) absorbing energy, enhance the luminescence efficiency by effective energy transfer to other activators; (2) the lower electronegativity of Gd^{3+} (χ = 1.20) compared to Y^{3+} (χ = 1.22) from which may emerge new emission properties and a possible improvement in emission intensity; (3) the higher theoretical density (5.97 gcm^{-3}) and atomic weight compared to YAG (4.47 gcm^{-3}) while aiming at scintillation applications. Therefore, recent research on GAG and GGG based optical materials emerges endlessly.[88]

Down-conversion (DC) materials with GAG-based host have been extensively studied in recent years. Though basically all rare-earth ions can serve as activators, Ce^{3+}, Eu^{3+}, Tb^{3+}, and Dy^{3+} have received more extensive research attention due to their ability to avoid non-radiative crossover relaxation, which is attributed to the wide energy gap between the lowest emission state and the ground state. Li et al conducted detailed studies on synthesis and optical properties of $[(Gd_{1-x}Lu_x)_{1-y}Ce_y]$AG yellow phosphors[89], $[(Gd_{1-x}Lu_x)_{1-y}Eu_y]$AG red phosphors[90], $(Gd_{1-x}Tb_X)$AG green phosphors[91], and $[(Gd_{1-x}Lu_x)_{1-y}Dy_y]$AG white phosphors[92] between 2013 to 2016. The GAG-based yellow phosphor exhibited a stronger red component in its emission making it more desirable for warm-white LED lighting than the well-known YAG: Ce^{3+} and LuAG: Ce^{3+} yellow phosphors (see ***Fig 1.15a***)[89] Since Gd ions can absorb energy and transfer it to rare earth ions, GAG phosphors exhibit better and stronger emission and better quantum efficiency[91]. It is also reported that using Gd as a sensitizer, by adjusting the content ratio of dual dopants, high-efficiency phosphors with different color emission can be prepared[92-93](see ***Fig 1.15b***).

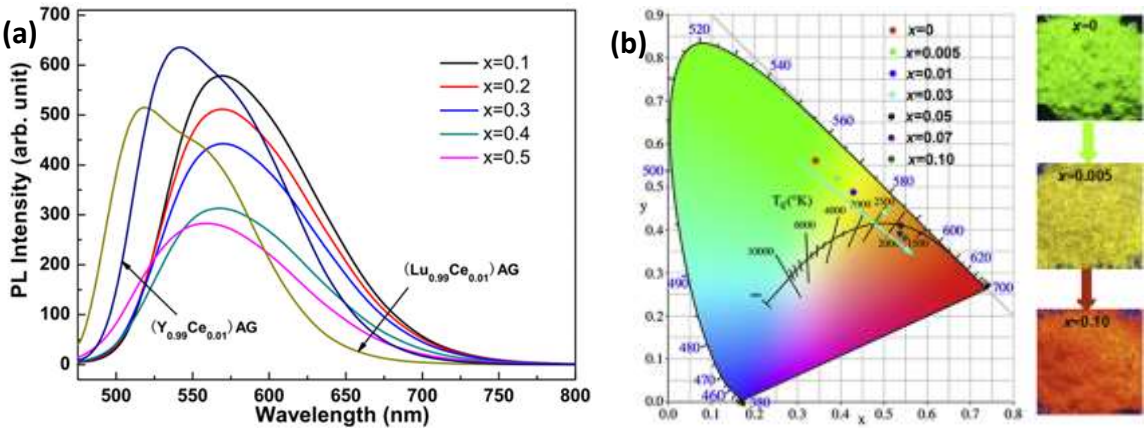

Fig 1.15 (a) *PL behaviors of the* $[(Gd_{1-x}Lu_x)_{0.99}Ce_{0.01}]AG$ *phosphors with the* $(Y_{0.99}Ce_{0.01})AG$ *sample included for comparison.*[89] ***(b)*** *CIE chromaticity diagram for the emission of* $[(Gd_{0.8}Lu_{0.2})_{0.9x}Tb_{0.1}Eu_x]AG$ *phosphors under 275 nm excitation.*[93]

Up-conversion (UC) materials have found a wide range of applications in photovoltaic cells, solid state lasers and anti-counterfeiting fields, as well as bio-labels for medical diagnosis and treatment due to their ability to convert long wavelength radiation (e.g. near infrared light) to short wavelength radiation (e.g. visible light) via a two-photon or multi-photon mechanism. Even though some activators such as Pr^{3+}, Sm^{3+}, Ho^{3+}, Er^{3+} and Tm^{3+} have themselves been able to produce UC emission, their efficiency is usually rather limited due to their unsatisfactory NIR/IR excitation. Therefore, Yb^{3+} is widely used as a co-dopant to improve NIR absorption. In the past decade, Ho^{3+}/Yb^{3+}, Er^{3+}/Yb^{3+}, Tm^{3+}/Yb^{3+}, Tb^{3+}/Yb^{3+}, Eu^{3+}/Yb^{3+} co-doped GAG and GGG up-conversion materials have been intensively investigated and shown excellent up-conversion performance. Lee et al. reported intense green and red emission in the GAG:3%Er^{3+}/10%Yb^{3+} system (see ***Fig 1.16a***)[94] and found that the up-conversion material GAG:Ho^{3+}/Yb^{3+} exhibited intense green and red emission with an emission behaviour of two-photon processes[95]. In 2005, Pandozzi et al. reported intense up-conversion UV ($^1D_2$-$^3H_6$), blue ($^1D_2$-$^3F_4$), blue-green ($^1G_4$-$^3H_6$), red ($^1G_4$-$^3F_4$) and near-IR ($^1G_4$-^{3} H_5/ $^3H_4$-$^3H_6$) emission by excitation of Yb^{3+} in GGG-doped Tm^{3+}/Yb^{3+} (see ***Fig 1.16b***)[96]. In 2009, Guez et al. synthesized nano-GGG: Tb^{3+}/Yb^{3+} and Eu^{3+}/Yb^{3+} materials and observed green/blue up conversion emission from $^5D_3$/ $^5D_4$ - ^f7F_J of Tb^{3+} and red up-conversion emission $^5D_0$ - ^7F_J of Eu^{3+} under 975 nm excitation of Yb^{3+}, respectively.[97]

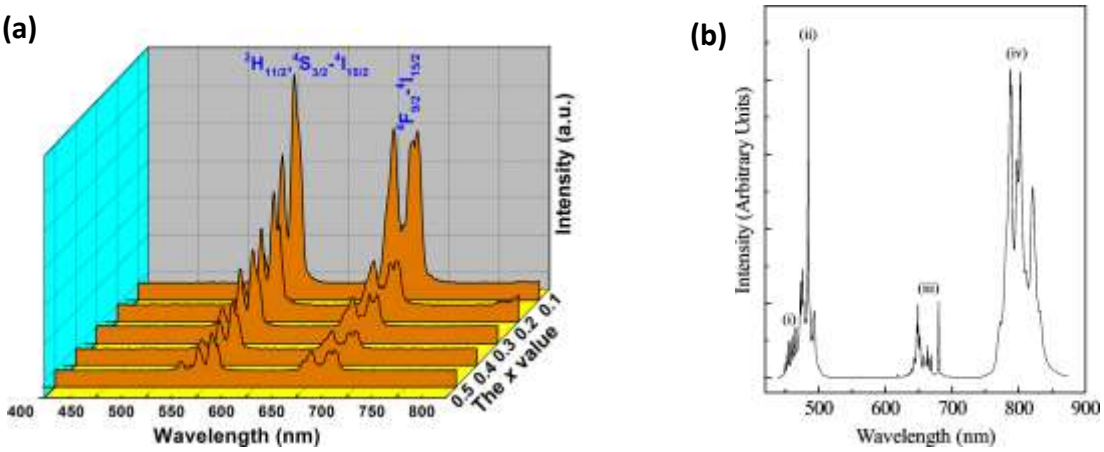

Fig 1.16 (a) *Comparison of the up-conversion spectra of* $(Gd_{1-x}Lu_x)_{0.948}Yb_{0.05}Er_{0.002}]_3Al_5O_{12}$ *with different x value.*[94] ***(b)*** *Room temperature up conversion spectrum of nano-crystalline* $Gd_3Ga_5O_{12}:Tm^{3+}/Yb^{3+}$ *showing the (i)* $^1D_2$-$^3F_4$*, (ii)* $^1G_4$-$^3H_6$*, (iii)* $^1G_4$-$^3F_4$*, and (iv)* $^1G_4$-$^3H_5$/$^3H_4$-$^3H_6$ *visible transitions.*[96]

Persistent phosphors continue to inspire researchers because of their wide range of civil possibilities such as security displays, decoration, as well as advanced technologies such as bio-imaging, optical image storage, anti-counterfeiting, water disinfection, etc.[98] The principle of persistent materials luminescence is typically explained as an electron capture and release process, which means that when a persistent phosphor is excited by effective optical charging (ultraviolet (UV) light, visible light, or NIR light), an electron-hole (e-h) pair is created and the excited electrons from the conduction band (CB) are trapped by an electron trap (capture process) and then the trapped electrons are released by thermal stimulation of the CB (release process) and are re-trapped by the luminescent centre, producing a form of thermo-luminescence. Therefore, a design strategy known as conduction band engineering, which is a adjusting of the depth between the bottom of the conduction band and the electron trap to create an energy gap that is conducive to electrons escape, is a key point in designing persistent phosphors.[99-100]

The larger dodecahedral sites and the smaller octahedral sites in the garnet structure are ideal for the lanthanide ions [$Ln^{2+/3+}$] and the smaller radius Cr^{3+}, respectively, making it possible to obtain a variety of doping strategies with different local crystal fields. Garnet-based persistent phosphor has therefore been extensively studied and has made great progress in recent years. In the study of garnet-based persistent materials, CB engineering has been applied and more lasting and brighter persistent materials have been

designed by adjusting the amount of Ga[101-102]. For example, the Ce^{3+}/Cr^{3+} doped YAGG[103], GAGG[104], LuAGG[103] exhibits excellent yellow to green persistent luminescence by adjusting the Al/Ga ratio (***Fig 1.17a***), and shows stronger persistent luminescence than conventional Sr-based persistent phosphors[105]. Bobert et al. reported that changing the Ga:Al ratio can modulate the energy gap and thus the spectral properties of $Gd_{2.97}Tb_{0.03}Ga_{5-x}Al_xO_{12}$ persistent luminescence phosphors, and discussed the effect of the Ga:Al ratio on the capture/release of electrons[106]. In addition, Xu et al. reported that GGG: Eu^{3+}/Cr^{3+} has excellent red persistent luminescence properties (see ***Fig 1.17c***)[107] and found that adjusting the concentration ratio from doped Tb^{3+} and Eu^{3+} in GGG host materials gives white long afterglow materials[108]. These results suggest that adjusting the ratio of Al/Ga at the B site can affect the depth of electron traps to prepare more lasting luminescent materials.

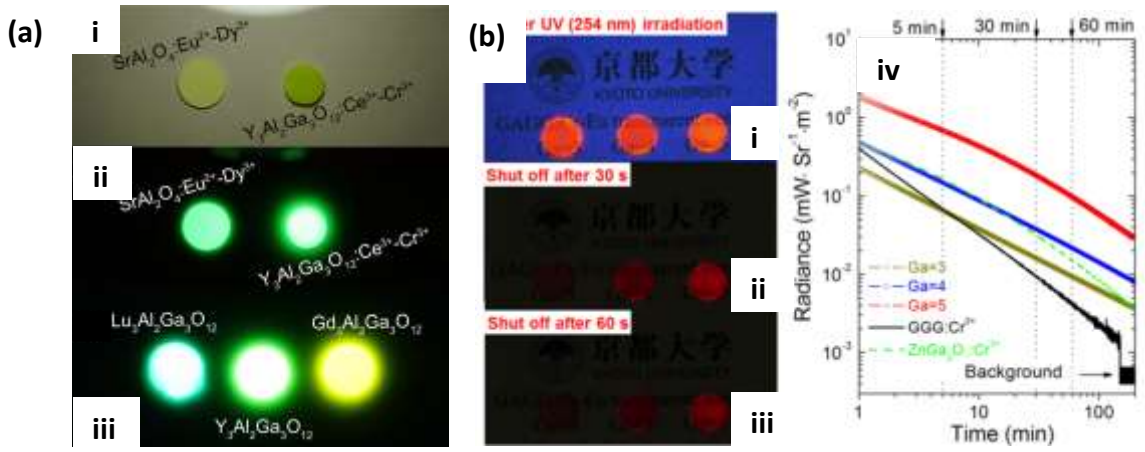

Fig 1.17 (a) *Image of $SrAl_2O_4$: Eu^{2+}-Dy^{3+} (left) and $Y_3Al_2Ga_3O_{12}$, $Lu_3Al_2Ga_3O_{12}$, and $Gd_3Al_2Ga_3O_{12}$: Ce^{3+}-Cr^{3+} (right) (i) under white-LED illumination and (ii) 5 min after excitations ceased.* ***(b)*** *Photographs of the GAGG: Cr^{3+}-Eu^{3+} transparent ceramics with different Ga^{3+} contents (x = 3, 4, 5) under UV 254 nm lamp and (iv) persistent decay curves.*

1.5 Monoclinic $Lu_4Al_2O_9$ and SiO_2 solubility

Feng et al.[75] developed a new $Lu_{3-x}Y_xMgAl_3SiO_{12}:Ce^{3+}$ garnet red phosphor that modifies the crystal field environment to enable emission redshift by replacing Lu in the dodecahedron with Y and substituting the AlO_6/AlO_4 chemical unit with an MgO_6/SiO_4 polyhedron. And in this work, PXRD consistently showed the presence of an unknown

second phase. SEM-EDS determined the composition of this new phase to be $Lu_{3.5}Mg_{0.5}Al_{1.5}Si_{0.5}O_9$. There does not appear to be any research on this compound through literature research. Instead, subsequent synthetic studies on this sample showed that its XRD pattern matches well with $Lu_4Al_2O_9$. In response to this finding, we suggest that Lu/Mg and Si/Al double-substituted solid solutions like garnet could exist base on the $Lu_4Al_2O_9$ structure. In addition, we believe that Si/Al substitution solid solutions may also be present. We therefore carried out a literature survey on $Lu_4Al_2O_9$, $Lu_4(Al/Si)_2O_9$ and $(Lu/Mg)_4(Al/Si)_2O_9$ solid solutions.

For $Lu_4Al_2O_9$ in Lu_2O_3-Al_2O_3 system (see ***Fig 1.18***)[109], despite Wu investigation of the phase diagram of the of the Lu_2O_3-Al_2O_3 system as early as in 1992, which revealed the existence and melting of $Lu_4Al_2O_9$ at 2313 K under an inert atmosphere[110], subsequent studies have demonstrated that $Lu_4Al_2O_9$ can only exist at high temperatures and decomposes during cooling to garnet and Al_2O_3[111-112]. Although the synthesis of $Lu_4Al_2O_9$ single crystals and their crystal structures were reported in 2020, studies of the optical properties of this compound have been missing[113]. In addition to monoclinic perovskite, $YAlO_3$ and $GdAlO_3$ have been reported to exist in a hexagonal perovskite phase, which is a potential optical material, while the synthesis of the isomorphic hexagonal $LuAlO_3$ is also worth exploring. Therefore, $Lu_4Al_2O_9$ and hexagonal $LuAlO_3$ compounds could have potential for optical applications, but their synthesis is a great challenge.

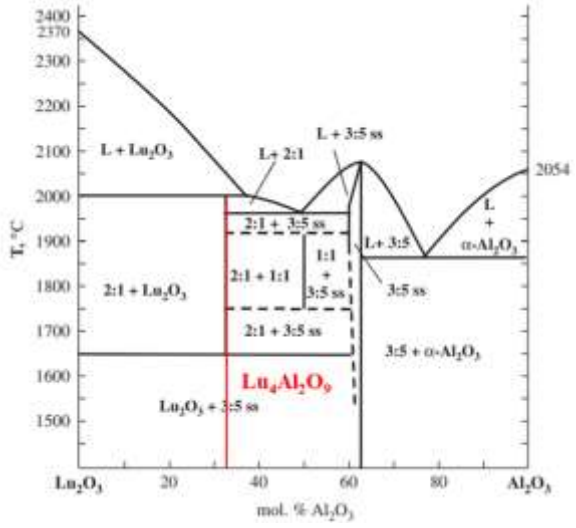

Fig 1.18[109] *Al_2O_3-Lu_2O_3 system phase diagram.(red line is $Lu_4Al_2O_9$ compound)*

1.5.1 $Lu_4Al_2O_9$ structure

In the RE_2O_3-Al_2O_3 system, in addition to $REAlO_3$ perovskite structure, $RE_3Al_5O_{12}$ garnet structure, rare earth aluminates with the formula $RE_4Al_2O_9$ (where RE = La, Nd, Ce, Eu, Gd, Tb, Dy, Ho, Er, Yb, Lu and Y) can be produced when RE_2O_3:Al_2O_3 = 2:1. The $RE_4Al_2O_9$ series of compounds exhibit a monoclinic crystal structure with the space group $P2_1/c$, as depicted in ***Fig 1.19***. The structure contains two crystallographically distinct Al sites, four RE sites, and nine O sites. Of the four Lu atoms, RE1 and RE3 are coordinated by seven oxygen atoms, and RE2 and RE4 are coordinated by six oxygen atoms to form a distorted octahedron as shown in ***Fig 1.19a*.** The two 4 coordinated Al tetrahedra are joined by a shared O5 atom to form an Al_2O_7 dihedral oxyaluminate group (Fig ***1.19b***)[113].

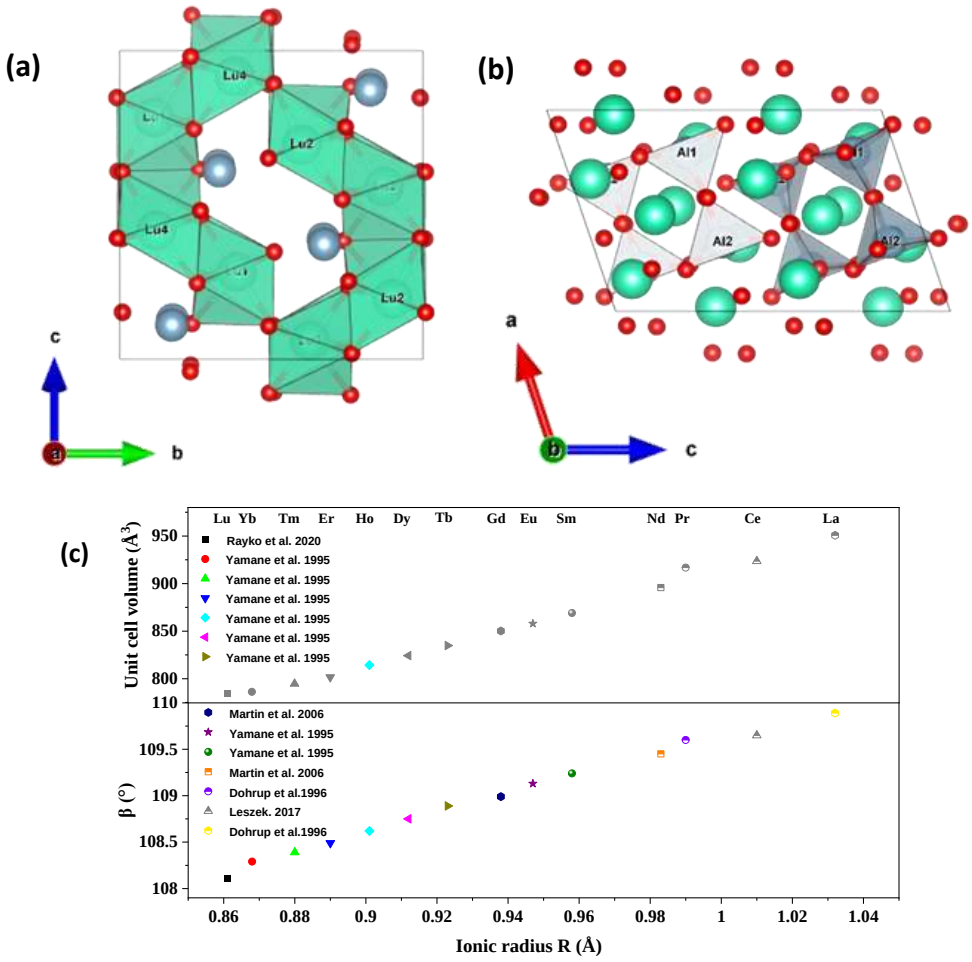

Fig 1.19 *Crystal structure of $Lu_4Al_2O_9$* ***(a)*** *the Lu centered polyhedra viewed down a axis* ***(b)*** *the Al_2O_7 ditetrahedra viewed down b axis.* ***(c)*** *The cell parameters β-angle and cell volume V of $RE_4Al_2O_9$ vs RE^{3+} ionic radius.*

A range of $RE_4Al_2O_9$ compounds have been reported in detail after Warshaw (1959) first reported the presence of $Y_4Al_2O_9$[114]. However, structural information on $Lu_4Al_2O_9$ has been missing, because $Lu_4Al_2O_9$ is only stable at temperatures of 1650-2000°C and decompose on cooling[112]. It was not until 2020 that a single crystal of $Lu_4Al_2O_9$ was synthesized to determine the detailed crystal parameters with cell parameter a = 7.236 (2) A˚ , b = 10.333 (2) A˚ , c = 11.096 (3) A˚ ,and = 108.38 (2)[113]. The cell parameters a, b, c, β-angle and cell volume V of $RE_4Al_2O_9$ vary linearly with increasing atomic radius as shown in ***Fig 1.19c***.[115]

1.5.2 Previous studies on $RE_4Al_2O_9$ optical materials.

The $Y_4Al_2O_9$ material is the most extensively studied optical host material in the $RE_4Al_2O_9$ family due to its exceptional properties, such as high stiffness, wide bandgap, high mechanical strength and high dielectric constant. Moreover, the large band gap (4eV) of YAM confirms its excellent transparency over the entire visible area, which strongly prevents any reabsorption capability of the emitted light and thus reduces the possibility of emission loss[116]. On the other hand, the YAM system is more complicated than the YAG and YAP systems, because its crystal structure contains four different Y^{3+} sites that can be replaced by trivalent rare earth (RE^{3+}) ions. Recent studies suggest that YAM: Ce^{3+} is a very promising scintillator material[40] and YAM: Eu^{3+} exhibits excellent luminescence properties[117]. The YAM structure contains four yttrium sites, which vary considerably in terms of positional symmetry, coordination number and backbone length. Therefore, understanding the correspondence between the crystal structure and spectral characteristics of this material allows for the design of new optical materials or improved optical properties. Kaczkan et al. employed optical absorption, laser selective excitation techniques and luminescence attenuation to reveal that the Sm^{3+}, Pr^{3+}, and Eu^{3+} ions in YAM occupy four, three different sites[118-121]. They also reported that the transition experiences a certain degree of shift and change in intensity at different sites due to the crystal field and local symmetry, affecting the emission color shift towards a high color rendering index. Although the related oxides of $RE_4Al_2O_9$ have been extensively studied for optical properties[122-123], the properties of $Lu_4Al_2O_9$ remain inadequately investigated.

1.5.3 Ternary solid solutions based on $RE_4Al_2O_9$ in the Re_2O_3–Al_2O_3–SiO_2 system

In the RE_2O_3-Al_2O_3-SiO_2 system, two extended ternary solid solutions, $RE_{9.33+2x}(Si_{1-x}Al_xO_4)_6$ (x = 0 - ~ 0.3) and $RE_4Al_{2(1-x)}Si_{2x}O_{9+x}$ (x = 0 - ~ 0.4) based on the quasi-binary phases $RE_{9.33}(SiO_4)_6O_2$ and $RE_4Al_2O_9$, respectively, have been reported[124]. The chemical formulae of the solid solutions $Y_4Al_{2(1-x)}Si_{2x}O_{9+x}$ (x = 0 - ~ 0.3)[125], $Nd_4Al_{2(1-x)}Si_{2x}O_{9+x}$ (x = 0 - ~ 0.4)[126] and $Gd_4Al_{2(1-x)}Si_{2x}O_{9+x}$ (x = 0 - ~ 0.33)[127] based on monoclinic $RE_4Al_2O_9$ were determined by SEM-EDX and illustrate the different Al/Si-order-disorder states at different temperatures. However, the crystal structures of the solid solutions were not examined in detail. Thus, it is worth exploring the synthesis and detailed crystal structures of $Lu_4Al_2O_9$ and solid solutions of Si substituted Al in $Lu_4Al_2O_9$ as they may serve as potential new optical host materials. These results give us some ideas about the possible development of new luminescence materials by the substitution strategy of substituting the tetra-coordinated Al^{3+} (0.535 Å) with the smaller Si^{4+} (0.4 Å) or substitution of Lu-Al by Mg-Al in $Lu_4Al_2O_9$ may be a viable.

1.6 Chapter conclusion

In this chapter, non-equilibrium crystallization methods (crystallisation from the glass and melt) are discussed as effective synthetic approaches for preparing new metastable compounds. ADL combined with laser heating is an effective technique to achieve rapid crystallisation from melt and glass preparation, as the laser heating can reach temperatures of up to 2500°C, allowing for a containerless rapid cooling process that can suppress heterogeneous and liquid phase crystallisation. Our group has used ADL to synthesise a range of new materials with potential applications in optical, energy storage and has found an important ceramic material system RE_2O_3-$(Al/Ga)_2O_3$ in which some compounds have not yet been synthesised and studied. Importantly, in this system a range of highly non-stoichiometric YAGs was reported and it was demonstrated that up to 20% of the octahedral Al sites can be occupied by Y allowing it to accommodate smaller rare-earth ions.

In contrast, these rare earth ions can only occupy the dodecahedral site in the stoichiometric garnet. The distribution of the rare earth ions in two different crystallography sites results in a significant impact on the luminescence properties. My PhD work on non-stoichiometric garnets is based on this work. Furthermore, this chapter also presents the background related to the new solid solution compound $Lu_4(Al/Si)_2O_9$ found in the work on $(Lu/Mg)_3(Al/Si)_5O_{12}$ garnet. Literature review of this system has revealed a lack of studies on the optical applications of $Lu_4Al_2O_9$ compounds and on the structure and applications of $Lu_4(Al/Si)_2O_9$ solid solutions, while isomorphic compounds $RE_4Al_2O_9$ of $Lu_4Al_2O_9$ have been investigated as potential optical materials. In conclusion, it can be seen that it is feasible to use ADL techniques to attempt the synthesis of unreported compounds in RE_2O_3-$(Al/Ga)_2O_3$ system using crystallisation from glass and melt methods. In turn, it would be of interest to explore the relationship between the structure and properties of highly non-stoichiometric garnets, as well as to understand the structure of $Lu_4(Al/Si)_2O_9$ solid solutions and explore their optical applications.

References

*[1] D.M. Herlach, Materials Science and Engineering: A. **1997**, 226-228, 348-356.*

*[2] L. Sun, G. Yuan, L. Gao et al., Nature Reviews Methods Primers. **2021**, 1, 5.*

*[3] D. Bokov, A. Turki Jalil, S. Chupradit et al., Advances in Materials Science and Engineering. **2021**, 2021, 5102014.*

*[4] H.-U. Krebs, M. Weisheit, J. Faupel et al., Advances in Solid State Physics. **2003**, 43, 101-107.*

*[5] C. Wang , Z.-H.Cheng. W. Ji, Physics. **2023**, 52, 381-393.*

*[6] Y. Cui, L. Liu, H.H. Lin et al., Science. **2023**, 380, 1179-1184.*

*[7] X.D. Zheng, W. Han, L.K. Yang et al., Science Advances. **2022**, 8, eabo0773.*

[8] J. Shelbyy. Introduction to Glass Science and Technology. 2005.

*[9] E.D. ZanottoJ.C. Mauro, Journal of Non-Crystalline Solids. **2017**, 471, 490-495.*

*[10] J.W.P. Schmelzer, V.M. Fokin, A.S. Abyzov, International Journal of Applied Glass Science. **2016**, 7, 253-261.*

*[11] H. Rawson. Inorganic glass-forming systems. Academic Press. **1967**.*

*[12] C.A. Angell, Science. **1995**, 267, 1924-1935.*

*[13] W.H. Zachariasen, Journal of the American Chemical Society. **1932**, 54, 3841–3851.*

*[14] D. Turnbull, Contemporary Physics. **1969**, 10, 473-488.*

*[15] A.S. Alzahrani, Advances in Materials Physics and Chemistry. **2022**, 12, 261-288.*

*[16] C.J. Benmore, J.K.R. Weber, Advances in Physics: X. **2017**, 2, 717-736.*

*[17] D. Erdemir, A.Y. Lee, A.S. Myerson, **2019**, 76-114.*

*[18] R.T. Southin, G.A. Chadwick, Science Progress. **1969**, 57, 353-370.*

*[19] L. Hennet, V. Cristiglio, J. Kozaily et al., The European Physical Journal Special Topics. **2011**, 196, 151-165.*

*[20] W.W. Cao, A. Isabel Becerro, V. Castaing et al., Advanced Functional Materials. **2023**, 33, 2213418.*

*[21] G. Shete, S. KaragaddeA. Srivastava, SN Applied Sciences. **2021**, 3,*

*[22] M. Allix, S. Alahrache, F. Fayon et al., Advanced Materials. **2012**, 24, 5570-5575.*

*[23] M. Boyera, E. Vérona, A. Isabel Becerro et al., CrystEngComm. **2015**, 17, 6127-6135.*

*[24] J. Fan, V. Sarou-Kanian, X. Yang et al., Chemistry of Materials. **2020**, 32, 9016-9025.*

*[25] L.J. Zhou, J.G. Xu. M. Allix et al., The Chemical Record. **2020**, 20, 1117-1128.*

*[26] Y.Z. Zhang, L.F. Ye, Z.P. Zeng et al., Journal of Advanced Ceramics. **2022**, 11, 1613-1625.*

*[27] C. Genevois, H. Bazzaoui, M. Boyer et al., Inorg Chem. **2021**, 60, 12339-12354.*

*[28] C. Xu, C. Wang, J. Yu et al., Journal of the American Ceramic Society. **2017**, 100, 2852-2858.*

*[29] S. Alahraché, K. Al Saghir, S. Chenu et al., Chemistry of Materials. **2013**, 25, 4017-4024.*

*[30] A. Masuno, S. Kohara, A.C. Hannon et al., Chemistry of Materials. **2013**, 25, 3056-3061.*

*[31] J.D. Yu, Y. Arai, T. Masaki et al., Chemistry of Materials. **2006**, 18, 2169–2173.*

*[32] K. Yoshimoto, A. Masuno, H. Inoue et al., Journal of the American Ceramic Society. **2012**, 95, 3501-3504.*

*[33] M. Mizuno, T. Yamada, Journal of the Ceramic Society of Japan. **1993**, 93, 26-31.*

*[34] I.A. Bondar, N.A. Toropov, Russian Chemical Bulletin. **1966**, 15, 195-199.*

*[35] D.S. Abell, I.R. Harris. Journal of Materials Science. **1974**, 9, 527-537.*

*[36] A.G. Petrosyan, G.O. Shirinyan, K.L. Ovanesyana et al., Journal of Crystal Growth. **1981**, 52, 556—560.*

*[37] T. Shishido, Journal of Materials Science. **1979**, 14, 8 2 3 - 8 3 0.*

*[38] V. Bachmann, C.Ronda, A. Meijerink, Chemistry of Materials. **2009**, 21, 2077–2084.*

[39] M. Nikl, A. Yoshikawa, K. Kamada et al., Progress in Crystal Growth and Characterization of Materials.

***2013**, 59, 47-72.*

*[40] G. Okada, M. Akatsuka, H. Kimura et al., Sensors and Materials. **2018**, 30, 1547.*

*[41] A. Matkovski, A. Durygin, A. Suchocki et al., Optical Materials. **1999**, 12, 75–81.*

*[42] J. Nicola, J. Couture, J.P. Coutures, Journal of Solid State Chemistry. **1984**, 52, 101-113*

*[43] V.F. Popova, A.G. Petrosyan, E.A. Tugova et al., Russian Journal of Inorganic Chemistry. **2009**, 54, 624-629.*

*[44] Y. Takebuchi, D. Shiratori, T. Kato et al., Sensors and Materials. **2023**, 35, 507.*

*[45] Y.D. Zhang, Z.Y. Wei. B.I Zhou et al., Optics Letters. **2009**, 34, 3316-3318.*

*[46] A.N. Romanov, E.V. Haula, D.P. Shashkin et al., Journal of Luminescence. **2020**, 228, 117652.*

*[47] P. Haritha, I.R. Martín, K. Linganna et al., Journal of Applied Physics. **2014**, 116, 174308.*

*[48] M. Paddison, J.A. Jacobsen, H. Petrenko et al., Science. **2015**, 350, 179-181.*

*[49] X.Q. Yin, Y.L. Zhong, Y.M. Cao et al., Journal of Applied Crystallography. **2021**, 54, 1641-1646.*

*[50] A. Iakovleva, A. Chesnaud, I. Animitsa et al., International Journal of Hydrogen Energy. **2016**, 41, 14941-14951.*

*[51] P. Singh, R. Pandey, T. Miruszewski et al., ACS Omega. **2020**, 5, 30395-30404.*

*[52] A.S. Gandhi, C.G. Levi, Journal of Materials Research. **2005**, 20, 1017-1025.*

*[53] S. Geller, G.P. Esipinosa, P. B. Crandall, Journal of Applied Crystallography. **1969**, 2, 86-88.*

*[54] M.K. Ashurov, Y.K. Voronko, V.V. Osiko et al., Physica status solidi (a). **1977**, 42, 101-110.*

*[55] A.P. Patel, M.R. Levy, R.W. Grimes et al., Applied Physics Letters. **2008**, 93, 191902.*

*[56] A.P. Patel, C.R. Stanek, R.W. Grimes, physica status solidi (b). **2013**, 250, 1624-1631.*

*[57] C.R. Stanek, K.J. McClellan, M.R. Levy et al., Journal of Applied Physics. **2006**, 99, 113518.*

*[58] G. Amthauer, K. Katz-Lehnert, D. Lattard et al., Zeitschrift für Kristallographie. **1989**, 189, 43-56.*

*[59] Y.N.-Xu, W.Y. Ching, Physical Review B. **1998**, 59, 10530-10535.*

*[60] S. Geller, M.A. Gilleo, Journal of Physics and Chemistry of Solids. **1957**, 3, 30-36.*

*[61] C.D. Brandle, D.C. Miller, J.W. Nielsen, Journal of Crystal Growth. **1972**, 12, 195-200.*

*[62] E. Garskaite, N. Dubnikova, A. Katelnikovas et al., Collection of Czechoslovak Chemical Communications. **2007**, 72, 321-333.*

*[63] N. Aparnadevi, K. Saravana Kumar, M. Manikandan et al., Journal of Materials Science: Materials in Electronics. **2020**, 31, 2081-2088.*

*[64] V. Laguta, M. Buryi, J. Pejchal et al., Physical Review Applied. **2018**, 10, 2331-7019.*

[65] R. Inada, S. Yasuda, M. Tojo et al., Frontiers in Energy Research. ***2016****, 4, 190363.*

[66] A. Nakatsuka, A. Yoshiasa, T.u. Yamanaka, Acta Crystallographica. ***1999****, B55, 266–272.*

[67] J.E. Geusic, H.M. Marcos, L.G. Van Uitert, Applied Physics Letters. ***1964****, 4, 182-184.*

[68] Y. Rao, D. Zhang, L. Jin et al., Journal of Magnetism and Magnetic Materials. ***2020****, 497, 165817.*

[69] P.B.A. Fechine, H.H.B. Rocha, R.S.T. Moretzsohn et al., IET Microwaves, Antennas & Propagation. ***2009****, 3, 1191.*

[70] D.R. Bhosale, S.M. Yusuf, A. Kumar et al., Physical Review Materials. ***2017****, 1,015001.*

[71] M. Kubicek, A. Wachter-Welzl, D. Rettenwander et al., Chemistry of Materials. ***2017****, 29, 7189-7196.*

[72] M.H. Phan, M.B. Morales, C.N. Chinnasamy et al., Journal of Physics D: Applied Physics. ***2009****, 42, 115007.*

[73] D.Mateika, E. Volkel, Journal of Crystal Growth. ***1990****, 102, 994-1013.*

[74] J.L. Wu, G. Gundiah, A.K. Cheetham, Chemical Physics Letters. ***2007****, 441, 250-254.*

[75] S. Feng, Y. Guo, M. Allix et al., Cell Reports Physical Science. ***2022****, 3, 101044.*

[76] Y.K. Voronko, A.A. Sobol, Physica status solidi (a). ***1975****, 27, 657-663.*

[77] C. Milanese, V. Buscaglia. F. Maglia et al., Chemistry of Materials. ***2004****, 16, 1232-1239.*

[78] Y. Zorenko, A. Voloshinovskii, I. Konstankevych et al., Radiation Measurements. ***2004****, 38, 677-680.*

[79] Y. Zorenko, physica status solidi (c). ***2005****, 2, 375-379.*

[80] Y. Zorenko, A. Voloshinovskii, V. Savchyn et al., physica status solidi (b). ***2007****, 244, 2180-2189.*

[81] C. Hu, S. Liu, Y. Shi et al., physica status solidi (b). ***2015****, 252, 1993-1999.*

[82] L.B. Skinner, A.C. Barnes, P.S. Salmon et al., Journal of Physics: Condensed Matter. ***2008****, 20, 205103.*

[83] X.G Ma, X.Y Li, J.Q. Li et al., Nature Communications. ***2018****, 9, 1175.*

[84] R. Weber, C.J. Benmore, J. Siewenie et al., Physical Chemistry Chemical Physics. ***2004****, 6, 2480.*

[85] Y. Watanabe, A. Masuno, H. Inoue, Journal of Non-Crystalline Solids. ***2012****, 358, 3563-3566.*

[86] M. Allix, A.I. Becerro, W.W Cao et al., International application published under the patent coorperation treaty. ***2022****, WO2022/167133 A1.*

[87] S. Kostić, Z.Ž. Lazarević, V. Radojević et al., Materials Research Bulletin. ***2015****, 63, 80-87.*

[88] G. Liu, B. Wang, J. Li et al., Physica B: Condensed Matter. ***2021****, 603, 412775.*

[89] J. Li, J.G. Li, S. Liu et al., Science and Technology of Advanced Materials. ***2013****, 14, 054201.*

[90] J. Kaur, S. Rani, B. Lal, Optik. ***2020****, 212, 164745.*

[91] X. Teng, J.G. Li, G. Duan et al., Journal of Luminescence. ***2016****, 179, 165-170.*

[92] J.K. Li, J.G. Li, j. Li et al., Journal of Materials Chemistry C. ***2013****, 1, 7614.*

[93] J.K. Li, J.G. Li, j. Li et al., Journal of Alloys and Compounds. ***2016****, 670, 161-169.*

[94] J.K. Li, J.G. Li, j. Li et al., Ceramics International. ***2016****, 42, 3268-3274.*

[95] J.F. Tang, J. Gou, G.N. Li et al., RSC Advances. ***2016****, 6, 54435-54439.*

[96] F. Pandozzi, F. Vetrone, J. C. Boyer et al., The Journal of Physical Chemistry B. ***2005****, 109, 400–17405.*

[97] R. Martı´n-Rodrı´guez, R. Valiente, S. Polizzi et al., The Journal of Physical Chemistry C. ***2009****, 113, 12195–12200.*

[98] Y. Li, M. Geceviciua, J.R. Qiu. Chemical Society Reviews. ***2016****, 45, 2090-2136.*

[99] J. Ueda, Bulletin of the Chemical Society of Japan. ***2021****, 94, 2807-2821.*

[100] J. Xu, S. Tanabe, Journal of Luminescence. ***2019****, 205, 581-620.*

[101] J. Xu, J. Ueda, S. Tanabe, Journal of the American Ceramic Society. ***2017****, 100, 4033-4044.*

[102] K. Van den Eeckhout, A.J.J. Bos, D. Poelman, et al., Physical Review B. ***2013****, 87, 045126.*

[103] J. Ueda, K.Kuroishi, S. Tanabe, Applied Physics Letters. ***2014****, 104, 101904.*

[104] J. Ueda, K. Kuroishi, S. Tanabe, Applied Physics Express. ***2014****, 7, 062201.*

[105] T. Matsuzawa, Y. Aoki, N. Takeuchi et al., Journal of The Electrochemical Society. ***2019****, 143, 2670-2673.*

[106] R. Tomala, K. Korkus, V. Boiko et al., Journal of Alloys and Compounds. ***2021****, 889, 161745.*

[107] J. Xu, J. Ueda, S. Tanabe, Optical Materials Express. ***2015****, 5, 963.*

[108] J. Ueda, S. Miyano, J. Xu et al., Advanced Photonics Research. ***2021****, 2, 2000102.*

[109] A.G. Petrosyan, V.F. Popova, V.V. Gusarov et al., Journal of Crystal Growth. ***2006****, 293, 74-77.*

[110] P. Wu, A.D. Pelton, Journal of Alloys and Compounds. ***1992****, 17, 259-287.*

[111] H. Yamane, K.Ogawara, M. OmoriT.Hirai, Journal of the American Ceramic Society. ***1995****,78, 2385-2390.*

[112] A.G. Petrosyan, V.F. Popova, V.L. Ugolkov et al., Journal of Crystal Growth. ***2013****, 377, 178-183.*

[113] R. Simura, H. Yamane, Acta Crystallogr E Crystallogr Commun. ***2020****, 76, 752-755.*

[114] I. Warshaw, R. roy, Journal of the American Ceramic Society. ***1959****, 42, 434-438.*

[115] L. Kepinski, Journal of the American Ceramic Society. ***2018****, 101, 1356-1360.*

[116] A. Das, S. Saha, K. Panigrahi et al., CrystEngComm. ***2018****, 20, 2540-2552.*

[117] D. Singh, S. Kadyan, Journal of Materials Science: Materials in Electronics. ***2017****, 28, 11142-11150.*

[118] M. Kaczkan, Z. Boruc, S. Turczyński et al., Journal of Luminescence. ***2016****, 170, 330-335.*

[119] M. Kaczkan, S. Turczyński, D.A. Pawlak et al., Optical Materials. ***2016****, 58, 412-417.*

[120] B. Fetlinski, Z. Boruc, M. Kaczkan et al., Journal of Luminescence. ***2017****, 181, 133-137.*

[121] M. Kaczkan, D.A. Pawlak, S. Turczynski et al., Journal of Alloys and Compounds. ***2017****, 728, 1009-1015.*

[122] J.K. Li, J.-G. Li, J. Li et al., Journal of Solid State Chemistry. ***2013****, 206, 104-112.*

[123] Y.-s. Lian, Y. Wang, J.-F. Li et al., Vacuum. ***2020****, 173, 109165.*

[124] U. Kolitsch, H.J. Scifert, F. Aldinger, Journal of Phase Equilibria. ***1998****, 19, 426.*

[125] U. Kolitsch, H.J. Seifert, T. Ludwig et al., Journal of Materials Research. ***1999****, 14, 447–455.*

[126] J.P. Coutures, E.Antic, P. Caro, Materials Research Bulletin. ***1967****, 11, 699-706.*

[127] U. Kolitsch, H.J. Seifert, F. Aldinger, Journal of Alloys and Compounds. ***1999****, 257, 104-114.*

Chapter II: Structure and luminescence properties of highly non-stoichiometric $Gd_{3+x}Al_{5-x}O_{12}$ garnet

2.1 Introduction

As described in Chapter 1, in addition to cation substitution strategy[1-4], garnet deviations from the ideal stoichiometry were proved to have an impact on the luminescence properties of phosphors[5]. The work on highly non-stoichiometric YAG reported that two different crystallographic RE^{3+} sites affect the emission colour in ns-YAG: Er^{3+}/Yb^{3+} system[5]. These results motivated us to study new highly nonstoichiometric garnets and the distribution trends of different size of dopants in two crystallographic sites in non-stoichiometric garnet, and the effect of new REO_6 sites on the luminescence properties. Besides non-stoichiometric YAG, non-stoichiometric GAG and GGG ($Gd_{3.2}Al_{4.8}O_{12}$ and $Gd_{3.2}Ga_{4.8}O_{12}$) have been shown to be accessible by ADL and are worth further exploration for their synthesis of solid solution in non-stoichiometric and their application in optical applications.[5]

Moreover, the work of highly nonstoichiometric YAGs reports that Ce^{3+} and Er^{3+}/Yb^{3+} have different site selection preferences in non-stoichiometric structures due to their different sizes. The larger radius Ce^{3+} can only be accommodated by dodecahedral sites, while the smaller Er^{3+} prefers to occupy octahedral sites. Whereas in the case of non-stoichiometric ratio GAGs, where Gd^{3+} (0.94 Å) has a much larger radius than Y^{3+} (0.9 Å), an excess of Gd occupying octahedral sites may provide more possibility to accommodate larger sized rare earth dopants. Therefore, the kind of dopant that can occupy octahedral sites to form new luminescent sites in GAGs is worth further exploration.

In this chapter, the solid solution $Gd_{3+x}Al_{5-x}O_{12}$ were synthesized using the crystallization from glass method. The glass precursors were synthesized by ADL. The solid solution will be determined by XRD and the structural evolution will be investigated by SPD. SEM, VT-XRD were used to explore the microstructure, compound composition and phase thermal stability. In addition, the tendency of different size ions (Tb^{3+}, Yb^{3+}, Tm^{3+}) occupied in octahedral sites in the non-stoichiometric GAG will be investigated by STEM, EXAFS. The sensitivity of dopants (Ce^{3+}, Tb^{3+}, Er^{3+}, Tm^{3+}, Ho^{3+}) to the local site environment and luminescence properties of the phosphor was investigated spectroscopically.

2.2 $Gd_{3+x}Al_{5-x}O_{12}$ (GAG) ($0 \leq x \leq 0.6$) synthesis and structure analysis

2.2.1 Synthesis and general crystal structure analysis

The ADL combined with laser heating was utilized to synthesize a range of $Gd_{3+x}Al_{5-x}O_{12}$ (x = 0 - 0.7) glass beads, and then the GAG solid solutions crystalline beads obtained by crystallisation from glass (detailed process is described in the ADL section of **Chapter 1** and the synthesis conditions are listed in ***Table A.1.3***). In the YAG synthesis work described in **Chapter 1**, we know that the cooling rate has an effect on the state of the obtained sample. The cooling rate is in turn influenced by the type of the levitation gas and the mass of the melt. Therefore, in this work different type of levitation gases have been tried to control the appropriate cooling rate to obtain the target phase. The photos of white crystalline bead (GAP), transparent bead (glass) of composition $Gd_{3.2}Al_{4.8}O_{12}$ were obtained during the free cooling of the melt from a temperature of 2200 ℃ levitated with argon and oxygen, respectively, as shown in ***Fig 2.1a*** inset (beads with a diameter of about 2mm). The process of crystallisation of glass beads is a thermal heating in a muffle furnace at 950°C in air for 3 hours. The crystallization temperature of 950°C was determined by a strong exothermic peak in the DSC curve, shown in the ***Fig 2.1c***. The PXRD patterns of the beads obtained, as presented in ***Fig 2.1b*****,** demonstrate that white beads are GAP/Al_2O_3 mixture phases, transparent beads are glass, and glass beads crystallized as single garnet phase after thermal treatment (***Fig 2.1a*** inset). The cooling curve of the sample levitated by argon and oxygen, as displayed in ***Fig 2.1a***, clearly indicates that the phase of sample is dependent on the cooling rate, which is influenced by the species of levitated gas. Comparing the cooling rates required for the formation of glass and crystalline GAP/Al_2O_3, calculated from temperatures ranging from 2000 to 1800°C, reveals that higher cooling rates (2000 ^{o}C/s) are more favorable for the formation of glass. Here, we attempted to control the cooling rate and the crystallisation temperature of the undercooling melt using direct crystallisation from the melt to synthesize GAG garnet based on the synthetic conditions reported by nonstoichiometric YAG[5], however it was not possible to obtain a single garnet phase of nonstoichiometric GAG.

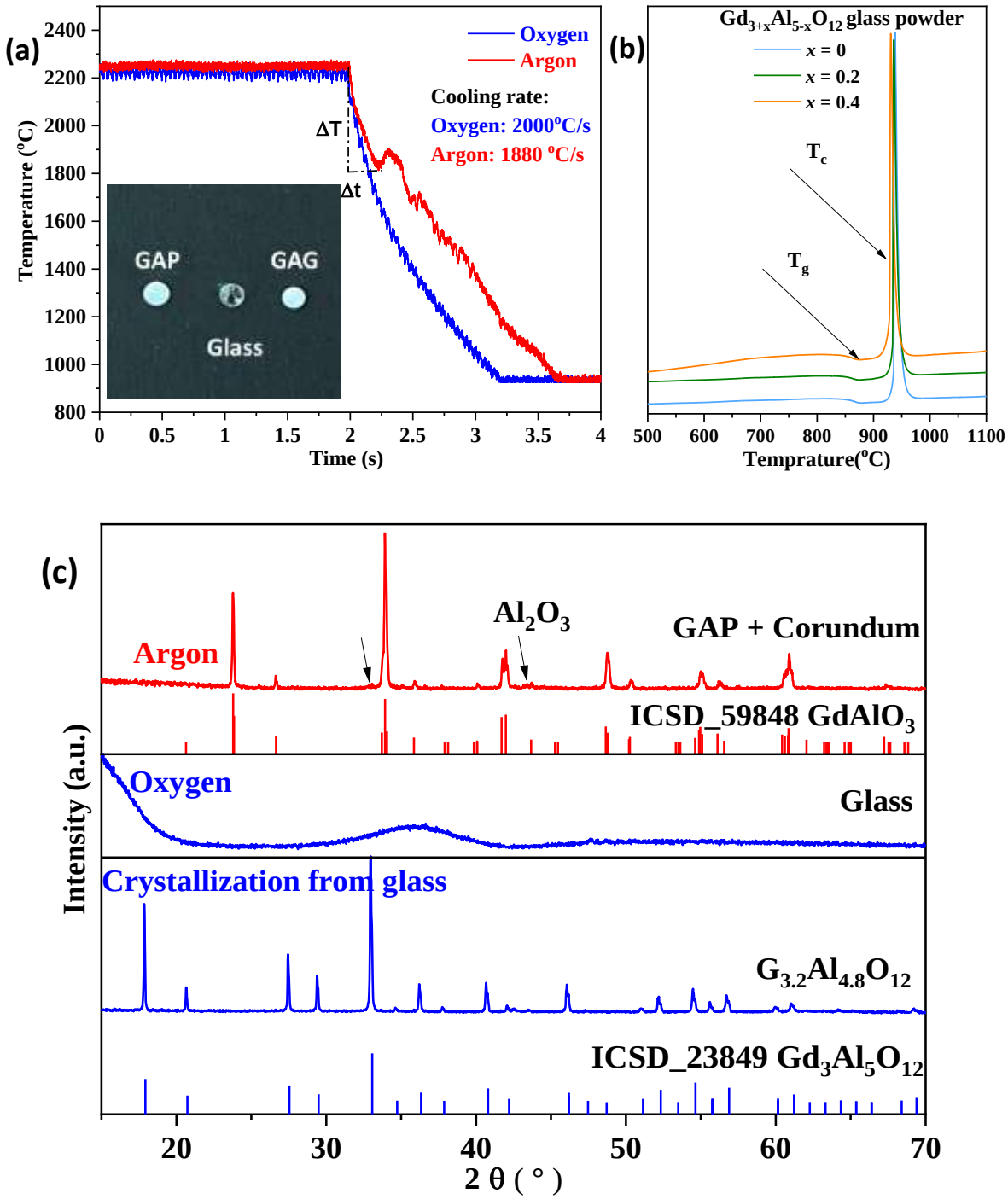

Fig 2.1 (a) *Cooling curve of $Gd_{3.2}Al_{4.8}O_{12}$ melt levitated by oxygen (blue) and argon (red) (inset shows a photograph of GAP perovskite (GAP), glass (Glass) and garnet (GAG) bead)* ***(b)*** *DSC curves of $Gd_{3+x}Al_{5-x}O_{12}$ (x = 0, 0.2, 0.4) collected on air at a heating rate of 10°C/min. The exothermic peak at about 950°C is the crystallization of GAG glass.* ***(c)*** *PXRD patterns of the synthesized GAP-Al_2O_3, glass, and garnet samples.*

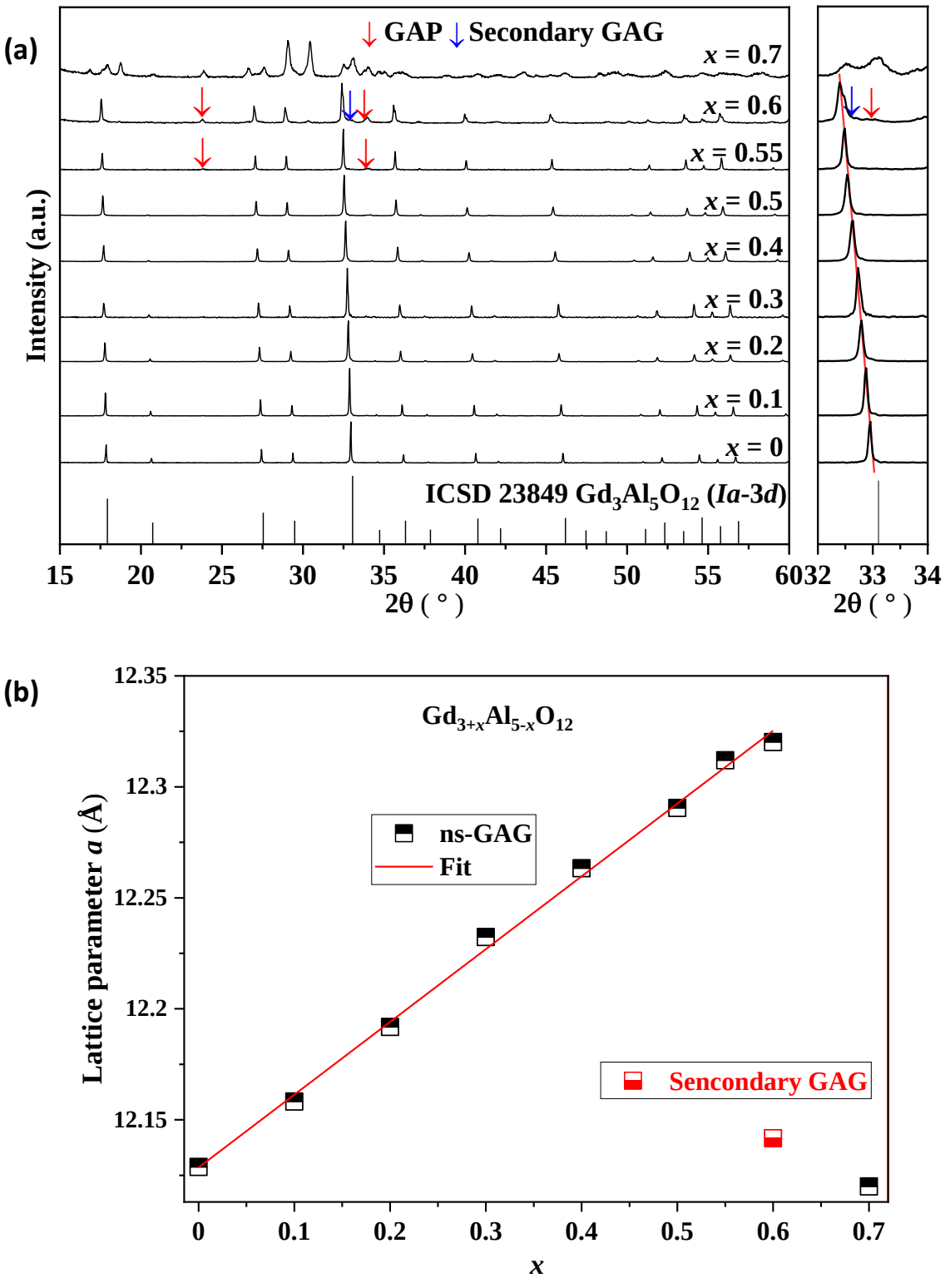

Fig 2.2 (a) *Laboratory X-ray diffraction pattern of* $Gd_{3+x}Al_{5-x}O_{12}$ *(*$0 \leq x \leq 0.7$*) with zoom of the (211) plane shift on left (red and blue arrow marks are GAP perovskite peaks and secondary GAG peaks, respectively)* ***(b)*** *Laboratory PXRD data refined lattice parameter a of ns-GAG (black points) and secondary GAG (red point) with different x value.(red line is a linear fit to the data.)*

Laboratory PXRD patterns of $Gd_{3+x}Al_{5-x}O_{12}$ ($0 \leq x \leq 0.7$) synthesized via crystallization from glass is displayed in ***Fig 2.2a***. It is evident that the diffraction patterns of $Gd_{3-x}Al_{5+x}O_{12}$ ($0 \leq x \leq 0.6$) match well with the card ICSD 23849, which represents the garnet structure of space group *Ia*-3*d*, implying the successful synthesis of a series of garnet phase compounds. Notably, the diffraction peaks shift systematically to lower 2θ values as the value of x gradually increases, as illustrated by the peak position of the (211) plane in the enlargement on the left of ***Fig 2.2a***, indicating an expansion of the unit cell parameters. In addition, about 16.7 wt% of $GdAlO_3$ and small amounts of 8.1wt% secondary stoichiometric garnet phase were observed at x = 0.6, while at x = 0.7, a mixture of $GdAlO_3$ and stoichiometric garnet was formed. PXRD Rietveld refinement reveals a linear increase in the lattice parameter *a* as x values increasing from 0 to 0.6, as demonstrated in ***Fig 2.2b***, confirming the formation of highly nonstoichiometric GAG solid solutions. The abrupt drop in the cell parameter at $Gd_{3.7}Al_{4.3}O_{12}$ (cell parameter close to that of x = 0) confirms that the limit of the solid solution lies range $0.6 < x < 0.7$. This abrupt drop in cell volume mirrors the behavior of the ns-YAG series (drop at x = 0.5).

2.2.2 Structure evolution

Structural evolution and detailed structural information of the $Gd_{3+x}Al_{5-x}O_{12}$ ($0 \leq x \leq 0.6$) series were analyzed by high-resolution SPD Rietveld refinement results, as displayed in ***Fig 2.3***. ***Fig 2.3a*** shows the refinement profile of $Gd_{3.4}Al_{4.6}O_{12}$, while $Gd_3Al_5O_{12}$ and non-stoichiometric $Gd_{3.2}Al_{4.8}O_{12}$, $Gd_{3.6}Al_{4.4}O_{12}$ refinement profiles are listed in ***Fig B.1.1-3,*** respectively. $Gd_3Al_5O_{12}$ was used as the starting structure model to Rietveld refinement of all compositions, and the fitting parameters of the processing (see ***Text B.1.1***) and refinement results of the atomic positions, occupation numbers, and U_{iso} are provided in ***Table 2.1***. The results of the refinement revealed that the cell parameter *a* linearly increases with x ranging from 0 - 0.6 (***Fig 2.3b*** upper) and the six coordinate Gd^{3+} content was found to increase linearly with x, consistent with the theoretical solid solution formula (***Fig 2.3b*** lower). Surprisingly, in $Gd_{3.6}Al_{4.4}O_{12}$, up to almost 30% of Gd^{3+} occupies the six coordinated Al^{3+} site, which is 50% higher than 20% of octahedral Al^{3+} substituted by Y^{3+} in the nonstoichiometric

$Y_{3.4}Al_{4.8}O_{12}$[5], despite the fact that Gd^{3+} is larger than Y^{3+}.

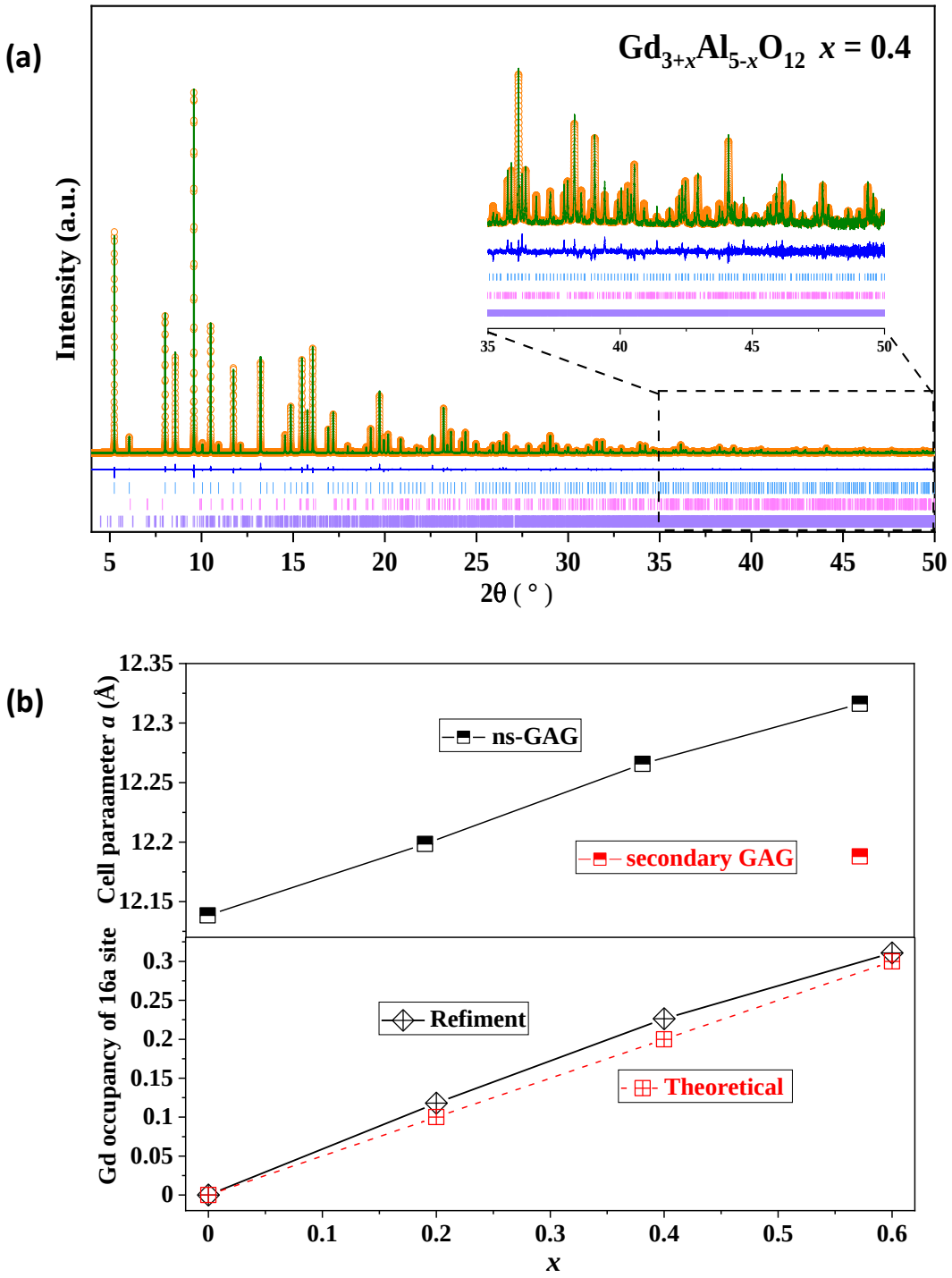

Fig 2.3 (a) *SPD Rietveld refinement profile of $Gd_{3.4}Al_{4.6}O_{12}$ (R_{wp} = 9.17%, Gof = 1.89) (blue, pink, and purple tick marks correspond to GAG, 0.50(1)wt% $GdAlO_3$ perovskite and 0.09(1)wt% $Gd_4Al_2O_9$ reflections, respectively).* ***(b)*** *Refined lattice parameter a of ns-GAG (black line) and secondary GAG (red line) with different x value (upper), plots of refined occupancy of the AlO_6 octahedral site by Gd^{3+} (black line) and theoretical occupancy (red line) vs x value (lower).*

Table 2.1 *Refined cell parameters and fitting results obtained from SPD data.*

$Gd_{3+x}Al_{5-x}O_{12}$	atom	site	x	y	z	occupancy	U_{iso}*100(Å^2)
	Gd1	24c	0.125	0	0.25	1	0.474(2)
	Gd2	16a	0	0	0	0.0312(4)	0.246(1)
x = 0	Al1	16a	0	0	0	0.9688(4)	0.246(1)
	Al2	24d	0.375	0	0.25	1	0.4858(2)
	O1	96h	-0.03265(6)	0.04880(7)	0.14885(6)	1	0.576(1)
Lattice parameter: *a = 12.13842(1) Å*			*Secondary phases:* *2.36(1) wt% Al_2O_3*			*Fitting parameters:* *R_{wp} = 7.41%, Gof = 1.76*	
	Gd1	24c	0.125	0	0.25	1	0.679(3)
	Gd2	16a	0	0	0	0.1289(6)	0.48(1)
x = 0.2	Al1	16a	0	0	0	0.8710(6)	0.48(1)
	Al2	24d	0.375	0	0.25	1	0.52(1)
	O1	96h	-0.03266(8)	0.05058(9)	0.15046(9)	1	0.89(2)
Lattice parameter: *a = 12.19837(2) Å*			*Secondary phases:* *1.35(1) wt% Al_2O_3 and* *0.35(1)wt% $GdAlO_3$*			*Fitting parameters:* *R_{wp} = 9.17%, Gof = 1.89*	
	Gd1	24c	0.125	0	0.25	1	0.733(2)
	Gd2	16a	0	0	0	0.2342(5)	0.374(8)
x = 0.4	Al1	16a	0	0	0	0.7657(5)	0.374(8)
	Al2	24d	0.375	0	0.25	1	0.504(9)
	O1	96h	-0.03337(7)	0.05260(8)	0.15168(8)	1	1.05(1)
Lattice parameter: *a = 12.26576(1) Å*			*Secondary phases:* *0.50(1) wt% $GdAlO_3$ and* *0.09(1) wt% $1Gd_4Al_2O_9$*			*Fitting parameters:* *R_{wp} = 7.9%, Gof = 1.41*	
	Gd1	24c	0.125	0	0.25	1	1.00(5)
	Gd2	16a	0	0	0	0.310(1)	0.37(1)
x = 0.6	Al1	16a	0	0	0	0.689(1)	0.37(1)
	Al2	24d	0.375	0	0.25	1	0.76(2)
	O1	96h	-0.0342(1)	0.0522(1)	0.1533(1)	1	1.50(4)
Lattice parameter: *a = 12.31626(1) Å*			*Secondary phases:* *Mixed impurities 16.3(9)wt%* *(GAG2, GAP, GAM, Al_2O_3)*			*Fitting parameters:* *R_{wp} = 10.38%, Gof = 1.99*	

A point to note here is that the sample with x = 0 appears to be not strictly non-stoichiometric GAG, but rather a non-stoichiometric GAG with x ≈ 0.06, which explains the secondary Al_2O_3 phase. The crystal structure of $Gd_{3.4}Al_{4.6}O_{12}$ resulting from the Rietveld refinement is presented in ***Fig 2.4a***, revealing that the 24c site of dodecahedron (grey) is completely occupied by Gd^{3+}, and the excess Gd^{3+} occupies the 6 coordinate Al^{3+} octahedral

sites (pale blue) rather than the AlO_4 tetrahedron (deep blue) (**see *Fig 2.4b***). Meanwhile, the variations in bond lengths of d(Gd1-O_L/Gd1-O_S), d(Al1/Gd2-O), and d(Al2-O) are shown in ***Fig 2.4c***. It should be noteworthy that the two different Gd-O bond lengths at the 24c sites exhibit different trends, with the longer Gd-O_L bond lengths becoming progressively shorter and the shorter Gd1-O_S bond lengths linear increase with the values of excess Gd^{3+} in 16a site. Moreover, a strong linear increase of the Al1/Gd2-O bond length with *x* in the range $0 \leq x \leq 0.6$ is observed, which results from the larger Gd^{3+}(0.94 Å) occupying the Al^{3+}(0.39 Å) site. The detailed information on bond lengths of the GAG solid solution is given in ***Table 2.2***.

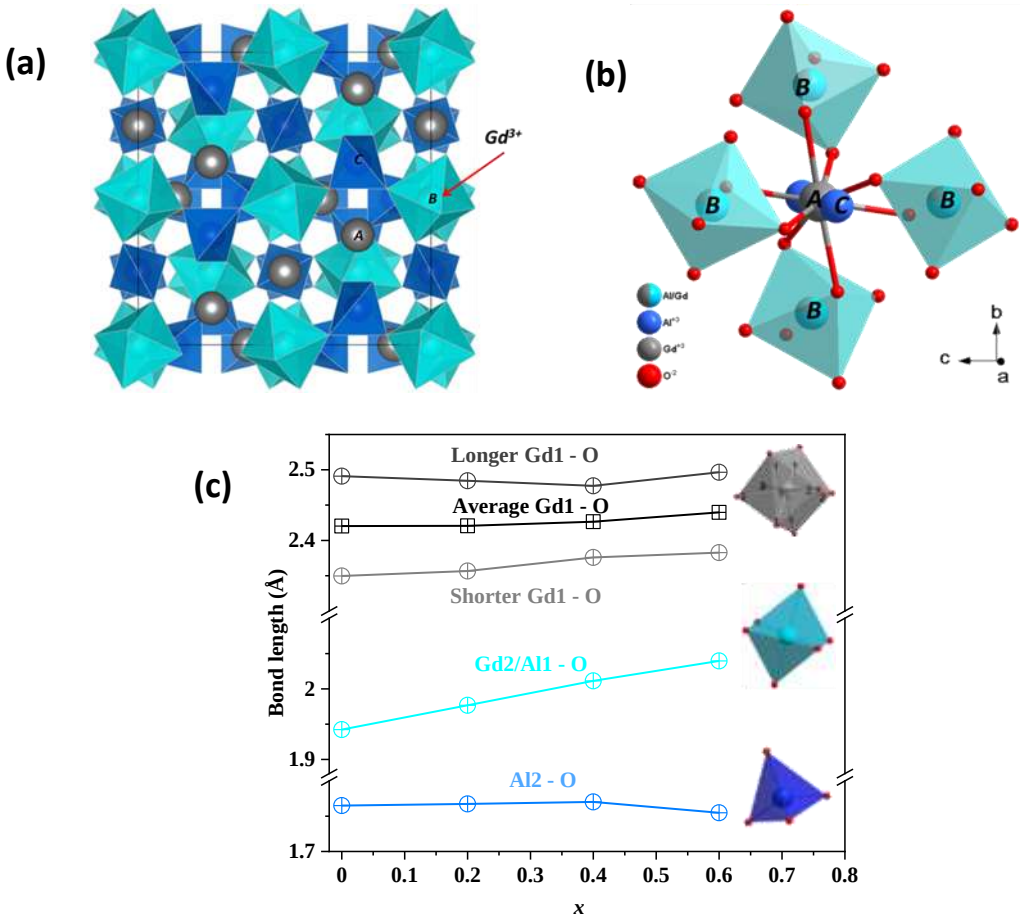

Fig 2.4 (a) *Refined garnet structure of $Gd_{3.4}Al_{4.6}O_{12}$ viewed from c axes and* ***(b)*** *a fragment projected along the a-axis displaying the A site and the surrounding B and C sites (gray, mixed gray and pale blue, and deep blue atom is Gd, Gd/Al1 and Al2. Gray dodecahedra is GdO_8, pale blue octahedron is Gd/AlO_6; deep blue tetrahedron is AlO_4).* ***(c)*** *Refined metal-oxygen distances (gray lines are Gd-O bands, black line is the average bond length of Gd-O, pale blue is Gd/Al1-O band, and deep blue is Al2-O band).*

Table 2.2 *Bond lengths of $Gd_{3+x}Al_{5-x}O_{12}$ (x = 0, 0.2, 0.4, 0.6) from SPD refinement.*

x	Gd-O	Bond length (Å)	Al-O	Bond length (Å)
x = 0	$Gd1\text{-}O^S$	2.3496(7)	Al1-O	1.9423(8)
	$Gd1\text{-}O^L$	2.4910(8)	Al2-O	1.7650(8)
x = 0.2	$Gd1\text{-}O^S$	2.3567(10)	Al1/Gd2-O	1.9768(10)
	$Gd1\text{-}O^L$	2.4845(11)	Al2-O	1.7674(10)
x = 0.4	$Gd1\text{-}O^S$	2.3758(9)	Al1/Gd2-O	2.0113(10)
	$Gd1\text{-}O^L$	2.4773(10)	Al2-O	1.7702(10)
x = 0.6	$Gd1\text{-}O^S$	2.3827(17)	Al1/Gd2-O	2.0396(18)
	$Gd1\text{-}O^L$	2.4966(19)	Al2-O	1.7548(18)

2.3 Microstructure analysis

SEM images, EDS results are presented to observe the microscopic morphology, the composition of $Gd_{3+x}Al_{5-x}O_{12}$ (x= 0, 0.2, 0.4) beads. The SEM images of the polished single crystallised bead of each composition (see ***Fig 2.5***) show clearly the grain boundaries and irregular polygonal grains of 2 to 3 µm in length and width with no residual glass components indicating complete crystallisation. On closer inspection, it can be seen that each sample contains porosity and for this reason it was not possible to obtain a transparent ceramic. The same happens in ns-YAG samples[5], which is a common phenomenon in crystallization from glass because of the significant difference in density between the glass and crystalline sample[6]. In addition, we observe a difference in the contrast of the grains in the image, which is due to the different orientation of the grains. Approximately 20 points on crystal grain of each compound were selected for EDS analysis and the average measured compositions are listed in ***Table 2.3***, indicating that the measured compositions are close to the theoretical compositions.

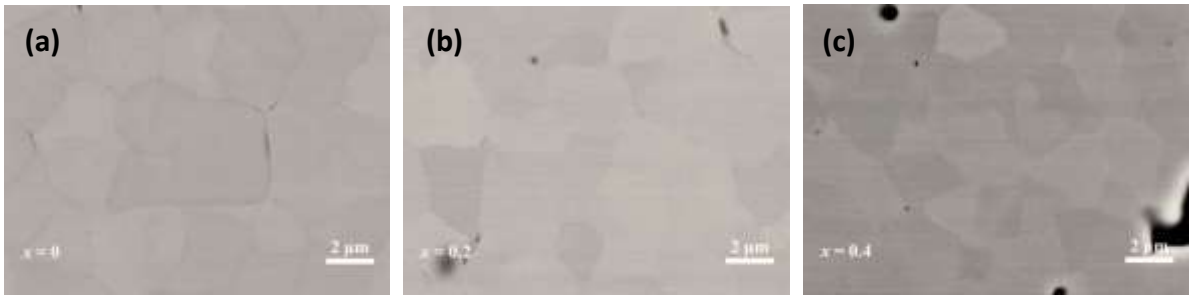

Fig 2.5 *SEM (BSE) image of pholished $Gd_{3+x}Al_{5-x}O_{12}$ crystallised beads.* ***(a)*** *x =0* ***(b)*** *x =0.2* ***(c)*** *x = 0.4*

Table 2.3 *SEM-EDS analysis of $Gd_{3+x}Al_{5-x}O_{12}$ (x =0, 0.2, 0.4)*

$Gd_{3+x}Al_{5-x}O_{12}$	Gd (At. %)	Al (At. %)	Experimental composition	Theoretical composition
x = 0	15.04	24.96	$Gd_{3.01(9)}Al_{4.99(9)}O_{12}$	$Gd_3Al_5O_{12}$
x = 0.2	16.35	23.65	$Gd_{3.27(8)}Al_{4.73(8)}O_{12}$	$Gd_{3.2}Al_{4.8}O_{12}$
x = 0.4	17.25	22.75	$Gd_{3.45(7)}Al_{4.55(7)}O_{12}$	$Gd_{3.4}Al_{4.6}O_{12}$

2.4 Thermal stability

To further understand the thermal stability and the phase evolution of ns-GAG in the process of high temperature heating, variable high temperature XRD data of $Gd_{3.4}Al_{4.8}O_{12}$ was recorded from room temperature up to 1600 ^{o}C, and the results are illustrated in **Fig *2.6a*** and ***b***. The diffraction peaks systematically shifted to lower value of 2θ as the temperature increased from 30 - 1200^{o}C due to thermal expansion. However, staring from 1200°C, the out of equilibrium ns-GAG gradually decomposes into perovskite $GdAlO_3$ (blue mark) and stoichiometric GAG phase (red mark), as shown in ***Fig 2.6b***. The lattice parameter evolution of ns-GAG from RT-1600°C is shown in ***Fig 2.6c*** (lower), demonstrating first a linear increase due to thermal expansion from room temperature up to 1200°C, followed by an abrupt decrease at 1250°C because the decomposition of $Gd_{3.4}Al_{4.8}O_{12}$. The content of the decomposed compounds, as shown in ***Fig 2.6c*** left axis, exhibits that the ns-GAG decomposes into ns-$Gd_{3.4-d}$ AG and GAP from 1200°C to 1400°C, and then ns-$Gd_{3.4-d}$ AG gradually decomposes into GAG and GAP after 1400°C.

The coefficient of thermal expansion of $Gd_{3.4}Al_{4.8}O_{12}$ from room temperature to 1200°C was be 8.12 × 10^{-6} K^{-1} calculated using equation $\alpha_L = \frac{1}{L}\frac{dL}{dT}$. The thermal stability of ns-YAG is reported to start decomposing at 1350°C and its coefficient of thermal expansion is 9.98 × 10^{-6} K^{-1}. Comparing the thermal stability of the two type garnets it can be seen that ns-GAG has a lower stable temperature than YAG due to its larger ionic radius, but exhibits a slightly lower thermal expansion coefficient.

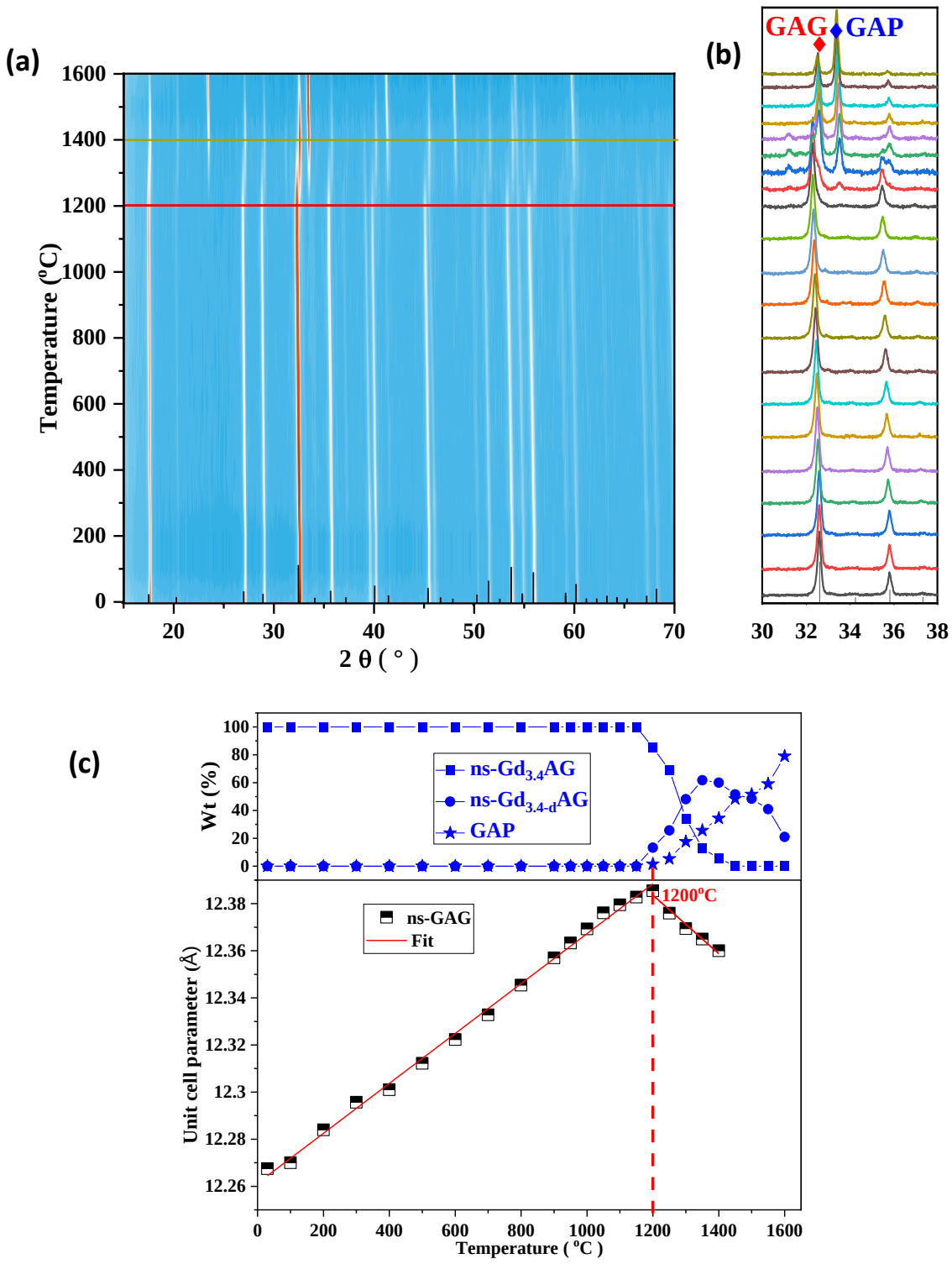

Fig 2.6 *VT-XRD measurement of $Gd_{3.4}Al_{4.5}O_{12}$ measured collected from room temperature to 1600°C at intervals of 50 °C* ***(a)*** *Contour figure of X-ray diffraction peaks from 15°- 70° (blue marks are $GdAlO_3$ perovskite phase)* ***(b)*** *Enlarged diffraction peak pattern from 30° - 38°.* ***(c)*** *The unit cell parameter evolution of ns-GAG (lower) and the wt% of decomposed phase with the temperature increasing (upper).*

2.5 Local structure analysis by EXAFS and STEM

To complement the average structure obtained from Rietveld refinement, here EXAFS was be used to characterize the local environment of Gd. And STEM was be used to observe the location of Gd from the atomic scale.

2.5.1 Local environments of Gd analysis by EXAFS

In order to probe the local environment around the Gd^{3+} ions, EXAFS measurements were carried out successively on the stoichiometric and nonstoichiometric GAG samples at the L_3 edges of Gd (7243 eV). The experimental Fourier transforms EXAFS spectra extracted from the linear absorption coefficient at the L_3 edges of Gd absorption threshold using the Athena software[7] shown in ***Fig 2.7a*** suggests a decrease in the amplitude of the first peaks, particularly on the first and third peaks, as well as a slight shift of the peaks towards the larger R's due to distance relaxation. This decrease confirmed that the excess Gd^{3+} ions substitute the Al^{3+} ions located at the octahedral site (6 oxygen neighbours) in the structure. These results are similar to those observed in the case of non-stoichiometric YAG samples ($Y_{3+x}Al_{5-x}O_{12}$)[5] characterised by NMR, XRD and EXAFS. The FEFF8[8] computational code was used to generate the EXAFS spectra by simulating the substitution of GdO_6 by 0, 2 and 3 in comparison with the experimental spectra in order to see if the decrease in amplitude and the shift of the peaks are consistent with the substitution of Al^{3+} by Gd^{3+} in the octahedral site (16a). The corresponding symmetrically unequal GAG cell (1 x 1 x 1, space group *P*1) structures were generated by Supercell[9] and the structure configurations are listed in ***Fig B.3.1***. According to the structural model proposed, the Fourier transform of the relaxed simulated EXAFS oscillations is shown in ***Fig 2.7b***, this decrease is due to the coexistence of Gd^{3+} ions surrounded by 8 and 6 oxygen neighbours as a result of the substitution of Al^{3+} ions by Gd^{3+} ions when the gadolinium content increases in the samples. As the Gd^{3+} ions are larger than the Al^{3+} ions they replace, this substitution is accompanied by a local deformation of the structure.

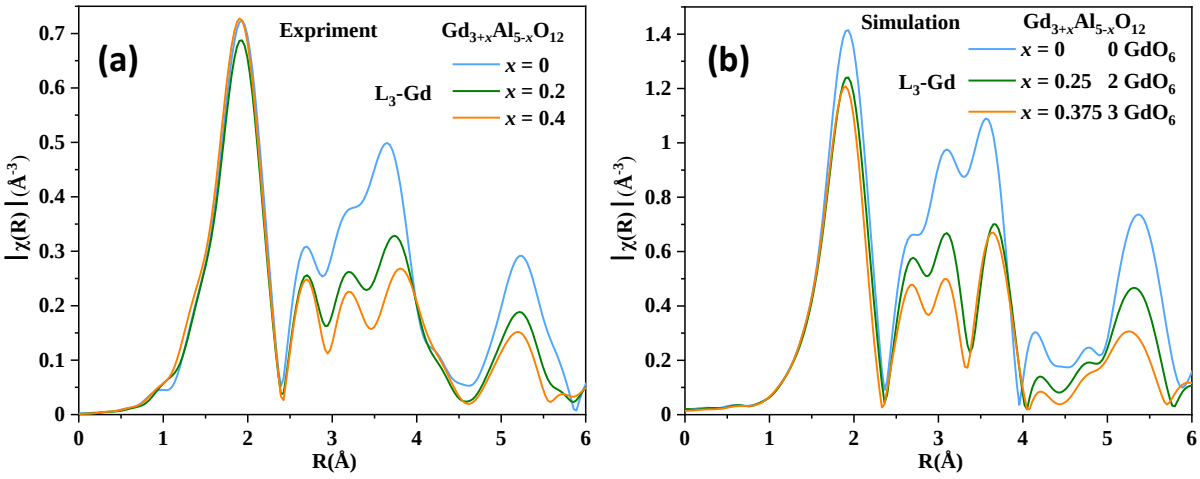

Fig 2.7 (a) *Experimental Fourier transforms EXAFS spectra extracted from the linear absorption coefficient measured at the Gd L_3-edge.* ***(b)*** *Fourier transforms of EXAFS spectra calculated by FEFF8 on 1 x 1 x 1 cells with 0, 2, and 3 substituted GdO_6 units after DFT relaxation.*

2.5.2 Location of Gd analysis at atom scale by STEM

In order to determine the location of Gd in the non-stoichiometric GAG at the atomic scale, the $(Gd_{0.9}Tb_{0.1})_{3.4}Al_{4.6}O_{12}$ (x = 0.4) sample was selected for STEM measurement. The high-angle annular dark field (STEM-HAADF) of the Z-contrast imaging mode is imaged by diffusely scattered electrons at high angles. Since the intensity of the Z-contrast image is proportional to the square of its atomic number (Z^2), and since the Z-contrast image does not vary significantly with specimen thickness or objective focus, there is no inversion of the image contrast, i.e. the atom or column of atoms is always a bright spot in the image. Therefore, on the atomic scale, the intensity of the bright spot is very sensitive to the number of atoms in the column, according to the $I \propto \sum_i (m_i Z_i^n)$ where *I* is intensity, i is number of elements, m is elemental ratio, and *Z* is atomic number of elements. We can therefore distinguish the atoms on each column at the atomic scale by the intensity of the HAADF image [10-12]. In the garnet structure, an atomic column containing only the octahedral Al_{16a} B site can be observed along the [001] orientation, from which the Gd atom substitution at B site is directly observed, while the atomic columns at all other sites include atoms at different crystallography sites (see ***Fig 2.8a***). ***Fig 2.8b*** shows the SAED diagram to ensure that the observed HAADF image is along the [001] orientation.

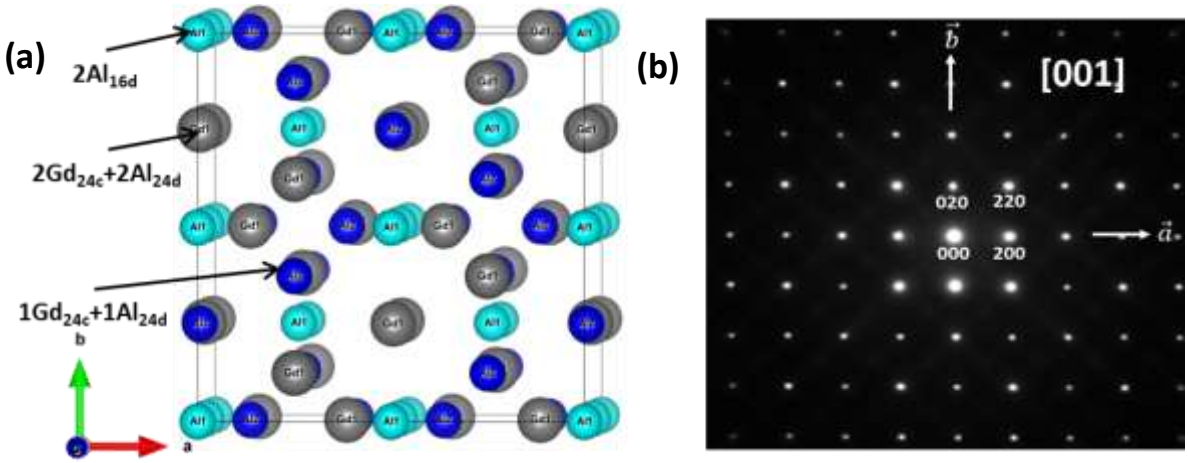

Fig 2.8 (a) *The figure of Gd and Al atoms distribution along the [001] axis in GAG structure (gray, pale blue and deep blue atom are Gd1, Al1 and Al2, respectively.)* ***(b)*** *SAED pattern of* $(Gd_{0.9}Tb_{0.1})_{3.4}Al_{4.6}O_{12}$ *along the [001] orientation.*

Fig 2.9a shows a STEM-HAADF image along the [001] orientation obtain by JEMS software[13], with the corresponding atomic column distribution superimposed on the image. The brightness of each spot in the HAADF image correlates with the composition of each atomic column. Theoretically, the brightness of the atomic columns at each position from bright to dark should be $2Gd_{24c}+2Al_{24d} > 1Gd_{24c}+1Al_{24d} > 2Al_{16a}$. For non-stoichiometric GAG, partial occupation of Al by Gd results in a brighter spot of $(2-x)Al_{16a}+ xGd_{16a}$ than $2Al_{16a}$, because the atomic number of Gd (Z = 64) is much larger than that of Al (Z = 13). As can be seen in the ***Fig 2.9a***, the brightest spot is $2Gd_{24c}+2Al_{24d}$, followed by $1Gd_{24c}+1Al_{24d}$, and the darkest spot represents $2Al_{16a}$ which agrees with the theory. A closer look (red arrows in ***Fig 2.9a***) reveals that the spot of $2Al_{16}$ exhibit different brightness intensities, suggesting a disordered substitution of Gd for Al and the atomic column should be $(2-x)Al_{16a}+ xGd_{16a}$. ***Fig 2.9 b*** is the intensity profile extracted from the red box in the HAADF image, with the high intensity peaks representing the $2Gd_{24c}+2Al_{24d}$ atomic column and the low intensity peaks representing the $(2-x)Al_{16a}+ xGd_{16a}$ atomic column. Comparison of the volumes of the peaks in each column shows that each $2Gd_{24c}+2Al_{24d}$ atomic column is essentially uniform indicating consistency of composition and homogeneity of thickness at each site, while the variation in intensity of each $(2-x)Al_{16a}+ xGd_{16a}$ column indicates differences in Gd content at each Al_{16a} site, suggesting disordered Gd occupation of the Al_{16a} site. This intensity

modulation is also seen in ns-YAG[5], but the signals of the GAG samples show stronger variations due to the increased Z contrast.

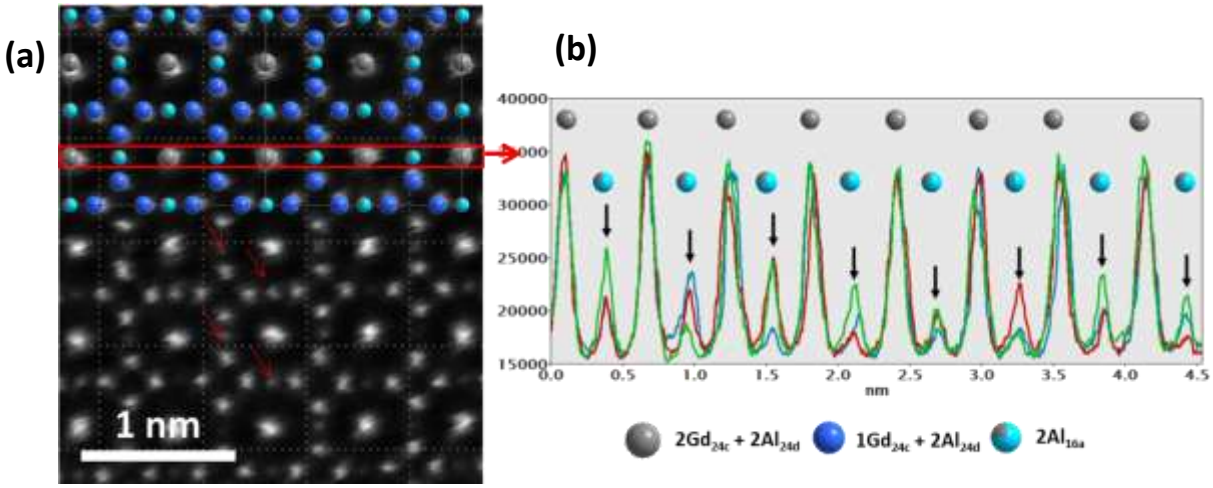

Fig 2.9 *STEM information of* $(Gd_{0.9}Tb_{0.1})_{3.4}Al_{4.6}O_{12}$ ***(a)*** *STEM-HAADF image along [001] orientation and corresponding atoms distribution image superimposed on the HAADF image (the red arrow indicates the bright spot of the 2Al atomic column)* ***(b)*** *Intensity profile extracted from the red box in the HAADF image.*

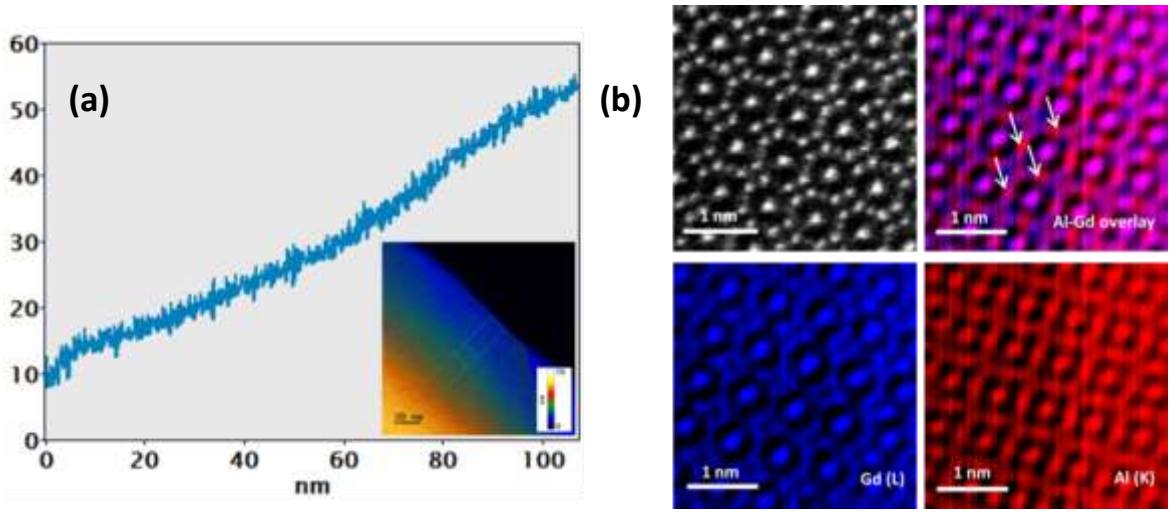

Fig 2.10 (a) *Thickness mapping of measured* $(Gd_{0.9}Tb_{0.1})_{3.4}Al_{4.8}O_{12}$ *sample (inset is thickness profile).* ***(b)*** *STEM-HAADF image and atomic resolution EDS maps of Al (red), Gd (blue) and overlay (Al + Gd)*

The thickness map shows a very thin area near the surface of the sample (see ***Fig 2.10a*** thickness profile). The thickness of the selected area in the STEM-HAADF is approximately 20

nm, which corresponds to the superimposition of around 16-17 cells. Quantified by the total intensity of scattered electrons (V) of individual atomic columns in STEM-HAADF images, the composition of atomic columns can be analysed by the equations $V \approx \sum_i (m_i Z_i^n)$ with n ≈ 2 (m_i is the weights of the different elements i composing the atomic columns, V is the volume of the peak and Z is the atomic number of each site). Using this information, it is possible to determine the distribution of Al/Gd on the each atomic column of Al2 site[14-15]. Here we have only measured non-stoichiometric samples, without only Al atomic columns as a reference, and therefore we cannot calculate the compositional information of the atomic columns in detail. However, the variations in the intensity of each atomic column indicate that the Gd disorder occupies the Al site. The corresponding atomic EDS mappings shown in ***Fig 2.10b*** clearly indicate that Al (red) is distributed at each site, whereas the color (blue) distribution of Gd is visually difficult to confirm the presence of Gd at the Al_{16a} site, but the difference in colour at each B site can be faintly seen (see white arrows in Gd and Gd-Al overlay mapping in ***Fig 2.10b***) From the above information provided by STEM-EDS we know that in the non-stoichiometric ratio GAG, the excess Gd ions replace the octahedral Al in a disordered way.

2.6 Average structure, dopant distribution and RE^{3+} location analysis of RE^{3+} doped $Gd_{3+x}Al_{5-x}O_{12}$ ($0 \leq x \leq 0.4$)

From the work on ns-YAG[5] we know that the distribution trends of the dopants in the non-stoichiometric structure are different for different RE^{3+} sizes. The smaller Er^{3+} tends to occupy the *B* site, while large Ce^{3+} only occupy at the *A* site in the non-stoichiometric YAG. In GAG, since the larger ionic radii of Gd occupy Al, and more Gd^{3+} replaces Al^{3+} than YAG, these facts may make the octahedron create greater possibilities to accommodate larger size dopants. Therefore here several dopant ions of different sizes (Tb^{3+}, Yb^{3+}, Tm^{3+}) are selected to study their distribution homogeneous and occupy tendency in non-stoichiometric GAGs by microprobe, EXAFS, STEM-EDS analysis.

2.6.1 Synthesis and average structure of RE^{3+} (RE = Ce, Tb, Er, Ho, Tm, Yb) doped GAG

The doping concentration chosen for doped here is the optimal doping concentration determined through literature review[16-19]. The synthetic GAG doped with RE^{3+} samples were synthesised in a similar process to the GAG samples. A series of glass samples were synthesised using ADL in combination with a laser heating device and then heat treated in a muffle furnace at 950 ^{o}C in air for 3 hours to fully crystallised. To ensure that the valence of Ce is +3 in the Ce doped GAG sample, they were crystallised in a reducing atmosphere of 95% Ar/5% H_2. The specific composition of all samples and the specific conditions of the reactions are listed in ***Table A.1.2*** and ***Table A.1.3.***

The XRD diffraction patterns of GAG: 2%Ce^{3+}, GAG: 10%Tb^{3+} and GAG: 2%Er^{3+}/10%Yb^{3+} shown in ***Fig 2.10*** indicates that both stoichiometric and non-stoichiometric doped samples are single garnets phase with no phase separation and second phase even with higher concentrations of doping, and the position of the peaks gradually move to the lower 2θ values as the x value increases (see ***Fig 2.10*** enlarge of main peak). The cell parameters of the three samples after refinement are shown on the right side of ***Fig 2.10***, indicating a linear increasing with increasing x values. For Ce-doped samples, the cell parameter of x = 0 (a = 12.1672(2) Å) are larger than that of undoped GAG (a = 12.13842(1) Å) due to the fact that Ce^{3+} is larger than Gd^{3+}. The ionic radius of Tb^{3+} is slightly smaller than that of Gd^{3+}, so the cell parameters of x = 0 (a = 12.1288(1) Å) are slightly smaller than those of undoped GAG (a = 12.13842(1) Å). For the higher concentration doped GAG: 2%Er^{3+}/10%Yb^{3+} system, the cell parameters of x = 0 (a = 12.0999(1) Å) are much smaller than that of undoped GAG (a = 12.13842(1) Å) because Yb^{3+} is smaller than Gd^{3+}. The PXRD pattern of the GAG: Ho^{3+}/Yb^{3+} and GAG: Tm^{3+}/Yb^{3+} samples shown in ***Fig B.1.4***, respectively, indicate that the doped sample is a single garnet phase with no phase separation and secondary phase. Detailed refinement parameters are listed in ***Table B.1.1***.

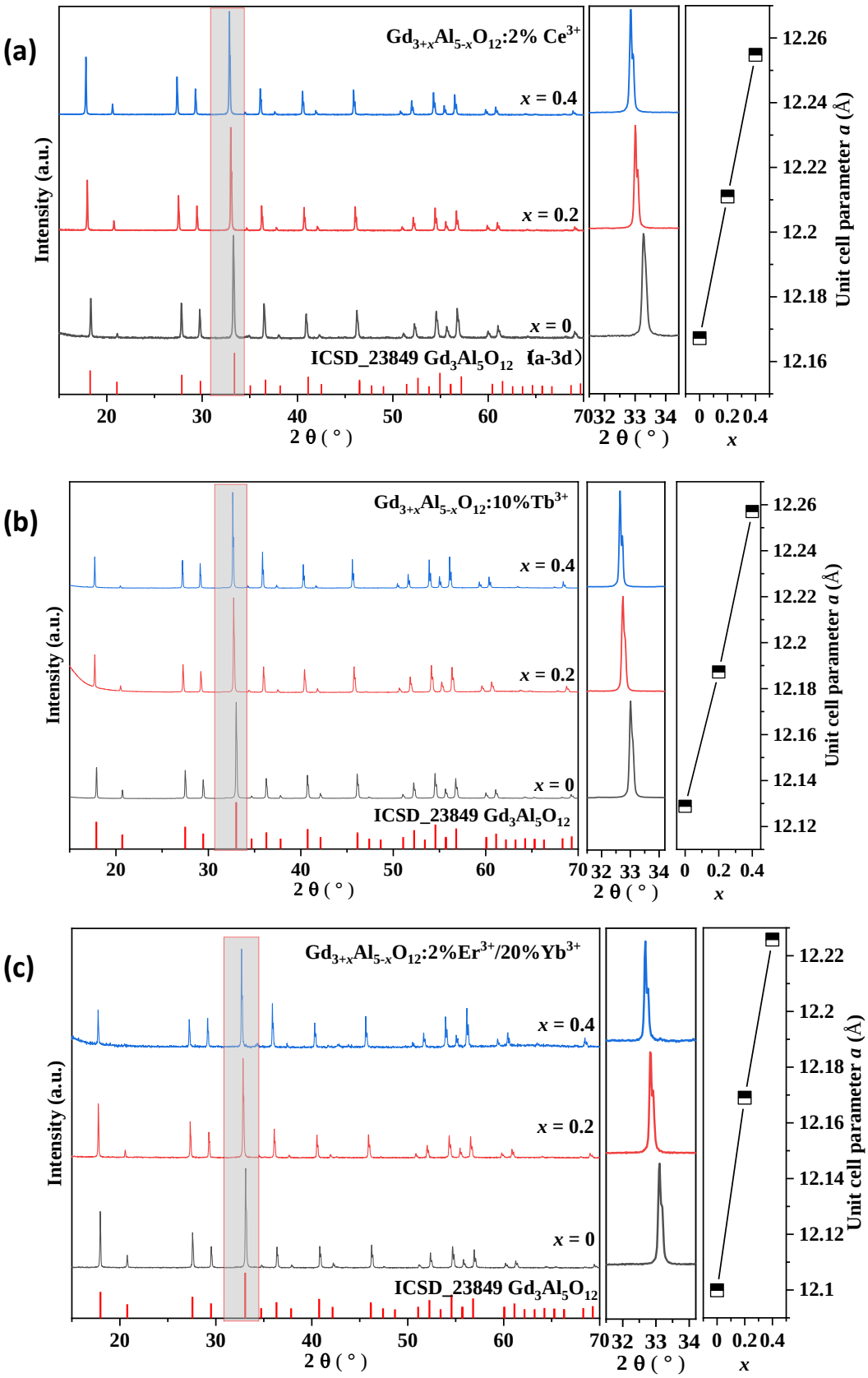

Fig 2.11 *The PXRD pattern with zoom of the (211) plane shift and refinement cell parameter a as x value increasing of* ***(a)*** *GAG: 2%Ce*$^{3+}$ ***(b)*** *GAG: 10%Tb*$^{3+}$ *and* ***(c)*** *GAG: 2%Er*$^{3+}$*/20%Yb*$^{3+}$*.*

2.6.2 Elemental distribution analysis by microprobe

Here, high-precision microprobe measurements at the microstructural level were used to check the homogeneous of element distribution with smaller concentrations of doping ions. ***Fig 2.12*** illustrates the electron microprobe elemental mapping of the GAG: 2%Ce^{3+} bead sample. It can be observed that the samples contain a large amount of porosity and the Gd, Al and low concentration of doped Ce elements are uniformly distributed in the grains without obvious aggregation. A total of 40 acquisition points collected at 20 µm intervals from the centre to the edge of the bead were used for compositional analysis. The average compositions listed in ***Table 2.4*** show a general agreement with the theoretical composition. The microprobe elemental mapping of GAG: 2%Er^{3+}/20%Yb^{3+} and GAG: 1%Tm^{3+}/10%Yb^{3+} the samples displayed in ***Fig B.2.1*** and ***Fig B.2.2*** suggests homogeneity distribution of Er, Yb, Tm elemental. For the detailed information and analysis, see ***Appendix B.2***.

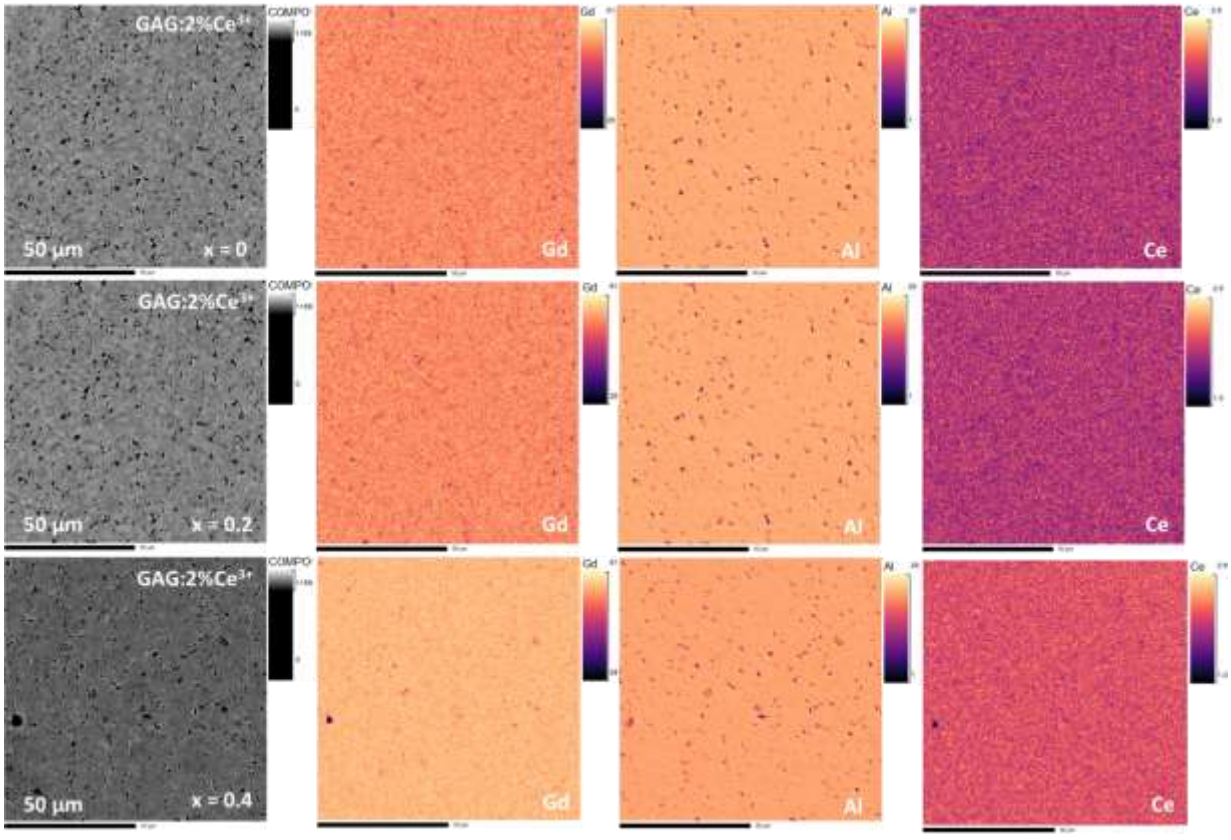

Fig 2.12 *Electron microprobe elemental mapping of GAG: 2% Ce^{3+}(x = 0, 0.2, 0.4).*

Table 2.4 *Microprobe compositional analysis of GAG: 2%Ce^{3+}(x = 0, 0.2, 0.4).*

$(Gd_{0.98}Ce_{0.02})_{3+x}Al_{5-x}O_{12}$	Experimental composition	Theoretical composition
x = 0	$Gd_{2.88(3)}Ce_{0.054(1)}Al_{5.07(3)}O_{12}$	$Gd_{2.94}Ce_{0.06}Al_5O_{12}$
x = 0.2	$Gd_{3.05(3)}Ce_{0.068(2)}Al_{4.88(4)}O_{12}$	$Gd_{3.136}Ce_{0.064}Al_{4.8}O_{12}$
x = 0.4	$Gd_{3.27(5)}Ce_{0.070(2)}Al_{4.66(5)}O_{12}$	$Gd_{3.332}Ce_{0.068}Al_{4.6}O_{12}$

Synchrotron PXRD can be used to quantify the distribution of Gd^{3+} at the *B* site due to the good contrast of Gd^{3+}/Al^{3+}, but the distribution of doped rare earth cations (e.g., Ce, Tb, Yb, Tm, Er, Ho) cannot be detected due to the weak scattering contrast with Gd^{3+}. Therefore, the laboratory PXRD data here can only provide the evolution of the cell parameters with the x value, and it is not possible to know the distribution of rare-earth dopant ions. As for the occupation of dopant ions in nonstoichiometric GAG, we have used atomic-scale STEM-EDS and EXAFS spectra (see **2.6.3** and **2.6.4** section)

2.6.3 Tb location analysis by STEM-EDS

The Tb ion was chosen to observe its distribution in the nonstoichiometric GAG as Tb has a similar ionic radius to Gd may be considered to occupy the eight coordinated Al site. The doping content of Tb in GAG: 10%Tb^{3+} too low to determine the site and content of Tb by changes in intensity of HAADF image in the case of Gd occupying the Al_{16a} site. It is therefore useful to have extracted an atomic scale STEM-EDS profile on a given atomic column to obtain information about the composition of that column.

The sample is equipped with an EDS probe and a suitable energy window is selected to excite the characteristic X-rays of Gd and Tb. Based on the intensity and wavelength distribution of the X-rays, elemental mapping and semi-quantitative compositional information of the sample is obtained. ***Fig 2.13a*** shows the spectrum as an accumulation of 16 spectra extracted at the Al_{16a} site to improve the signal-to-noise ratio. The clear L-lines of Tb can be distinguished from Gd-lines indicating independence from the Gd signal as well as from neighbouring sites. The average composition found from the 16 spectra is 56.5 at% Al, 37.5 at% Gd and 6 at% Tb, which suggest that not only Gd but also Tb occupies Al_{16a} site.

This makes chemical sense, due to the very similar ionic radii of Gd^{3+} and Tb^{3+}. The extracted EDS spectra from the other sites and global mapping are shown in ***Fig 2.13b*** ($1Gd_{24c}+1Al_{24d}$) and ***Fig 2.13c*** ($2Gd_{24c}+2Al_{24d}$) and ***Fig 2.13d*** (global), respectively. All spectra are accumulated from 16 spectra and quantified using the same energy rays to improve the signal-to-noise ratio. The results of the overall EDS quantification indicated the presence of 43.3 at% Al, 50.1 at% Gd and 6.6 at% Tb with the overestimation in RE content due to the L-lines used differing from the normalised composition with 38.3at% Gd and 4.25 at% Tb. The EDS quantification results for the $1Gd_{24c}+1Al_{24d}$ site and $2Gd_{24c}+2Al_{24d}$ site were 49.5 at% Al, 43.7 at% Gd, 6.8 at% Tb and 50.7 at% Al, 43 at% Gd, 6.3 at% Tb, respectively, corresponding to the normalized composition.

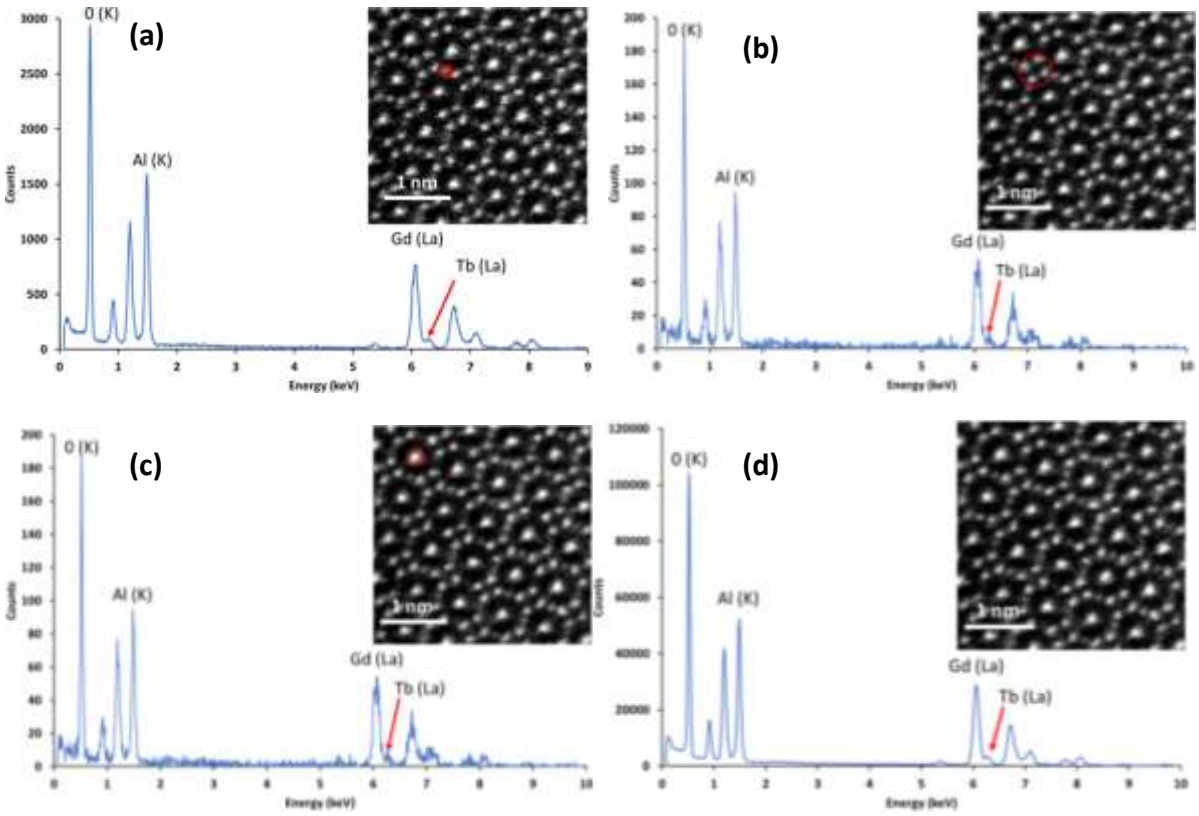

Fig 2.13 *(a) Thickness mapping of measured $(Gd_{0.9}Tb_{0.1})_{3.4}Al_{4.8}O_{12}$ sample (inset is thickness profile). EDS spectrum of (b) global map and extracted from the map on (c) $1Gd_{24d}+1Al_{24c}$ site (red circle in the HAADF image (c) inset) (d) $2Gd_{24d}+2Al_{24c}$ site (red circle in the HAADF image).*

2.6.4 Yb/Tm location analysis by EXAFS.

The doping concentration of Er^{3+} and Tm^{3+} in GAG: 2%Er^{3+}/20%Yb^{3+} and GAG: 1%Tm^{3+}/10%Yb^{3+} is too low to be detected by STEM-HAADF/EDS. Also the overlap of Yb and Gd characteristic X-ray emission lines does not allow to study the distribution of Yb by STEM-EDS. The X-ray scattering factors of these rare earths are very similar, and Gd absorbs neutrons very strongly. EXAFS is therefore the only established technique for analysing the distribution of rare earth in these materials. In order to probe the local environment around Gd and rare earth ions Yb^{3+}, Tm^{3+} in the Yb-doped $(Gd_{0.9}Yb_{0.1})_{3+x}Al_{5-x}O_{12}$ (x = 0, 0.2, 0.4) and Tm-doped $(Gd_{0.9}Tm_{0.1})_{3+x}Al_{5-x}O_{12}$ (x = 0, 0.2, 0.4) samples, EXAFS measurements were carried out at the L_3 edges of Gd (7243 eV), Yb (8944 eV) and Tm (8648 eV) on same sample.

For non-stoichiometric GAG samples doped with Yb^{3+} or Tm^{3+} ions, the same type of EXAFS oscillatory Fourier-transform evolution at the L_3 edges of Gd as in the undoped GAG samples when the Gd content increases (see ***Fig B.3.2***) was observed. From the gadolinium point of view, the amount and type of rare earth ions present in the structure has little effect on the local environment of Gd.

From the Fourier transform spectrum of Yb L_3 edge, it can be observed that the amplitude of the Fourier transform peak corresponding to the first neighbourhood around the rare earth ion increases as the rare earth content increases (see ***Fig B.3.3***). This observation tells us that there may exist different types of octahedral substitution in non-stoichiometric GAG. And these different substitution types could be Gd/AlO_6, doubly substituted (Gd and Yb)/AlO_6 or Yb/AlO_6. In order to determine a more favourable substitution models, structure for different artificial atomic substitution scenarios was generated by Supercell[9]. The aim is to generate the corresponding EXAFS signals using the FEFF code[7] and to fit them with experimental results. Here supercells with different structures models based on the substitution of 1 (x = 0.125) and 2 (x = 0.25) BO_6 units for AlO_6 were modelled. The different substitution models and different configuration numbers corresponding to specific compositions with 8% doping $Yb_{0.25}Gd_{2.75+x}Al_{5-x}O_{12}$ are listed in ***Table 2.5*** (the 8% doping content corresponds to two YbO_6 polyhedral units in a 1 × 1 × 1 supercell). The structure of the stoichiometric $Yb_{0.25}Gd_{2.75}Al_{4.8}O_{12}$ sample is modelled in only

one case i.e. the structure without BO_6-substituted units and good fit with experimental spectra as shown in ***Fig 2.14***. For the non-stoichiometric $Yb_{0.25}Gd_{2.875}Al_{4.875}O_{12}$ composition with 1 BO_6-substituted unit (x = 0.125) two cases exist: one YbO_6-substituted unit or one GdO_6-substituted unit. For the non-stoichiometric $Yb_{0.25}Gd_3Al_{4.75}O_{12}$ composition with 2 BO_6-substituted units (x = 0.25) three cases exist: two YbO_6-substituted units; one YbO_6 and one GdO_6-substituted unit; two GdO_6-substituted units.

Table 2.5 *Composition, different substitution case and number of configurations corresponding to 0, 1 and 2 substituted BO_6 units model in $Yb_{0.25}Gd_{2.75+x}Al_{5-x}O_{12}$*

$A_3B_2C_3O_{12}$			Site *A (24c)*			Site *B (16a)*		Site *C* (24d)	Configurations
x value	Composition	Case	GdO_8	YbO_8	GdO_6	YbO_6	AlO_6	AlO_4	Individual
x = 0 1 BO_6	$Yb_{0.25}Gd_{2.75}Al_5O_{12}$	Case1	22	2	0	0	16	24	8
x = 0.125 8%Yb	$Yb_{0.25}Gd_{2.875}Al_{4.875}O_{12}$	Case 1	23	1	0	1	15	24	4
		Case 2	22	2	1	0	15	24	48
x = 0.25 8%Yb	$Yb_{0.25}Gd_3Al_{4.75}O_{12}$	Case 1	24	0	0	2	14	24	5
		Case 2	23	1	1	1	14	24	60
		Case 3	22	2	2	0	14	24	388

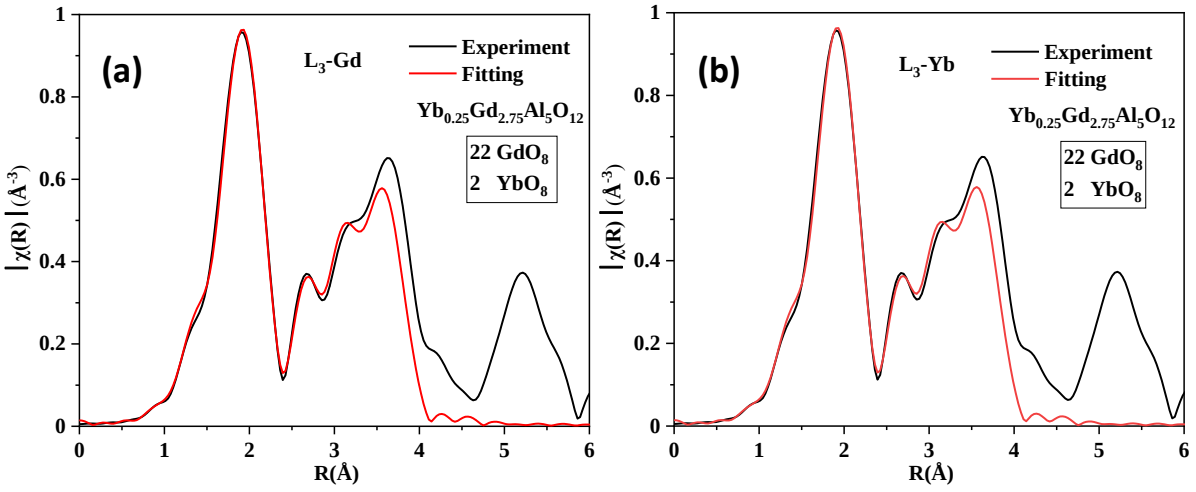

Fig 2.14 *$Yb_{0.25}Gd_{2.75}Al_5O_{12}$ (x = 0) Experiment (black line) and fitted (red) FT EXAFS spectrum at* ***(a)*** *L_3-Gd edge and* ***(b)*** *L_3-Yb edge (structure model without BO_6 substituted units)*

For $Yb_{0.25}Gd_{2.875}Al_{4.875}O_{12}$ composition with 1 BO_6-substituted units (x = 0.125), the same analyses were carried out. ***Fig 2.15*** presents the experimental and fitted FT EXAFS spectra at Gd and Yb L_3-edge based on two cases of different substitution structure models. By comparing the experimental and fitted FT EXAFS spectra of the two cases, it can be clearly observed that both the spectra of Gd (***Fig 2.15a***) and Yb-L_3 edge (***Fig 2.15b***) of the case 1 demonstrate a good fit with spectra on the first peak. This result indicates that the smaller ionic radius Yb has octahedral substitution preference in the case of a non-stoichiometric GAG with only one substitution *B*O_6 unit.

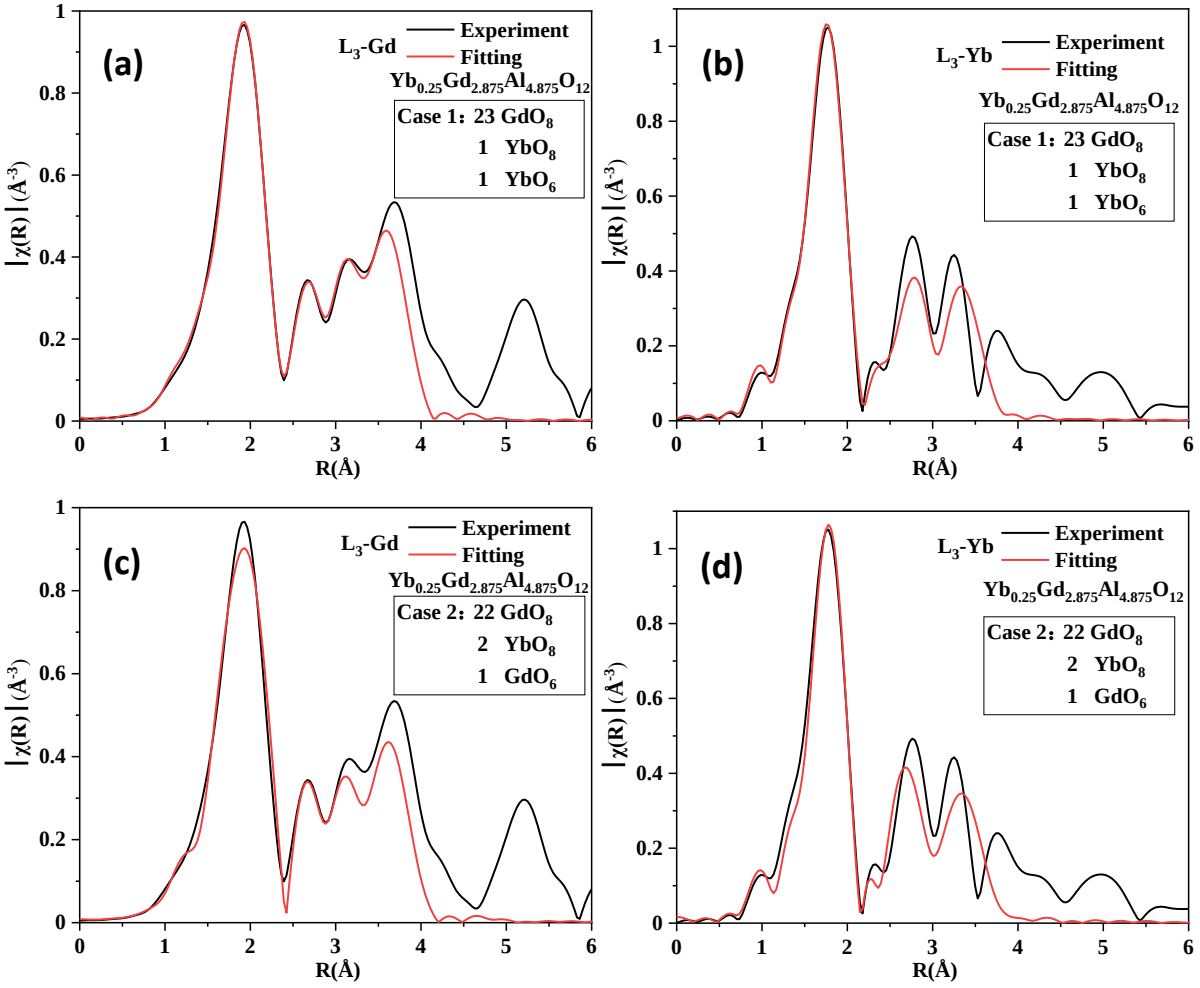

Fig 2.15 *$Yb_{0.25}Gd_{2.875}Al_{4.875}O_{12}$ (x = 0.125). Experiment (black line) and fitted (red) FT EXAFS spectrum at* ***(a)*** *L_3-Gd edge and* ***(b)*** *L_3-Yb edge of case 1 (structure model with one YbO_6-substituted units), and* ***(c)*** *L_3-Gd edge and* ***(d)*** *L_3-Yb of case 2 (structure model with one GdO_6-substituted units)*

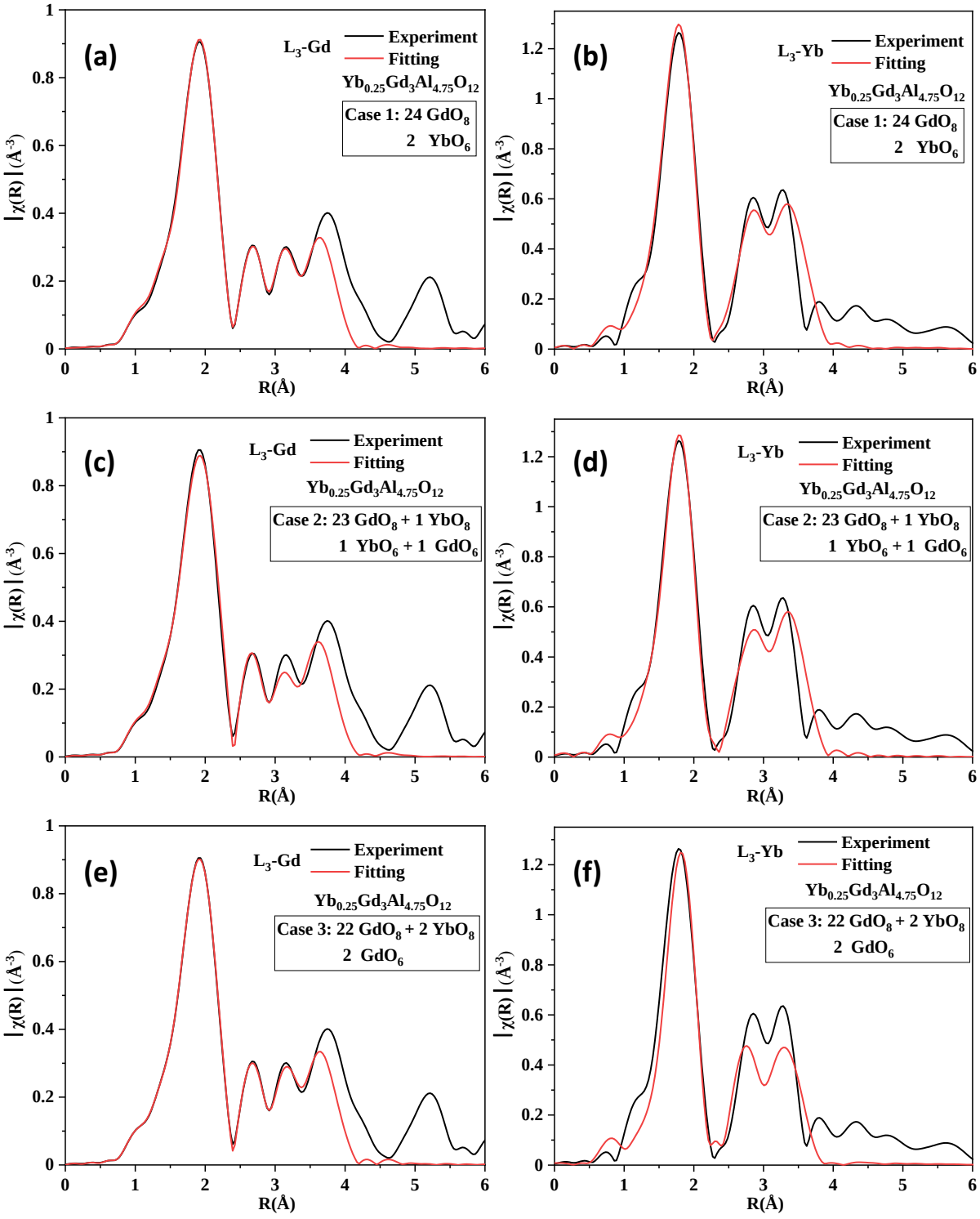

Fig 2.16 *$Yb_{0.25}Gd_3Al_{4.75}O_{12}$ (x = 0.25). Experiment (black line) and fitted (red) FT EXAFS spectrum at* ***(a)*** *L_3-Gd edge and* ***(b)*** *L_3-Yb edge of case 1 (structure model with twoYbO_6-substituted units)* ***(c)*** *L_3-Gd edge and* ***(d)*** *L_3-Yb of case 2 (structure model with one YbO_6 and one GdO_6-substituted unit)* ***(e)*** *L_3-Gd edge and* ***(f)*** *L_3-Yb of case 3 (structure model with two GdO_6-substituted units).*

For $Yb_{0.25}Gd_{2.875}Al_{4.875}O_{12}$ composition with 2 BO_6-substituted units (x = 0.125), three different substitution cases were analysed. ***Fig 2.16*** presents the experimental and fitted FT EXAFS spectra at Gd and Yb L_3-edge based on three cases of different substitution structure models: case 1 with two YbO_6 -substituted units (***Fig 2.16 a*** and ***b***); case 2 with one YbO_6 and one GdO_6 substituted units (***Fig 2.16 c*** and ***d***); case 3 with two GdO_6 substituted units (***Fig 2.16 e*** and ***f***). By carefully comparing the fitted and experimental spectra of the three cases, the Gd- and Yb- L_3 edge spectra of the first case are in good agreement with the experimental spectra. Thus it is know that the smaller doping Yb^{3+} ions have an octahedral substitution preference at higher nonstoichiometric contents.

This result shows that smaller doped ions (Yb^{3+}) have a strong octahedral substitution preference in nonstoichiometric GAG. For EXAFS spectra of Tm L_3 edge in $Tm_{0.1}Gd_{0.9})_{3+x}Al_{5-x}O_{12}$ (x = 0, 0.2, 0.4) are also being studied, and we speculate that ions smaller than Gd should also tend to occupy the octahedron in the non-stoichiometric GAG.

2.6.5 Multiple RE^{3+} crystallographic sites in nonstoichiometric GAG

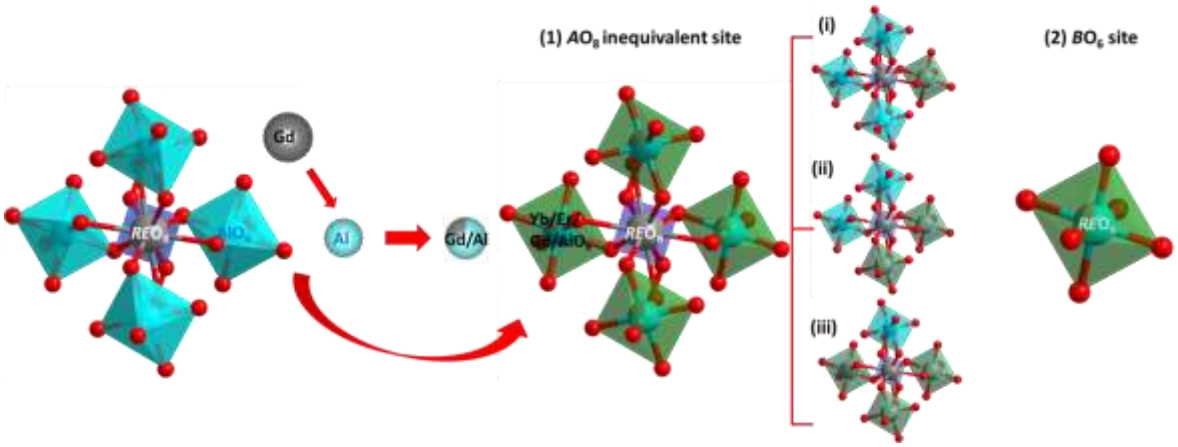

Fig 2.17 *Local structural framework diagrams of (1) the non-equivalent AO_8 sites caused by the substitution of the AlO_6 octahedras around the AO_8 by Gd^{3+}. (i), (ii) and (iii) denotes one, two, and three GdO_6 substitutions for AlO_6 around AO_8 respectively, (2) BO_6 site. (RE= Tb, Tm, Yb)*

Based on the results of the STEM, EXAFS local structure analysis, it can be concluded that in the non-stoichiometric ratio GAG, Gd^{3+} occupies the octahedron in a disordered manner and shows a higher degree of disorder with increasing nonstoichiometric content.

STEM-EDS study shows that larger-radius dopants (Tb) can be distributed evenly between the *A* dodecahedron and *B* octahedron site. EXAFS analysis suggests that the small-radius dopants (Yb) have a stronger tendency to occupy the B octahedron sites. We therefore suggest that the dopant ions in non-stoichiometric GAGs form unequal AO_8 sites (see ***Fig 2.17a***) and a new BO_6 symmetry site (see ***Fig 2.17b***) due to the disordered occupation of doping RE^{3+}, which provides new ideas for the improvement and the emission wavelengths creation of GAG-based luminescence materials.

2.7 Luminescence properties of $Gd_{3+x}Al_{5-x}O_{12}$ (x=0, 0.2, 0.4) host phosphors.

Different rare earth ions with different electronic configurations effect sensitivity of environmental changes in host. For example, the f - d transition of Ce^{3+} is sensitive to the local or surrounding environment, so its emission can span from 150 nm to 600 nm in different host materials. The f - f transitions of most rare earth ions are minimally influenced by their surroundings due to the shielding effect of the $^5S_2$ and $^5P_6$ shell layers so that their individual spectral intensity ratios and emission position remain almost unchanged from matrix to matrix. However, this shielding is not complete and changes in the crystal field cause changes in the spectral line shifts and the intensity of the spectral lines. The emission intensity of a particular type of transition known as a "super-sensitive transition" has been shown to be very sensitive to the surrounding environment (symmetry, coordination number, covalent bonding)[20]. In several papers, the results of investigations into the influence of the local environment on the spectral properties in garnet crystals doped with rare earth ions Nd^{3+}, Dy^{3+}, Ho^{3+}($^5I_8$-$^3H_6$,$^5I_8$-$^3G_6$), Er^{3+} ($^4I_{15/2}$-$^4G_{11/2}$ and $^4I_{15/2}$-$^2H_{11/2}$), Tm^{3+} ($^3H_6$-$^3H_4$) are presented[21-23]. Therefore, here we investigated the luminescence properties of different sizes rare earth ion-doped GAGs with different types of transition to clarify the luminescence spectral sensitivities to environmental changes associated with non-stoichiometry. They are Ce^{3+} (f - d transition), Tb^{3+} (f - f transition) doped down-conversion GAG materials and Er^{3+}, Tm^{3+}, Ho^{3+} hypersensitive transition co-doped Yb^{3+} up-conversion GAG materials.

2.7.1 Luminescence properties of down-conversion $Gd_{3+x}Al_{5-x}O_{12}$: 2%Ce^{3+}

Ce^{3+}-doped garnet is very well known as a down-conversion material for LEDs. Since Ce f - d transition is very sensitive to the local coordination environment, the cation substitution strategy is a useful way to change the emission colour to meet the wavelength required for LEDs[24-25]. It is difficult to determine experimentally the distribution of Ce^{3+} ions in the nonstoichiometric GAG, and given the disparity in the size of Ce^{3+} and Gd^{3+} ions and the result of the nonstoichiometric YAG system, we suggest that Ce^{3+} should be confined to the *A* site.

The photoluminescence excitation (dotted line) and emission (solid line) spectra of the $Gd_{3+x}Al_{5-x}O_{12}$ (x = 0, 0.2, 0.4): 2% Ce^{3+} powder measured at room temperature are shown in ***Fig 2.18a***. In ***Fig 2.18a*** left (dotted line), two broad excitation bands located around 300 - 340 nm and 400 - 500 nm are attributed to the 4f - $^2T_{2g}$ and 4f - ^2E_g transitions of Ce^{3+} ion[26-27]. In addition, the two different energy excitation bands shift in opposite directions (the excitation 4f - ^2E_g peak shifts to lower energy and the 4f - $^2T_{2g}$ peak shifts to higher energy) as the value of x increases. In the 5d - 4f transition of Ce^{3+}, two general factors can affect the shift in the excitation spectrum, namely the centroid shift and splitting of the 5d energy level due to electron cloud diffusion effects and crystal field effects, respectively. A centroid shift affects all excited 5d energy levels to shift in the same direction, while the crystal field split results in a shift in the opposite direction of the two energy excitation bands[28]. Here, therefore, the crystal field splitting of the Ce^{3+} ion owing to the occupation of the AlO_6 site by Gd^{3+} should be the main factor in the shift of the two excitation bands in opposite directions. Broad emission band attributed to the spin-allowed 5d – 4f transition of Ce^{3+} at 500 - 800 nm under λ_{ex} = 470 nm can be observed gradually red-shifted with increasing x-value in the emission spectrum from ***Fig 2.18a*** right (solid line). Perturbations to the local environment of Ce^{3+}, such as the bond lengths from the activator ion to the coordinating anions, the coordination environment, degree of covalency between the activator ion and its ligands, distortion of polyhedra, site local symmetry, etc. result in changes in the field strength of the crystal that correlate with the shift of the emission peak[28]. In this case, the substitution of Gd^{3+} to Al^{3+} causes a distortion of the dodecahedron,

and a larger distortion of the surrounding octahedron increasing the $5d^1$-$5d^2$ splitting thus causing a redshift on the emission peak. Furthermore, we can observe a gradual broadening and asymmetry of the emission peaks with increasing x values, which is due to the disorderly occupation of the Al octahedral sites by Gd^{3+} resulting in a variation of $5d_1$ state energy causing an inhomogeneous broadening[29]. A closer look at the emission curves shows that the emission band of x = 0.2 sample does not have a strong red shift, which corresponds to the YAG: Ce^{3+} emission spectra shown in ***Fig 2.18c***. We attribute the apparent redshift in the emission band of x = 0.4 to the greater degree of disordered occupation of Al^{3+} by Gd^{3+}.

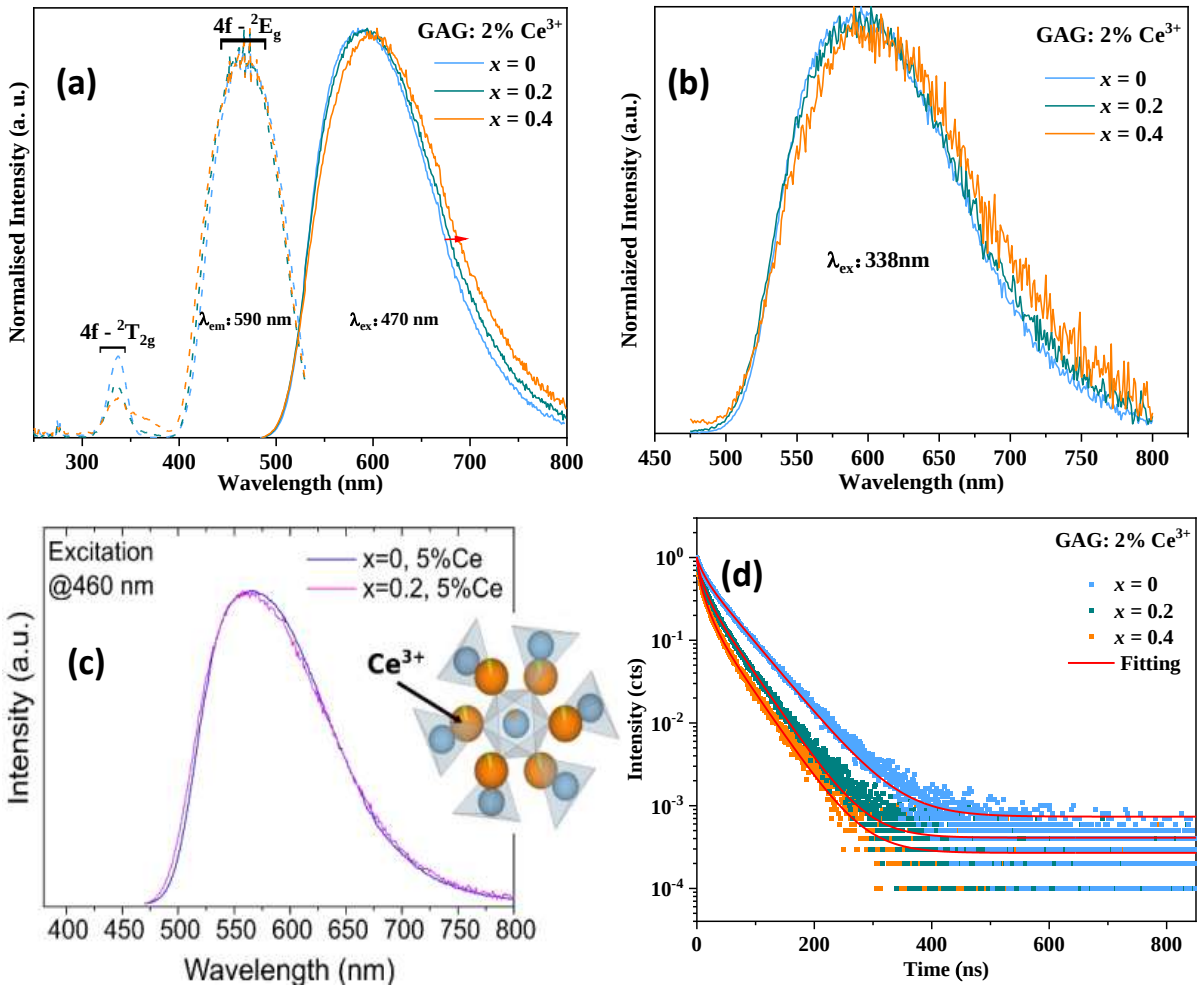

Fig 2.18 *Luminescence performance of $Gd_{3+x}Al_{5-x}O_{12}$ (x= 0, 0.2, 0.4): 2% Ce^{3+} powder measured at room temperature.* ***(a)*** *PLE (solid line) and PL (dotted line) spectra.* ***(b)*** *PLE spectra under 338 nm excitation. (The intensity of all spectra are normalised by the highest peaks)* ***(c)*** *PL spectra of ns-YAG: 5%Ce^{3+} under 460nm excitation[5].* ***(d)*** *Decay curves of Ce^{3+} 600 nm emission peak monitored under 338nm.*

Moreover, decay curves of GAG: 2% Ce^{3+} (x = 0, 0.2, and 0.4) at 600 nm emission were recorded, as shown in ***Fig 2.18d*****.** Fitting average decay times of Ce^{3+} in s-GAG and ns-GAG are 49, 35, and 31 ns, respectively, which becomes shorter with increasing non-stoichiometric content, as presented in ***Table 2.6***, suggesting that the electron lifetime at the 5d energy level getting shorter due to Gd^{3+} occupied BO_6 site[27]. We, therefore, suggest that the inequivalent BO_8 sites generated by Gd/Al substitution in BO_6 around the CeO_8 in the non-stoichiometric GAG are associated with a red-shift in the emission band, but cause a reduction in lifetime.

Table 2.6 *Fitting parameters and average lifetime obtained from decay curves fitting results of* $Gd_{3+x}Al_{5-x}O_{12}$*(x = 0, 0.2, 0.4): 2%*Ce^{3+}*.*

Samples	peak	A1%	t1(ns)	A2%	t2(ns)	T avg (ns)
x = 0	589nm	35.21%	20.50	64.79%	55.16	49.34
x = 0.2	593nm	51.04%	11.08	48.97%	41.57	34.94
x = 0.4	603nm	66.26%	12.68	33.74%	41.82	30.95

2.7.2 Luminescence properties of down-conversion $Gd_{3+x}Al_{5-x}O_{12}$(x = 0, 0.2, 0.4): 10%Tb^{3+}

Tb^{3+} ions are commonly used green phosphor dopant ions, which have been extensively studied in based garnet with highly efficient green emission. The Tb distribution in nonstoichiometric GAG was determined experimentally by STEM-EDS at *A* and *B* site. However the green emission of Tb originates from the insensitive f - f transition. Here, the effect of the nonstoichiometry on its green emission properties was investigated.

The excited spectra shown in ***Fig 2.19a*** consist of two broad bands at 277 nm ($E2^{1-3}$, spin allowed) and a weak broad band at 323 nm (E1, spin forbidden) which corresponds to the $^4f_8$ - $^4f_7{}^5d_1$ transition of Tb^{3+}, together with a weaker band at 353 nm corresponding to the $^7F_6$ - $^5D_2$ transition of Tb^{3+} (***Fig 2.19a*** inset enlarge). In addition, the f-f transition $^8S_{7/2}$–^6I_J of Gd^{3+} is located at 275 nm overlapping the f-d transition of Tb^{3+}[30]. The excitation peaks

ns-GAG at 275 nm and 323 nm show a clear blue shift compared to that of the stoichiometric GAG, which is mainly due to the replacement of Al^{3+} by Gd^{3+} by enhancing the crystal field splitting at the 5d energy level. The emission spectra of GAG: 10% Tb^{3+} (see ***Fig 2.19b***) reveals several emission peaks at 417, 437, 460, 491, 543, 591 and 628 nm, which are attributed to the f-d transitions of Tb^{3+}, respectively[16]. The emission spectra of GAG and ns-GAG show an intense green colour and do not differ significantly either in the position of the peaks or in their relative intensities, which may be since that the insensitivity of the f - f transition of Tb^{3+} to the changing of local environment even though STEM-EDS result confirms that Tb is distributed in different crystallographic symmetry sites. To avoid the effects of Gd^{3+} to Tb^{3+} energy transfer, the excitation and emission spectra of directly excited Tb^{3+} were studied, as shown in ***Fig B.4.1***. However, the emission peaks structure of the f-f transition do not differ between GAG and ns-GAG excited at 353nm, which suggests that the f-f transition of Tb^{3+} is insensitive to new local BO_6 sites.

Decay curves for the 544 nm emission under 270 nm excitation of GAG: 10%Tb were collected and are shown in ***Fig 2.19c***. The almost identical average lifetimes (given in ***Table 2.7***) indicate that the occupation of Al by Gd in the non-stoichiometric does not have much effect on the transfer of energy from Gd^{3+} to Tb^{3+}. For the non-stoichiometric sample GAG (x = 0.2 and x = 0.4), the decay curve requires a double exponential function of $I(t) = A1 \exp(-t/\tau1) + A2 \exp(-t/\tau2)$ to be fitted. In contrast, the decay curves for the stoichiometric ratios require only a single equation $I(t) = A \exp(-t/\tau)$ to get a good fit. This suggests that Tb is in two different environments in stoichiometric and non-stoichiometric GAG.

Even though distribution of Tb^{3+} over *A* and *B* by STEM-EDS, there is no strong change in the emission behaviour due to the fact that the f - f transition is shielded by $^5S_2$ and $^5P_6$ shell layers and is insensitive to environmental changes.

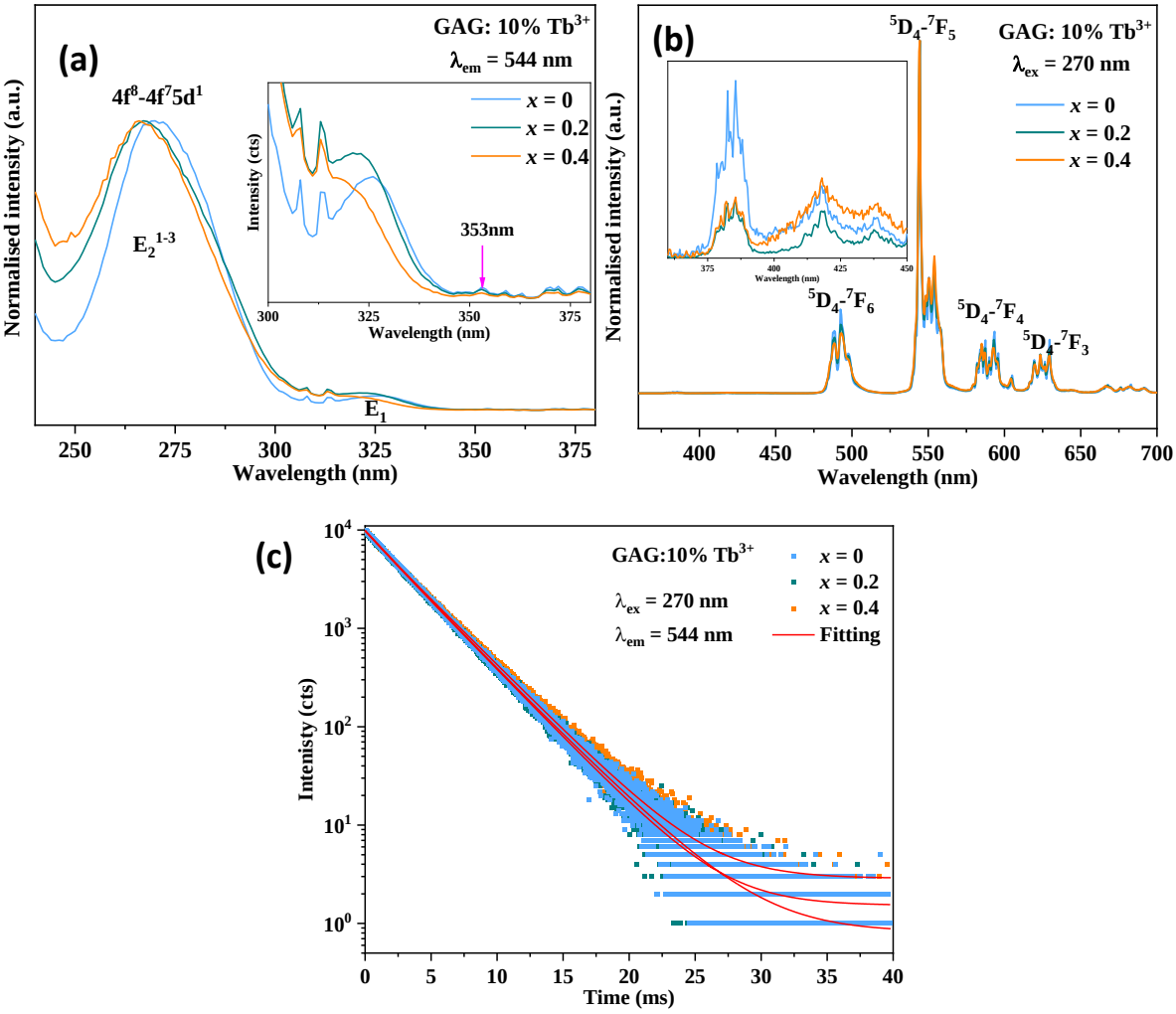

Fig 2.19 *Luminescence performance $Gd_{3+x}Al_{5-x}O_{12}$ (x= 0, 0.2, 0.4): 10% Tb^{3+} phosphors powder measured at room temperature.* ***(a)*** *PLE spectra record under 544nm,* ***(b)*** *PL spectra under record 270 nm. (The intensity of all spectra are normalised by the highest peaks) (c) Decay curves of Tb^{3+} with 544 nm emission peak monitored at 270 nm.*

Table 2.7 *Fitting parameters and average lifetime obtained from decay curves fitting results of $Gd_{03+x}Al_{5-x}O_{12}$: 10%Tb^{3+} (x = 0, 0.2, 0.4)*

Sample	A1%	t1(ms)	A2%	t2(ms)	T avg (ms)
x = 0	100%	3.06			3.06
x = 0.2	59%	2.80	41%	3.60	3.18
x = 0.4	19.5%	2.20	80.5%	3.50	3.33

2.7.3 Luminescence properties of up-conversion $Gd_{3+x}Al_{5-x}O_{12}$(x = 0, 0.2, 0.4): 2%Er^{3+}/20%Yb^{3+}

In the highly nonstoichiometric YAG system, up-conversion emission colour of Er^{3+}/Yb^{3+} was found to be sensitive to nonstoichiometry. And EXAFS experiments and simulations with different models show a strong octahedral substitution preference for smaller dopant ions.

Fig 2.20 shows the up-conversion luminescence performance of $Gd_{3+x}Al_{5-x}O_{12}$(x = 0, 0.2, 0.4): co-doped 2%Er^{3+}/20%Yb^{3+}. Two prominent emission bands at 510 to 590 nm (green emission) and 635 to 700 nm (red emission), corresponding to the transitions of $^4S_{3/2}$, $^2H_{11/2}$ - $^4I_{15/2}$ and $^4F_{9/2}$ - $^4I_{15/2}$ of Er^{3+}, respectively[31] can be observed in the up-conversion photoluminescence emission spectra of polished bead under a 980 nm excitation (see ***Fig 2.20a***). A comparison of the spectra of the three compositions shows that the profile and intensity of the red emission band are similar, but the position of the strongest peak in the green emission band attributed to the $^2H_{11/2}$ - $^4I_{15/2}$ hypersensitive transition of Er^{3+} at 555nm rather than 545 nm in the stoichiometric garnet. A closer look reveals that the I_{red}/I_{green} intensity ratio in the ns-GAG with x = 0.4 sample is 4.55 compared to the stoichiometric GAG (2.86) which is 37% higher. The highest peak blue shift and the decrease in intensity of the green emission band eventually lead to an emission colour change from orange in s-GAG to red in ns-GAG with x = 0.4, as shown in the CIE diagram (***Fig 2.20a*** Inset). Emission spectra measured on second face and edge of polished bead are displayed in **Fig *B.4.2a*** and ***b*** to avoid the randomness of the results, which demonstrate similar spectral behaviour. To avoid the effect of energy transfer from Yb^{3+} to Er^{3+}, the emission spectra of directly excited Er^{3+} (380 nm) were collected to demonstrate the environment change of Er^{3+} (see ***Fig 2.20b*****)**. The emission spectra under 380nm for the s- and ns-GAG exhibit a similar trend of a decrease in the intensity of the green emission peak as the up-conversion spectra excited under 980 nm.

The luminescence decay curves for the green emission (see ***Fig 2.20c***) and red emission (see ***Fig 2.20d***) of the stoichiometric sample can be fitted appropriately with a single exponential decay of $I(t) = I \exp(-t/\tau)$, whereas for the nonstoichiometric samples the decay

curves require a double exponential function of I(t) = A1 exp(-t/τ1) + A2 exp(-t/τ2) to ensure a good fit, suggesting different luminescence environment in the s- and ns-GAG compounds. The fitted parameters and fitting decay times for the red and green emissions of the two compounds listed in ***Table 2.8*** show shorter lifetimes in non-stoichiometric GAGs**.**

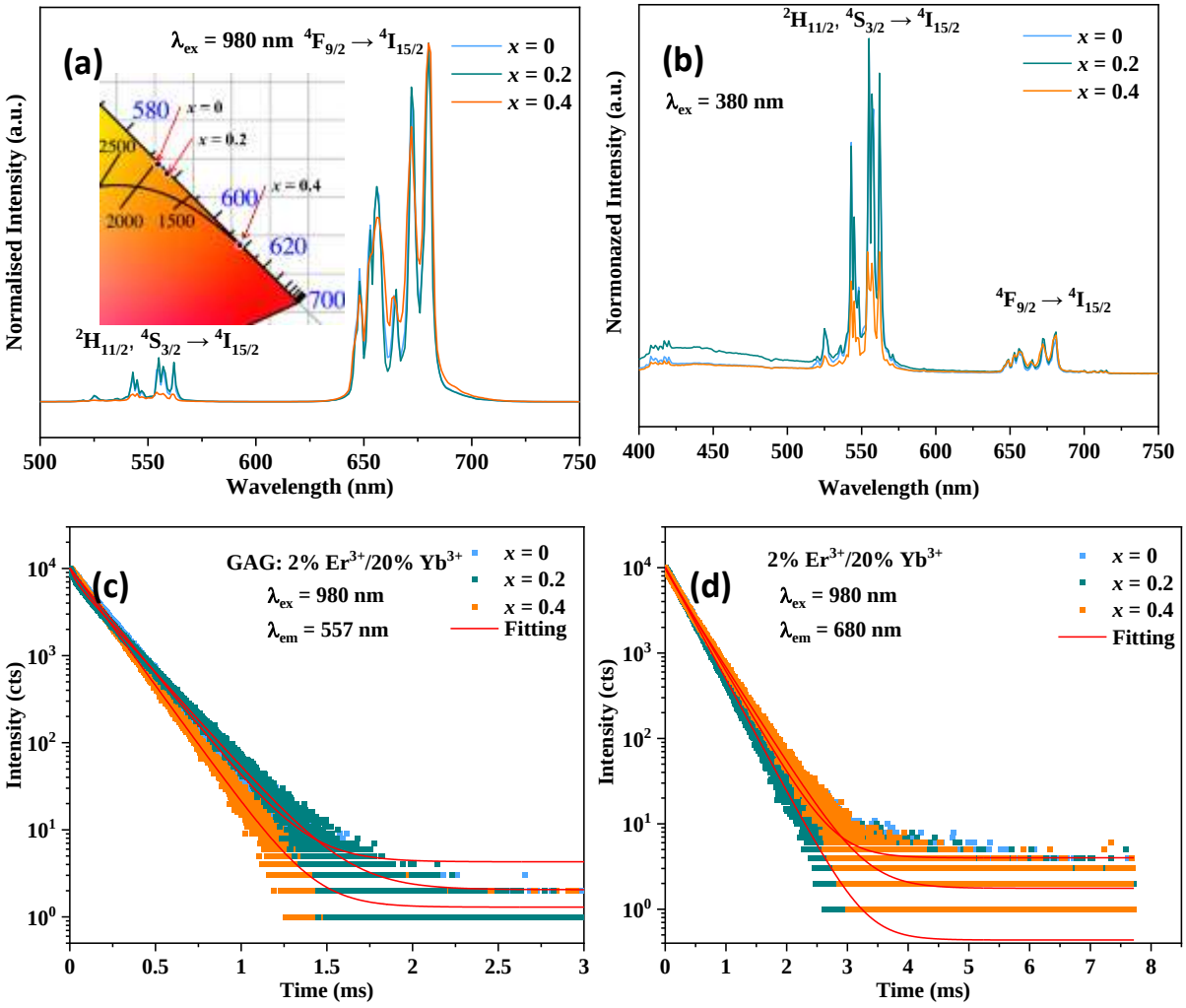

Fig 2.20 *Luminescence performance of* $Gd_{3+x}Al_{5-x}O_{12}$ *(x = 0, 0.2, 0.4): co-doped 2%*Er^{3+}*/20%*Yb^{3+} *polished bead measured at room temperature.* ***(a)*** *Up-conversion emission spectra (CIE chromaticity inset) under excitation at 980 nm.* ***(b)*** *Emission spectra of* Er^{3+} *under excitation at 380 nm. (The intensity of all spectra are normalised by the highest peaks) Decay curves of* Er^{3+} ***(c)*** *557 nm and* ***(d)*** *680nm emission peak.*

It is known from the ns-YAG paper that the non-stoichiometry does not change the two-photon up-conversion mechanism and the energy level diagram is presented in ***Fig B.4.2c***[31]. In up conversion emission, the emission intensity (I) is proportional to the power

of the infrared (IR) excitation intensity (P): $I \propto P^n$, where n is the number of IR photons required to be absorbed[17]. To further understand the UC process in s- and ns-GAG, the dependence of the emission intensity on the pump power is shown in a log-log plot in ***Fig B.4.2d*** and ***e*.** The relationship between log (I) and log (P) of GAG: Er^{3+}/Yb^{3+} system as a straight line with slope n. The fitting values of n for the green and red emissions in the x = 0 and 0.4 sample are 2.02, 1.99 and 1.88, 1.82, respectively, indicate that the s-GAG and ns-GAG: Er^{3+}/Yb^{3+} systems are both attributed to a two-phonon process, which corresponding to ns-YAG: Er^{3+}/Yb^{3+} system[5]. Similar to ns-YAG: Er/Yb system, the ns-GAG exhibits a tuning of the upconversion emission wavelength. The peak shift and wide color span through *A* or *B* site substitution in garnet up conversion materials cannot be achieved[32-33], and the local symmetry of dopants has been proved to be an effective way to achieve Er^{3+} emission wind span color adjustment[34]. We therefore suggest that this wide span of colour change is due to the two symmetries of activating ions in the ns-GAG affecting the emission intensity change of the $^2H_{11/2} \rightarrow {}^4I_{15/2}$ hypersensitive transition. Although Yb^{3+} was also confirmed by EXAFS to be distributed in dodecahedra AO_8 and octahedral BO_6, the efficiency of Yb^{3+} to Er^{3+} energy transfer in non-stoichiometric and stoichiometric GAG could not be compared due to the different areas of the test beads.

Table 2.8 *Fitting parameters and average lifetime obtained from decay curves fitting results.*

$Gd_{3+x}Al_{5-x}O_{12}$(x = 0, 0.2, 0.4): 2%Er^{3+}/20%Yb^{3+}

Sample	peak	**%**	**t1(ms)**	**%**	**t2(ms)**	**T avg (ms)**
x = 0	557nm	100	1.80			1.80
	680 nm	100	3.58			3.58
x = 0.2	557 nm	21%	0.3	79%	1.99	1.63
	680 nm	13.1%	1.48	86.9%	3.92	3.60
x = 0.4	557 nm	51.2%	1.5	48.5%	1.7	1.59
	680 nm	53.5%	3.02	46.5%	3.60	3.29

2.7.4 Luminescence properties of up-conversion $Gd_{3+x}Al_{5-x}O_{12}$(x=0, 0.2, 0.4): 1%Tm^{3+}/10%Yb^{3+}

Tm^{3+} was chosen for study because the near-infrared emission of Tm^{3+} corresponds to hypersensitive $^1G_4$-$^3H_5$/$^3H_4$-$^3H_6$ has been shown to be sensitive to environmental changes. Analysis of the Tm L3 edge EXAFS spectra is in progress, but comparing the EXAFS results for Yb^{3+} in ns-GAG, we believe that the smaller Tm^{3+} ions also have octahedral substitution preferences in nonstoichiometric GAG.

A comparison of the intense NIR emission band located at approximately 720 - 820 nm arising from the $^1G_4$-$^3H_5$/$^3H_4$-$^3H_6$ transition of GAG and ns-GAG under 980 nm excitation indicates that the most intense emission peak in x = 0.2 and x = 0.4 are red-shifted to 795 nm and 806 nm, rather than 783 nm in stoichiometric GAG, as shown in ***Fig 2.21a***. For this other weak blue emission appears in the red emission between 450 - 550 nm and 650 - 700 nm (Enlarge ***Fig 2.21a***), corresponding to the $^1G_4$-$^3H_6$ and $^1G_4$-$^3F_4$ transition of Tm^{3+}, respectively, with no significant variation in the stoichiometric GAG and non-stoichiometric GAG[18]. The calculated average lifetimes from the decay curves (see ***Fig 2.21b***) exhibit a shorter lifetime in ns-GAG than that of the GAG, as shown in ***Table 2.9***. We also analysed the relationship between log(I) and log(Pn) of near infrared, red and green of emission s- and ns-GAG as shown in ***Fig B.4.3a*** (near infrared emission), ***b*** (x = 0) and ***c*** (x = 0.4). The fitting values of n for the near infrared emissions in the x = 0, 0.2 and 0.4 sample are 1.94, 1.86 and 1.85, respectively, indicate that the s-GAG and ns-GAG: Tm^{3+}/Yb^{3+} systems are both attributed to a two-phonon process (see ***Fig B.4.3a***[18]). Here it is clear that the $^3H_4$-$^3H_6$ transition demonstrates sensitivity (shift and intensity changes of the emission peak) to environmental changes in the ns-GAG.

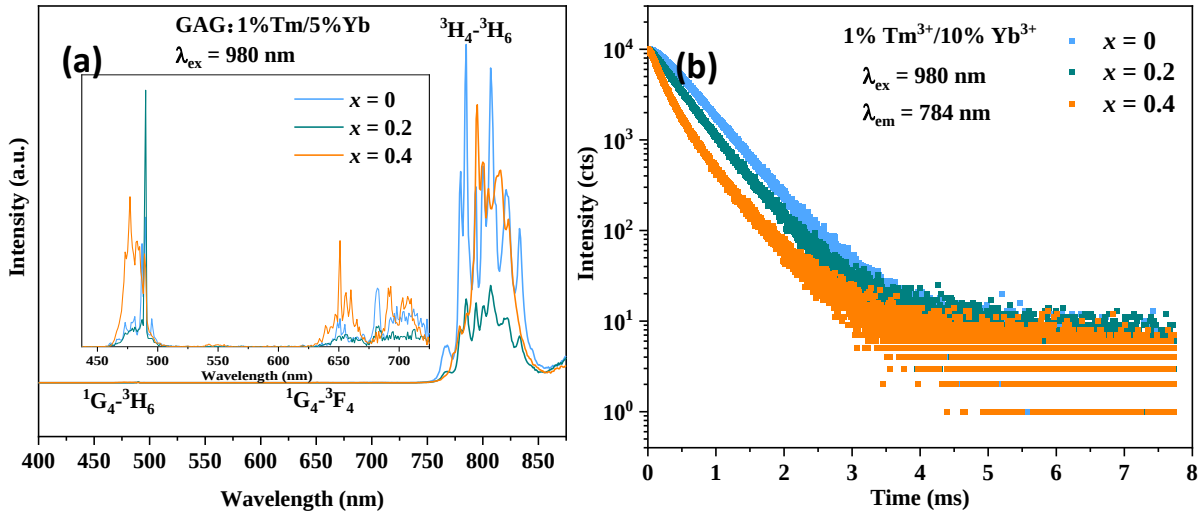

Fig 2.21 *Luminescence performance of $Gd_{3+x}Al_{5-x}O_{12}$ (x = 0, 0.2, 0.4): co-doped 2%Er^{3+}/20%Yb^{3+} polished bead measured at room temperature.* ***(a)*** *Up-conversion emission spectra under excitation at 980 nm.* ***(b)*** *Decay curves of Tm^{3+} at 784nm emission peak.*

Table 2.9 *Fitting parameters and average lifetime obtained from decay curves fitting results. $Gd_{3+x}Al_{5-x}O_{12}$(x = 0, 0.2, 0.4): 1%Tm^{3+}/10%Yb^{3+}*

Sample	peak	%	t1(ms)	%	t2(ms)	T avg (ms)
x = 0	784 nm	100%	5.29			5.29
x = 0.2	784 nm	88.94%	4.14	11.06%	6.20	4.37
x = 0.4	784 nm	87.65%	2.25	12.35%	6.18	2.72

2.7.5 Luminescence properties of up-conversion $Gd_{3+x}Al_{5-x}O_{12}$(x = 0, 0.2, 0.4): 1%Ho^{3+}/10%Yb^{3+}

Finally, Ho has been chosen for studies that can contrast with Er^{3+} and Tm^{3+} because the emission peaks of their supersensitive transition $^5I_8$-$^3H_6$, $^5I_8$-$^3G_6$ are located in the infrared region. Tb ions have been shown to be distributed in two sites, then smaller Ho ions are considered to be accommodated by octahedral sites. Up-conversion luminescence of the GAG: 1%Ho^{3+}/10%Yb^{3+} was measured under a 976 nm to pump the Yb^{3+} ions, shown in ***Fig 2.22a***. The two main emission bands at 535 nm and 656 nm should be ascribed to the $^5F_4$,

$^5S_2$ - $^5I_8$ and $^5F_5$ - $^5I_8$ transitions of Ho^{3+} ions, respectively, together with a weak peak located in 750nm assigning to $^5F_4$, $^5S_2$ - $^5I_7$. The absence of differences in intensity and peak positions in the emission spectra comparing stoichiometric and non-stoichiometric suggests that the $^5F_4$, $^5S_2$ - $^5I_8$ and $^5F_5$ - $^5I_8$ transition in Ho^{3+} is not very sensitive to the change of structure and local symmetry in non-stoichiometric GAG host[19]. Indeed, the $^3H_6$ - $^5I_8$ and $^5G_5$ - $^5I_8$ were shown to be the hypersensitive transition that is not observable within 800 nm. Similarly, to avoid randomness of the sample the emission spectra collected from both sides and edge of a bead are displayed in ***Fig B.4.4a*** and ***b***, which shows a similar behaviour in band intensity and position. The decay curves of Ho^{3+} with 669 nm and 550 nm emission peak of s- and ns-GAG are show in ***Fig 2.22b*** and ***Fig B.4.4c***, respectively. The fitting result of decay time listed in ***Table 2.10*** shows that ns-GAG with shorter average lifetimes than that in GAG. The relationship between log(I) and log(Pn) of s- and ns-GAG: 1%Ho^{3+}/10%Yb^{3+} as shown in ***Fig B.4.4e*** (x = 0) and ***Fig B.4.4f*** (x = 0.4) show that the up conversion mechanism for both samples was a two-photon up-conversion process (see ***Fig B.4.4d***)[35]. The fitting values of n for the green and red emissions in the x = 0 and 0.4 sample are 1.98, 1.97 and 1.89, 1.90, respectively. These results tell us that the transition within the visible emission of Ho^{3+} is not sensitive to environmental changes brought about by non-stoichiometry.

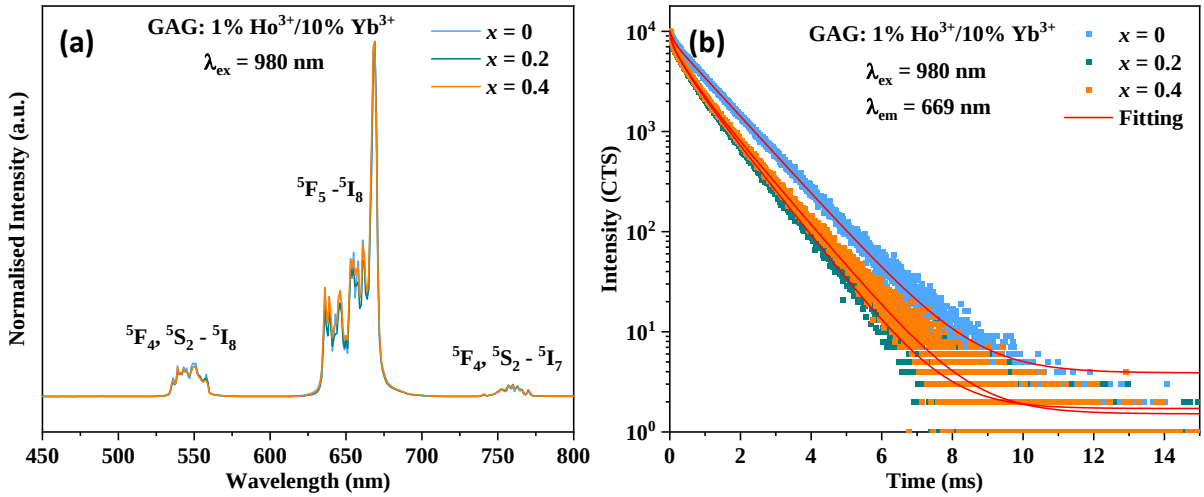

Fig 2.22 *Luminescence performance of $Gd_{3+x}Al_{5-x}O_{12}$ (x= 0, 0.2, 0.4): 1% Ho^{3+}/10% Yb^{3+} polished bead measured at room temperature.* ***(a)*** *Up conversion emission spectra under 980 nm. (The intensity of all spectra are normalised by the highest peaks)* ***(b)*** *Decay curves of Ho^{3+} in 669nm emission peak under 980nm excitation.*

Table 2.10 *Fitting parameters and average lifetime obtained from decay curves fitting results* $Gd_{3+x}Al_{5-x}O_{12}$ *(x= 0, 0.2, 0.4):1%*Ho^{3+}*/10%*Yb^{3+}*.*

Sample	peak	%	t1(ms)	%	t2(ms)	T avg (ms)
x = 0	555nm	100%	5.31			
	669nm	100%	11.27			
x = 0.2	555nm	44.32%	3.16	55.68%	5.12	4.25
	669nm	25.43%	11.29	74.57%	8.70	9.36
x= 0.4	555nm	26.903%	2.21	73.0965%	4.81	4.11
	669nm	31.06%	10.86	68.94%	9.18	9.70

2.6 Chapter conclusion and perspectives

In conclusion, here crystallisation from the glass synthesis method was used to synthesize a new series of highly non-stoichiometric $Gd_{3+x}Al_{5-x}O_{12}$ solid solution with a composition range of $0 \leq x \leq 0.6$. It was confirmed that up to 30 % of six coordinated Al is replaced by Gd^{3+} in $Gd_{3.6}Al_{4.6}O_{12}$, which allow the smaller radius dopant ions RE^{3+} (Tb^{3+}, Er^{3+}, Tm^{3+}, Yb^{3+}) to partially occupy the AlO_6 site, forming six coordinated REO_6 but excluding the large radius ions Ce^{3+}. The solid solution range of ns-GAG ($0 \leq x \leq 0.6$) is very surprising as it is much wider than that of ns-YAG ($0 \leq x \leq 0.4$), despite the fact that Gd^{3+} is much larger than Y^{3+}. This prompted the study o other RE nonstoichiometric garnets to understand the relationship between RE and the solid solution limit.

As a result, two crystallographic luminescence sites with (1) inequivalent AO_8 sites around with different BO_6 neighbours configurations and (2) BO_6 sites are created in ns-GAG which is responsible for the regulation of luminescent properties. The luminescence spectra study of Ce^{3+} shows that the non-stoichiometry affects the emission band to slight red shift due to the environmental change of AO_8 where Ce^{3+} locates. However, there is no obvious change in emission color because Ce^{3+} is only located at the A site instead of two sites, consistent with ns-YAG: Ce^{3+} system. Smaller Tb^{3+} are shown to be distributed at different sites AO_8 and BO_6, however, the emission spectra of ns- GAG do not exhibit significant differences due to the insensitivity of the f - f transition of Tb^{3+} to the environment. In

contrast, the emission spectra studies of GAG: Er^{3+}/Yb^{3+} and Tm^{3+}/Yb^{3+} up-conversion materials show a clear change in the emission peak and emission color, which is due to the hypersensitive transitions of Er^{3+} and Tm^{3+} are sensitive to the new local BO_6 site in the ns-GAG. In addition, the hypersensitive transition of Ho^{3+} is shown in the infrared region, while the emission peak in the visible region is not affected by the non-stoichiometry. Additionally we demonstrate that the new BO_6 site does not affect the mechanism of up conversion luminescence in GAG host.

The highly non-stoichiometric garnet GAG study provides a research basis for luminescence colour modulation and performance enhancement of commercially viable garnet-based optical materials. The study of the distribution trends of different size dopant ions in ns-GAGs and the study of the spectral sensitivity of different ions to symmetry changes provide a research reference for a range of optical studies of non-stoichiometric garnet bases host. Furthermore, in addition to the optical properties GAG materials may exhibit magnetic properties, and the effect of non-stoichiometric GAG on magnetic properties is interesting.

References

[1] Y. Chen, D. Feng, S. Xu et al., Materials Letters. ***2016****, 164, 180-182.*

[2] Z. Ming, J. Qiao, M.S. Molokeev et al., Inorgnic Chemistry. ***2020****, 59, 1405-1413.*

[3] Y. Ma, L. Zhang, J. Huang et al., Opt Express. ***2021****, 29, 9474-9493.*

[4] S. Feng, Y. Guo, M. Allix et al., Cell Reports Physical Science. ***2022****, 3, 101044.*

[5] W.W. Cao, A. Isabel Becerro, V. Castaing et al., Advanced Functional Materials. ***2023****, 33, 2213418.*

[6] X. Ma, X. Li, J. Li et al., Nat Commun. ***2018****, 9, 1175.*

[7] B. Ravel, M. Newville, J Synchrotron Radiat. ***2005****, 12, 537-541.*

[8] A.L. Ankudinov, B. Ravel, J.J. Rehr et al., Physical Review B. ***1998****, 58, 7565-7576.*

[9] K. Okhotnikov, T. Charpentier, S. Cadars, Journal of Cheminformatics. ***2016****, 8, 17.*

[10] S.J. Pennycook, L.A. Boatner, Nature. ***1988****, 336, 565-567.*

[11] P. Hartel, H. Rose, C. Dinges, Ultramicroscopy. ***1996****, 63, 93-114.*

[12] J.Y. Zhang, J. Hwang, B.J. Isaac, et al., Scientific Reports. ***2015****, 5, 12419.*

[13] P. Stadelmann, JEMS, https://www.jems-swiss.ch/.

[14] S. Van Aert, J. Verbeeck, R. Erni et al., Ultramicroscopy. ***2009****, 109, 1236-1244.*

[15] D.G. Sentürk, A. De Backer, T. Friedrich et al., Ultramicroscopy. ***2022****, 242, 113626.*

[16] X. Teng, J. Li, G. Duan, Z. Liu, Journal of Luminescence. ***2016****, 179, 165-170.*

[17] J.K. Li, J.-G. Li, X.D. Li et al., Ceramics International. ***2016****, 42, 3268-3274.*

[18] J.K. Li, J.-G. Li, J. Li et al., Journal of Alloys and Compounds. ***2014****, 582, 623-627.*

[19] J.G. Tang, J. Gou, G.N. Li, et al., RSC Advances. ***2016****, 6, 54435-54439.*

[20] M. Hatanaka, S. Yabushita, Theoretical Chemistry Accounts. ***2014****, 133, 1517.*

[21] E.V. Bol'shakova, A.V. Malov, P.A. Ryabochkina et al., Optics and Spectroscopy. ***2011****, 110, 910-916.*

[22] P.A. Ryabochkina, S.A. Antoshkina, E.V. Bolshakova et al., Journal of Luminescence. ***2012****, 132, 1900-1905.*

[23] Z. Pan, P. Loiko, Y. Wang et al., Journal of Alloys and Compounds. ***2021****, 853, 157100.*

[24] H.P. Ji, L. Wang, M. S. Molokeev, Journal of Materials Chemistry C. ***2016****, 4, 2359-2366.*

[25] W.H. Yuan, R. Pang, S.W. Wang et al., Light: Science & Applications volume. ***2022****, 11, 1-13.*

[26] Z. Sun, Z. Chen, M. Wang et al., Journal of the American Ceramic Society. ***2019****, 103, 809-818.*

[27] L. Fan, Y. Shi, Y. Wu et al., Journal of Luminescence. ***2017****, 190, 504-510.*

[28] Z.G. Xia, A. Meijerink, Chemical Society Reviews journal. ***2017****, 46, 275-299.*

[29] H.P. Ji, L. Wang, M.S. Molokeev et al., Journal of Materials Chemistry C. ***2012****, 4, 2359--2366.*

[30] J. Young, H. Park, C. Jung et al., Journal of Luminescence. ***2010****, 130, 478-482.*

[31] H. Choi, J.H. Kim, J.Y. Park et al., Journal of the Korean Physical Society. ***2011****, 59, 2329-2333.*

[32] W. Zhang, Y.L. Liang, Z.F. Hu et al., Journal of Nanoscience Nanotechnology. ***2016****, 16, 3517-3521.*

[33] W. Xiao, D. Wu, L. Zhang et al., The Journal of Physical Chemistry C. ***2017****, 121, 2998-3006.*

[34] D. Chen, Y. Yu, F. Huang et al., Chemical Communications journal. ***2011****, 47, 2601-2603.*

[35] J.K. Li, J.G. Li, S.H. Liu et al., Key Engineering Materials. ***2014****, 602-603, 1034-1038.*

Chapter III: Structure and persistent luminescence properties of highly non-stoichiometric $Gd_{3+x}Ga_{5-x}O_{12}$ and $Gd_{3+x}(Al_{0.4}Ga_{0.6})_{5-x}O_{12}$ garnet

3.1 Introduction

As detailed in **Chapter I,** garnet structured compounds are not only excellent host materials for up-conversion[1-2] and down-conversion[3-4] luminescence but they are also well-known matrix materials for persistent luminescence[5-7]. Based on the theory that the luminescence process of persistent luminescence is usually explained as a process of trapping and releasing of electrons, recent research has designed more lasting persistent luminescence materials by adjusting the "trap depth", which is an appropriate energy gap between the bottom of the CB (conduction band) and the impurity electron states[8]. Whereas garnet-based materials are of interest because of their special structure, particularly the larger dodecahedral site, which is ideal for the lanthanide ions [$Ln^{2+/3+}$], while the smaller octahedral and tetrahedral sites, which are suitable in size for the Cr^{3+} ions, allowing for a variety of doping strategies that can be used to obtain different crystalline fields and to adjust the electron trap depth[9].

In recent years, a series of garnet-based compounds with superior persistent luminescence properties have been reported to outperform $SrAl_2O_4$: Eu^{2+}-Dy^{3+} powder[10-12]. In garnet materials, Cr^{3+} ions serve as electron-capturing centers and create an ideal capturing depth for persistent luminescence at room temperature, resulting in long lasting persistent luminescence performance. In garnet-based materials, the energy level of the trap formed by Cr^{3+} ions remains constant, so the depth of electron traps can be controlled by changing the shift of the conduction band[9]. For example, studies in YAGG[12] and GAGG[10] doped Ce^{3+}/Cr^{3+} persistent luminescent materials have revealed that by adjusting the Ga/Al ratio, longer sustained luminescence can be obtained comparing GAG and GGG based materials and found that garnets with an Al/Ga ratio of 2/3 exhibited the best persistent luminescence properties. In theory, adjusting the ratio of A/B ions (non-stoichiometric ratio) can also shift the energy of the CB band, and thus adjust the depth of electron traps. Typically, different RE matrix materials or varying the concentration and type of dopant ions are used to achieve color tuning of the different emission wavelengths of persistent luminescent materials. Additionally, the perturbation of the crystal field environment of the *A* site caused by *A* ions substituting the *B* site may cause a change in the emission

wavelength, as demonstrated by the study of GAG: 2%Ce^{3+} in **Chapter 2**. It is noteworthy that, unlike GAG garnet, Ga^{3+} is larger than Al^{3+} (r_{Ga} (0.62 Å) > r_{Al} (0.53 Å)), which could create a more favorable environment for Gd^{3+} ions to occupy the B site due to the longer average B-O distances. This may cause significant perturbations to the environment of doping RE^{3+} ions. Consequently, modifications in the A/B ratio in non-stoichiometric materials could achieve persistent luminescent materials with both color and electron trap depth adjustment to produce persistent luminescent materials with longer persistence and an ideal emission wavelength.

In this chapter, a series of non-stoichiometric GGG and GAGG materials will be synthesized using crystallization from glass or crystallization from the melt method by ADL. Their structure will be studied using XRD and SPD, while SEM and VT-XRD will be employed to explore their microstructure, compound composition, and phase stability. Furthermore, the trend of different sized ions (Yb^{3+}, Tm^{3+}) occupying the octahedral sites in GGG will be examined through EXAFS. The persistent luminescence performance of a series of GGG and GAGG based materials will be studied to demonstrate the effect of non-stoichiometric ratio on the emission color and persistence of persistent luminescent performance.

3.2 Synthesis, structure, thermal stability, morphology analysis of $Gd_{3+x}Ga_{5-x}O_{12}$ ($0 \leq x \leq 0.6$)

3.2.1 Synthesis and general crystal structure analysis of GGG

Based on synthetic exploration of ns-GAG, synthesis of $Gd_{3+x}Ga_{5-x}O_{12}$ glass samples was attempted by ADL. To achieve faster cooling rates, a small mass of sample was chosen for synthesis using O_2 as a carrier gas. However, it was not possible to obtain GGG glass by this method. Therefore, an alternative method of direct crystallisation from the melt was employed to successfully obtain $Gd_3Ga_5O_{12}$ phase by ADL using Ar carrier gas (detailed procedure was described in the ADL section of **Chapter 1** and synthesis conditions are shown in ***Table A.1.3***). During the synthesis of the GGG (x = 0) compounds, it was found that two different appearances of beads could be obtained. The first type consisted of translucent

beads without cracks (see ***Fig 3.1 inset*** photo at left), while the second type consisted of beads with a crack dividing them into two parts (see ***Fig 3.1 inset*** photo at right). The PXRD patterns of both beads indicate that they were single GGG phase. However, the high resolution synchrotron powder diffraction pattern of the bead with crack revealed the presence of two garnet phases (see ***Fig 3.1*** inset enlarged view of main peaks). Therefore, throughout the synthesis process the synthesis conditions have to be very carefully controlled in order to obtain a suitable cooling rate to avoid phase separation and thus obtain GGG with a single garnet phase.

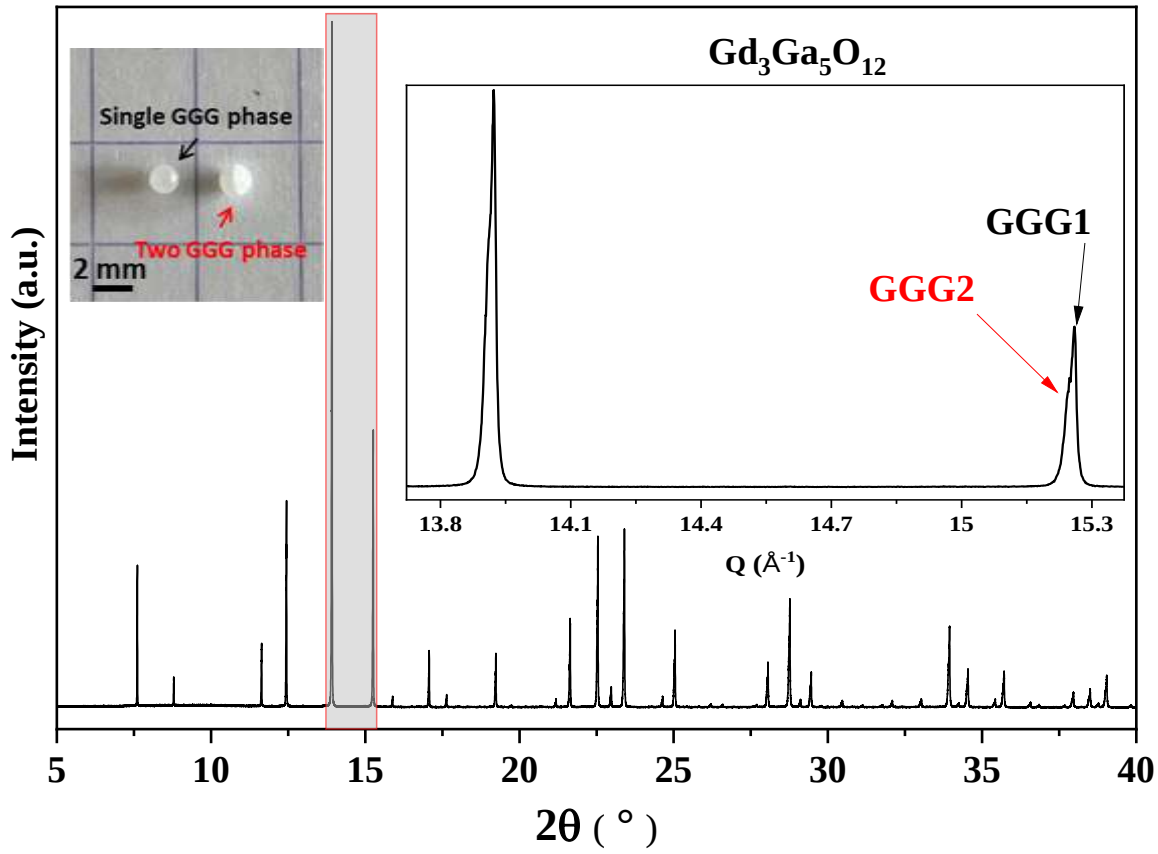

Fig 3.1 *Synchrotron powder diffraction pattern of the GGG bead with crack (enlarged view is inset). Inset on the left is a photograph of the two different types of beads.*

A range of $Gd_{3+x}Ga_{5-x}O_{12}$ ($0 \leq x \leq 0.8$) compounds were synthesised via direct crystallisation from the melt by ADL using Ar carrier gas. The laboratory X-ray diffraction pattern of $Gd_{3+x}Ga_{5-x}O_{12}$ ($0 \leq x \leq 0.8$) compounds shown in ***Fig 3.2a*** demonstrates that the compounds with x = 0 - 0.6 exhibit a single garnet phase, matching well with the $Gd_3Ga_5O_{12}$ (ICSD 9237). An enlarged view of the (211) peak on the right of ***Fig 3.2a*** shows a gradual

shift of 2θ to lower value as x value increases, indicating an expansion of the lattice parameters. In contrast, the compound at x = 0.7 exhibits phase separation with secondary nonstoichiometric GGG phases, while the compound with x = 0.8 is a mixture nonstoichiometric, stoichiometric GGG phases and $GdGaO_3$ phase. ***Fig 3.2b*** shows the linear increase of lattice parameters of $Gd_{3+x}Ga_{5-x}O_{12}$ ($0 \le x \le 0.8$) from PXRD data refinement as x value from 0 to 0.6, which indicates the formation of the nonstoichiometric GGG solid solution. The abrupt drop of the lattice parameter for the x = 0.8 mixture phase suggests that the solid solution limit of nonstoichiometric GGG lies between x = 0.7 to 0.8.

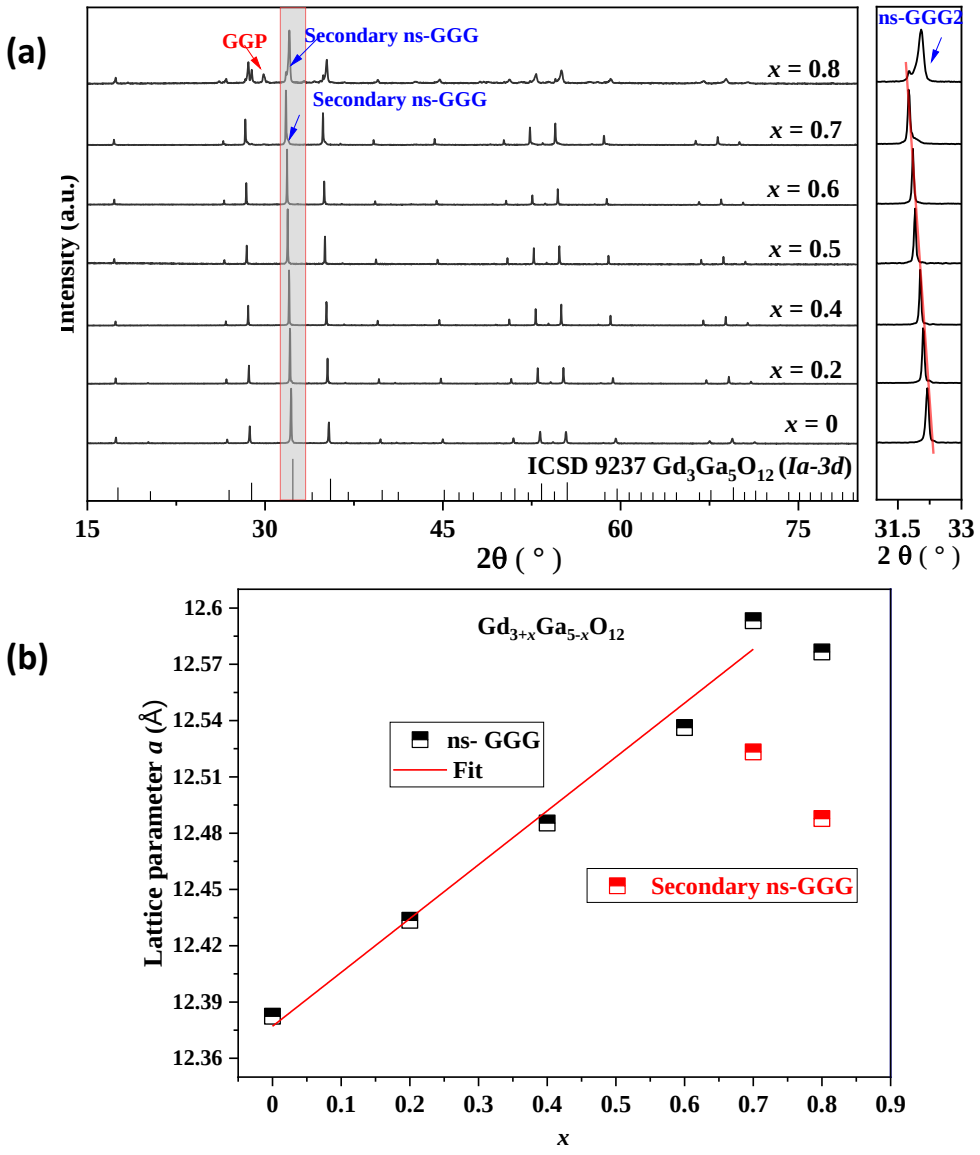

Fig 3.2 (a) *Laboratory XRD pattern of $Gd_{3+x}Ga_{5-x}O_{12}$ (x = 0 - 0.8) solid solution (enlarged view of the (211) peak at right side)* ***(b)*** *Laboratory XRD data refined lattice parameter a of ns-GGG (black points) and secondary GGG (red points) with different x value (red line is linear fit to the data).*

3.2.2 Structure evolution analysis of GGG

The results obtained from the high resolution SPD Rietveld refinement were used to analyze the detailed structure and structural evolution of the non-stoichiometric GGG solid solution, as illustrated in ***Fig 3.3***. $Gd_3Ga_5O_{12}$ was used as the staring structure of the Rietveld refinement for all $Gd_{3+x}Ga_{5-x}O_{12}$ ($0 \le x \le 0.6$) compositions. ***Fig 3.3a*** exhibits the refinement profile of $Gd_{3.4}Ga_{4.6}O_{12}$, while the refinement profiles of $Gd_3Ga_5O_{12}$, $Gd_{3.2}Ga_{4.8}O_{12}$ and $Gd_{3.6}Ga_{4.4}O_{12}$ are presented in ***Fig C.1.1*** and ***Fig C.1.2 a*** *and* ***b***, respectively. The refinement fitting parameters and detailed structural information (atomic positions, occupation numbers and U_{iso}) of the $Gd_{3+x}Ga_{5-x}O_{12}$ ($0 \le x \le 0.6$) compounds are provided in ***Table 3.1***. The refinement results indicate that the lattice parameter *a* linearly increases with x in the range 0 - 0.6 (see ***Fig 3.3b*** upper) and that the occupied number of eight-coordinated Gd^{3+} linearly increases with x, in agreement with the theoretical occupied number (see ***Fig 3.3b*** lower). In contrast to the $Gd_{3.6}Al_{4.4}O_{12}$ solid solution, where 30% of the Gd^{3+} occupies the six-coordinated Al^{3+} sites, Ga demonstrates greater solid solution capacity due to the fact that the ionic radius of Ga^{3+} (0.65 Å) is larger than that of Al^{3+}(0.39 Å). The crystal structure of $Gd_{3.4}Ga_{4.6}O_{12}$ obtained from Rietveld refinement, shown in ***Fig 3.4c***, demonstrates that the 24c site of the dodecahedron (grey) is completely occupied by Gd^{3+}, with the excess Gd^{3+} occupying the six coordinate Ga^{3+} octahedral sites (light green) instead of the GaO_4 tetrahedra site (dark green). In non-stoichiometric GGG, the occupation of octahedra by Gd result in changes in bond lengths the crystal structure, as depicted in ***Fig 3.4***. The variations in bond lengths of d(Gd1-O_L/Gd1-O_S), d(Ga1/Gd2-O), and d(Ga2-O) of GGG shown in ***Fig 3.4a*** suggest that Gd-O bond lengths increase linearly, and there is a strong linear increase of the Ga1/Gd2-O bond length with *x* in the range $0 \le x \le 0.6$, which is attributed to the larger Gd^{3+}(0.94 Å) occupying the Ga^{3+}(0.65 Å) site. The bond lengths of the ns-GGG solid solution are given in ***Table C.1.1.***

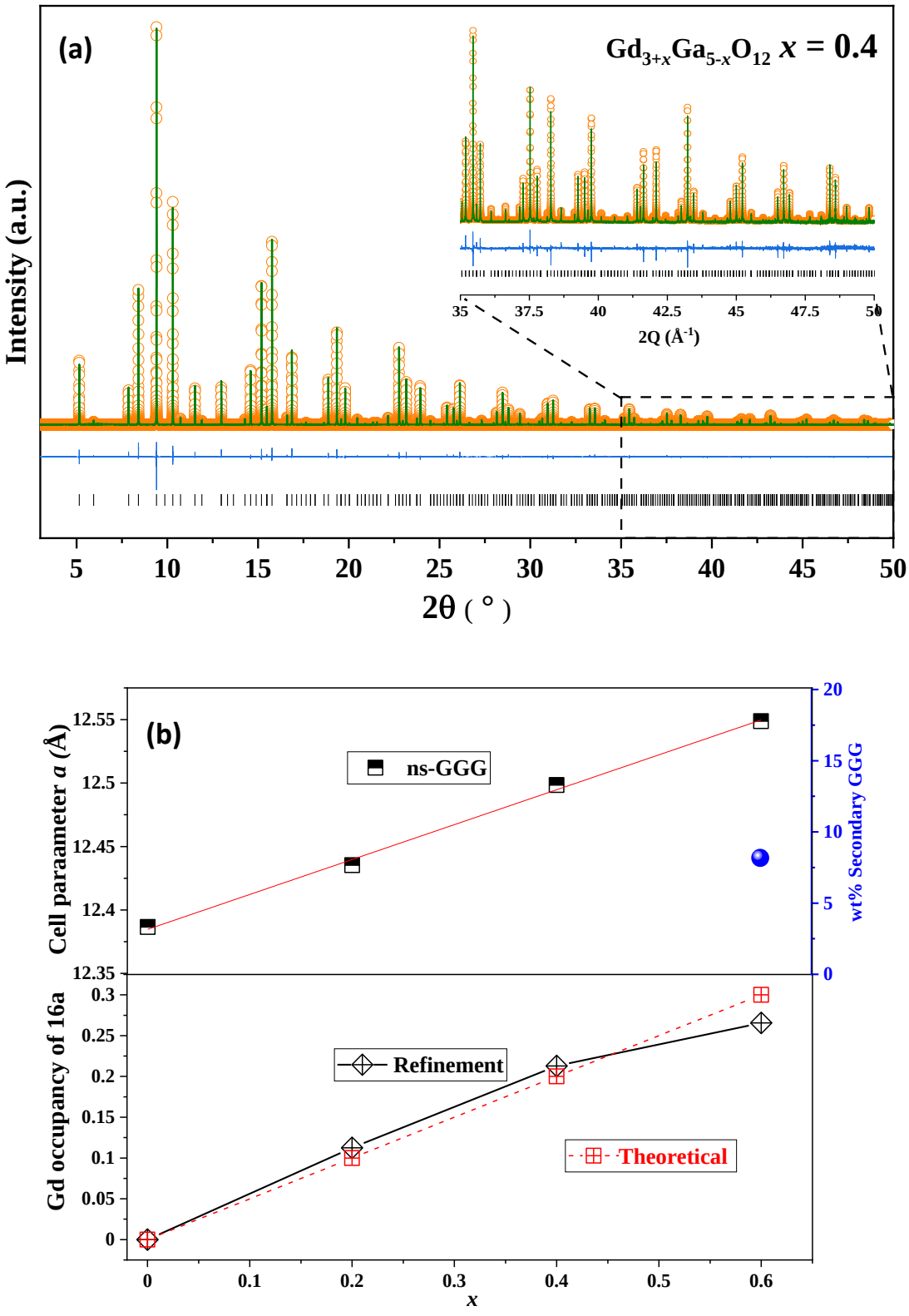

Fig 3.3 (a) *SPD Rietveld refinement profile of $Gd_{3.4}Ga_{4.6}O_{12}$ (R_{wp} = 10.54%, Gof = 1.92)* ***(b)*** *Refined lattice parameter a of ns-GGG (black points) and secondary GGG (blue point) with different x value (upper), plots of refined occupancy of the GaO_6 octahedral site by Gd^{3+} (black line) and theoretical occupancy (red line) vs x value (lower).*

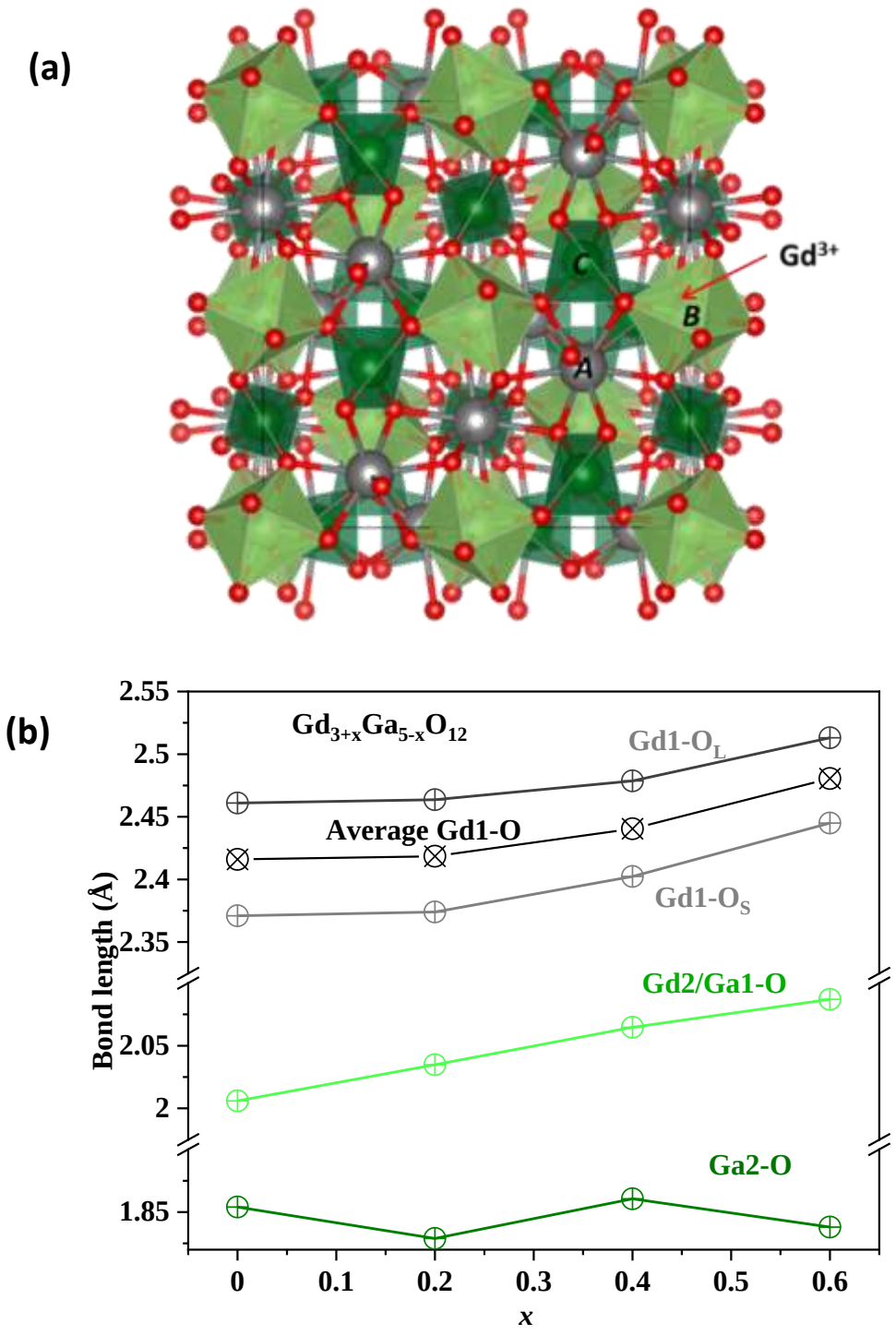

Fig 3.4 *(a) Refined garnet structure of* $Gd_{3.4}Ga_{4.6}O_{12}$ *viewed from c axes (gray, mixed gray and pale green, and deep green atom is Gd, Gd/Ga1 and Ga2. (Gray dodecahedron is* GdO_8*, pale green octahedron is* Gd/GaO_6*; deep green tetrahedron is* GaO_4*). (b)* XRD refined metal-oxygen distances of $Gd_{3+x}(Ga_{0.6}Al_{0.4})_{5-x}O_{12}$ (x = 0, 0.2, 0.4, 0.6) (gray lines are Gd1-O bonds, black lines is average bond length of Gd-O, pale green is Gd2/Ga1-O bond, and deep green is Ga2-O bond).

Table 3.1 *Refined structural information and fitting results of GGG obtained from SPD data.*

$Gd_{3+x}Ga_{5-x}O_{12}$	atom	site	x	y	z	occupancy	U_{iso}*100(Å^2)
x = 0 (PXRD)	Gd1	24c	0.125	0	0.25	1	0.38(3)
	Ga1	16a	0	0	0	1	0.31(3)
	Ga2	24d	0.375	0	0.25	1	0.37(3)
	O1	96h	0.0284(3)	0.0549(4)	0.6497(3)	1	0.10(8)
Lattice parameter:			*Secondary phases:*			*Fitting parameters:*	
a = 12.3865(8)Å			*1.2(1) wt% $GdGaO_3$*			*R_{wp} = 3.85% Gof = 1.97*	
x = 0.2	Gd1	24c	0.125	0	0.25	1	0.472(4)
	Gd2	16a	0	0	0	0.113(2)	0.32(1)
	Ga1	16a	0	0	0	0.887(2)	0.32(1)
	Ga2	24d	0.375	0	0.25	1	0.473(8)
	O1	96h	0.0251(1)	0.0561(1)	0.6503(1)	1	0.47(3)
Lattice parameter:			*Secondary phases:*			*Fitting parameters:*	
a = 12.4353(1)Å			*16.8(1) wt% ns-GGG2*			*R_{wp} = 10.41%, Gof = 1.23*	
x = 0.4	Gd1	24c	0.125	0	0.25	1	0.766(3)
	Gd2	16a	0	0	0	0.213(1)	0.447(8)
	Ga1	16a	0	0	0	0.787(1)	0.447(8)
	Ga2	24d	0.375	0	0.25	1	0.729(8)
	O1	96h	0.0278(1)	0.0568(1)	0.652(1)	1	0.87(2)
Lattice parameter:						*Fitting parameters:*	
a = 12.49836(5)Å						*R_{wp} = 10.54%, Gof = 1.92*	
x = 0.6	Gd1	24c	0.125	0	0.25	1	0.849(8)
	Gd2	16a	0	0	0	0.266(2)	0.27(1)
	Ga1	16a	0	0	0	0.734(2)	0.27(1)
	Ga2	24d	0.375	0	0.25	1	0.94(1)
	O1	96h	0.0373(2)	0.0590(2)	0.6840(2)	1	0.53(5)
Lattice parameter:			*Secondary phases:*			*Fitting parameters:*	
a =12.4353(1) Å			*8.2(3)% GGG2*			*R_{wp} = 13.10%, Gof = 1.25*	

3.2.3 Thermal stability

To further understand the thermal stability and the phase evolution of ns-GAG in the process of high temperature heating, VT-XRD data of $Gd_{3.4}Al_{4.8}O_{12}$ was recorded from room temperature up to 1600^{o}C, as illustrated in ***Fig 3.5***. Due to thermal expansion, the diffraction peaks systematically shift to large 2θ value as the temperature increases from 30-1100°C. However, above 1100°C, ns-GGG gradually decomposes into stoichiometric GGG (x = 0.4-d) and Gd_3GaO_6 (blue mark), and at 1350°C, ns-GGG further decomposes into Gd_2O_3 (green

mark) and Gd_3GaO_6 (blue mark). The VT-XRD results demonstrate that the non-stoichiometric GGG is stable up to 1100 °C, which is similar to the thermal stability of ns-GAG (1150 °C). ns-YAG (1350 °C) shows a better thermal stability than ns-GAG and ns-GGG due to the smaller Y occupied at B site.

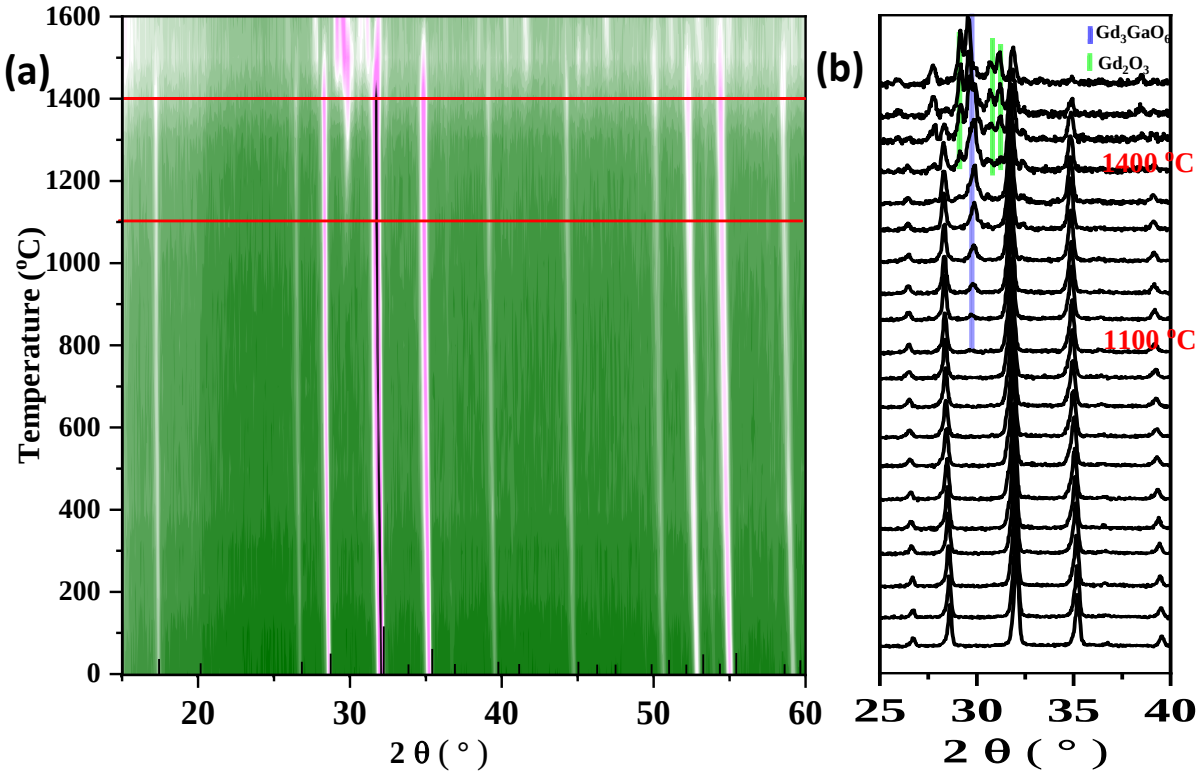

Fig 3.5 *X-ray diffraction peaks Contour figure from 15°- 70°* ***(b)*** *Enlarged diffraction peak pattern from 30° - 38° (blue mark is Gd_3GaO_6 phase and green mark is Gd_2O_3 phase) of $Gd_{3.4}Ga_{4.6}O_{12}$ measured from room temperature to 1600 °C at intervals of 50 °C.*

3.2.4 Microstructure analysis

The micromorphology, homogeneity and composition of the GGG samples were analysed by SEM images and EDS results. BSE images of polished beads of GGG x = 0 (see ***Fig 3.6a***) show that the sample is a single phase, and the grains with a length and width of about 20 to 50 µm. A closer look reveals that the sample contains porosity, thus making it impossible to obtain a transparent ceramic. However, for the BSE image of x = 0.4 sample (***Fig 3.6b***), it is shown as three distinct phases (phase 1: gray, phase 2: white, phase 3, black), and the phase 2 and phase 3 are clustered at the grain boundaries of phase 1. ***Table 3.2*** lists

the results of the EDS compositional analysis of the two samples by 20 points analysis. The composition deviates from the theoretical values due to lack of reference and SEM-EDS imprecision, but shows an increase in Gd content as the x-value increases. The compositional analysis for x = 0.4 shows that phases 1 and 2 are two non-stoichiometric garnet with different Gd/Ga ratio and phase 3 is $Gd_4Ga_2O_9$. Due to the low content we do not observe a second phase in the SPD data. However, as the x value increases it is always accompanied by the existence of a small amount of a secondary ns-GGG phase, as we know from the SPD data.

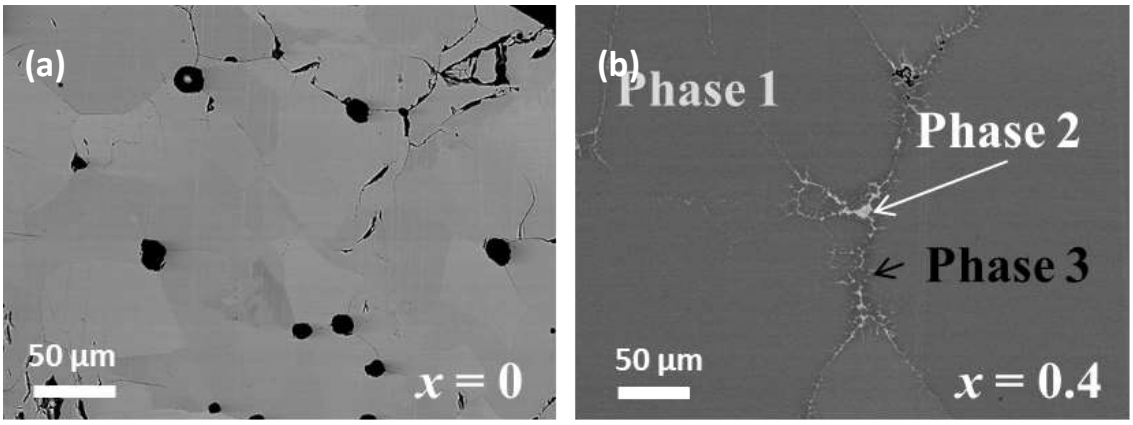

Fig 3.6 *SEM (BSE) image of pholished* ***(a)*** *$Gd_3Al_5O_{12}$ and* ***(b)*** *$Gd_{3.4}Al_{4.6}O_{12}$ crystallised beads.*

Table 3.2 *SEM-EDS analysis of $Gd_{3+x}Ga_{5-x}O_{12}$ (x =0, 0.2, 0.4)*

$Gd_{3+x}Ga_{5-x}O_{12}$		Gd (At. %)	Al (At. %)	Experimental composition	Theoretical composition
x = 0	Single phase	15.45	23.55	$Gd_{3.3(1)}Ga_{4.7(1)}O_{12}$	$Gd_3Ga_5O_{12}$
x = 0.2	Single phase	17.34	22.66	$Gd_{3.5(1)}Ga_{4.5(1)}O_{12}$	$Gd_{3.2}Ga_{4.8}O_{12}$
	Phase 1	18.12	21.88	$Gd_{3.62(9)}Ga_{4.38(9)}O_{12}$	
x = 0.4	Phase 2	19.3	20.7	$Gd_{3.86(3)}Ga_{4.24(3)}O_{12}$	$Gd_{3.4}Ga_{4.6}O_{12}$
	Phase 3	24.75	15.25	$Gd_4Ga_2O_9$	

3.2.5 Local structure analysis of GGG by EXAFS

Here to probe the local environment around Gd^{3+} ions in GGG, EXAFS spectra at L_3 edge (7243 eV) of Gd was collected. ***Fig 3.7a*** and ***b*** illustrate the EXAFS oscillations and the EXAFS Fourier transform spectra of the $Gd_{3+x}Ga_{5-x}O_{12}$(x = 0, 0.2, 0.4), respectively. From the EXAFS oscillations spectra, we can observe similar spectra variations with x value increasing to those of the GAG samples: the amplitude of these oscillations gradually decreases, and also slightly shifted towards a lower k. The Fourier transform EXAFS spectrum corresponding to these variation exhibits a decrease in the amplitude of the first peaks and third peaks, as well as a slight shift of the peaks towards the larger R's due to distance relaxation. This result confirmed that the excess Gd^{3+} ions substitute the Ga^{3+} ions located at the octahedral site in the structure, which are similar to those observed in the case of non-stoichiometric GAG samples. At the same time, in order to further identify such variations, geometrical optimisation of artificially generated structures with different atomic substitution scenarios by means of FEFF8 calculation is in progress.

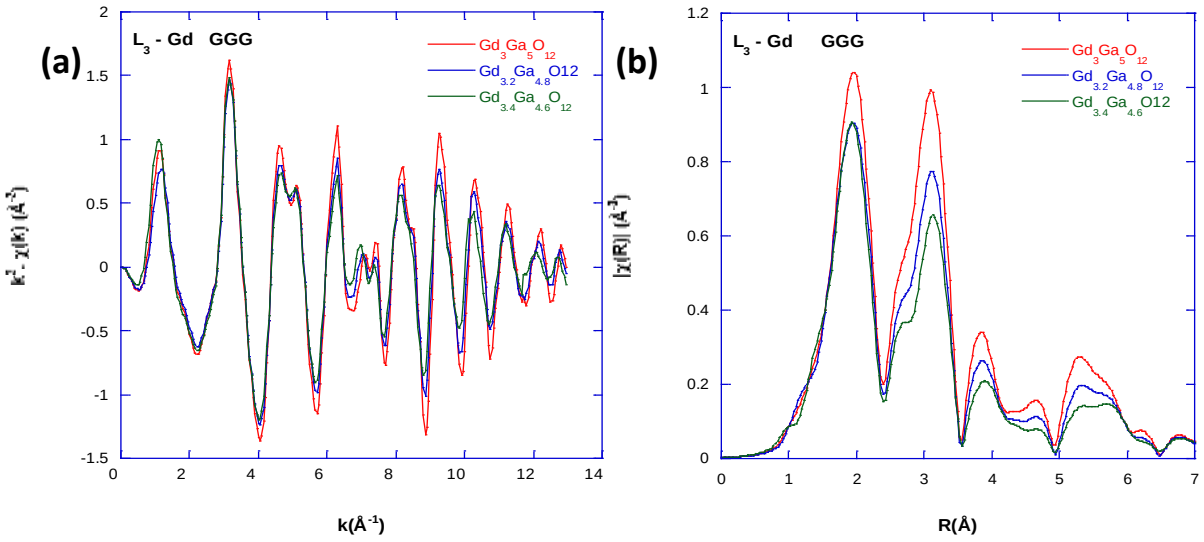

Fig 3.7 (a) *EXAFS spectra extracted from the linear absorption coefficient and* ***(b)*** *Fourier transforms of the EXAFS spectra of* $Gd_{3+x}Ga_{5-x}O_{12}$ *(x = 0, 0.2, 0.4) measured at Gd* L_3 *edge (7243 eV)*

3.2.6 RE doping of GGG and analysis of dopant distribution by EXAFS

Similar to GAG, synchrotron PXRD can be used to quantify the distribution of Gd^{3+} at the B site due to the better contrast of Gd^{3+}/Al^{3+}, but the distribution of doped rare earth cations (e.g., Yb, Tm) cannot be detected due to the weaker scattering contrast with Gd^{3+}. GGG doped with 1%Tm^{3+}/10%Yb^{3+} was reported to be upconversion materials[13] therefore was chosen for further study. The doping concentration of Tm^{3+} in GGG: 1%Tm^{3+}/10%Yb^{3+} is too low to be detected by STEM-HAADF/EDS. Also, the overlap of Yb and Gd characteristic X-ray emission lines does not allow to study the distribution of Yb in GGG by STEM-EDS. The X-ray scattering factors of these rare earths are very similar, and Gd absorbs neutrons very strongly. EXAFS is therefore the only established technique for analysing the distribution of rare earth in these materials.

For the spectral evolution at the L_3-Gd in non-stoichiometric GGG samples doped with Yb^{3+} or Tm^{3+} ions, the same qualitative behavior of EXAFS Fourier-transform as the un-doped GAG samples as the Gd content is increased was found. At the same time, the L_3 Gd spectra exhibit similar evolution in the two Tm/Yb doped samples (see ***Fig C.2.1***). It can be concluded that the number and type of rare earth ions in the structure have little effect on the local environment of Gd^{3+}.

The EXAFS spectra at L_3 edge Yb of $(Yb_{0.1}Gd_{0.9})_{3+x}Ga_{5-x}O_{12}$ and Tm of $(Tm_{0.1}Gd_{0.9})_{3+x}Ga_{5-x}O_{12}$ are demonstrated in ***Fig 3.8a*** and ***b***. It can be observed that the amplitude of the corresponding Fourier transform peaks of the first neighbourhood around the rare earth ions increases with increasing rare earth content. This observation suggests a change in the number of neighbouring oxygen atoms of Yb and Tm ions. Consistent with the behavior of GAG, this indicated that there are different substitution models Tm or YbO_6, Tm or Yb/GdO_6, or GdO_6 in ns-GGG. However, compared to the L_3 edge Yb spectrum of $(Yb_{0.1}Gd_{0.9})_{3+x}Al_{5-x}O_{12}$, it is observed that the first peak in nonstoichiometric $(Yb_{0.1}Gd_{0.9})_{3+x}Ga_{5-x}O_{12}$ is shifted to a lower R and split into a strong peak near 3.3 $Å^{-1}$ and a collapsed peak near the 3.8 $Å^{-1}$. This observation tells us that the type of ion at the B-site may affect the distribution trend of dopant ions (see ***Fig 3.8a***). The FT spectrum of Tm L_3-edge in ***Fig 3.8b*** indicated that the amplitude of the first peak decreases with increasing X

and is accompanied by a clear shift towards larger R values. As for the possible different substitution types of Yb and Tm in GAG and GGG that may be influenced by different B-site ions need to be further determined by DFT geometry optimisation, this is also in progress.

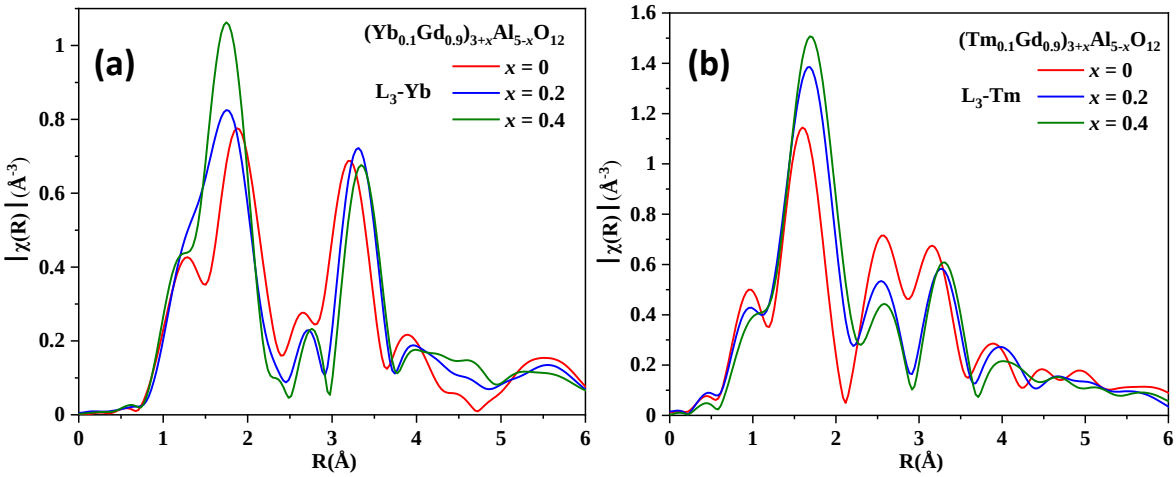

Fig 3.8 *Fourier transforms of the EXAFS spectra of* ***(a)*** *$(Yb_{0.1}Gd_{0.9})_{3+x}Ga_{5-x}O_{12}$ (x = 0, 0.2, 0.4) measured at Yb L_3 edge and* ***(b)*** *$(Yb_{0.1}Gd_{0.9})_{3+x}Ga_{5-x}O_{12}$ (x = 0, 0.2, 0.4) measured at Tm L_3 edge.*

3.3 Synthesis and structure analysis of $Gd_{3+x}(Ga_{0.6}Al_{0.4})_{5-x}O_{12}$ (GAGG) (0 ≤ x ≤0.6)

3.3.1 Synthesis and general crystal structure analysis of GAGG

The synthesis of $Gd_{3+x}(Ga_{0.6}Al_{0.4})_{5-x}O_{12}$ (x = 0 - 0.6) solid solution has been attempted using both the crystallization from melt and crystallization from glass methods based on the synthetic exploration of ns-GAG and ns-GGG. ***Fig 3.9a*** (lower) depicts the X-ray diffraction pattern of $Gd_{3+x}(Ga_{0.6}Al_{0.4})_{5-x}O_{12}$ (x = 0 - 0.4) synthesised via the crystallisation from melt method, which indicates that the compounds with x = 0 and x = 0.2 exhibit a single garnet phase, while the compound with x = 0.4 is a mixture of two garnet and perovskite phases. Comparison with the cell parameter *a* of GAG and GGG indicates that the two garnet phases are GAGG phases with different nonstoichiometric ratios Gd/(Al/Ga). On the other hand, the crystallization from glass method successfully produced $Gd_{3+x}(Ga_{0.6}Al_{0.4})_{5-x}O_{12}$ (x = 0 - 0.6) glass precursor, which crystallized into a garnet phase after a heat treatment of 900 ^{o}C for 3

hours in air, as confirmed by the XRD diffraction patterns shown in ***Fig 3.9a*** (upper). The DSC curve for the $Gd_{3.2}Ga_{2.88}Al_{1.92}O_{12}$ glass precursors illustrated in ***Fig 3.9b*** exhibits that the GAGG glasses crystallize at a temperature of approximately 850°C, and no clear exothermic peaks indicative of decomposition were observed. Thermal stabilization studies of ns-GAG and ns-GGG show that the decomposition of non-stoichiometric garnet is gradual, therefore it is difficult to observe the exothermic peak by DSC.

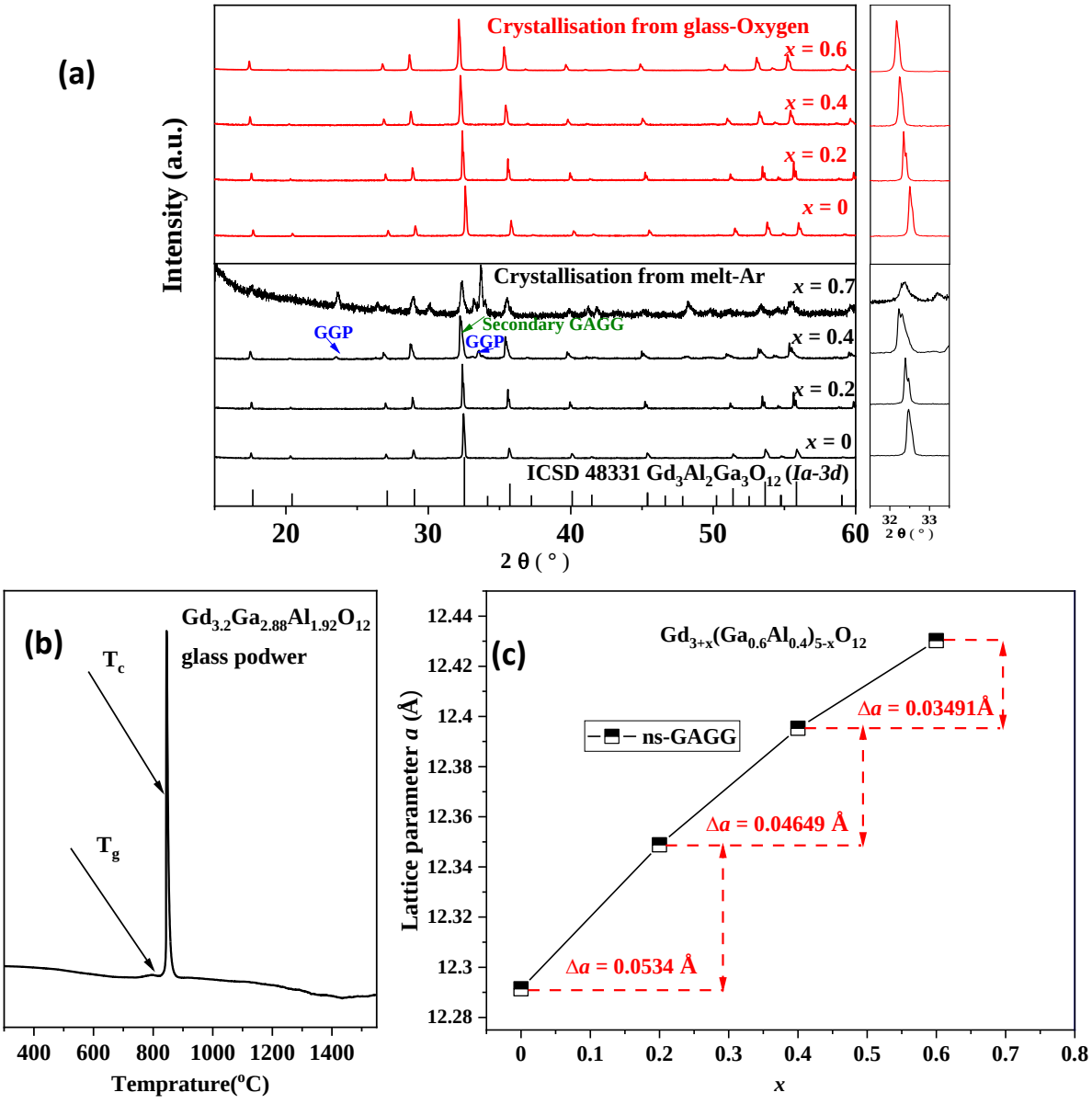

Fig 3.9 (a) *Laboratory XRD pattern of* $Gd_{3+x}(Ga_{0.6}Al_{0.4})_{5-x}O_{12}$ *(x = 0 - 0.4) solid solution synthesized by crystallization from glass (upper) and crystallization from melt method (lower).* ***(b)*** *Laboratory PXRD data refined lattice parameter a of ns-GAGG (black line) synthesized by crystallization from glass.* ***(c)*** DSC curve of $Gd_{3.2}Ga_{2.88}Al_{1.92}O_{12}$ glass powder.

As seen in the enlarged view on the right of ***Fig 3.9a*** (upper), the main diffraction peak of compound with x = 0, 0.2, 0.4 and 0.6 gradually shifts to a lower 2θ value as x increases. The plot of lattice parameters obtained from the refinement of the XRD data shown in **Fig *3.9c*** displays an increase of the lattice parameter *a* from x = 0 to 0.6. The x = 0.7 sample could not form a glass precursor, and here a single GAGG phase could not obtained by direct crystallization from the melt, but rather a mixture of GAG, GGG, $GdGa/AlO_3$,Gd_4Ga/Al_2O_9 (see ***Fig 3.9a***). This indicates a solid solution range of non-stoichiometric $Gd_{3+x}(Ga_{0.6}Al_{0.4})_{5-x}O_{12}$ with a limit at x = 0.6 - 0.7. A closer look at the evolution of the cell parameters *a* reveals that it does not strictly follow a linear increase with increasing x. This may be due to variations in Ga and Al distributions between the octahedral and tetrahedral sites. Therefore, the Rietveld refinement of PXRD data was performed to account for this evolution, and the detailed refinement results and fitting parameter are provided in ***Table 3.3***.

3.3.2 Structure evolution analysis of GAGG

The XRD refinement profile of $Gd_{3.4}(Ga_{0.6}Al_{0.4})_{4.6}O_{12}$ is shown in ***Fig 3.10a*****,** and the refinement profiles of $Gd_{3+x}(Ga_{0.6}Al_{0.4})_{5-x}O_{12}$ (x = 0, 0.2, 0.4, 0.6) are presented in ***Fig C.3.1-3***. The refinement results of $Gd_{3+x}(Ga_{0.6}Al_{0.4})_{5-x}O_{12}$ (x = 0) show that the occupy numbers of Ga and Al in the octahedra are 0.470(6) and 0.530(6), respectively, in agreement with the data reported in the literature[14]. The refined results of the occupancy of Ga/Al in octahedra and tetrahedra for the non-stoichiometric $Gd_{3+x}(Ga_{0.6}Al_{0.4})_{5-x}O_{12}$ (x = 0.2, 0.4, 0.6) show that the Ga/Al ratio in the tetrahedral and octahedral sites decrease as the x value increase, which leads to a non-linear increasing of the cell parameters *a* (see ***Fig 3.10b***). In ns-GAGG, Gd replaces octahedral Ga and Al in the ratio of 3/2. The variations in bond lengths of $d(Gd1\text{-}O_L/Gd1\text{-}O_S)$, d(Ga1/Al1/Gd2-O), and d(Ga2/Al2-O) of GAGG shown in ***Fig C.3.4*** suggest that Gd-O bond lengths increase, and there is an increase of the Ga1/Al1/Gd2-O bond length with *x* in the range $0 \leq x \leq 0.6$, which is attributed to the larger Gd^{3+}(0.94 Å) occupying the Ga/Al site. The bond lengths of the ns-GAGG are given in ***Table C.3.1.***

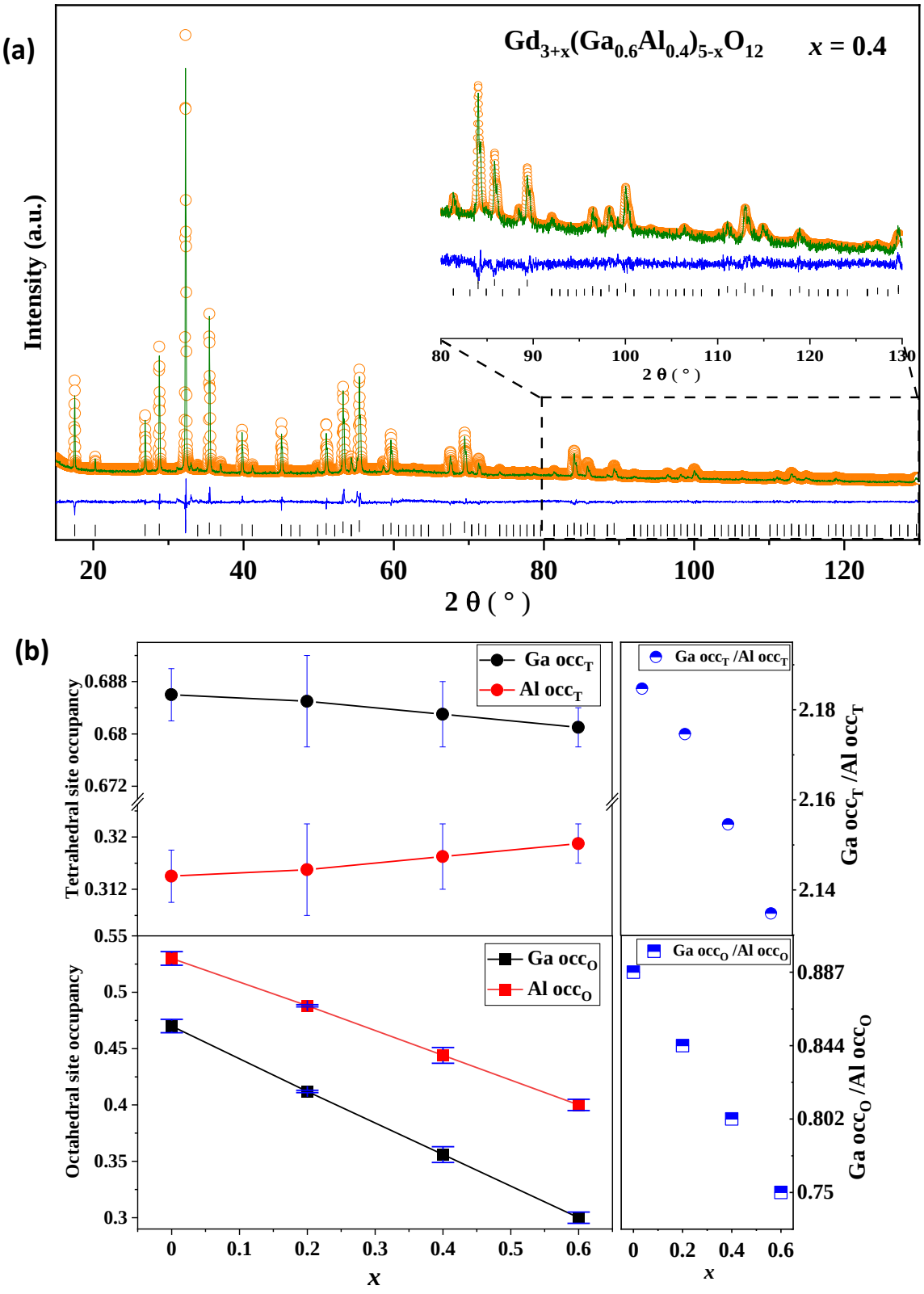

Fig 3.10 (a) *XRD Rietveld refinement profile of* $Gd_{3.4}(Ga_{0.6}Al_{0.4})_{4.6}O_{12}$ *(* R_{wp} = 4.64%, *Gof = 1.50)* ***(b)*** *Occupancy of Ga (black line) and Al (red line) in octahedra (lower) and tetrahedral (upper).*

Table 3.3 *Refined cell parameters of GAGG and fitting results obtained from XRD data.*

$Gd_{3+x}(Ga_{0.6}Al_{0.4})_{5-x}O_{12}$	atom	site	x	y	z	occupancy	U_{iso}*100
x = 0	Gd1	24c	0.125	0	0.25	1	0.3(1)
	Ga1	16a	0	0	0	0.470(6)	0.5(5)
	Al1	16a	0	0	0	0.530(6)	0.5(5)
	Ga2	24d	0.375	0	0.25	0.686(4)	0.98(3)
	Al2	24d	0.375	0	0.25	0.314(4)	0.98(3)
	O1	96h	0.9617(5)	0.0530(6)	0.1539(6)	1	1.1(3)
Lattice parameter： *a* = 12.2918(1) Å				*Fitting parameters:* R_{wp} *= 8.09% Gof = 1.18*			
x = 0.2	Gd1	24c	0.125	0	0.25	1	1.02(4)
	Gd2	16a	0	0	0	0.1	1.4(1)
	Ga1	16a	0	0	0	0.412(1)	1.4(1)
	Al1	16a	0	0	0	0.488(1)	1.4(1)
	Ga2	24d	0.375	0	0.25	0.685(7)	0.45(6)
	Al2	24d	0.375	0	0.25	0.315(7)	0.45(6)
	O1	96h	0.9626(2)	0.0516(3)	0.1498(3)	1	0.10(1)
Lattice parameter： *a* = 12.34879(9) Å				*Fitting parameters:* R_{wp} *= 3.48%, Gof = 1.85*			
x = 0.4	Gd1	24c	0.125	0	0.25	1	2.79(4)
	Gd2	16a	0	0	0	0.2	1.93(7)
	Ga1	16a	0	0	0	0.356(7)	1.93(7)
	Al1	16a	0	0	0	0.444(7)	1.93(7)
	Ga2	24d	0.375	0	0.25	0.683(5)	2.38(6)
	Al2	24d	0.375	0	0.25	0.317(5)	2.38(6)
	O1	96h	0.9628(3)	0.0520(4)	0.1507(4)	1	2.8(1)
Lattice parameter： *a* = 12.39544(7) Å				*Fitting parameters:* R_{wp} = 4.64%, *Gof = 1.50*			
x = 0.6	Gd1	24c	0.125	0	0.25	1	0.43(2)
	Gd2	16a	0	0	0	0.3	0.66(7)
	Ga1	16a	0	0	0	0.300(5)	0.66(7)
	Al1	16a	0	0	0	0.400(5)	0.66(7)
	Ga2	24d	0.375	0	0.25	0.681(3)	0.10(5)
	Al2	24d	0.375	0	0.25	0.319(3)	0.10(5)
	O1	96h	0.9620(2)	0.0570(3)	0.1529(3)	1	0.11(1)
Lattice parameter： *a* =12.43186(2) Å			*Secondary phases:* *1.1(8)% $GdGaO_3$*		*Fitting parameters:* R_{wp} = 5.84%, *Gof = 1.65*		

The cell parameters evolutionary trends of the three type garnets GAG, GGG, and GAGG with increasing of x-values are presented in ***Fig 3.11***. As Al^{3+} (0.54 Å) smaller that Ga (0.62 Å), occupation of Gd^{3+} (0.94 Å) at *B* site leading to larger linear expansion of the cell parameters ($\Delta a/a_{(x = 0)}$ = 0.01578) compared to Ga ($\Delta a/a_{(x = 0)}$ = 0.01243). In ns-GAGG, the

lattice expansion is much smaller than it in GAG and GGG system due to the variation of the Ga/Al ratio in the octahedron with the substitution of Gd. However, the change in the Ga/Al ratio in the octahedron due to the Gd substitution in ns-GAGG results in the larger bond length change on the dodecahedron comparing to GAG and GGG, which affects the luminescent ion crystal field environment and thus affects the emission wavelength.

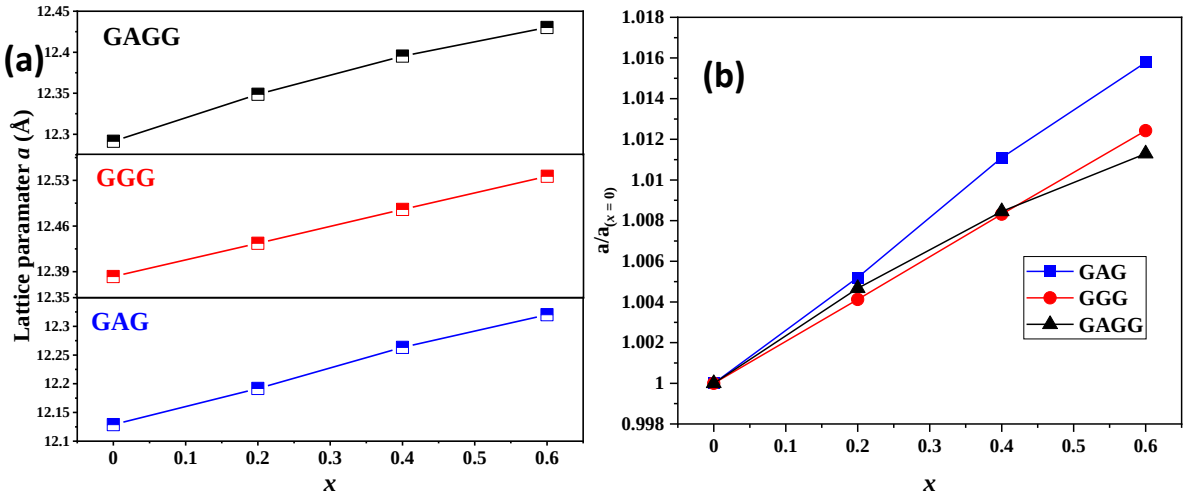

Fig 3.11 (a) *Laboratory PXRD data refined lattice parameter a and* ***(b)*** *$a/a_{(x=0)}$ values of $Gd_{3+x}Al_{5-x}O_{12}$, $Gd_{3+x}Ga_{5-x}O_{12}$ and $Gd_{3+x}(Al_{0.4}Ga_{0.6})_{5-x}O_{12}$ plot with x ($0 \leq x \leq 0.6$) as the function.*

3.3.3 Microstructure analysis of GAGG

In order to understand the presence of significant inhomogeneities in GAGG as well as its microscopic morphology and composition, SEM images and EDS were carried out. EBS image of polished single beads of each composition (see ***Fig 3.12***) shows grain boundaries and irregular polygonal grains with 0.3 to 1 µm in length and width, with no residual glassy components. Each sample contains porosity, which is why transparent ceramics GAGG cannot be obtained by crystallisation from glass. ***Table 3.4*** lists the measured average compositions, indicating that the measured compositions are close to the theoretical compositions. Whereas observation of the SEM image of the x = 0.6 sample (***Fig 3.13***) revealed that the bead sample has a layer with a thickness of about 43 µm (see ***Fig 3.13a***). A closer look (see ***Fig 3.13b***) shows that the microstructure of the outer layer is completely different from the centre. The microscopic morphology of the central part (see ***Fig 3.13c***) is

similar to that of the other GAGG samples, whereas the grains in the layer portion are short fibres (see ***Fig 3.13d***). Twenty points on crystal grain were selected for EDS analysis to know the composition of two different morphologies parts. The results listed in ***Table 3.4*** show that the compositions of two parts are essentially the same without different A/B ratios. It is possible that the difference in the morphology of x = 0.6 sample may be due to the different Ga/Al ratios in *B* and *C* site.

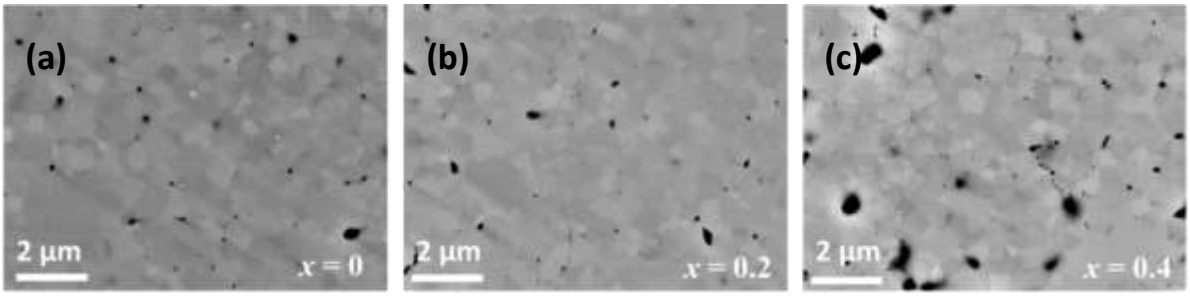

Fig 3.12 *SEM (BSE) image of pholished* $Gd_{3+x}(Al_{0.4}Ga_{0.6})_{5-x}O_{12}$ *beads* ***(a)*** *x =0* ***(b)*** *x = 0.2,* ***(c)*** *x = 0.4.*

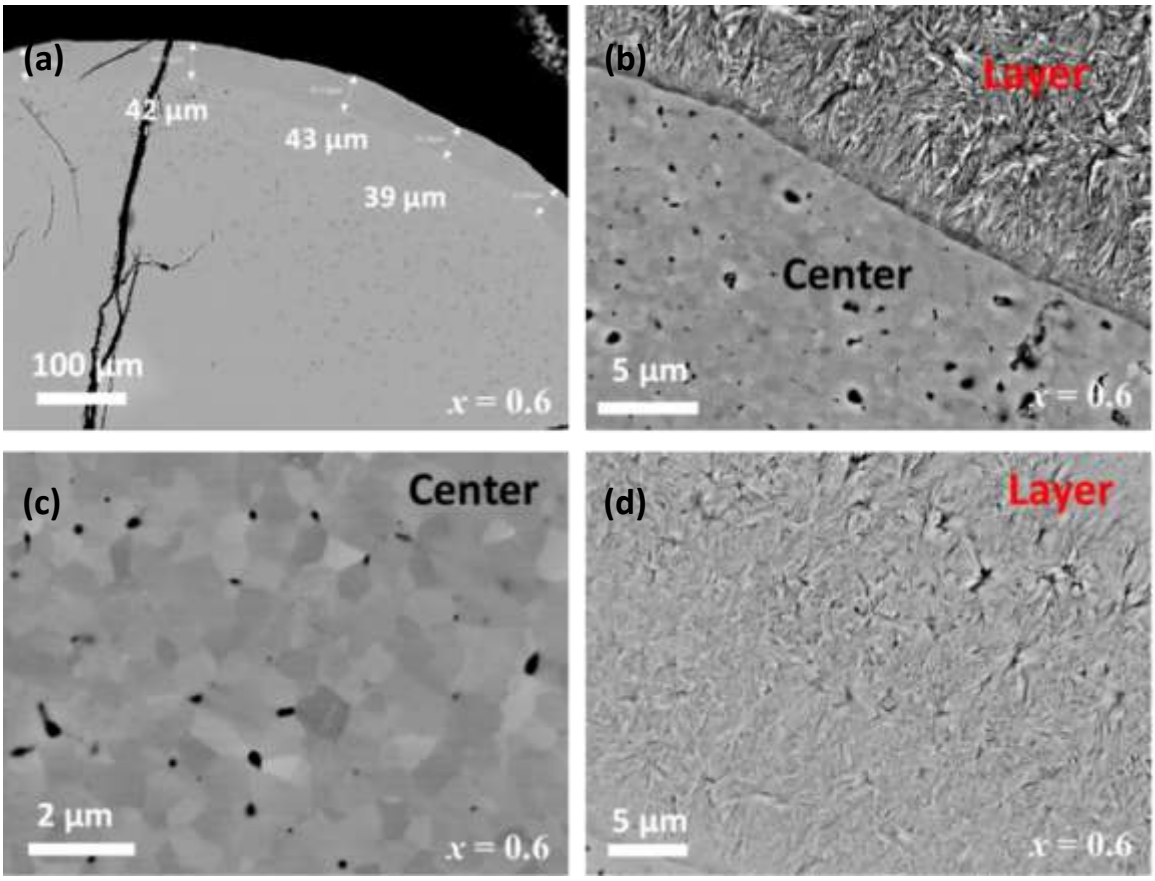

Fig 3.13 *SEM (BSE) image of pholished* $Gd_{3+x}(Al_{0.4}Ga_{0.6})_{5-x}O_{12}$ *(x = 0.6) bead.* ***(a-b)*** *Overall microscopic morphology image of a bead surface. Microscopic morphology of the* ***(c)*** *central and* ***(d)*** *layer part.*

Table 3.4 *SEM-EDS analysis of $Gd_{3+x}(Al_{0.4}Ga_{0.6})_{5-x}O_{12}$ (x =0, 0.2, 0.4, 0.6)*

GAGG	Phase	Gd (At.%)	Al (At.%)	Ga (At.%)	Experimental composition	Theoretical composition
x = 0	Single phase	15.50	11.64	12.86	$Gd_{3.1(1)}Al_{2.3(1)}Ga_{2.6(1)}O_{12}$	$Gd_3Al_2Ga_3O_{12}$
x = 0.2	Single phase	16.45	10.35	13.20	$Gd_{3.29(9)}Al_{2.07(9)}Ga_{2.64(9)}O_{12}$	$Gd_{3.2}Al_{1.92}Ga_{2.88}O_{12}$
x = 0.4	Single phase	17.24	9.3	13.46	$Gd_{3.45(9)}Al_{1.86(9)}Ga_{2.69(9)}O_{12}$	$Gd_{3.4}Al_{1.84}Ga_{2.76}O_{12}$
x = 0.6	Center	17.76	10.45	11.79	$Gd_{3.55(9)}Al_{2.09(9)}Ga_{2.36(9)}O_{12}$	$Gd_{3.6}Al_{1.76}Ga_{2.64}O_{12}$
	Layer	17.74	10.64	11.62	$Gd_{3.55(9)}Al_{2.13(9)}Ga_{2.32(9)}O_{12}$	

3.4 Synthesis and microstructure analysis of GAGG doped with Ce^{3+}/Cr^{3+}

Here $Gd_{3+x}(Al_{0.4}Ga_{0.6})_{5-x}O_{12}$: 0.5% Ce^{3+}/0.05% Cr^{3+} (x = 0, 0.2, 0.4) materials were synthesised to explore the effect of non-stoichiometric ratios on persistent luminescence properties. In order to ensure that the valence state of Ce in the doped samples is +3, the glass beads synthesised using ADL be placed in a reducing atmosphere of 5% H_2 and 95% argon for crystallisation at 900 ^oC for 2 hours. The XRD patterns of the samples presented in ***Fig 3.14*** show that the sample of x = 0 and 0.2 are the single garnet, while a small amount of secondary perovskite phase occurs in the x = 0.4 sample. The enlarged view of the main peak on the right of ***Fig 3.14*** demonstrates that the main peak moves towards higher 2θ values as x increases. Here the inability to obtain x = 0.6 glass samples may be due to the doping of Ce^{3+}/Cr^{3+}. The refined cell parameters exhibited in ***Fig 3.14b*** shows the expansion of the cell parameters as x increases. The detailed refinement parameters and the occupancy of Ga/Al on *B* and *C* site are listed in ***Table C.3.2.*** Comparison of the Ga/Al ratio on the octahedral sites of doped and undoped GAGG (x = 0) reveals that the ratio (1.94) in doped GAGG is significantly higher than that of the undoped GAGG (0.89), which may be due to the introduction of Ce^{3+}/Cr^{3+} or to the crystallisation atmosphere (this is an open question that can be explored in a future study).

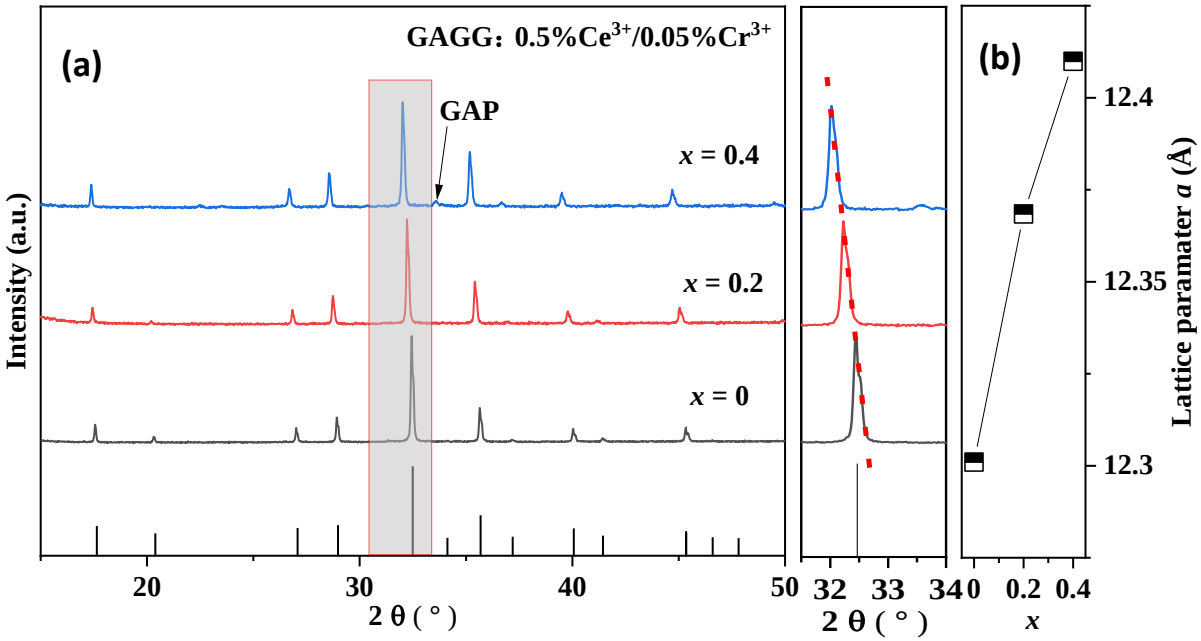

Fig 3.14 (a) *Laboratory PXRD pattern and* ***(b)*** *PXRD data refined lattice parameter a of* $Gd_{3+x}(Ga_{0.6}Al_{0.4})_{5-x}O_{12}$ *(x = 0, 0.2, 0.4): 0.5%*Ce^{3+} */0.05%*Cr^{3+}

In order to explore the effect of crystallisation atmosphere and temperature on crystal grain morphology, we collected SEM images of GAGG (x = 0.4): 0.5%Ce^{3+}/0.05%Cr^{3+} crystallisation at 900 °C (***Fig 3.15 a*** and ***b***) and 950 °C (***Fig 3.15 c*** and ***d***) in 5% H_2/95% Ar for 2h. Here we observe that the two samples exhibit similar morphology, which agrees with the GAGG x = 0.6 sample, suggesting that this morphology does not originate from the crystallisation temperature and atmosphere. In addition, the Ga/Al ratios of the GAGG (x = 0.6) samples and GAGG (x = 0.4): 0.5%Ce^{3+}/0.05%Cr^{3+} are different, indicating that this morphology is not due to Ga/Al either. Also, comparing the central part of two samples crystallised at different temperatures (see ***Fig 3.15b*** and ***d***), it can be seen that the grain size becomes larger at higher crystallisation temperatures. This should be brought to our attention as it has been reported[15] that grain size affects the emission wavelength of garnet based persistent luminescence. In addition, 20 points were collected for EDS compositional analysis in the layers and central parts of each sample and the results are listed in ***Table 3.5***. These results show that the crystallisation temperature does not affect the composition of the two parts and that the composition of the two parts with different morphology is the same and consistent with the theoretical composition.

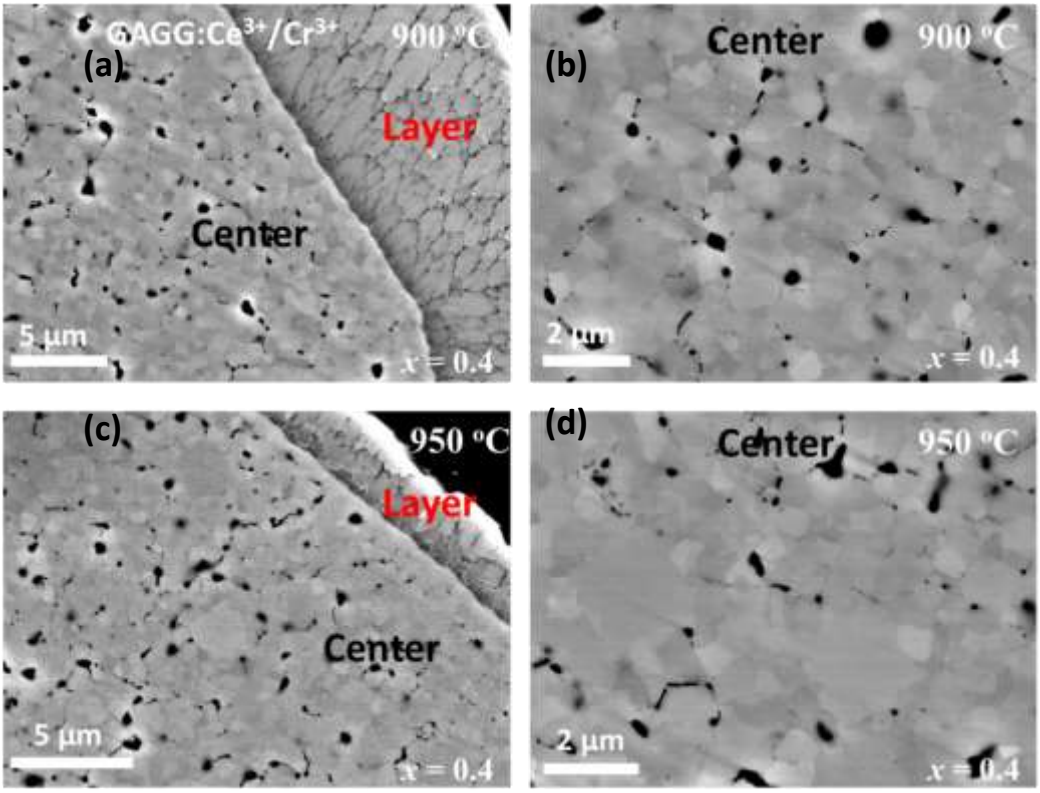

Fig 3.15 *SEM (BSE) image of pholished* $Gd_{3+x}(Al_{0.4}Ga_{0.6})_{5-x}O_{12}$ *(x = 0.4) bead crystallisation at* ***(a-b)*** *900* ^{o}C *and* ***(c-d)*** *950* ^{o}C

Table 3.5 *SEM-EDS analysis of* $Gd_{3+x}(Al_{0.4}Ga_{0.6})_{5-x}O_{12}$ *(x = 0.4) bead crystallisation at 900* ^{o}C *and 950* ^{o}C*.*

GAGG : Ce/Cr (x = 0.4)	Phase	Gd (At. %)	Al (At. %)	Ga (At. %)	Experimental composition	Theoretical composition
900 ^{o}C	Center	18.01	10.36	11.63	$Gd_{3.6(1)}Al_{2.1(1)}Ga_{2.3(1)}O_{12}$	$Gd_{3.385}Ce_{0.015}Al_{1.84}Ga_{2.76}Cr_{0.001}O_{12}$
	layer	17.73	10.91	11.35	$Gd_{3.55(9)}Al_{2.18(9)}Ga_{2.27(9)}O_{12}$	
950 ^{o}C	Center	17.50	9.53	12.97	$Gd_{3.5(1)}Al_{1.9(1)}Ga_{2.6(1)}O_{12}$	
	Layer	17.67	9.58	12.75	$Gd_{3.5(1)}Al_{1.9(1)}Ga_{2.6(1)}O_{12}$	

3.5 Persistent luminescence properties of GAGG and GGG based materials.

3.5.1 Persistent luminescence properties of GAGG-based material.

Previous studies on GAGG: 0.05%Ce^{3+}/0.5%Cr^{3+}[10] and GAGG: 1%Tb^{3+}[16] have reported that modifying the Ga/Al ratio yield more durable persistent luminescent materials. Theoretically, the substitution of Gd for the Ga/Al in the octahedron may affect the depth of the electron trap which in turn could affect the persistent luminescence properties. The study of non-stoichiometric GAG: 2%Ce^{3+} (chapter 2) has indicated that the occupation of excess-Gd^{3+} in the Al octahedron site causes a redshift of the emission peak, while studies on GAG: 10%Tb^{3+} has shown that Tb is distributed over the dodecahedron and octahedral sites. Therefore, here we synthesised $Gd_{3+x}(Ga_{0.6}Al_{0.4})_{5-x}O_{12}$ (x = 0, 0.2, 0.4): 0.05%Ce^{3+}/0.5%Cr^{3+} and $Gd_{3+x}(Ga_{0.6}Al_{0.4})_{5-x}O_{12}$ (x = 0, 0.2,0.4):Tb^{3+} to investigate the effect of non-stoichiometric A/B ratio on the colour and duration of the persistent luminescence properties.

Fig 3.16a displays the PLE and PL spectra of $Gd_{3+x}(Ga_{0.6}Al_{0.4})_{5-x}O_{12}$ (x = 0, 0.2, 0.4): 0.5%Ce^{3+}/0.05%Cr^{3+}. The two excitation bands observed at around 440 nm and 355 nm are attributed to transitions from the 4f energy level to the lowest $5d^1$ and second lowest $5d^2$ energy levels of Ce^{3+} [10]. The lower energy excitation bands are blue-shifted and the higher energy excitation bands are red-shifted in the x = 0.4 sample, which is caused by the enhanced 5d energy level splitting resulting from the crystal field changes induced by Gd occupying Al. An intense luminescence peak is observed at 560 nm, which corresponds to the transition of Ce^{3+} from the lowest $5d^1$ energy level to the 4f energy level. The red-shift of emission peak at 580 nm in the non-stoichiometric GAGG sample is caused by the splitting of the Eg energy level due to the increased crystal field distortion. Under UV excitation, the colour shifts from green to yellow in the stoichiometric and non-stoichiometric GAGG, as can be observed in the CIE diagram (see ***Fig 3.16b***). A wider red shift (20 nm) is observed compared to that in GAG: 2% Ce^{3+} (4 nm), which we believe is due to the more decrease in

the Ce-O distance (0.025 Å) than that in GAG (0.0063 Å) resulting in a greater change in the crystal field of dodecahedron.

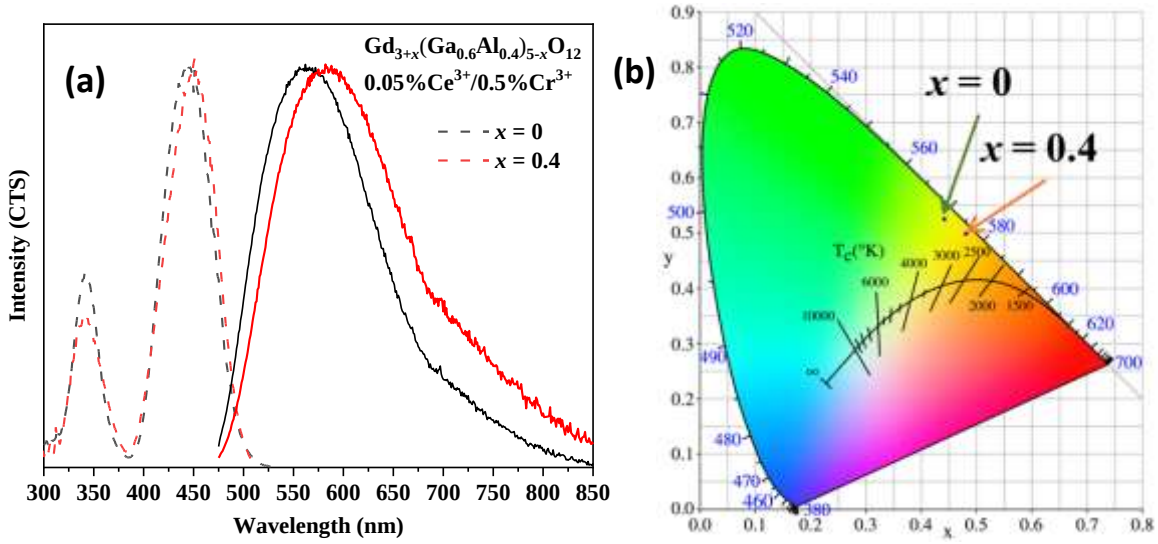

Fig 3.16 *Luminescence performance of $Gd_{3+x}(Ga_{0.6}Al_{0.4})_{5-x}O_{12}$ (x = 0, 0.4): 0.5%Ce^{3+}/0.05%Cr^{3+} powder. (a) Photoluminescence excitation (dotted line on felt) and photoluminescence (solid line on right) spectra, (b) ICE diagram*

The persistent excitation and emission spectra of $Gd_{3+x}(Ga_{0.6}Al_{0.4})_{5-x}O_{12}$ (x = 0, 0.2, 0.4): 0.5%Ce^{3+}/0.05%Cr^{3+} powders shown in ***Fig 3.17a*** are similar to their photoluminescence spectra behavior, with an intense luminescence band at 540 nm, corresponding to transitions from the lowest 5d1 level to the 4f levels of Ce^{3+} after the 460 nm blue-light excitation. The emission wavelength at 560 nm of non-stoichiometric sample with x = 0.4 is 20 nm longer than the stoichiometric phosphor, indicating that Gd^{3+} occupies the octahedral Al/Ga causing a red shift in the persistent luminescence emission. Compared to the conventional $SrAl_2O_4$: Eu^{2+}/Dy^{3+} (510 nm)[17], $Y_3Al_2Ga_3O_{12}$: Ce^{3+}/Cr^{3+} (505 nm)[12] and $Gd_3Al_2Ga_3O_{12}$: Ce^{3+}/Cr^{3+} (540 nm)[10] transparent persistent luminescence emission colours, the persistent luminescence of the nonstoichiometric $Gd_3Al_2Ga_3O_{12}$: Ce^{3+}/Cr^{3+} phosphor exhibits a colour at 560 nm that is closer to the sensitive colour of the human eye (sensitivity peak of the photopic cell is located at 555 nm)[10]. The decay curves of the persistent luminescence of all the samples shown in ***Fig 3.17b*** indicate a very strong brightness of persistent luminescence after excitation stoppage. The normalized curve shown in the inset of ***Fig 3.17b*** shows that the persistent luminescence of ns-GGAG decays more slowly than

GAGG, probably due to the increase in the conduction band gap caused by Gd occupying the octahedron and thus obtaining deeper electron traps. However, the intensity of persistent luminescence here cannot be compared exactly due to the quantity of the powder tested and the fact that the test area cannot be guaranteed to be identical.

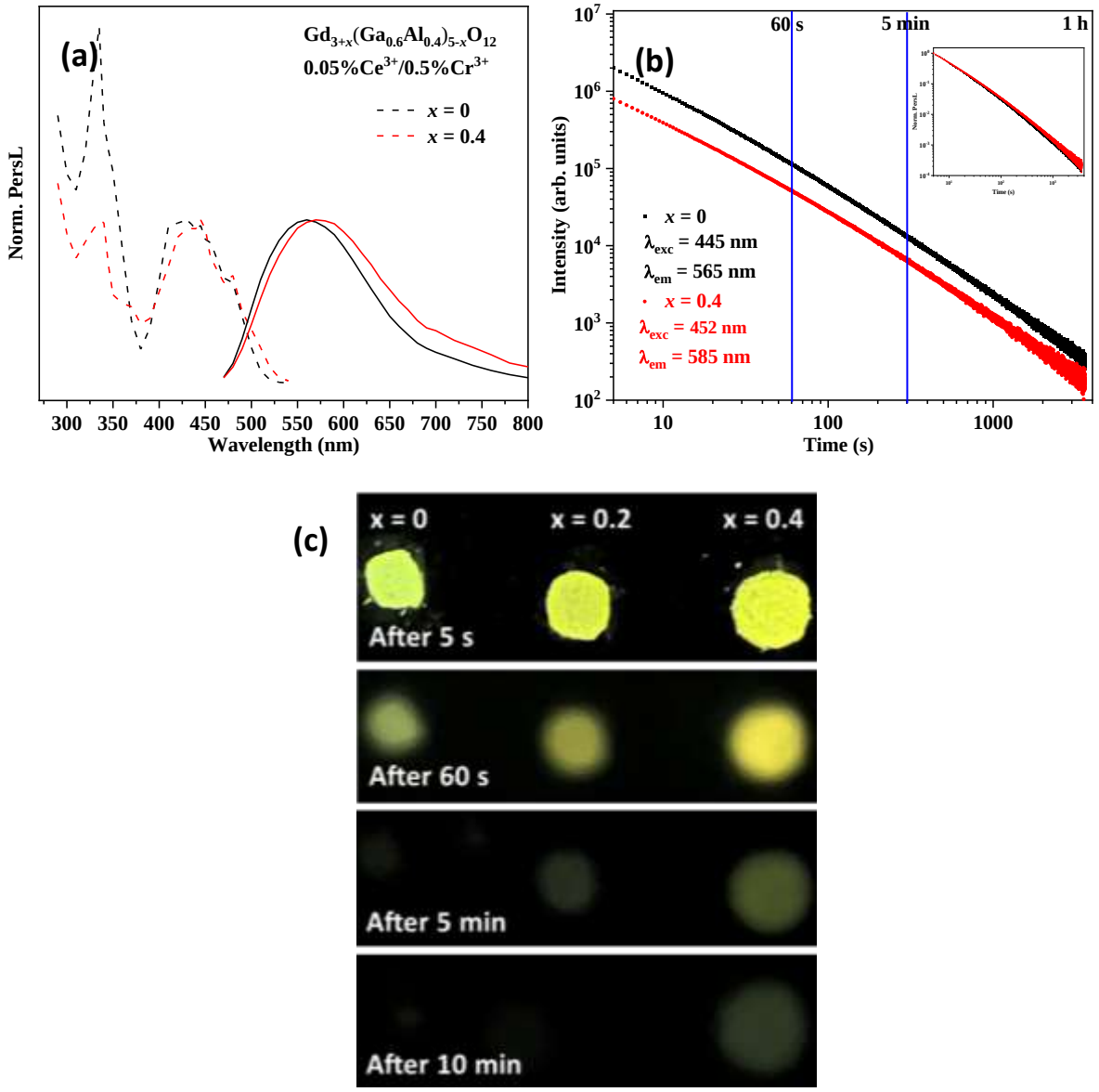

Fig 3.17 *Persistent luminescence performance of $Gd_{3+x}(Ga_{0.6}Al_{0.4})_{5-x}O_{12}$ (x = 0, 0.4): 0.05%Ce^{3+}/0.5%Cr^{3+} powder.* ***(a)*** *Persistent photoluminescence excitation (dotted line on left) and persistent photoluminescence (solid line on right) spectra,* ***(b)*** *persistent luminance decay curves for 1h after 450 nm blue-light irradiation (blue line are the timeline of 60s and 1min after cessation of excitation) and* ***(c)*** *Images of persistent emission taken 5s - 10 min after irradiation ceasing in dark of ns-GAGG (x = 0, 0.2, 0.4).*

Fig 3.17c shows photographs of persistent emission taken 5 - 600s after cessation of excitation. The stoichiometric ratio of the material exhibits a green emission colour similar to that reported for GAGG transparent ceramics[18], however the non-stoichiometric GAGG shows a yellow emission colour and shifts towards red with increasing x values. In addition, it can be observed that the duration of the persistent emission increases with increasing degree of non-metric ratio. Thus, it can be concluded that the duration and intensity of the persistent luminescence can be simultaneously regulated by changing the Gd/(Al/Ga) ratio. The occupation of the B-site by Gd causes a change of crystal field in the dodecahedron resulting in a red shift of the emission peak from green to yellow, and affects the width of the energy gap in the host increasing the lasting time of the persistent luminescence.

A literature report on the $Gd_{2.97}Tb_{0.03}Ga_{5-y}Al_yO_{12}$ family (y = 0, 1, 2, 3, 4, 5)[16] reports that the total Ga/Al content of GAGG (y) has an impact on the emission colour and duration of the persistent luminescence of samples made by the ceramic method, with a maximum intensity and decay lifetime found at y = 4, as shown in their photograph which is reproduced in ***Fig 3.18a***. To see whether increasing the Al content would have a similar influence on the PL performance of the non-stoichiometric glass-crystallised GAGG systems, three new Al-rich nonstoichiometric compositions $Gd_{3+x}Al_{(0.8}Ga_{0.2)_{5-x}}O_{12}$: 1%$Tb^{3+}$ (x = 0, 0.2, 0.4) were synthesized by glass crystallization. ***Fig 3.18b*** shows photographs of these $Gd_{3+x}Al_{(0.8}Ga_{0.2)_{5-x}}O_{12}$: 1%$Tb^{3+}$ powders under 254 nm excitation and after the excitation 5s, indicating that there is no significant colour change, which is consistent with that reported for GAG: 10% Tb^{3+} system. These were not explored further due to their undesirable decay times and the brightness intensities.

GAG: 10% Tb^{3+} was investigated for the effect of non-stoichiometry on persistent luminescence as well, as shown in ***Fig 3.18c***. The photographs of the persistent luminescence after excitation exhibit a similar luminescence colour in GAG and ns-GAG, with no improvement in persistence lasting time, while there was no perceptible persistent luminescence for the non-stoichiometric sample with x = 0.4. GAG: 5% Tb^{3+} was also studied to avoid the effect of concentration on persistent luminescence performance. The photograph of the persistent luminescence after excitation shown in ***Fig 3.18d*** shows a similar phenomenon to GAG: 10% Tb^{3+} sample, indicating that the high stoichiometric GAG

has a trap depth that is too deep to produce persistent luminescence. This exploration here suggests that Tb^{3+} ions are not sensitive to changes in the ratio of Gd/(Ga/Al) at the octahedral sites and did not affect their emission colours in nonstoichiometric GAGG, which is consistent with the GAG: 10%Tb^{3+} results. In addition the non-stoichiometry does not improve the persistence of the persistent luminescence of GAGG-based: Tb^{3+} system, and may even produce depths unsuitable for the escape of Tb^{3+} ions thus losing the persistent luminescence performance.

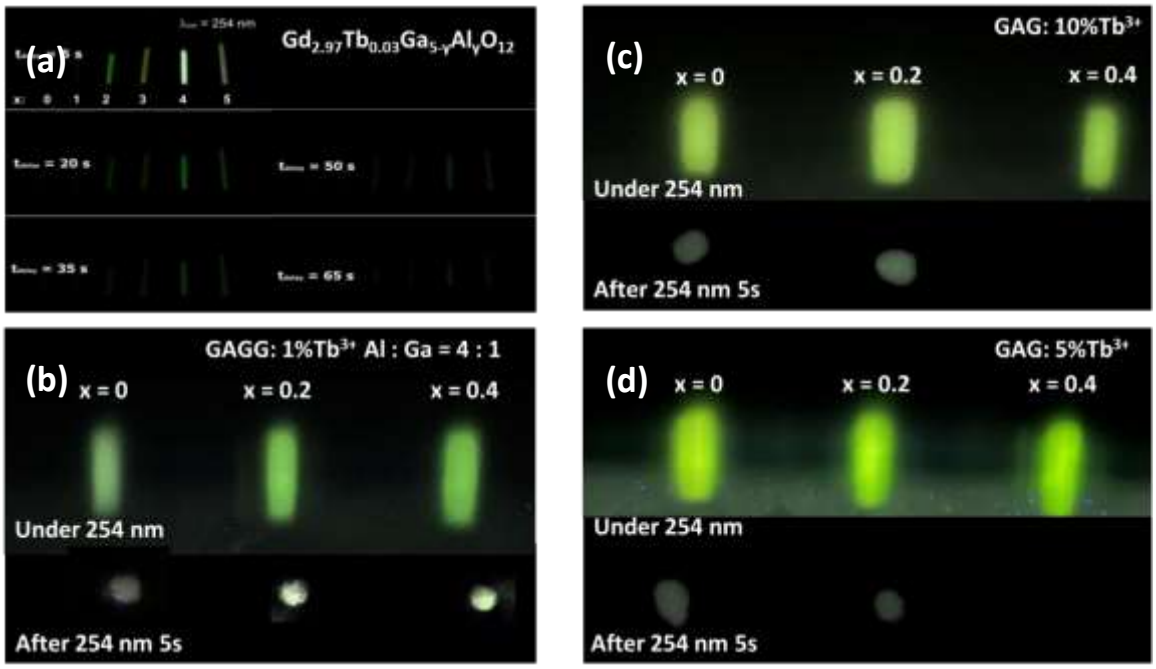

Fig 3.18 *The photographs of (a) $Gd_{2.97}Tb_{0.03}Ga_{5-y}Al_yO_{12}$ (adapted from Tomala's paper[16]), (b) $Gd_{3+x}Al_{(0.8}Ga_{0.2)_{5-x}}O_{12}$: 1%$Tb^{3+}$ (this work), (c) GAG:10%Tb^{3+} (this work) and (d) 5%Tb^{3+} (this work) emission under 254nm and persistent emission after excitation taken in dark.*

3.5.2 Exploration of highly non-stoichiometric GGG-based persistent materials

The work on GAGG: Ce^{3+}/Cr^{3+} in ***3.5.1*** section indicated that the non-stoichiometric A/B ratio can be adjusted not only in terms of emission colour but also of lasting time of persistent luminescence material. Therefore, the Ga/Al ratio can be adjusted to tailor electron trap depths to suit different dopant ions and obtain persistent luminescence

materials with varyious emission. The trap depth of the GGG based material has been reported to be adapted to Eu^{3+}/Cr^{3+}, resulting in a red persistent luminescence material[18]. It has also been reported that adjusting the concentration of dopant $Tb^{3+}/Eu^{3+}/Pr^{3+}$ in the GGG host results in blue-red and white long persistent luminescence materials[19]. These reports provide insight into the exploration of non-stoichiometric GGG based persistent luminescence materials. Therefore, this subsection aims to investigate the effect of the non-stoichiometric A/B ratio on emission colour and persistence by studying on ns-GGG: Eu^{3+}/Cr^{3+} and ns-GGG: $Tb^{3+}/Eu^{3+}/Pr^{3+}$ materials.

GGG: 0.07%Eu^{3+}/0.5%Cr^{3+} and GGG: 0.1%Tb^{3+}/0.1% Eu^{3+} synthesized via crystallization from melt by ADL using oxygen as carried gas. ***Fig 3.19a*** displays the XRD pattern of GGG: Eu^{3+}/Cr^{3+} indicating that the x = 0 compound are single garnet phases, while the x = 0.2 and x = 0.4 compound are mixture of two garnet phases. The enlarged view of the (211) diffraction peak on the right side of ***Fig 3.19a*** shows that the diffraction peak shifts to a lower 2θ as the x value increases. The refined cell parameters show that the x = 0.4 sample deviates from the theoretical value due to the presence of the 31.0(7) wt% secondary GGG phase. The XRD patterns of the GGG: 0.1%Tb^{3+}/0.1% Eu^{3+} shown in ***Fig 3.19c*** illustrate that the x = 0 and x = 0.2 samples are single GGG phase, while a secondary ns-GGG phase begins to appear at x = 0.4. Their cell parameters showed linear variation and were consistent with those of the undoped GGG samples (see ***Fig 3.19d***). Detailed information on the fitting parameters are listed in ***Table C.1.2.*** It was found to be difficult to obtain a single non-stoichiometric garnet phase doped with RE^{3+} by ADL methods even with low doping concentration, which affects the further study of optical properties.

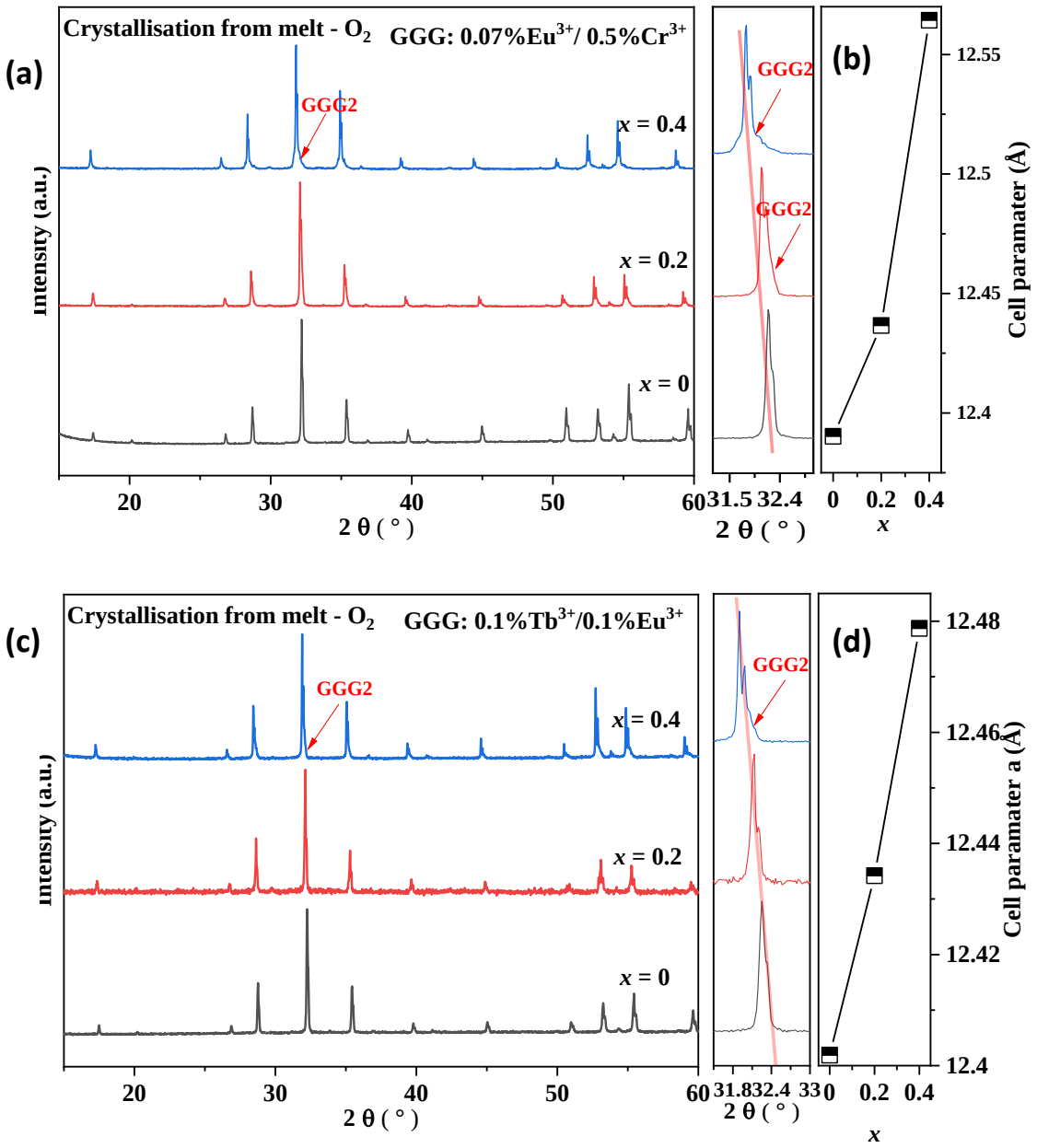

Fig 3.19 *Lab-XRD patterns of $Gd_{3+x}Ga_{5-x}O_{12}$ (x = 0, 0.2, 0.4):* ***(a)*** *0.7%Eu^{3+}/0.05%Cr^{3+} and* ***(b)*** *0.1%Eu^{3+}/0.1%Tb^{3+}. Refined cell parameters a of $Gd_{3+x}Ga_{5-x}O_{12}$ (x = 0, 0.2, 0.4)* ***(c)*** *0.7%Eu^{3+}/0.05%Cr^{3+} and* ***(d)*** *0.1%Eu^{3+}/0.1%Tb^{3+} (an enlarged view of the main peak is on the right.)*

The emission colour photos of the GGG: Eu^{3+}/Cr^{3+} samples under 245 nm irradiation are displayed in ***Fig 3.20a***, revealing that three samples exhibit red emission, and that the emission brightness increase as increasing of x value, but without significant colour change. However, all three samples fail to show any persistent luminescence after charging stops. The GGG: Eu^{3+}/Cr^{3+} material does not exhibit the persistent luminescence as reported[18]. Persistent luminescence properties have not been replicated even synthesized $Gd_3Ga_5O_{12}$

composition by solid-state reaction based on literature[18]. In ***Fig 3.20b***, the images of emission colour under 254nm excitation (upper) and the persistent luminescence after excitation (lower) are displayed. All samples exhibit red luminescence under 254nm excitation and blue persistent luminescence after excitation, but there is no significant colour adjustment between n-GGG and ns-GGG. We believe that even though it has been shown that the Tb^{3+} ion tends to occupy the *A* and *B*-site in the non-stoichiometric garnet structure, the fact that the f-f transition of Tb^{3+} is not sensitive to changes in the symmetry of the luminescent site has been confirmed by studies of GAG: 10% Tb^{3+} system. The lack of significant improvement in persistence time could be attributed to changes in depth of electron trap caused by the substitution Gd for Ga, which may no longer be suitable for the persistent luminescence process of Tb^{3+} ions.

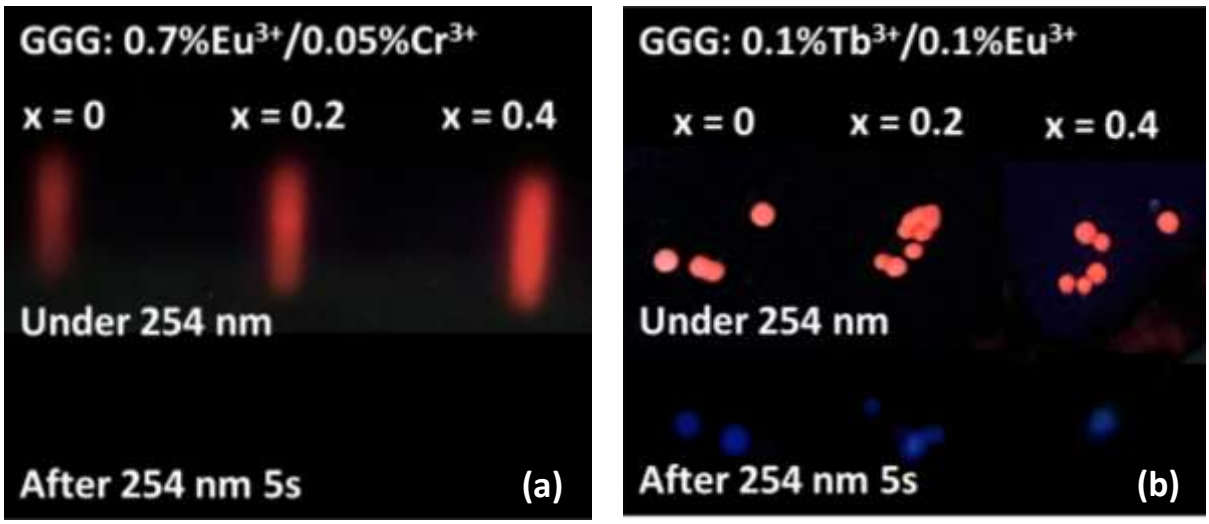

Fig 3.20 *The photographs of GGG: 0.7%Eu^{3+}/0.05%Cr^{3+} (a) and GGG: 0.1%Eu^{3+}/0.1%Tb^{3+} (b) under 254 nm (upper) and after 254 nm 5s (lower).*

The studies presented in ***Chapters 2*** and ***3*** indicate that non-stoichiometry has an impact on the luminescence performance of garnet materials such as GAG, GGG, and GAGG. Garnet structures materials have a wide range of applications in various fields [20-23], it is then important to explore other types of non-stoichiometric (see ***Appendix D.1*** for detailed information). By attempting to synthesise a series of non-stoichiometric garnets (SmAG, EuAG, GAG, LuAG), it is concluded that the formation of non-stoichiometric garnet $RE_3Al_5O_{12}$ is not only related to the radius of the RE^{3+} ion, but also to synthesis method. The ionic

radius of Lu^{3+} is smaller than that of Gd/Y, but no non-stoichiometric LuAG can be obtained, which is attributed to the lack of glass-forming ability of the LuAG composition. In addition to $RE_3Al_5O_{12}$ garnet, other types of garnet YIG, etc., and non-stoichiometric perovskite have tried to synthesise, but no any other types of non-stoichiometric garnet and non-stoichiometric perovskite has found (see section ***Appendix D.2*** and ***D.3*** for details).

3.6 Chapter conclusion and perspectives

In conclusion, a highly non-stoichiometric $Gd_{3+x}Ga_{5-x}O_{12}$ solid solution with a composition range of $0 \leq x \leq 0.7$ was successfully synthesised using crystallisation from melt by ADL. Analysis of the SPD shows that more than 30% of the six-coordinated Ga is occupied by Gd in ns-GGG (x = 0.7). Comparison of the solid solution ranges of GAG ($0 \leq x \leq 0.6$) and GGG ($0 \leq x \leq 0.7$) shows that larger B-site ions may be able to accommodate more A-site ions. Comparison of the solid solution of ns-YAG ($0 \leq x \leq 0.4$) indicates that the size of the A-site ions is not a determining factor affecting the solid solution range of non-stoichiometric garnet. Analysis of the EXAFS spectra illustrates the disordered occupation of the B-site by the Gd^{3+} ion. DFT geometry optimisation to generate simulated EXAFS spectra for several different substitution scenarios is in progress. The persistent luminescence exploration of GGG: Eu^{3+}/Cr^{3+} revealed that neither the stoichiometric nor the non-stoichiometric ratios exhibited the persistent luminescence phenomenon similar to the reported. The GGG: Eu^{3+}/Tb^{3+} persistent luminescence experiment has shown that no change in the emission color resulting from the f-f transition of Tb^{3+} ions insensitive to new BO_6 sites.

Highly nonstoichiometric $Gd_{3+x}(Ga_{0.6}Al_{0.4})_{5-x}O_{12}$ (x = 0 - 0.6) garnets were synthesized by crystallisation from glass. PXRD refinement results shown that up to 30% six coordinated Al/Ga site can substituted by Gd. The ratio of Ga/Al on the octahedron decreases with the occupation of Gd, which leads to cell parameter changes that are not strictly linear growing with increasing x values. Here, persistent luminescent properties of ns-GAGG: Ce^{3+}/Cr^{3+} suggest that changes in the dodecahedral crystal field caused by the occupation of Al/Ga by Gd affect the changes in the persistent luminescence emission colour from green to yellow

and additionally affect the trap depth thus changing the decay rate of the persistent luminescence. In summary, the adjustment of the A/B ratio in non-stoichiometric garnets is a very effective way of not only regulating the emission of persistent luminescence, but also of varying the decay time of the persistent luminescence by adjusting the depth of the electron trap.

In addition, the synthesis of a range of non-stoichiometric garnets and perovskite compounds were explored. These results tell us that the synthesis of nonstoichiometric garnets is not absolutely dependent on the RE radius. Samples capable of forming glass can be obtained non-stoichiometric garnet by crystallizing from the glass. These results suggest that new metastable compounds can be developed by taking advantage of direct crystallization from melt and glass. These non-stoichiometric garnets may yield new applications in other areas that need to be further explored in the future. For example the nonstoichiometry may have an effect on the magnetic properties of GGG garnet.

References

[1] H. Choi, J.H. Kim, J.Y. Park et al., Journal of the Korean Physical Society. ***2011****, 59, 2329-2333.*

[2] W. Zhang, Y.L. Liang, Z.F. Hu et al., Journal of Nanoscience Nanotechnology. ***2016****, 16, 3517-3521.*

[3] J. Li, J.G. Li, S. Liu et al., Sci Technol Adv Mater. ***2013****, 14, 054201.*

[4] X. Teng, J. Li, G. DuanZ. Liu, Journal of Luminescence. ***2016****, 179, 165-170.*

[5] J. Xu, J. Ueda, S. Tanabe, Journal of the American Ceramic Society. ***2017****, 100, 4033-4044.*

[6] M. Fasoli, A. Vedda, M. Nikl et al., Physical Review B. ***2011****, 84, 081102.*

[7] K. Van den Eeckhout, A.J.J. Bos, D. Poelman et al., Physical Review B. ***2013****, 87,045126.*

[8] Yang Li, M. Geceviciusa, J.R. Qiu.Chemical Society Reviews. ***2016****, 45, 2090-2136.*

[9] J. Ueda, Bulletin of the Chemical Society of Japan. ***2021****, 94, 2807-2821.*

[10] J. Ueda, K. Kuroishi, S. Tanabe, Applied Physics Express. ***2014****, 7, 062201.*

[11] J.Ueda, K. Kuroishi, S. Tanabe, Applied Physics Letters. ***2014****, 104, 101904.*

[12] J. Ueda, S. Tanabe, Jian Xu, J. Mater. Chem. C. ***2016****, 4, 4380-4386.*

[13] F. Pandozzi, F. Vetrone, J.C. Boyer et al., The Journal of Physical Chemistry B. ***2005****, 109, 17400 -17405.*

[14] A.C. Sackville Hamilton, G.I. Lampronti, S.E. Rowley et al., Journal of Physics: Condensed Matter. ***2014****,*

26, 116001.

[15] P. Głuchowski, R. Tomala, D. Kujawa et al., The Journal of Physical Chemistry C. ***2022****, 126, 7127-7142.*

[16] R. Tomala, K. Korkus, V. Boiko et al., Journal of Alloys and Compounds. ***2021****, 889, 161745.*

[17] T. Matsuzawa, Y. Aoki, N. TakeuchiY. Murayama, Journal of The Electrochemical Society. ***2019****, 143, 2670-2673.*

[18] J. Xu, J. Ueda, S. Tanabe, Optical Materials Express. ***2015****, 5, 963.*

[19] J. Ueda, S. Miyano, J. Xu et al., Advanced Photonics Research. ***2021****, 2, 2000102.*

[20] M. Nikl, A. Yoshikawa, K. Kamada et al., Progress in Crystal Growth and Characterization of Materials. ***2013****, 59, 47-72.*

[21] J. Kim, S. Oh, Y.J. Kim, Symposium Digest of Technical Papers. ***2019****, 50(1), 1702-1704.*

[22] L. Feng, Z. Wang, C. Cao et al., Journal of Rare Earths. ***2017****, 35, 47-52.*

[23] Y. Rao, D. Zhang, L. Jin et al., Journal of Magnetism and Magnetic Materials. ***2020****, 497, 165817.*

Chapter IV: Structure and luminescence properties of the $Lu_{4-\alpha}Al_{2-x}Si_xO_{9+\delta}$ ($0 \leq x \leq 1$) solid solution

4.1 Introduction

As stated in the introduction of **Chapter 1**, in our group's collaboration with Feng's work on $(Lu/Mg)_3(Al/Si)_5O_{12}$, they found the presence of a unknown secondary phase of $(Lu/Mg)_4(Al/Si)_2O_9$, which was determined by EDS[1]. Subsequent synthetic studies of this sample showed that its XRD pattern matches that of $Lu_4Al_2O_9$. In view of this finding, it was suggested that on the basis of the $Lu_4Al_2O_9$ structure, Al/Si or Lu/Mg and Si/Al double substitutional solid solutions may exist. Therefore, a literature survey is carried out here on $Lu_4Al_2O_9$ and $Lu_4(Al/Si)_2O_9$ solid solutions.

In the RE_2O_3-Al_2O_3 system, in addition to the $REAlO_3$ perovskite, $RE_3Al_5O_{12}$ garnet, $RE_4Al_2O_9$ can be produced when RE_2O_3 : Al_2O_3 = 2 : 1. These compounds have been reported as famous optical materials. The members of the $RE_4Al_2O_9$ family, RE = La, Nd, Ce, Eu, Gd, Tb, Dy, Ho, Er, Yb, and Y have been extensively investigated on their structures and optical applications[2-5](as described in ***Chapter 1 1.5.3 section***). The structure of $RE_4Al_2O_9$ is monoclinic and contains two crystallographically distinct Al sites, four RE sites, and nine O sites. Of the four RE atoms, RE1 and RE3 are coordinated by seven oxygen atoms, and RE2 and RE4 are coordinated by six oxygen atoms to form a distorted octahedron as shown in ***Fig 4.1a*.** The two four coordinated Al tetrahedra are vertex-linked by a shared O5 atom to form an Al_2O_7 dihedral oxyaluminate group (***Fig 4.1b***)[6]. The cell parameters *β* and cell volume *V* of $RE_4Al_2O_9$ vary linearly with increasing atomic radius as shown in ***Fig 4.1c***. Due to challenges in the synthesis of $Lu_4Al_2O_9$ it can only exist at high temperatures and decomposes during cooling to garnet and Al_2O_3[7], metastable $Lu_4Al_2O_9$ has only recently been discovered [8]. It was not until 2020 that the first single crystal of $Lu_4Al_2O_9$ was successfully synthesized, and its crystal structure was determined to exhibit a monoclinic symmetry in the space group $P2_1/c$ with cell parameter a = 7.236 (2) Å, b = 10.333 (2) Å, c = 11.096 (3) Å, and = 108.38(2)^o[6]. Therefore, the synthesis of $Lu_4Al_2O_9$ and the exploration of its optical properties are promising and interesting. Levitation combined with laser heating is a valuable technological approach for producing new glasses and metastable phase by using equilibrium synthesis methods[9]. Thus, the ADL synthesis serves as a promising alternative with the potential to successfully synthesise metastable $Lu_4Al_2O_9$, which cannot be achieved

using solid state reaction methods.

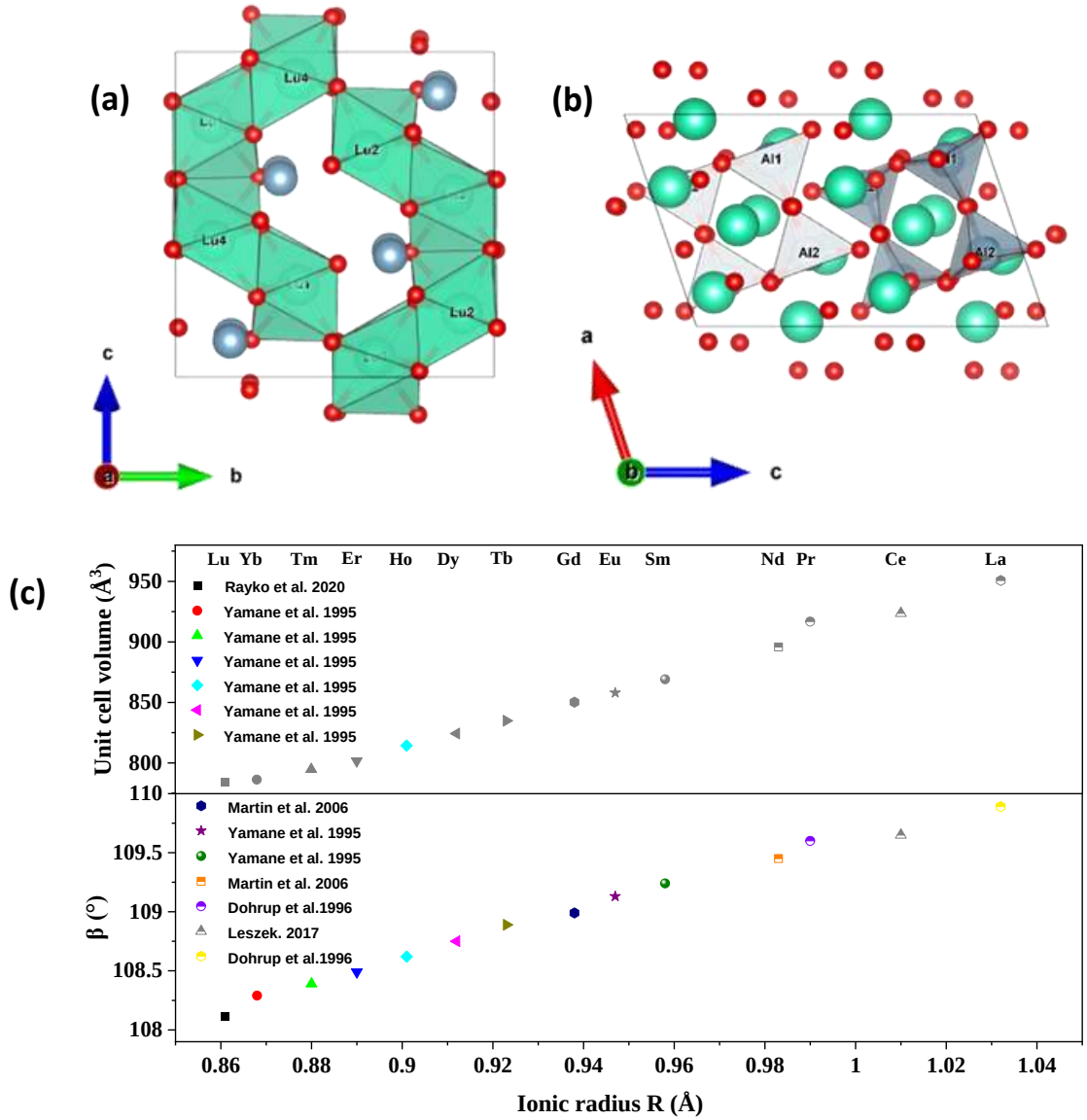

Fig 4.1 *Crystal structure of $RE_4Al_2O_9$* ***(a)*** *the RE centered polyhedra viewed down a axis* ***(b)*** *the Al_2O_7 ditetrahedra viewed down b axis.* ***(c)*** *The evolution of the cell parameters β and cell volume V of $RE_4Al_2O_9$ vs RE^{3+} ionic radius.*

The literature review for $Lu_8Al_3SiO_{18}$ compound found that in the RE_2O_3-Al_2O_3-SiO_2 system, two extended ternary solid solutions, $RE_{9.33+2x}(Si_{1-x}Al_xO_4)_6$ (x = 0 - ~ 0.3) and $RE_4Al_{2(1-x)}Si_{2x}O_{9+x}$ (x = 0 - ~ 0.4) based on the quasi-binary phases $RE_{9.33}(SiO_4)_6O_2$ and $RE_4Al_2O_9$, respectively, have been reported[10]. The chemical formulae of the solid solutions $Y_4Al_{2(1-x)}Si_{2x}O_{9+x}$ (x = 0 - ~ 0.3)[11], $Nd_4Al_{2(1-x)}Si_{2x}O_{9+x}$ (x = 0 - ~ 0.4)[12] and $Gd_4Al_{2(1-x)}Si_{2x}O_{9+x}$ (x = 0 - ~ 0.33)[13] based on monoclinic $RE_4Al_2O_9$ were determined by SEM-EDX and illustrate

the different Al/Si-order-disorder states at different temperatures. However, the crystal structures of the solid solutions were not examined in detail. Thus, it is worth exploring the synthesis and detailed crystal structures of solid solutions with Si substituted Al in $Lu_4Al_2O_9$.

Feng et al. developed a new $Lu_{3-x}Y_xMgAl_3SiO_{12}:Ce^{3+}$ garnet red phosphor that modifies the crystal field environment to enable emission redshift by replacing Lu in the dodecahedron with Y and substituting the AlO_6/AlO_4 chemical unit with an MgO_6/SiO_4 polyhedron[1]. This work discovered a new $(Lu/Mg)_4Al/Si_2O_9$ compounds and provided a substitution strategy for $Lu_4Al_2O_9$. Notably, within the REAM system, trivalent RE^{3+} can substitute at four different sites, and the diverse cationic REO_6/REO_7 and AlO_4 polyhedra in the structure provide the possibilities for multiple substitution designs that influence the activator's environment[14-17]. The exploration for new color phosphor material is predicted to be feasible through a substitution design strategy, wherein the tetra-coordinated Al^{3+} (0.535 Å) is replaced with smaller sized Si^{4+} (0.4 Å), and Lu^{3+} - Al^{3+} is substituted by Mg^{2+}-Si^{4+} in $Lu_4Al_2O_9$. The substitution of Si^{4+} for Al^{3+} was considered due to charge compensation, which can introduce Lu vacancies or additional oxygen into the $Lu_{4-\alpha}(Al/Si)_2O_{9+\delta}$ solid solution. Consequently, the synthesis and structural examination of $Lu_4Al_2O_9$ and $Lu_{4-\alpha}(Al/Si)_2O_{9+\delta}$ solid solution, as well as the investigation of photoluminescence response to the local structural defects in Lu sites and Al/Si disorder on the luminescence properties, are of significance for elucidating the luminescence processes in $Lu_4Al_2O_9$ and $Lu_{4-x}(Al/Si)_2O_{9+\delta}$ host materials.

In this chapter, $Lu_4Al_2O_9$ and solid solution compounds $Lu_{4-\alpha}Al_{2-x}Si_xO_{9+\delta}$ ($x = (\alpha/3 + \delta/2) = 0.5, 1, 1.25$) were synthesized for the first time using direct crystallisation from the melt method by the ADL method. The comprehensive structure investigation on the new orthorhombic compound $Lu_{4-\alpha}Al_{2-x}Si_xO_{9+\delta}$ was studied by synchrotron powder diffraction (SPD), scanning electron microscope (SEM), solid state nuclear magnetic resonance (NMR). The luminescence properties of LuAM $(Lu_4Al_2O_9):Ce^{3+}$, LuASO $(Lu_{3.889}AlSiO_{9.33}):Ce^{3+}$ and LuAM: Eu^{3+}, LuASO: Eu^{3+} phosphors were studied in detail. The elucidation of the correspondence between the crystal structure and the spectral properties of $Lu_4Al_2O_9$ and $Lu_{4-\alpha}Al_{2-x}Si_xO_{9+\delta}$ solid solution holds significant importance for the design, modification and application of a range of $RE_4Al_2O_9$ host materials.

4.2 Synthesis and crystal structure analysis

4.2.1 Synthesis and general structure analysis

The initial approach for synthesizing $Lu_4Al_2O_9$ involved a conventional solid state reaction. However, the XRD pattern depicted in ***Fig 4.2a*** revealed a mixture of $Lu_3Al_5O_{12}$ and Lu_2O_3, instead of the expected monoclinic phase, as reported in the previous studies that $Lu_4Al_2O_9$ to be stable only at high temperatures[8]. Subsequently, a single phase of monoclinic $Lu_4Al_2O_9$ was synthesised using crystallisation from the melt by ADL, as evidenced by the XRD pattern shown ***Fig 4.2b***, which matches well with the reported monoclinic $Lu_4Al_2O_9$ single crystal structure[6]. ***Fig 4.3*** displays the Rietveld refinement profile from SPD data of $Lu_4Al_2O_9$ using the monoclinic $Lu_4Al_2O_9$ structure as the starting model. The refinement results indicate that the main phase fit well with the space group $P2_1/c$ with cell parameters of a = 7.21736(1) Å, b = 10.29742(2) Å, c = 11.03267(3) Å, β = 108.121(1)°, along with a small amount (1.7 wt%) of $LuAlO_3$ as a secondary phase. Detailed refinement structural information can be found in ***Table 4.1***.

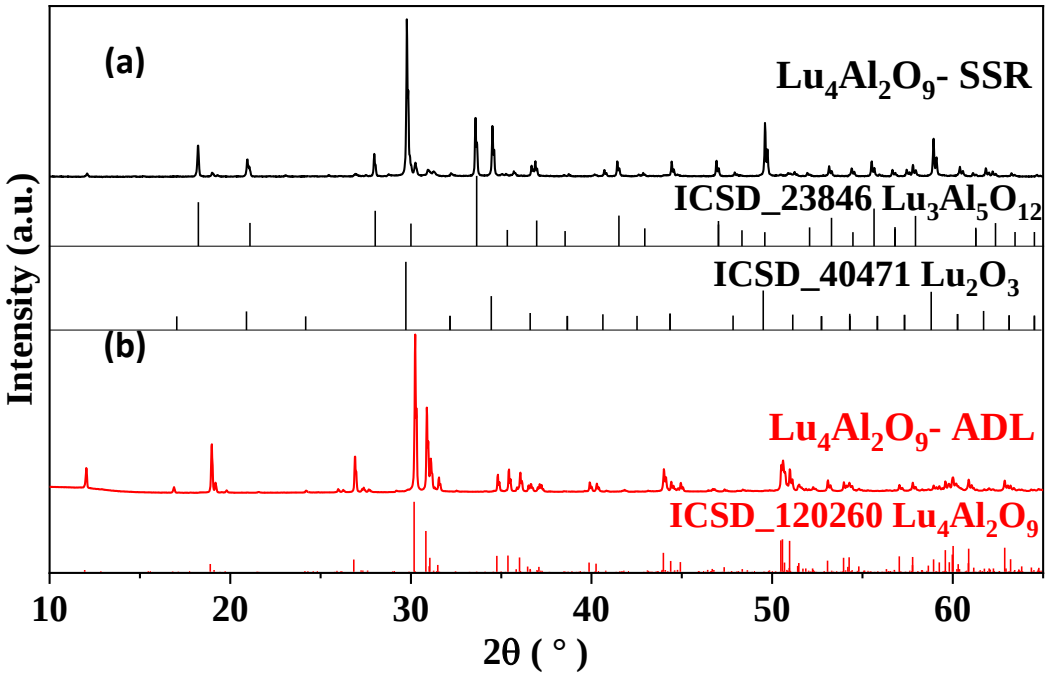

Fig 4.2 *PXRD pattern of $Lu_4Al_2O_9$ synthesized by (a) SSR and (b) ADL method.*

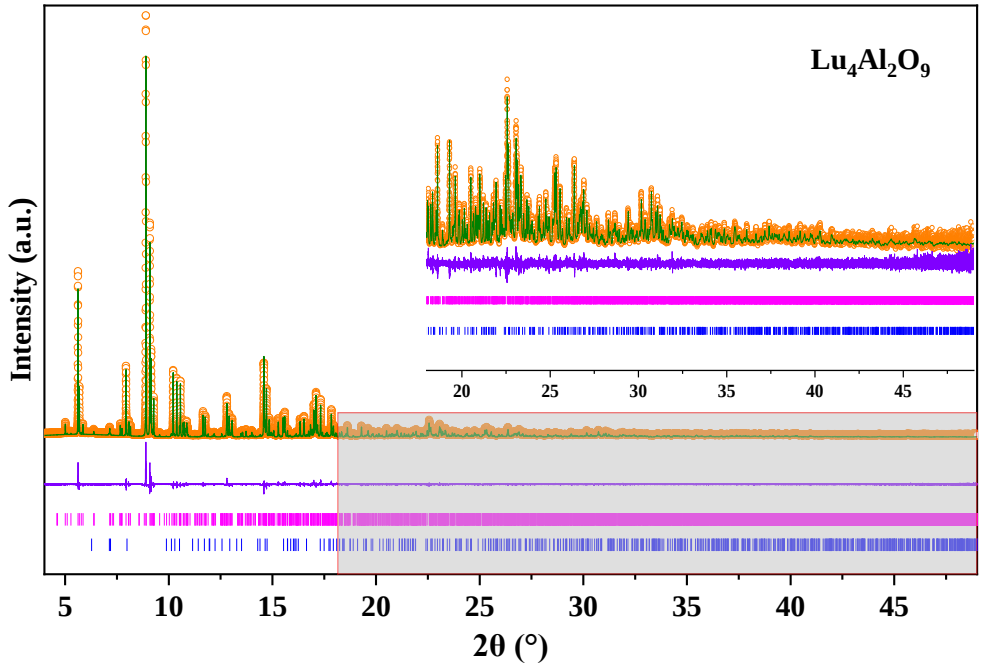

Fig 4.3 *Rietveld refinement SPD patterns of $Lu_4Al_2O_9$ synthesized by ADL (pink marks are $Lu_4Al_2O_9$, blue marks correspond to 1.74(4) wt% $LuAlO_3$).*

Table 4.1 *Structural information from SPD Rietveld refinement result of $Lu_4Al_2O_9$.*

Atom	Site	x	y	z	Occupancy	U_{iso}*100 (Å^2)
Lu1	4e	0.5231(1)	0.11393(8)	0.78434(8)	1	0.43(1)
Lu2	4e	0.0218(1)	0.10129(8)	0.80430(8)	1	0.57(1)
Lu3	4e	0.3420(1)	0.1276(1)	0.44012(9)	1	0.50(1)
Lu4	4e	0.8388(1)	0.1211(1)	0.41689(8)	1	0.47(1)
Al1	4e	0.2145(8)	0.1757(5)	0.1246(5)	1	0.26(1)
Al2	4e	0.6555(8)	0.1699(5)	0.1066(4)	1	0.02(1)
O1	4e	0.809(1)	0.247(1)	0.75515(9)	1	0.71(1)*
O2	4e	0.240(1)	0.247(1)	0.7769(9)	1	0.71(1)*
O3	4e	0.226(1)	0.012(1)	0.158(2)	1	0.71(1)*
O4	4e	0.067(1)	0.222(1)	0.9889(9)	1	0.71(1)*
O5	4e	0.433(1)	0.2447(8)	0.116(1)	1	0.71(1)*
O6	4e	0.630(1)	0.219(1)	0.9607(9)	1	0.71(1)*
O7	4e	0.709(1)	0.011(1)	0.153(1)	1	0.71(1)*
O8	4e	0.2145(8)	0.1757(5)	0.1246(5)	1	0.71(1)*
O9	4e	0.6555(8)	0.1699(5)	0.1066(4)	1	0.71(1)*

**Constrained to the same value*

Lattice parameters:	*Secondary phases:*	*Fitting parameters:*
a = 7.21736(1) Å b = 10.29742(2) Å c = 11.03267(3) Å β = 108.121(1)°	1.74(4) wt% $LuAlO_3$	R_{wp} = 10.04%, Gof = 1.23

For the solid solution of $Lu_4Al_2O_9$ with Si solubility, two different solid solutions can be considered, a $Lu_4Al_{2-x}Si_xO_{9+x/2}$ containing extra O to form AlO_5 corresponding to the reported solid solution compositions of $Gd_4Al_{2-x}Si_xO_{9+x/2}$, or a $Lu_{4-x/3}Al_{2-x}Si_xO_9$ solid solution containing Lu vacancies. The syntheses of the solid solutions $Lu_4Al_{2-x}Si_xO_{9+x/2}$ (x = 0.5) and $Lu_{4-x/3}Al_{2-x}Si_xO_9$ (x = 0.5) were attempted using solid state reactions (SSR) and ADL and the PXRD pattern of the samples were shown in ***Fig 4.4***. PXRD pattern of the two compositions synthesised using SSR (see ***Fig 4.4a*** and ***b***) showed the sample with excess secondary Lu_2O_3 phase and its peak position is not significantly shifted compared to $Lu_4Al_2O_9$. Subsequently two compositions were synthesised by ADL. The XRD pattern of $Lu_4Al_{2-x}Si_xO_{9+x/2}$ (x = 0.5) in ***Fig 4.4c*** reveals excess of 2.3 wt% Lu_2O_3 in the sample. In contrast, $Lu_{4-x/3}Al_{2-x}Si_xO_9$ (x = 0.5) samples were obtained with a single phase, accompanied by a shift of the peak to a lower value of 2θ (see ***Fig 4.4d***). Therefore, solid solutions containing Lu vacancies, denoted by nominal the chemical formula $Lu_{4-x/3}Al_{2-x}Si_xO_9$ rather than $Lu_4Al_{2-x}Si_xO_{9+x/2}$ were considered for further synthesis.

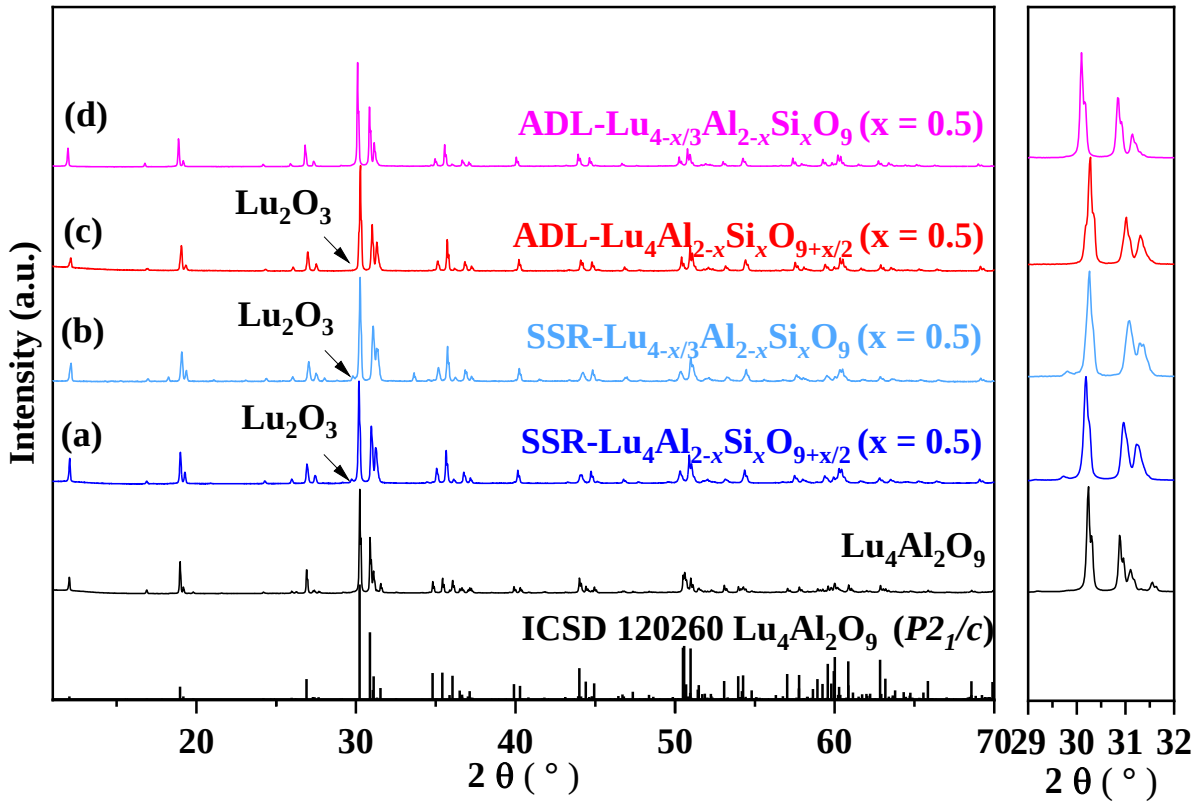

Fig 4.4 *PXRD pattern of $Lu_4Al_{2-x}Si_xO_{9+x/2}$ (x = 0.5) and $Lu_{4-x/3}Al_{2-x}Si_xO_9$ (x = 0.5) synthesized by ADL and SSR.*

The diffraction peaks of the nominal solid solution $Lu_{4-x/3}Al_{2-x}Si_xO_9$ (x = 0.5, 1, 1.25, 1.5) synthesized by ADL are given in ***Fig 4.5*** and generally match well with the $Lu_4Al_2O_9$ $P2_1/c$ phase patterns. However, a closer inspection (see red box in ***Fig 4.5***) reveals that the number of diffraction peaks of $Lu_{4-x/3}Al_{2-x}Si_xO_9$ is significantly reduced compared to that of $Lu_4Al_2O_9$, which may be attributed to the increased symmetry of the crystal structure resulting from Si substitution. Additionally, the gradual broadening and large d-spacing shift of the diffraction peaks are observed with increasing Si substitution, as demonstrated by the enlarged PXRD patterns in the range of 30° to 32° on the right side of ***Fig 4.5***, which are attributed to lattice distortion caused by the disorderly substitution of Si^{4+} for Al^{3+}. Furthermore, the appearance of a secondary phase in the composition with x = 1.5 suggests that the solid solution interval for $Lu_{4-x/3}Al_{2-x}Si_xO_9$ is within $0 \le x \le 1.5$. The fast cooling rate of 1128 $^oCs^{-1}$ (see cooling curve in ***Fig 4.6***) provided by ADL enables the $Lu_4Al_2O_9$ melt to solidify into a monoclinic phase at high temperatures (1600°C) and single-phase $Lu_{4-x/3}Al_{2-x}Si_xO_9$ solid solution were successfully synthesized.

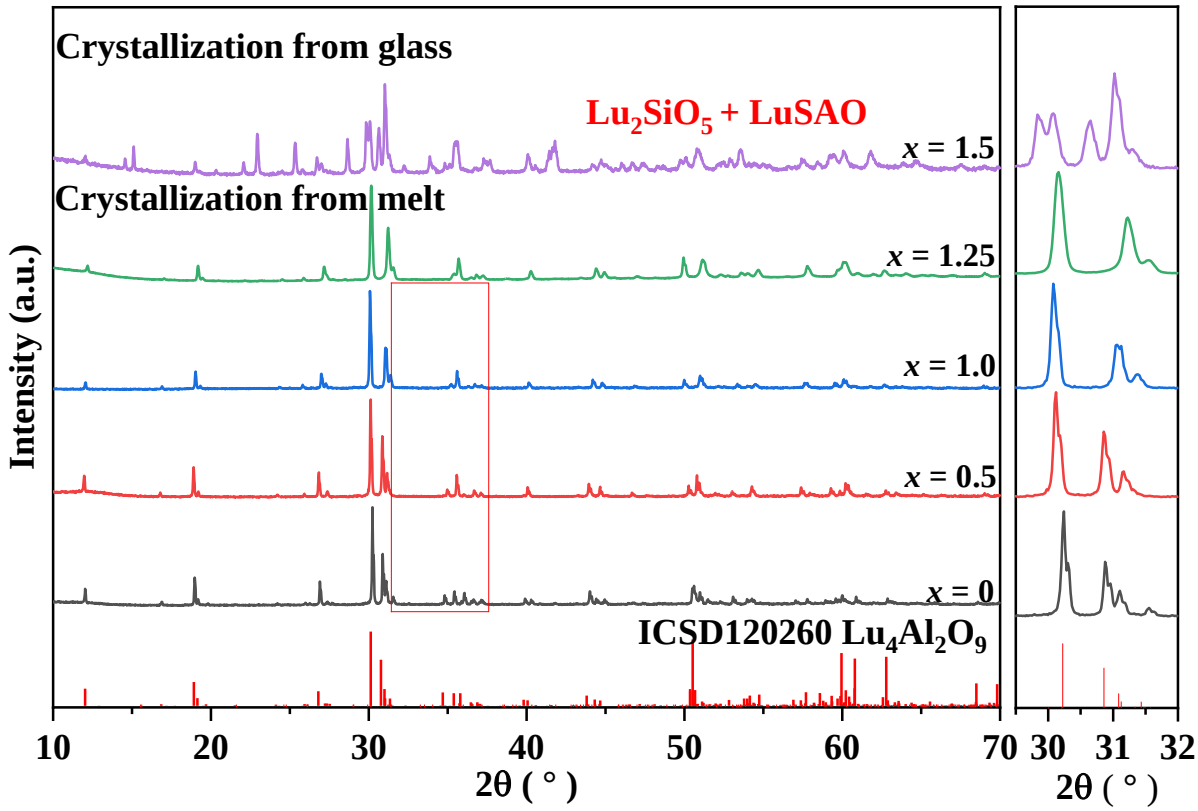

Fig 4.5 *PXRD patterns of the $Lu_{4-x/3}Al_{1-x}Si_xO_9$ (x = 0.5, 1, 1.25, 1.5) synthesized by ADL.*

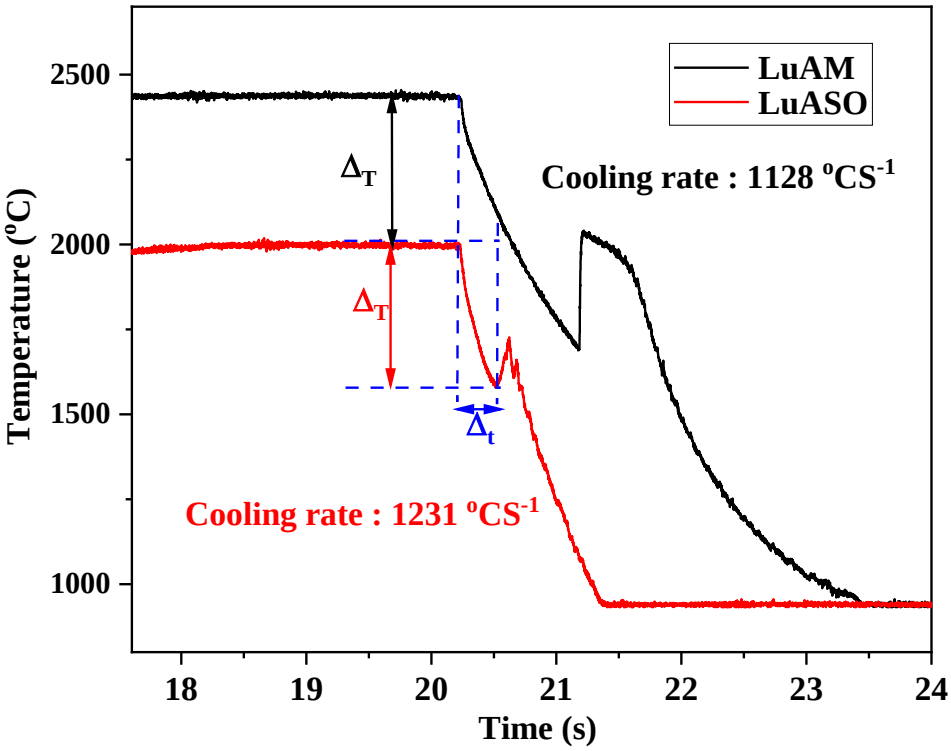

Fig 4.6 *Cooling curves of LuAM (black) and LuASO (red) melt levitated by oxygen.*

4.2.2 Structural evolution from monoclinic to orthorhombic structure

A thorough comparison of higher resolution SPD data for $Lu_4Al_2O_9$ (x = 0) and nominal composition $Lu_{3.667}AlSiO_9$ (x = 1) shows $Lu_{3.667}AlSiO_9$ has significantly fewer Bragg peaks than $Lu_4Al_2O_9$, and they can be fully indexed to an orthorhombic unit cell—(see ***Fig 4.7*** enlargement, red box). Through the indexation process using the SPD of $Lu_{4-x/3}Al_{2-x}Si_xO_9$ (x = 0.5) composition, its space group was determined to be *Pbnm*, and a structural model containing –Lu vacancies was established via JANA[18].

To determine the solid solution structure, SPD Rietveld refinement data were compared using $P2_1/c$ and *Pbnm* space groups as starting models, respectively. Firstly, the refinement unit cell parameters of $Lu_{4-x/3}Al_{2-x}Si_xO_9$ (x = 0, 0.5, 1, 1.25) using $P2_1/c$ as the starting structural model as shown in ***Fig 4.8a*** indicated a sudden increase in *c* and β angle at x = 0.5, while a gradual decrease in cell volume corresponds to the substitution of smaller radii of Si for Al. These findings suggest a potential phase transition upon Si^{4+} replacing Al^{3+}. Furthermore, the unit cell parameters associated with the orthorhombic phase (as depicted in ***Fig 4.8b***) can be derived from the symmetry of the monoclinic crystal structure through

the following transformation using Bilbao crystallographic server[19], indicating a phase transition from monoclinic to orthorhombic upon the substitution of Si^{4+} for Al^{3+} in $Lu_4Al_2O_9$.

$$\begin{pmatrix} a \\ b \\ c \end{pmatrix} = \begin{pmatrix} 100 \\ 010 \\ 102 \end{pmatrix} \begin{pmatrix} a_m \\ b_m \\ c_m \end{pmatrix}$$

Fig 4.8c illustrates the unit cell parameters of $Lu_{4-x/3}Al_{2-x}Si_xO_9$ (x = 0, 0.5, 1, 1.25) obtained through refinement using *Pbnm* as the structural model, consistent with the results derived from the monoclinic phase transition. Detailed structural parameters of $Lu_{3.667}AlSiO_9$ refined using *Pbnm* as the structural model are listed in ***Table E.1.1***. Better matching of peaks number with *Pbnm* as the refinement model compared to *$P2_1/c$* (see ***Fig 4.9*** SPD Rietveld refinement profile) and better refinement parameters (***Table 4.2***) suggest that *Pbnm* should be considered as the crystal structure of the $Lu_{4-x/3}Al_{2-x}Si_xO_9$ solid solution.

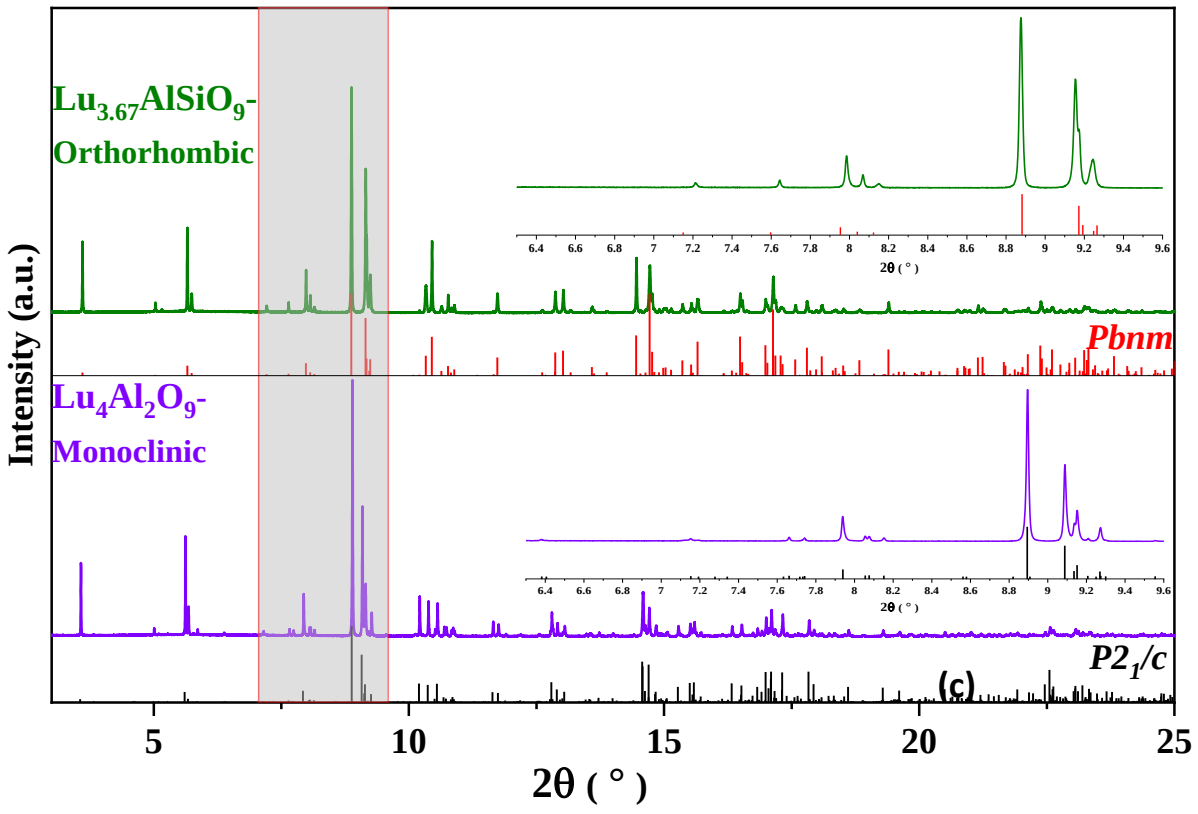

Fig 4.7 *(a) SPD patterns comparison of $Lu_4Al_2O_9$ (x = 0) and $Lu_{3.66}AlSiO_9$ (x = 1)*

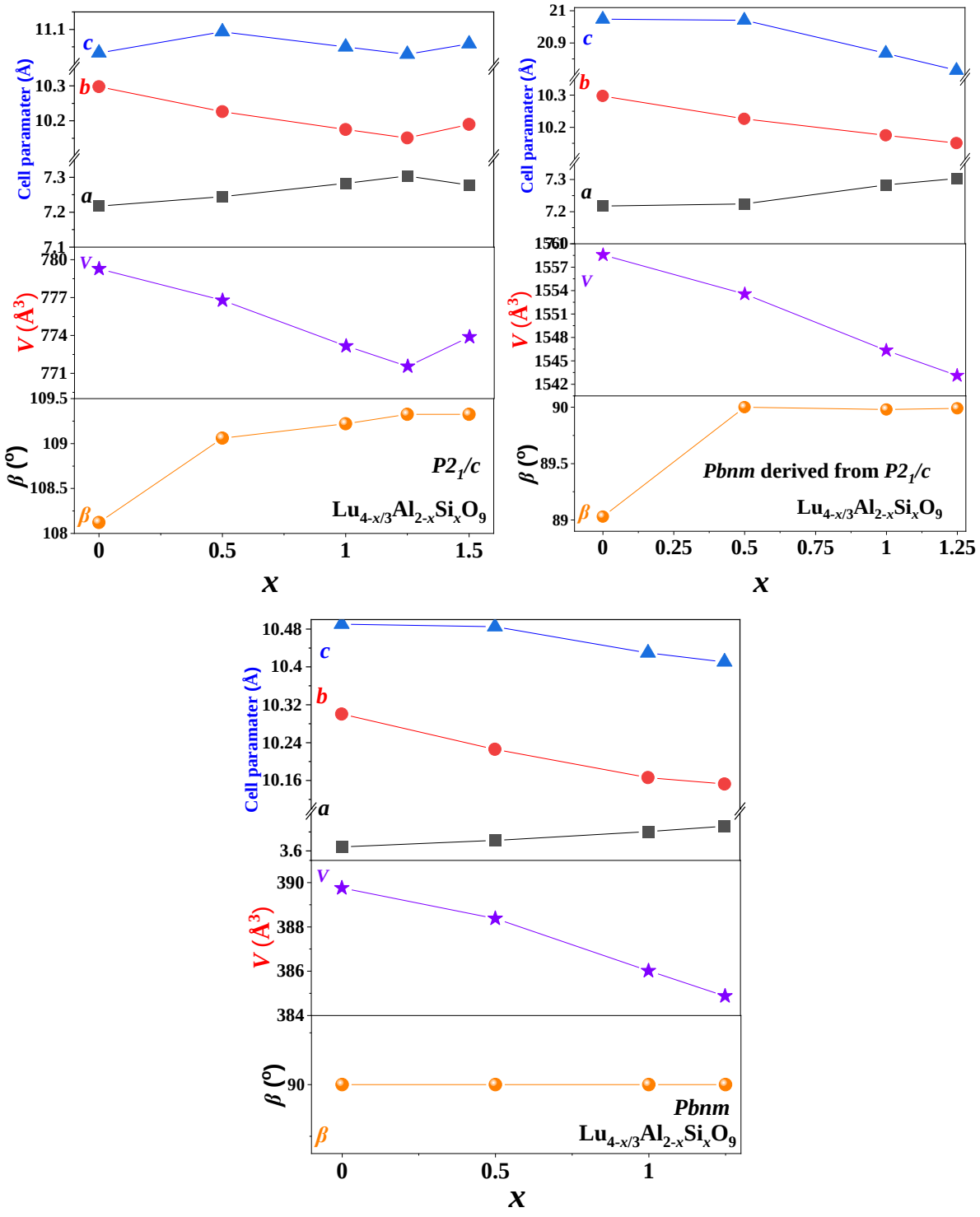

Fig 4.8 *(a) Unit cell parameters of $Lu_{4-x/3}Al_{2-x}Si_xO_9$ ($0 \le x \le 1.5$) solid solution obtained (a) by PXRD refinement using $P2_1/c$ as the structural model, (b) transform of the monoclinic cell from PXRD refinement by Bilbao crystallographic server[19], (c) by PXRD refinement using Pbnm as the structural model .*

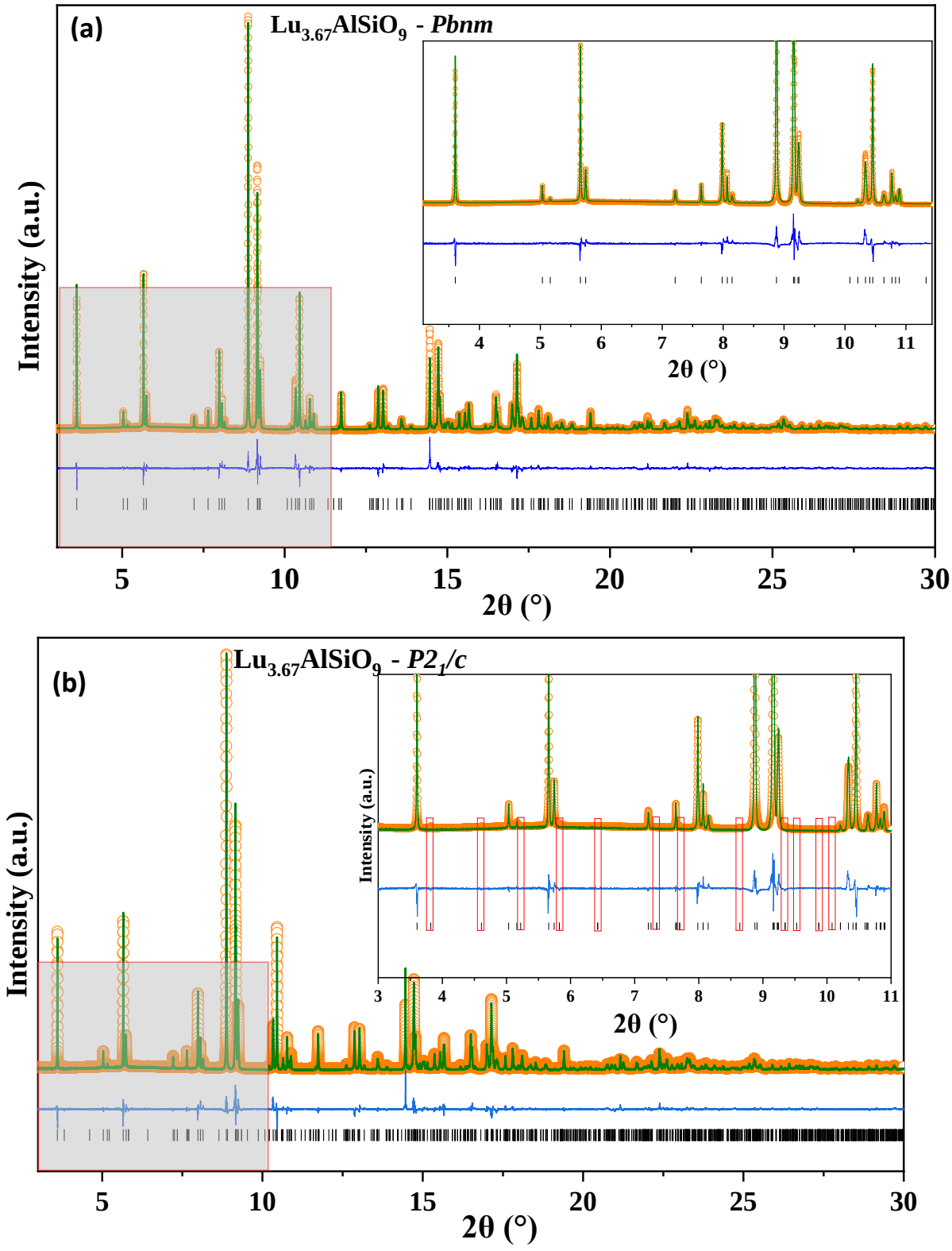

Fig 4.9 *Comparison of $Lu_{3.67}AlSiO_9$ SPD refinement profiles with two different structural models. (a) Pbnm, the enlarge image from 3 to 11° shows that each peak is able to match the Pbnm peak exactly (R_{wp} = 11.39%, Gof = 1.55). (b) $P2_1/c$, missing peaks (marked in red boxes) in observed peaks compared to the peaks of $P2_1/c$. (R_{wp} = 11.43%, Gof = 1.56)*

Table 4.2 *Unit cell parameters and refinement parameters of $Lu_{3.667}SiAlO_9$ from SPD refinement with $P2_1/c$ and Pbnm as structural model.*

Composition	Model	Cell parameter (Å)	R_{wp}%	GOF
$Lu_{3.667}AlSiO_9$	$P2_1/c$	a = 7.28264(4) b = 10.17473(7) c = 11.04972(6) β = 109.2281(8)	11.43%	1.56
$Lu_{3.667}AlSiO_9$	*Pbnm*	a = 10.43294(4) b = 10.17436(5) c = 3.64122(1)	11.39%	1.55

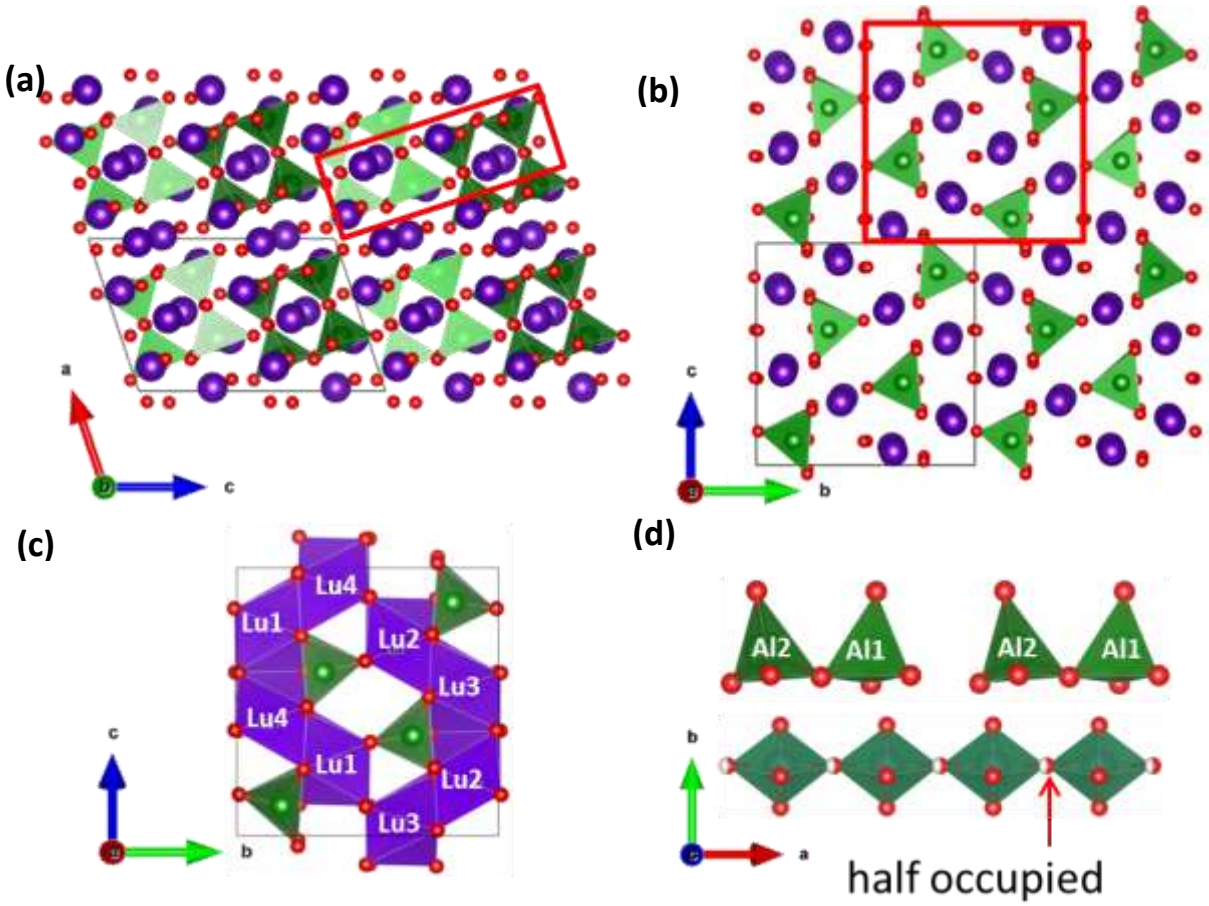

Fig 4.10 *Crystal structures of monoclinic $Lu_4Al_2O_9$ (black box) and orthorhombic $Lu_{3.67}SiAlO_9$ (red box) along the (a) b-axis and (b) a-axis. (c) The Lu centered polyhedra and Al_2O_7 ditetrahedra viewed along the a axis. (d) Al_2O_7 ditetrahedra chain (upper) in monoclinic $Lu_4Al_2O_9$ and Al/SiO_4 chain in $Lu_{3.67}AlSiO_{9.33}$.*

A crystal structure diagram of monoclinic $Lu_4Al_2O_9$ and the orthogonal phase structure of $Lu_{3.667}AlSiO_9$ derived from monoclinic are shown in ***Fig 4.10a*** (along *b* axis) and ***Fig 4.10b*** (along *a* axis). The monoclinic $Lu_4Al_2O_9$ structure (black box) comprises four Lu sites coordinated with six or seven oxygen ions (***Fig 4.10c*** along a axis) and two Al tetrahedra linked by a shared O5 atom, form an Al_2O_7 dimeric oxyaluminate group (see ***Fig 4.10d*** upper). For the solid solution $Lu_{4-3/x}Al_{1-x}Si_xO_9$ structure (red box), $Lu1O_6$ and $Lu2O_7$ are linked together by sharing an edge, and two adjacent Al/Si tetrahedra share an O, forming an Al/Si tetrahedral chain (see ***Fig 4.10d*** lower).

4.2.3 Substitution of Al by Si analysis by ^{27}Al and ^{29}Si solid-state NMR

4.2.3.1 ^{27}Al-NMR

Solid state NMR spectroscopy was employed to further investigate the local ordering in the Si/Al framework and elucidate the structural evolution, as display in ***Fig 4.11***. The ^{27}Al NMR spectrum of $Lu_4Al_2O_9$ (see black curve in ***Fig 4.11a***) exhibits a perfect fit with two resonance peaks at 50 and 70 ppm. Quantification results (see ***Fig E.2.1***) indicated an equal distribution of 50% for each of the two [AlO_4] peaks, corresponding to the two distinct tetrahedral [AlO_4] sites in the monoclinic phase. However, in the NMR spectrum of the $Lu_{3.667}AlSiO_9$ (x = 1) compound (see blue curves ***Fig 4.11a***), two peaks at 65 and 35 ppm were observed, corresponding to [AlO_4] and [AlO_5] polyhedra with an approximate content ratio of 1:2, which is inconsistent with the designed solid solution with Lu vacancies in the form of $Lu_{4-x/3}Al_{2-x}Si_xO_9$. The presence of the [$AlO_5$] coordination polyhedra suggests the presence of extra oxygen in the structure, indicating that the designed composition deviates from the experimentally obtained composition. SEM composition analysis confirmed the presence of a significant amount of Si-rich amorphous phase in the $Lu_{3.667}AlSiO_9$ sample, and the primary phase composition was identified at 20 points as $Lu_{3.735}Al_{1.04}Si_{0.96}O_{9.0815}$ (see ***Fig E.2.2a*** and ***Table E.2.1***), revealing that $Lu_{3.667}AlSiO_9$ is not the correct solid solution composition.

The correct solid solution composition is difficult to predict because the ratio of Lu vacancies to additional oxygen cannot be determined. Therefore, quantitative analysis of the ^{27}Al NMR spectra of $Lu_4Al_{2-x}Si_xO_{9+x/2}$ (x = 1) (a mixture of solid solution and excess Lu_2O_3)

shown in ***Fig 4.11a*** (blue curve) determined the ratio of AlO_4/AlO_5. The derived ratios allow to calculate the maximum amount of extra oxygen δ can be formed in the solid solution (Si = 1). If this amount is not sufficient to fully compensate for the charge introduced by Si substitution, it must be compensated by α ($3\alpha + 2\delta = 1$) Lu vacancies.

The composition $Lu_{3.89}AlSiO_{9.33}$ (x = 1, δ = 0.33, α = 0.11) calculated from the derived 1:2 ratios of the $[AlO_4]$ and $[AlO_5]$ polyhedra by using the NMR quantification results (see ***Fig 4.11b***) was successful synthesized as a single phase, which was confirmed by XRD (see ***Fig E.2.3***) and SEM analysis (see ***Fig E.2.2b***). The high-resolution SDP refinement results are listed in ***Table E.1.2***, and the profile is shown in ***Fig E.1.1.*** In addition, the consistency between the NMR spectrum of the nominal compositions $Lu_{3.89}AlSiO_{9.33}$ (green curves in **Fig 4.11a**) and $Lu_4AlSiO_{9.5}$ (blue curves in **Fig 4.11a**) confirms the right composition of solid solution. Furthermore, the NMR spectrum of amorphous in the $Lu_{3.667}AlSiO_9$ composition (yellow curve in **Fig 4.11a**) indicates that the presence of $[AlO_5]$ is not attributed to the Si-rich amorphous phase (inferred by comparision with a $Lu_{3.667}AlSiO_9$ glass sample synthesised by ADL).

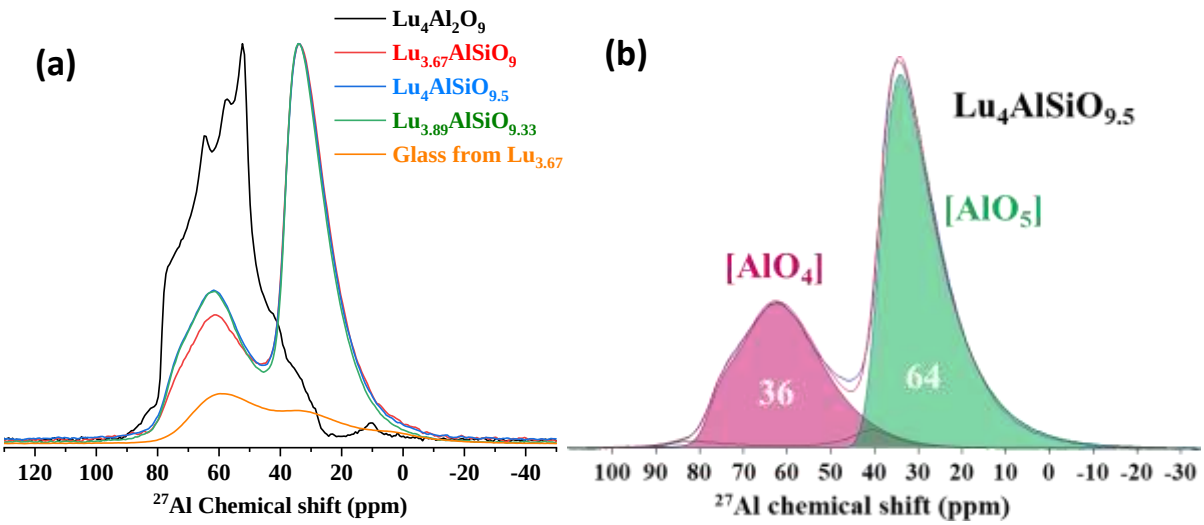

Fig 4.11 *(a) ^{27}Al NMR spectrum of $Lu_4Al_2O_9$ (black line), $Lu_{3.67}AlSiO_9$ (red line), $Lu_4AlSiO_{9.5}$ (blue line), $Lu_{3.89}AlSiO_{9.33}$ (green line), and glass phase in $Lu_{3.67}AlSiO_9$ composition (yellow line). (b) Quantitative fitted NMR spectrum for $Lu_4AlSiO_{9.5}$. (peak integration $[AlO_5]$: $[AlO_4]$ = 64 : 36).*

Similarly, solid solution compositions of $Lu_4Al_{1.5}Si_{0.5}O_{9.25}$ (x = 0.5) and $Lu_{3.78}Al_{0.75}Si_{1.25}O_{9.293}$ (x = 1.25) were determined based on the ^{27}Al NMR spectrum of

$Lu_4Al_{1.5}Si_{0.5}O_{9.25}$ and $Lu_4Al_{0.75}Si_{1.25}O_{9.625}$ (see ***Fig 4.12a*** and ***4.12c***). The SEM composition analysis of $Lu_4Al_{1.5}Si_{0.5}O_{9.25}$ (x = 0.5) displayed in ***Fig E.2.4a*** indicates that the composition of solid solution is $Lu_4Al_{1.5}Si_{0.5}O_{9.25}$ but contains a small amount of the Al_2O_3-$LuAlO_3$ amorphous phase (see ***Table E.2.3***). This result is similar to the previously reported results for $Y_4Al_{1.5}Si_{0.5}O_{9.25}$ and $Gd_4Al_{1.5}Si_{0.5}O_{9.25}$ [10-11-13]. In the case of $Lu_{3.78}Al_{0.75}Si_{1.25}O_{9.293}$ (x = 1.25), even though the composition was determined by NMR (see ***Fig 4.12c***), the SEM results displayed in ***Fig E.2.4b*** indicated that the compound is a mixture of two solid solutions with different Al/Si ratios (major phase: $Lu_{3.76(2)}Al_{0.75(9)}Si_{0.88(1)}O$ and minor phase: $Lu_{3.47(2)}Al_{0.75(1)}Si_{0.96(1)}O$) and Si-rich amorphous phase see ***Table E.2.3***), which suggests that the composition with x = 1.25 lies outside the solid solution range.

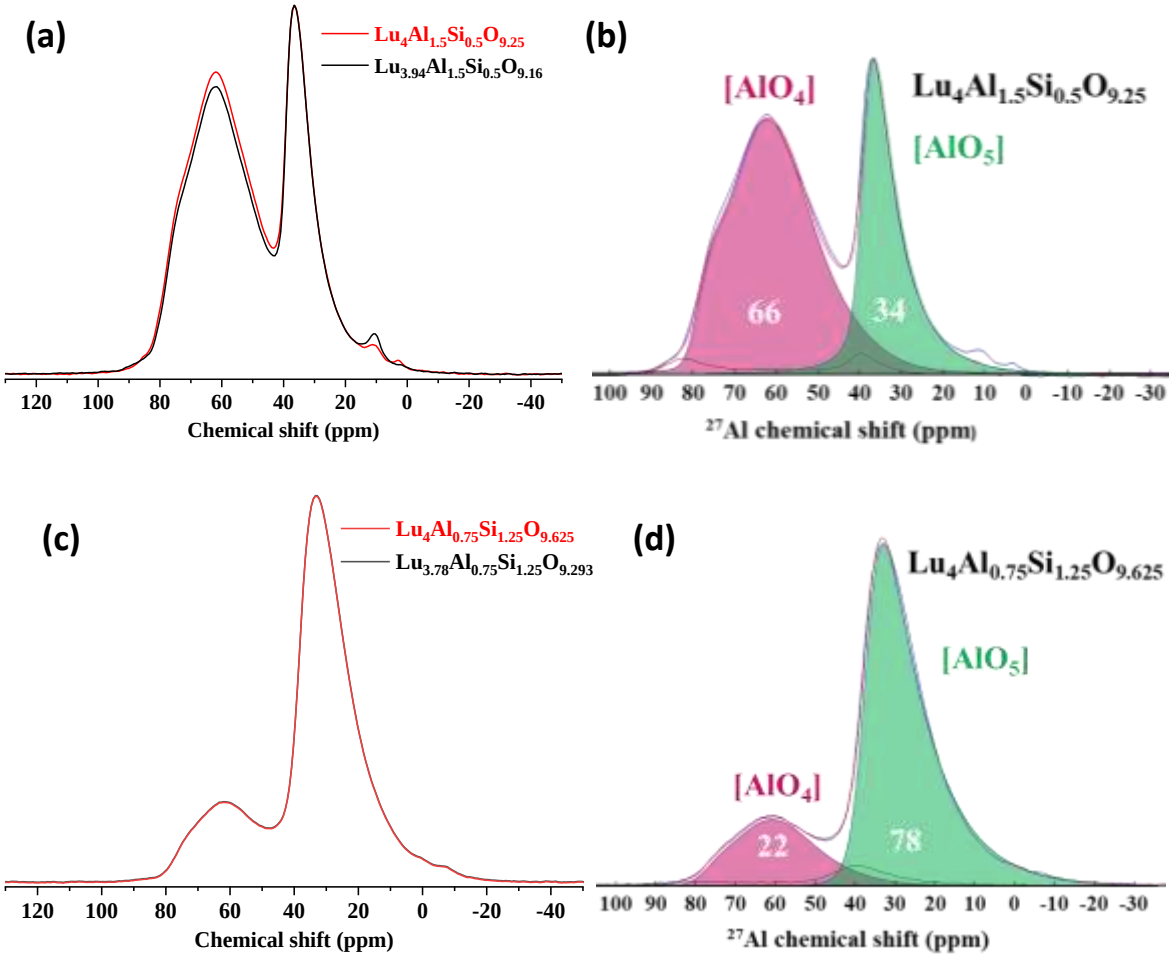

Fig 4.12 *(a) ^{27}Al NMR spectrum of $Lu_4Al_{1.5}Si_{0.5}O_{9.25}$ and $Lu_{3.94}Al_{1.5}Si_{0.5}O_{9.167}$. (b) ^{27}Al NMR fitted spectrum of $Lu_4AlSiO_{9.5}$ ($[AlO_5]$: $[AlO_4]$ = 34 : 66). (c) ^{27}Al NMR spectrum of $Lu_4Al_{0.75}Si_{1.25}O_{9.625}$ and $Lu_{3.86}Al_{0.75}Si_{1.25}O_{9.415}$. (d) ^{27}Al NMR fitted spectrum of $Lu_{3.94}Al_{1.5}Si_{0.5}O_{9.167}$ (peak integration $[AlO_5]$: $[AlO_4]$ = 78 : 22).*

A comparison of the NMR spectra of the two solid solutions at x = 0.5 and x = 1, as shown in ***Fig 4.13***, reveals a gradual increase in the proportion of [AlO_5] as Si^{4+} replaces Al^{3+} in the structure (see ***Fig 4.13b***). This observation can be attributed to the preference for the formation of [AlO_5] to maintain charge balance upon Si substitution. Furthermore, the NMR quantification results for x = 1 indicate that the formation of up to 66% [AlO_5] (corresponding to δ = 0.33) is possible, with the remaining charge compensation achieved through the creation of Lu vacancies. It can therefore be concluded that the substitution of Si^{4+} for Al^{3+} results in the formation of a solid solution $Lu_4Al_{2-x}Si_xO_{9+x/2}$ with a solid solution range of x = 0 - 0.66. This finding is consistent with previously reported on $Gd_4Al_{2-x}Si_xO_{9+x/2}$ (x = 0 - 0.6). However, it was found that when Si substitution (x) exceeds 0.66, a solid solution with coexistence of Lu vacancies and extra oxygen is formed, as indicated by the chemical formula $Lu_{4-(x-0.66)/3}Al_{2-x}Si_xO_{9.33}$. Solid solutions of $Y_{3.89}AlSiO_{9.33}$ and $Gd_{3.89}AlSiO_{9.33}$ were successfully synthesized, which were confirmed as single phase by XRD pattern (see ***Fig E.2.5***). Further investigations involving SEM and Al NMR spectroscopy will be conducted to gain additional insights into these materials.

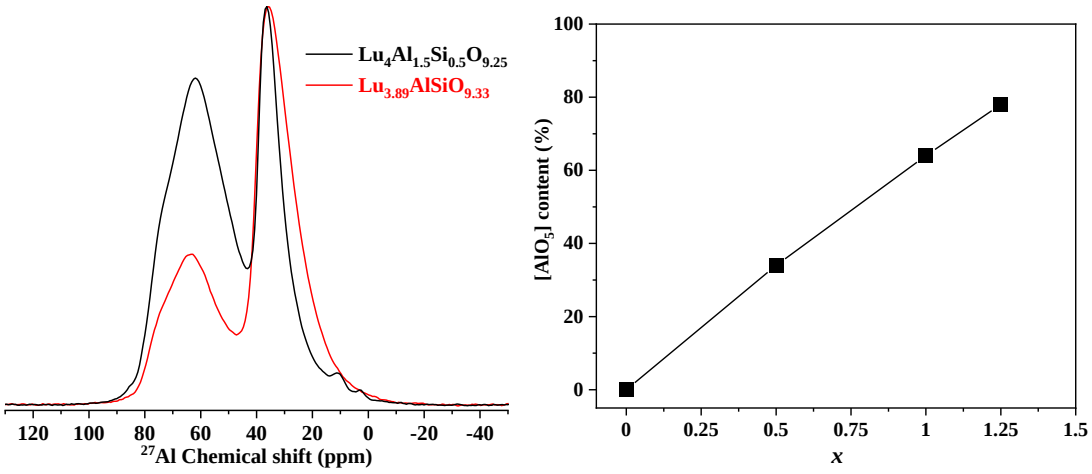

Fig 4.13 *^{27}Al NMR spectrum of $Lu_4Al_{1.5}Si_{0.5}O_{9.25}$ (black curve) and $Lu_{3.89}AlSiO_{9.33}$ (red curve). (b)* [AlO_5] *content as a function of x.*

4.3.3.2 ^{29}Si NMR

Whilst 5-coordinate Al is observed by ^{27}Al NMR in $Lu_{3.89}AlSiO_{9.33}$, Si shows a very strong preference for 4-coordination in ambient-pressure silicates. This implies that Al and Si should

not be distributed randomly in the structural chains. In order to further determine the local arrangements in the $[SiO_4]/[AlO_4]/[AlO_5]$ chains in the $Lu_{3.89}AlSiO_{9.33}$ solid solution, investigations were conducted using ^{29}Si NMR spectra as well as computational spectra of possible structural configuration. ***Fig 4.14*** shows the ^{29} Si NMR spectrum of $Lu_{3.89}AlSiO_{9.33}$, wherein the peak at -76ppm corresponds to the $[SiO_4]$ tetrahedra with Q1 connectivity. This corresponds to the majority of the sample and suggests that the $[SiO_4]$ units terminate the aluminosilicate chains. However, a weak unknown peak at -127 ppm is also observed. The ^{29}Si NMR spectrum of amorphous in $Lu_{3.89}AlSiO_{9.33}$ in ***Fig E.2.6*** indicates that this unknown peak is not derived from the impurity phase. To determine the unknown peak, 2D ^{29}Si NMR spectra and simulations NMR spectra of several possible structural models were performed further (see ***Fig 4.15***) using DFT. These ongoing studies aim to provide a comprehensive understanding of the structural and the arrangement of Si/Al polyhedra chains of $Lu_{3.89}AlSiO_{9.33}$ solid solution.

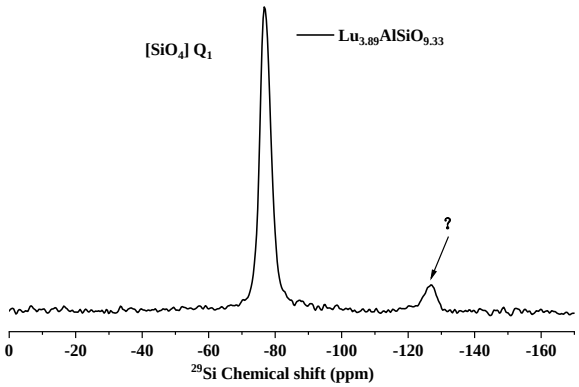

Fig 4.14 *^{29}Si NMR spectrum of $Lu_{3.89}AlSiO_{9.33}$.(? is unknown peak that needs further determination)*

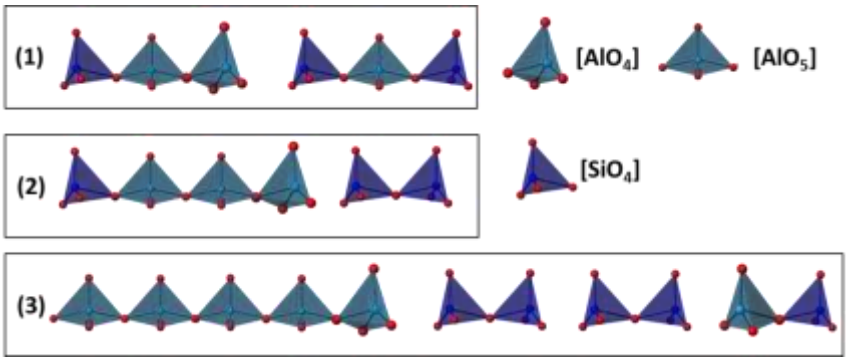

Fig 4.15 *Three possible arrangements of polyhedral chains in $Lu_{3.89}AlSiO_{9.33}$ with $[SiO_4]$ in different chain-terminating configurations.*

4.3 Thermal stability and phase transition

To clarify the thermal stability of $Lu_4Al_2O_9$ and to elucidate if it undergoes a reversible phase transition from monoclinic to orthorhombic at high temperatures, similar to what has been reported for $Gd_4Al_2O_9$[20] and $Y_4Al_2O_9$[21], DSC measurements and variable temperature XRD were conducted, as depicted in ***Fig 4.16*** and ***Fig 4.17***. DSC curves were measured for monoclinic $Lu_4Al_2O_9$ from room temperature up to 1400°C are shown in ***Fig 4.16a***. An exothermic peak at 1341°C during heating and an exothermic peak at 1500°C during cooling were observed, indicating a reversible phase transition with a hysteresis at high temperature in $Lu_4Al_2O_9$. However, the XRD pattern of the sample after the 1400° DSC test showed partial decomposition of the sample to Lu_2O_3 and $Lu_3Al_5O_2$ (see XRD pattern shown in ***Fig 4.16b*** red line), which indicates that $Lu_4Al_2O_9$ decomposed before 1400°C.

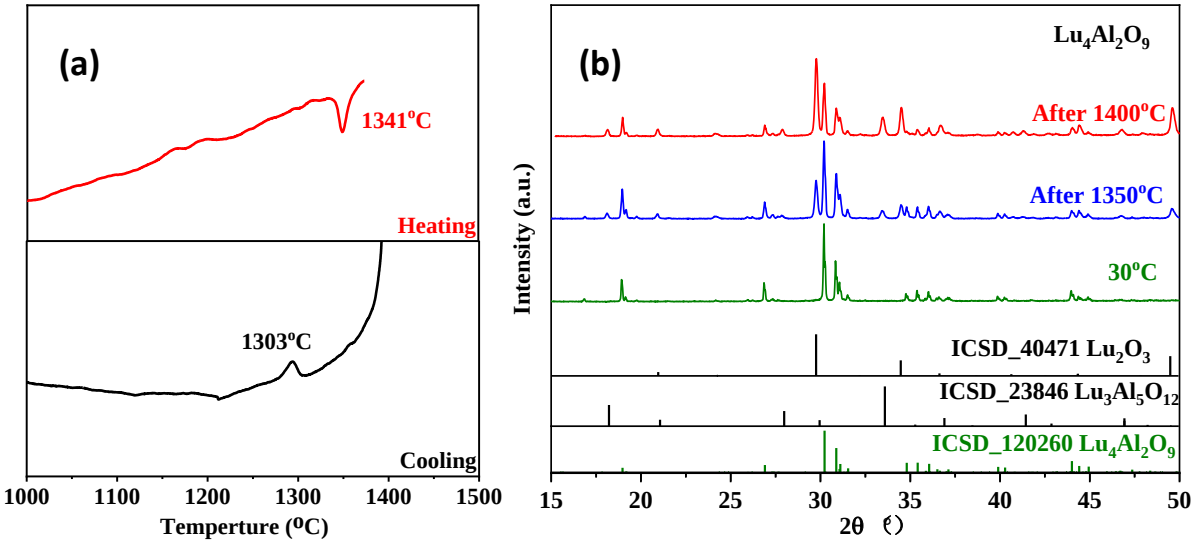

Fig 4.16 *(a) DSC curve of $Lu_4Al_2O_9$ collected in air at a heating rate of 10°C/min from room temperature to 1400°C (heating process in upper, cooling process in lower). (b) PXRD pattern of the $Lu_4Al_2O_9$ after DSC measurement.*

Additionally, the VT- XRD pattern of $Lu_4Al_2O_9$ (with 3.2 wt% secondary phase of Lu_2O_3) in ***Fig 4.17a*** demonstrated similar phase transition behaviour. During heating, the main peak shifts to low angle with increasing temperature up to 1250°C (consistent with thermal expansion of the lattice), but abruptly shifts to higher angle at 1300° (orange box) and gradually begins to decompose into Lu_2O_3 (purple line) and $Lu_3Al_5O_2$ (blue line). The

corresponding variation in unit cell parameters are shown in ***Fig 4.17b*** demonstrating an expansion of the cell parameter *V* as the temperature rises to 1250°C, followed by a sudden drop at 1300°C, which indicates that a phase transition occurs at 1300°C. During cooling, the main peak of the small amount of incompletely decomposed $Lu_4Al_2O_9$ shifts to higher angle as the temperature decreased, but suddenly shifts to lower angle at 1250°C (green box), indicating a sudden expansion of the unit cell, which echoed to the DSC results.

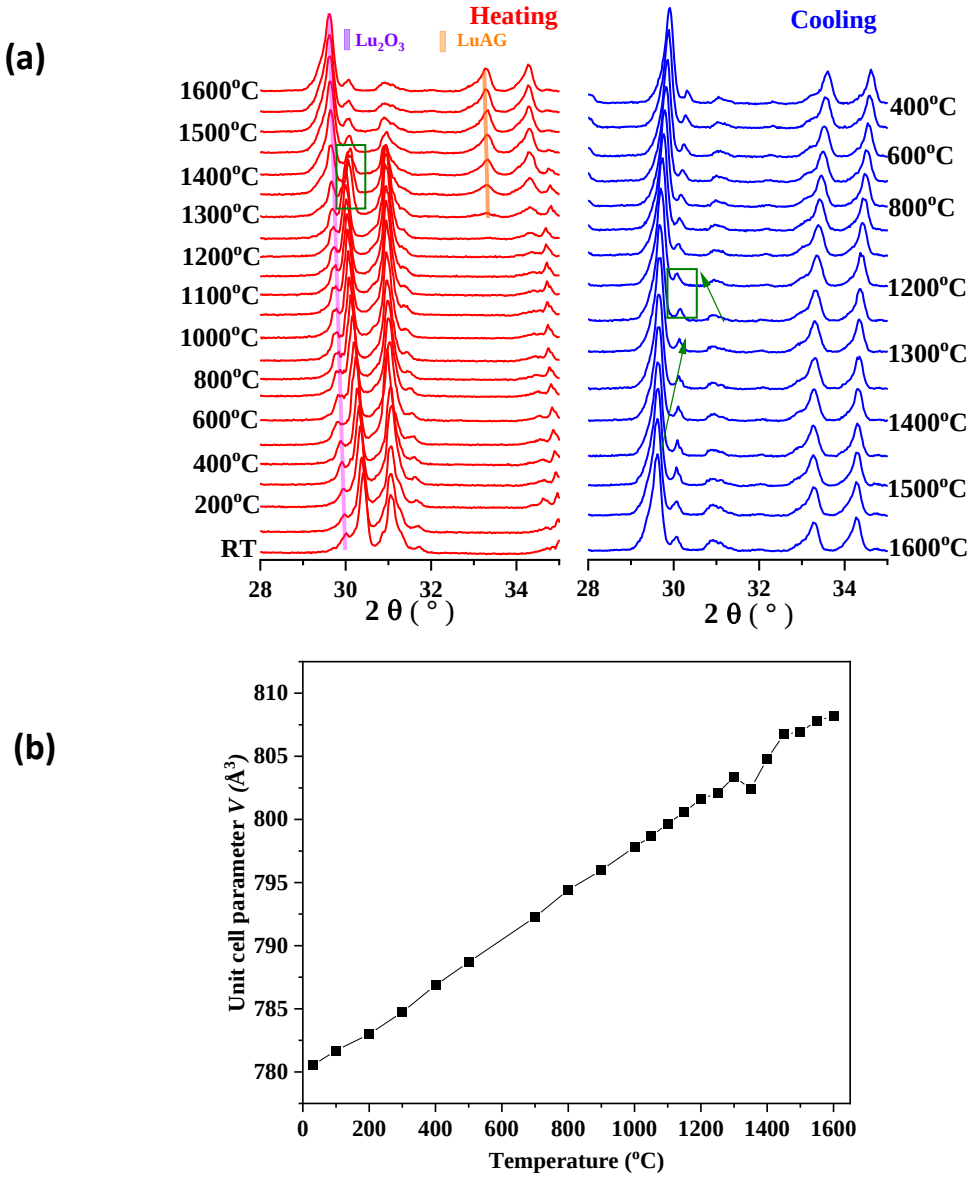

Fig 4.17 *(a) VT-X-ray diffraction peaks from 15°- 70° of $Lu_4Al_2O_9$ collected from room temperature to 1600°C (heating process in left, cooling process in right). The purple mark is second phase of Lu_2O_3, green marker is $Lu_3Al_5O_{12}$ garnet phase. (b) Lattice parameter V of $Lu_4Al_2O_9$ from VT-XRD data refinement.*

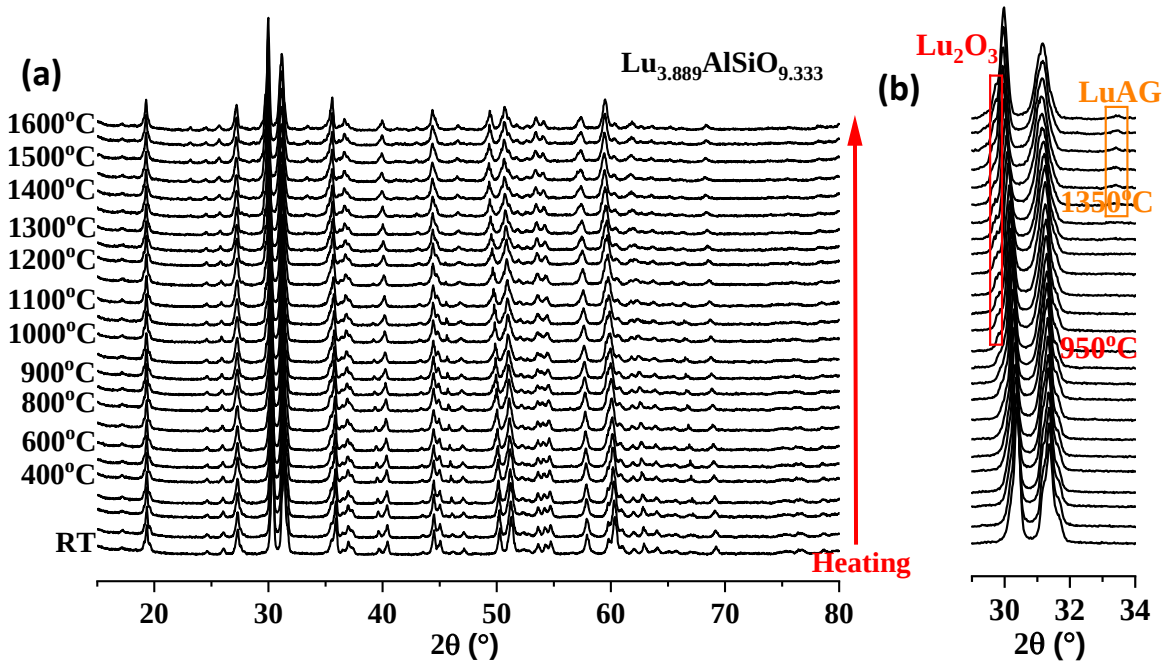

Fig 4.18 (a) *VT-XRD pattern from 15°- 70° and (b) 29°-34° enlarged view of $Lu_{3.889}AlSiO_{9.33}$ collected from room temperature to 1600°C.*

At the same time, VT-XRD measurements were carried out on $Lu_{3.889}AlSiO_{9.33}$ from room temperature to 1600 °C, as shown in ***Fig 4.18a.*** Careful observation (see ***Fig 4.18b***) revealed the appearance of Lu_2O_3 peaks starting at 950 °C and LuAG peaks at 1350°C, suggesting that the compound may decompose into Lu_2O_3 and Lu(Al/Si)G garnet at high temperatures. In addition the result of SEM shows that the compound contains a small amount of amorphous secondary phase, and these diffraction peaks appearing at high temperatures may be attributed to the secondary crystalline phase. The VT-XRD data refinement results show that the content of Lu_2O_3 does not increase with increasing temperature which suggests that the phase appearing at high temperatures originates from the amorphous second phase.

4.4 Homogeneity analysis by microprobe

To further complement the compositional results of the SEM-EDS analyses, and to know the homogeneity of the samples as well as the distribution of the dopant elements, high-precision microprobes were performed. A large number of cracks can be observed and

the mapping of Al and Lu indicates homogeneity of the LuAM: 2%Ce^{3+}sample (see ***Fig 4.19)*** However, for small amounts of doped Ce, it tends to accumulate at the cracks. A total of 47 collection points were used for the compositional analysis and the average compositions listed in ***Table 4.3.*** This shows that the content of Ce is less than the theoretical value due to the aggregation of Ce at the cracks. The electron microprobe elemental mapping of the LuAM: 2%Ce^{3+} sample shown in ***Fig. 4.20*** indicates that the sample contains a Si rich secondary phase ($Lu_{2.2(4)}Al_{1.00(9)}Si_{2.23(2)}O_{9.38(6)}$), which is consistent with the SEM results. In addition, it can be observed form the mapping of Al that the samples are not very homogeneous. Ce is favoured to be distributed in the secondary phase. The compositional analyses listed in ***Table 4.3*** show that Si and Ce deviate from the theoretical values due to the formation of a Si rich secondary phase with aggregation of Ce.

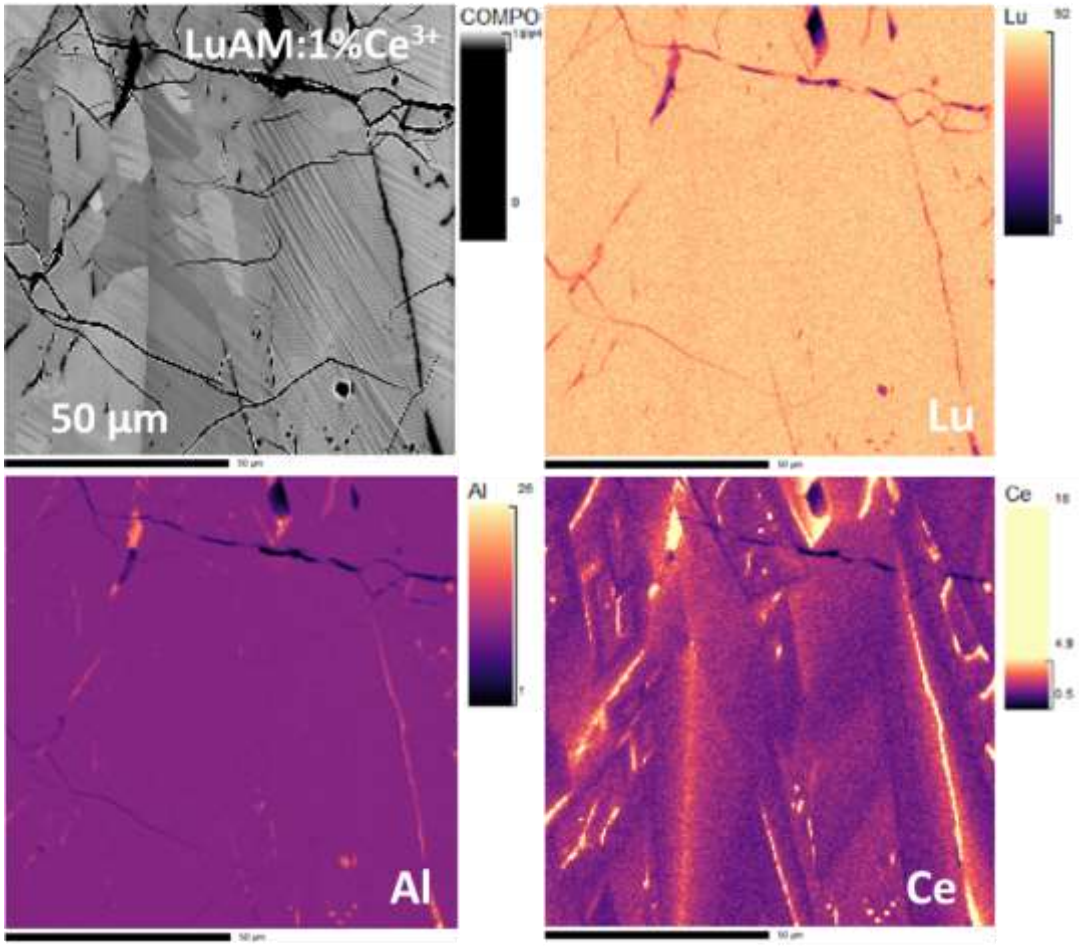

Fig 4.19 *Electron microprobe elemental mapping of LuAM:2%Ce^{3+}*

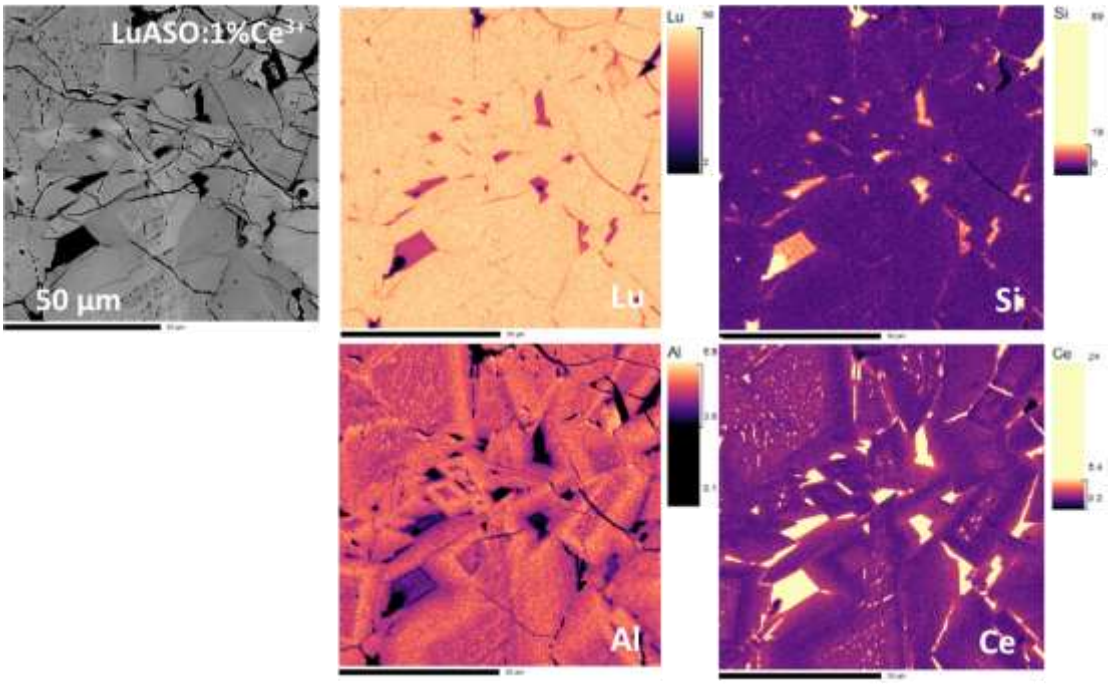

Fig 4.20 *Electron microprobe elemental mapping of LuASO:2%Ce^{3+}*

Table 4.3 *Composition analysis of LuAM:2%Ce^{3} and LuASO:2%Ce^{3+} by electron microprobe measurements.*

Sample	Experimental composition	Theoretical composition
LuAM:2%Ce^{3+}	$Lu_{3.8(2)}Ce_{0.035(3)}Al_2O_9$	$Lu_{3.92}Ce_{0.08}Al_2O_9$
LuASO:2%Ce^{3+}	$Lu_{3.8(2)}Ce_{0.06(2)}AlSi_{0.93(7)}O_y$	$Lu_{3.8089}Ce_{0.08}AlSiO_{9.33}$

4.5 Luminescence properties

The substitution of Si^{4+} for Al^{3+} in LuAM leads to an increase in crystal symmetry from monoclinic to orthorhombic. This change in crystal symmetry results in the dopant ions being located in different local symmetry sites in LuAM (LuO_7 and LuO_6, C_1) and LuASO (LuO_7 and LuO_6, C_s). In this study, the influence of crystal structure on the luminescence properties was investigated. The f-d transition of Ce^{3+} exhibits high sensitivity to the local environment. Variations in the crystal field environment, such as coordination number, coordination bond length, and crystal symmetry, have a significant impact on the energy level structure and emission spectra of Ce^{3+}. The emission colour of Ce^{3+} varies widely across different crystal

environments, spanning from the ultraviolet to the red region[22-23]. Therefore, Ce^{3+} ions are very commonly used dopant ions in different matrices to develop the phosphor with specific luminescence wavelengths for white light-emitting diodes (WLEDs) applications. In addition, The $^5D_0 \rightarrow {}^7F_J$ (J = 0 - 4) transition of Eu^{3+}, emitting red light, is particularly advantageous for the development of WLEDs due to its high color rendering index (CRI) and low correlated color temperature (CCT) values[14-16]. Therefore, using Ce^{3+} or Eu^{3+} doped LuAM and LuASO with two different crystal structures could lead to the development of phosphors with two distinct emission wavelengths. Additionally, the f-f transition of Er^{3+} ions shows hypersensitivity to the symmetry of the surroundings, and Er^{3+}/Yb^{3+} doped up conversion materials may exhibit different luminescent properties in two crystal structures[24].

4.5.1 Luminescence properties of LuAM and LuASO doped with Ce^{3+}

4.5.1.1 Luminescence properties at room temperature

Fig 4.21a shows the PLE and PL spectra of LAM ($Lu_4Al_2O_9$) and LASO ($Lu_{3.889}AlSiO_{9.33}$) powder measured at room temperature. The PL excitation spectrum of LuAM:1%Ce^{3+} shown in **Fig *4.21a*** left (red dotted curve) presents an intense excitation band peaking at 445nm between 400 and 500 nm and a weak excitation band at 300nm to 400nm, which is attributed to $4f \rightarrow 5d^1$ and $4f \rightarrow 5d^2$ transitions of Ce^{3+}[5]. Under 445 nm UV excitation, the emission spectrum of LuAM: 1%Ce^{3+} is displayed in ***Fig 4.21a*** right (red solid curve), showing an asymmetric broad band extending from 470 to 700 nm (FWHM is about 114 nm) with maximum values located at 594 nm, which is attributed to 5d - 4f transition of Ce^{3+}. The asymmetry peak can be fitted with two bands centered at 611 nm (16367 cm^{-1}) and 550 nm (18182 cm^{-1}) by Gaussian deconvolution, suggesting the splitting of the ground state $^2F_{7/2}$ and $^2F_{5/2}$ of Ce^{3+}[25]. However, the excitation spectrum of the LuASO: 1%Ce^{3+} shown in **Fig *4.21a*** left (blue dotted curve) presents several broad peaks ranging from 200 to 450 nm with the maximum at 365nm, which correspond to excitations from $^2F_{5/2}$ state to different levels of $5d_2$ orbitals. In contrast to the $5d_2$ excitation peaks observed in LAM, these excitation peaks indicate a splitting of the crystal field, which is attributed to the variation in local symmetry. The emission spectrum of LuASO: 1%Ce^{3+} under 365nm can be decomposed into

two bands centered at 468 (21367 cm^{-1}) and 532 nm (18797 cm^{-1}) by Gaussian deconvolution, which may belong to transition of Ce^{3+} at two different environments. ***Fig 4.21b*** presents a comparison of the emission spectra of LuAM and LuASO at 365 nm excitation, showing a redshift of 20 nm in LuASO, which also indicates an increase in crystal field strength due to the change in symmetry of the Ce^{3+} site. The significant differences in excitation and emission spectra between LuAM (monoclinic) and LuASO (orthorhombic) attribute to distinct crystal field environments for Ce^{3+} in the two compounds.

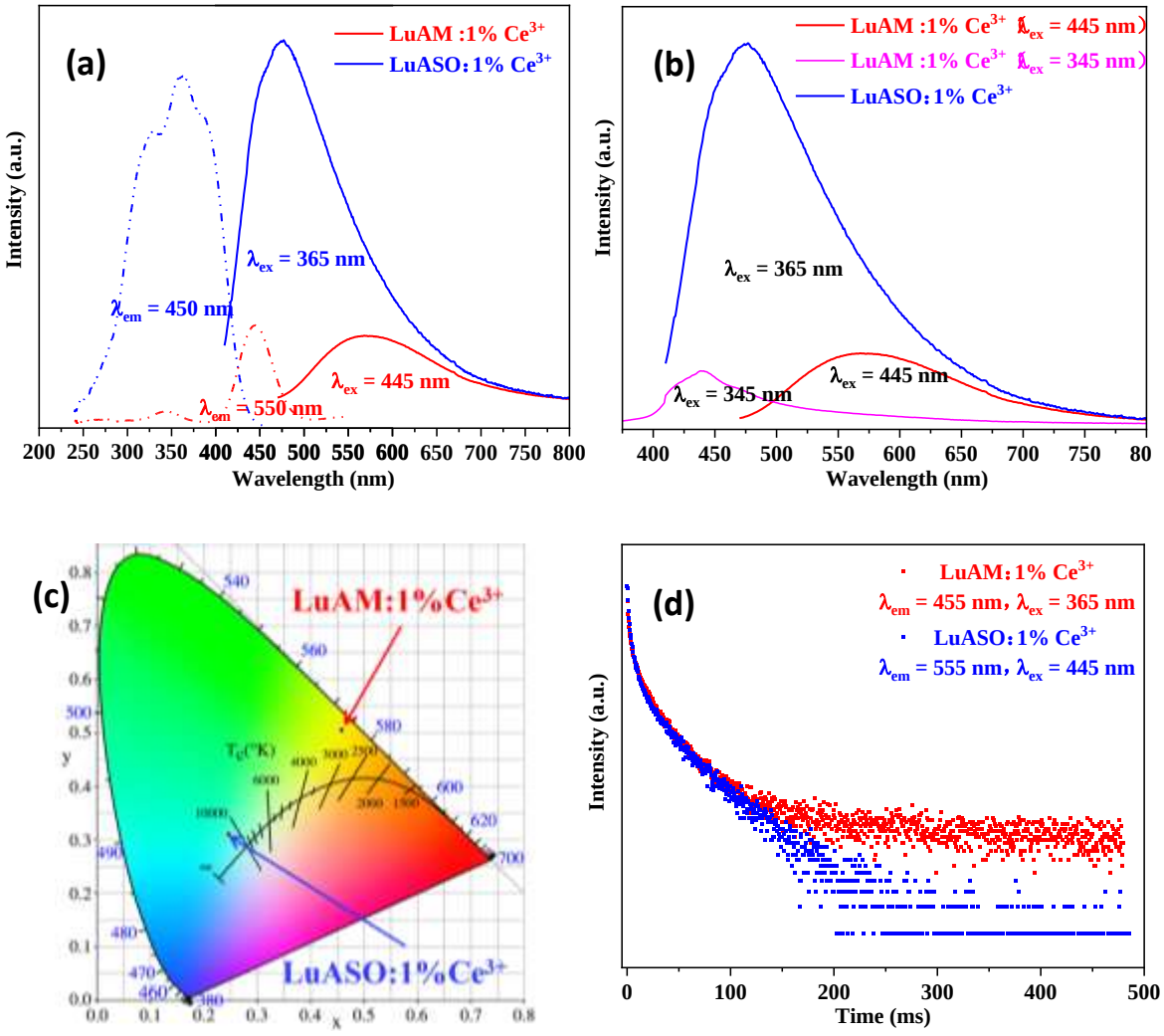

Fig 4.21 *Luminescence properties of LuAM: 1%Ce^{3+} (red curves) and LuASO: 1%Ce^{3+} (blue curves) powder measured at room-temperature.* ***(a)*** *PLE (dotted curves) under emission 450nm for LuAM and 550 nm for LuASO and PL spectra (solid curves) under excitation 365nm for LuAM and 445 nm for LuASO.* ***(b)*** *PL spectra under excitation 345/445nm for LuAM (red and pink curve) and 365nm excitation for LuASO (blue curve)* ***(c)*** *CIE chromaticity coordinates diagram, and* ***(d)*** *decay curves.*

Under 445 nm excitation for LuAM and under 365 excitation for LuASO, the compounds exhibit yellow and blue emission, respectively, as depicted in the CIE diagram presented in ***Fig 4.21c***, indicating that LuAM has potential as a yellow phosphor, while LuASO could serve as a blue phosphor for the development of GaN-excited and UV-excited white LEDs, respectively. The decay curves for LuAM and LuASO are shown in ***Fig 4.21d***. The decay times were fitting using the exponential function $I(t) = A1 \exp(-t/\tau1) + A2 \exp(-t/\tau2) + A3 \exp(-t/\tau3)$ for LuAM and double exponential function of $I(t) = A1 \exp(-t/\tau1) + A2 \exp(-t/\tau2)$ for LuASO, and fitting results are provided in ***Table 4.3***. It appears from the lifetime results that the lifetime of LuASO is shorter than that of LuAM. This could be due to the Lu vacancies, extra oxygen or Si/Al disorder polyhedron caused by the substitution of Al^{3+} by Si^{4+}, which promotes the nonradiative transition of the luminescence centre.

4.5.1.2 Structural dependence of luminescence properties

It has been reported[23] that Ce^{3+} occupies four inequivalent Y sites in YAM, consisting of two unequal YO_7 ($Y1/Y3O_7$) and two unequal YO_6 ($Y2/Y4O_6$) sites. However, due to the significantly smaller radius of the Lu^{3+} (0.86 Å) compared to Y^{3+} (0.9 Å) and Ce^{3+}(1.02 Å), the site of Ce^{3+} in LuAM requires further investigation. ***Fig 4.22a*** and ***b*** displays the PLE and PL spectra of LuAM and LuASO measured at various temperatures ranging from 80 K to 280 K, aiming to determine the Ce^{3+} site in LuAM. Based on the PLE and PL spectra at low temperature depicted in **Fig *4.22a*** (upper), it is evident that the profiles of both excitation and emission peaks maintain their structure consistently across varying temperatures. Comparison of the average bond lengths four Lu-O and BVSs value of Lu in LuAM listed in ***Table E.1.3*** suggests that Ce^{3+} should prefer to occupy the LuO_7 site, which corresponds to one Ce^{3+} emission site of the low-temperature spectroscopic response. This observation suggests that within LuAM, the Ce atom exclusively occupies the LuO_7 site, as illustrated in ***Fig 4.22a***, which represents the local environment of Ce^{3+} in LuAM.

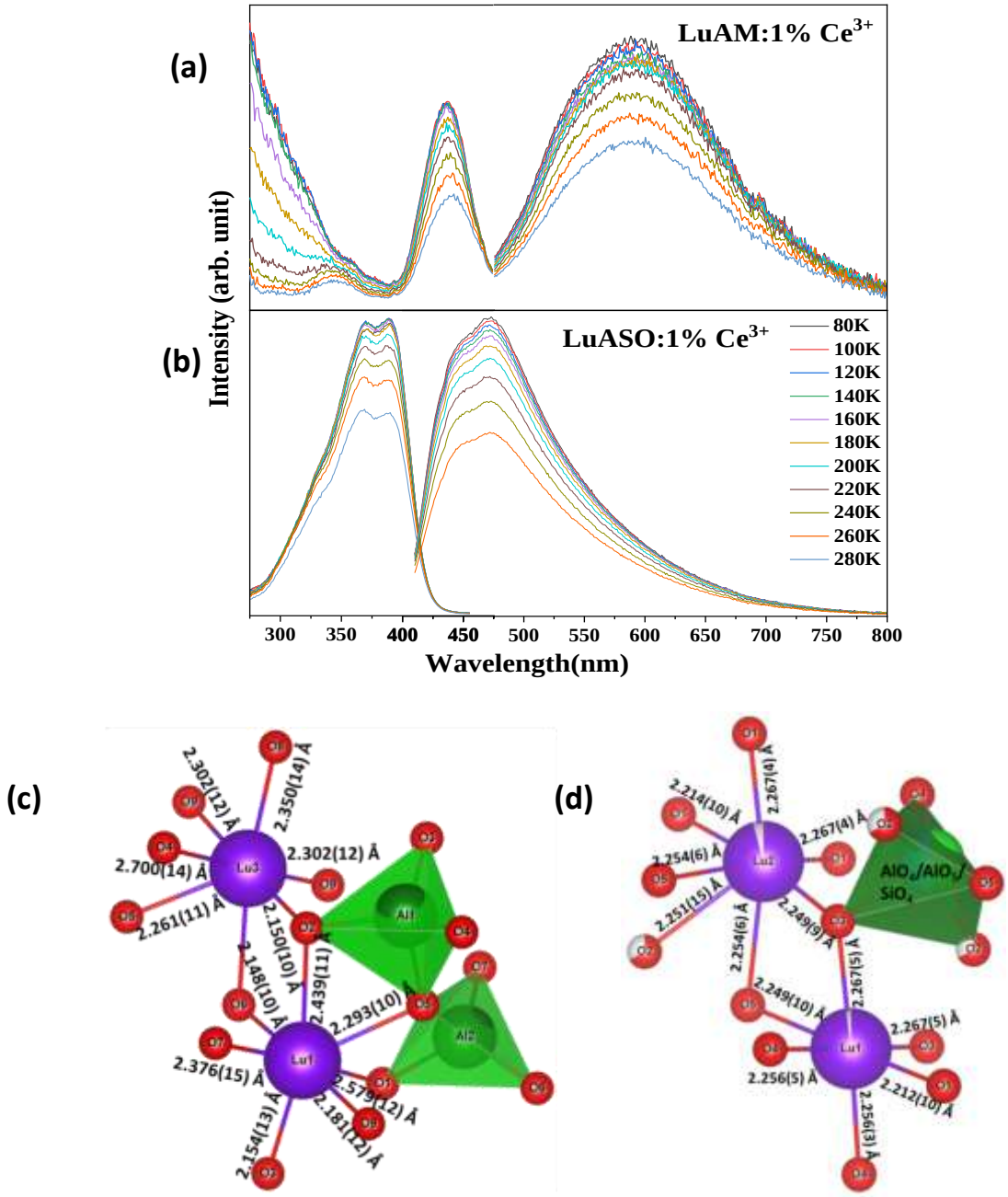

Fig 4.22 *PLE and PL spectra of* ***(a)*** *LuAM and* ***(b)*** *LuASO measured at low-temperature ranging from 80k -280k. Ce^{3+} environment in two compounds* ***(c)*** *$Lu1/Lu3O_7$ in LuAM and* ***(d)*** *$Lu1O_6$, $Lu2O_7$ in LuASO.*

The emission spectra of LuASO exhibit two distinct bands centered at 468 nm and 532 nm in ***Fig 4.22b***. The difference between them is equivalent to 2570 cm^{-1}, which significantly deviates from the theoretically expected energy gap of 2000 cm^{-1} between the $^2F_{7/2}$ and $^2F_{5/2}$ states of Ce^{3+}[25], indicating that it is caused by the transition from two different Ce^{3+} sites. In LuASO, there are two coordination sites, $Lu1O_6$ and $Lu2O_7$ with similar average bond lengths

and BVS (see ***Table E.1.4***), which both linked to the Al/Si polyhedron. Two emission bands are present in the LuASO emission spectra, with one band centered at 532 and 468 nm ascribed to the $Ce1O_6$ and $Ce2O_7$ (see ***Fig 4.22c***, the Ce^{3+} emission site in LuASO). However, the disordered substitution of Si for Al introduces variations in the strength of the crystal field, resulting in the formation of distinct Ce^{3+} environment, which are CeO_6 /CeO_7 connected to AlO_4, AlO_5 or SiO_4, respectively. Due to the potentially very large number of different local configurations available to Ce^{3+} in LuASO (due to Lu vacancies, different types of chains) present here, it is not possible to assign a precise local configuration in which the Ce^{3+} ion is located. However, regardless of which environment, Ce^{3+} is at two LuO_7 and LuO_6 sites in LuASO, while it occupies only the LuO_7 site in LuAM, which causes the two hosts to show different emission wavelengths and the emission is strongly blue-shifted by Si substitution

4.5.1.3 Concentration quenching properties

Fig 4.23a and ***b*** show the emission curves for LAM and LuASO doped with varying concentrations of Ce^{3+}, respectively. It was observed that an abrupt decrease in emission intensity occurred as the Ce^{3+} concentration increased from 1% to 5% caused by concentrations quenching of Ce^{3+}, which suggests that the optimum doping concentration of Ce^{3+} in these materials is likely to be less than 1%. In addition, the blue shift in the emission band can be attributed to the increasing of crystal field strength with the increasing of doping concentration, resulting from a bond length increasing due to more Ce^{3+} occupying the Lu^{3+} site, as shown in the normalized emission spectrum in ***Fig 4.23a*** and ***b*** inset. No other emission bands were observed in the different Ce^{3+}doped LuAM samples, suggesting that Ce^{3+} is unable to occupy the other LuO_6 crystalline sites despite the increase in Ce^{3+} concentration.

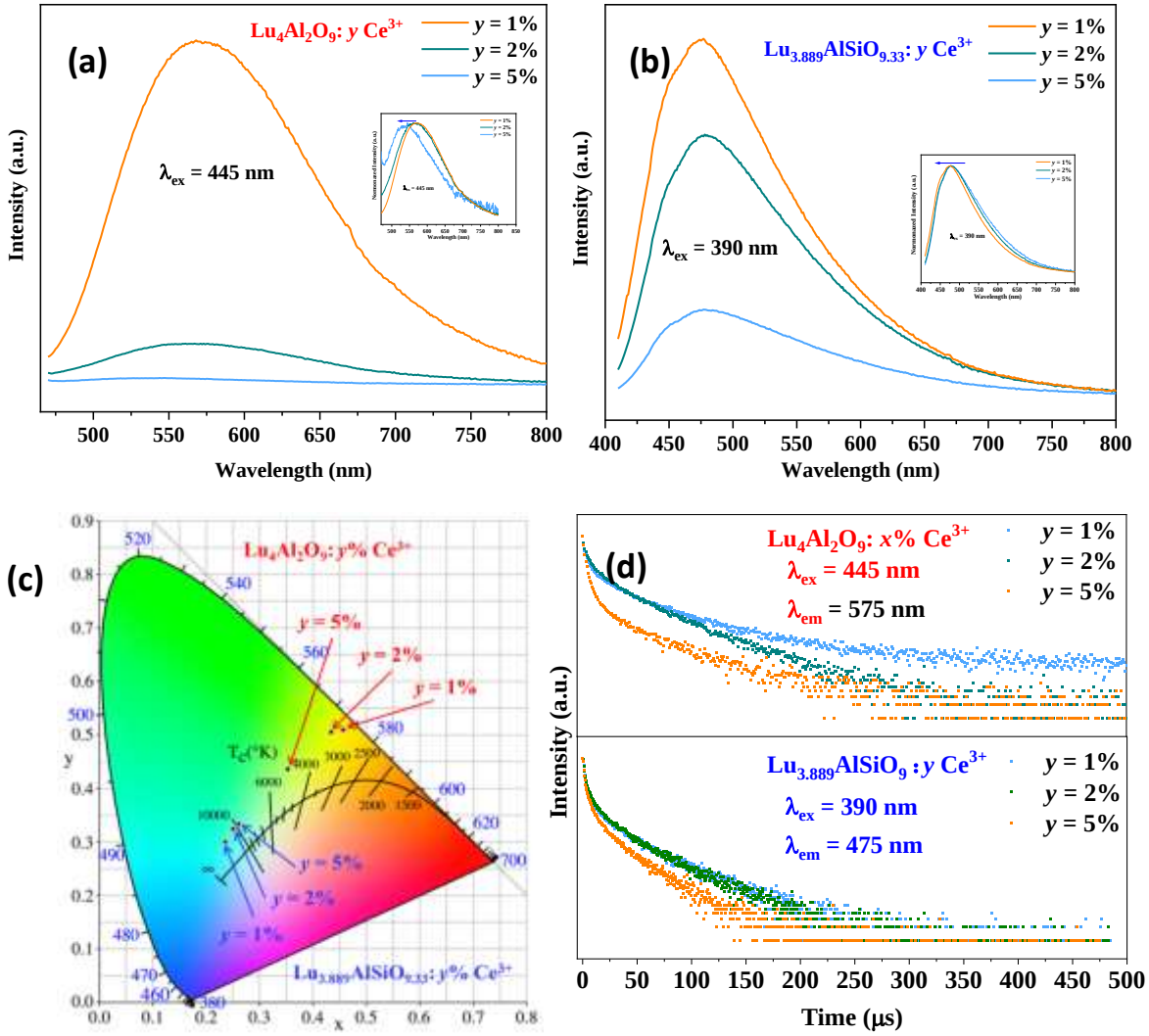

Fig 4.23 *PL emission spectra of* ***(a)*** *LuAM: yCe^{3+} and* ***(b)*** *LuASO: yCe^{3+}.* ***(c)*** *CIE chromaticity coordinates diagram.* ***(d)*** *Decay curve of LuAM: yCe^{3+} and LuASO: yCe^{3+}.*

With increasing doping concentration, LuAM shifting from yellow to green and LuASO shifting from blue to green, as depicted in the CIE chromaticity diagram shown in ***Fig 4.23c***. The decay curves of Ce^{3+} in LuAM and LuASO with different doping concentrations are plotted in ***Fig 4.23d*** and ***e***. All curves can be fitted well using triple exponential function of I(t) = A1 exp(-t/τ1) + A2 exp(-t/τ2) + A3 exp(-t/τ3) for LuAM and double exponential function of I(t) = A1 exp(-t/τ1) + A2 exp(-t/τ2) for LuASO and the fitting lifetimes are list in ***Table 4.3***. The decrease in decay time with increasing concentration indicates that the distance between Ce^{3+} is too short to accelerate the energy transfer.

Table 4.3 *Fitting parameters and lifetime obtained from LuAM: yCe^{3+} and LuASO: yCe^{3+} decay curves fitting results.*

Sample	Ce^{3+}%	A1%	t1(μs)	A2%	t2(μs)	A3%	t3(μs)	T avg(μs)
LuAM	1%	54.97	1.27	31.75	6.948	13.28	46.62	9.09
	2%	50.83	1.5	32.10	7.7	17.07	37.94	9.7
	5%	82.86	1.787	15.35	7.781	1.79	48.32	2.06
LuASO	1%	82.08	1.69	17.92	8.43			2.90
	2%	79.89	1.60	20.11	8.65			3.10
	5%	81.59	1.24	18.41	7.19			2.34

4.5.2 Luminescence properties of LuAM and LuASO doped with Eu^{3+}

4.5.2.1 Luminescence properties at room temperature

The PLE and PL spectra of LuAM: 2.5%Eu^{3+} and LuASO: 2.5%Eu^{3+} measured at room temperature are presented in ***Fig 4.24a*** and ***b***. In the excitation spectra shown in ***Fig 4.24a***, a CT band located at the range of 200 - 300 nm and a range of peaks at 298, 318, 361, 381, 393, and 404 nm corresponding to the $^7F_0 \rightarrow {}^5H_6$, $^7F_0 \rightarrow {}^5H_3$, $^7F_0 \rightarrow {}^5D_4$, $^7F_0 \rightarrow {}^5G_3$, $^7F_0 \rightarrow {}^5L_6$, and $^7F_0 \rightarrow {}^5D_3$ transitions of Eu^{3+}, respectively, can be observed[2]. Notably, LuASO exhibits a significant red shift in the center of the CT band compared to LuAM, suggesting a distinct environment (covalency, coordination numbers, and Eu-O bond length) for Eu^{3+} in the two different hosts. Eu^{3+} has been reported[16] to occupy three different Y sites (Y1/$Y3O_7$ and $Y2O_6$) of C_1 symmetry in YAM. Further site selection spectroscopic studies are needed to determine the exact location of Eu^{3+} in LuAM. Here, based on the average bond length and BVS value, it was suggested that Eu tends to occupy Lu1/$Lu3O_7$ and $Lu2O_6$, in agreement with the reported in YAM (see ***Table E.1.3)***. While LuO_7 and LuO_6 sites of C_s symmetry with different environments caused by disorder (Si substitution and Lu vacancies) are present in LuASO. Here it cannot be determined which specific local configuration site Eu^{3+} is at, but in any case the symmetry is different from that of LuO_7/LuO_6 sites in LuAM. The emission spectra of LuAM: Eu^{3+} and LuASO: Eu^{3+} under 393 nm excitation are displayed in ***Fig 4.24b***, demonstrating a series of peaks at 589, 594, 608, 629, 647, 651, 694, 698, and 708 nm assigning to the $^5D_0 \rightarrow {}^7F_J$ (J = 0 - 4) transitions[26]. The intensity of the $^5D_0 \rightarrow {}^7F_1$ transition

does not vary significantly between the two samples since it is a magnetic dipole (MD) transition that is largely independent of the surrounding chemical environment[27]. Notably, the dominant emission associated with supersensitive ED, and its intensity is greatly influenced by the site symmetry and coordinate environment. In the observation of $^5D_0 \rightarrow {}^7F_2$ transition, it can be found that the $^5D_0 \rightarrow {}^7F_2$ transition exhibits three spectral lines in LuAM and two spectral lines in LuASO, which are attributed to the inter-energy level merging of Eu^{3+} within the C_s symmetry[14].

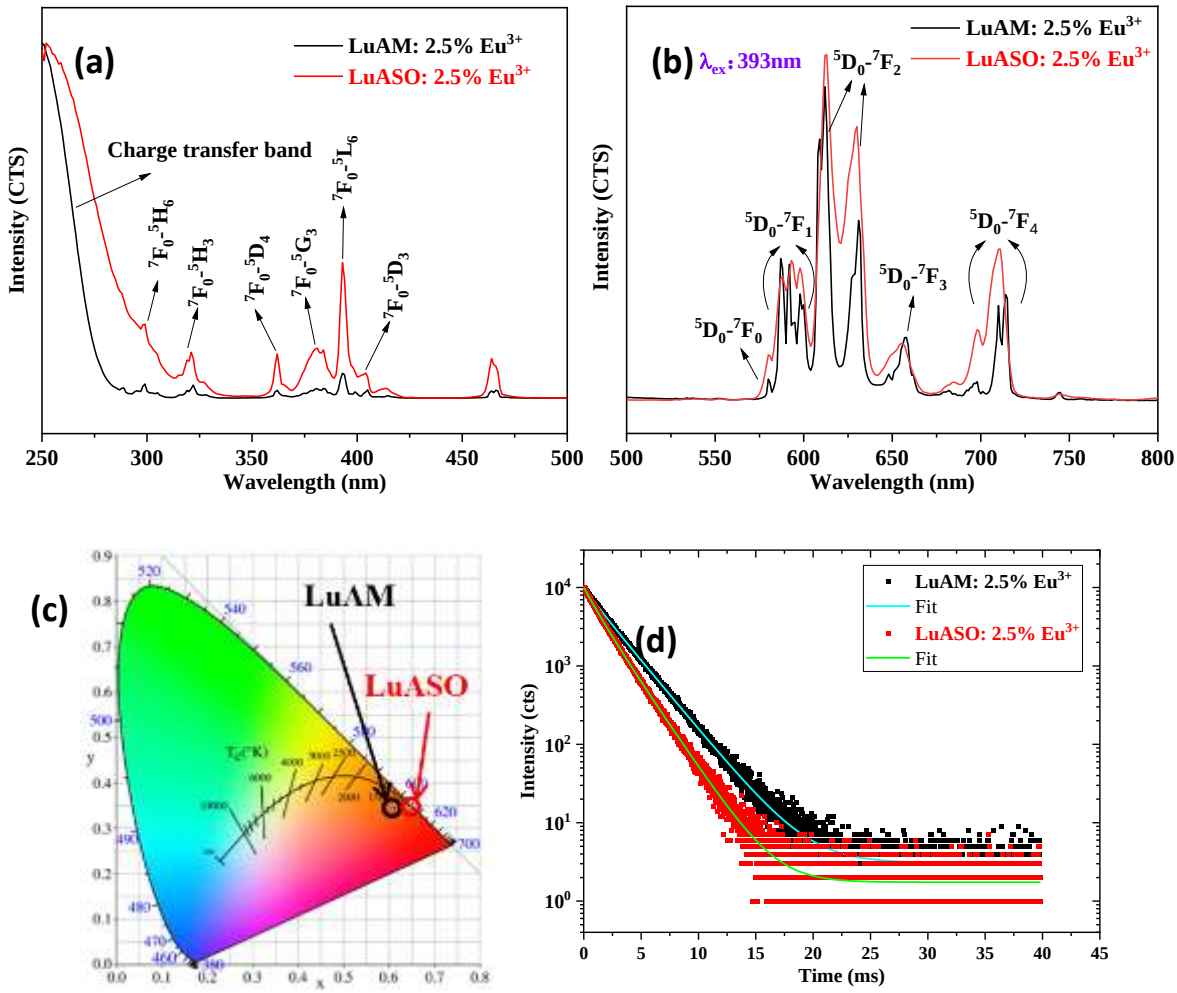

Fig 4.24 *Luminescence properties of LuAM: 2.5%Eu^{3+} and LuASO: 2.5%Eu^{3+}* ***(a)*** *PLE and* ***(b)*** *PL spectra measured at room-temperature.* ***(c)*** *CIE chromaticity coordinates diagram.* ***(d)*** *Decay curves.*

Ultimately, this alteration in local symmetry from C_1 to C_s leads to LuASO exhibiting red emission instead of orange emission in LuAM, as illustrated in the CIE diagram in ***Fig 4.24c***. This red emission is more advantageous for UV-white LEDs. The emission spectra at 250 nm excitation are shown in ***Fig E.3.1a*** Due to the increased symmetry of Eu^{3+}, the emission peak

of LuASO broadens and decreases in intensity. The emission colour of the two compounds is red without great deviation, as shown in the **Fig *E.3.1b*** CIE diagram. The decay curves of LuAM: 2.5%Eu^{3+} and LuASO:2.5%Eu^{3+} were recorded (see ***Fig 4.24d***). All of the decay curves can be fitted well using the double-exponential equation of I(t) = A1 exp(-t/τ1) + A2 exp(-t/τ2). The fitting results (see ***Table 4.4***) indicate that the lifetime of LuAM phosphor (τ = 2.4 μs) is longer than that of LuASO (τ = 1.85 μs), suggesting a higher probability of nonradiative transition and a lower photoluminescence quantum yield compared to LuASO. These results tell us that the change in symmetry from monoclinic to orthorhombic caused by the introduction of Si results in Eu^{3+} being in a different local environment which adjusts its emission colour.

4.5.2.2 Concentration quenching properties

Fig 4.25a and ***b*** present the emission spectra of LuAM: yEu^{3+} and LuASO: yEu^{3+} (y = 2.5%, 5%, 10%) to investigate the effect of Eu^{3+} doping concentration on the luminescence intensity. It can be observed that the luminescence intensity increases as the Eu^{3+} concentration from 2.5% to 10%, indicating that the quenching concentration is not reached at 10%. The PLE spectrum and PL spectrum under 260 nm excitation of LuAM: yEu^{3+} and LuASO: yEu^{3+} (y = 2.5%, 5%, 10%) are display in ***Fig E.3.2*** showing an increase in spectral intensity with increasing concentration. Meanwhile, the decay curves for different doping concentrations of LuAM are depicted in ***Fig 4.25c*** and ***d***, indicating that lifetime becomes shorter with increasing concentration, thereby accelerating energy transfer due to closer proximity. All curves were fitted by double-exponential equations of I(t) = A1 exp(-t/τ1) + A2 exp(-t/τ2) and the fitted parameters and results are listed in ***Table 4.4***.

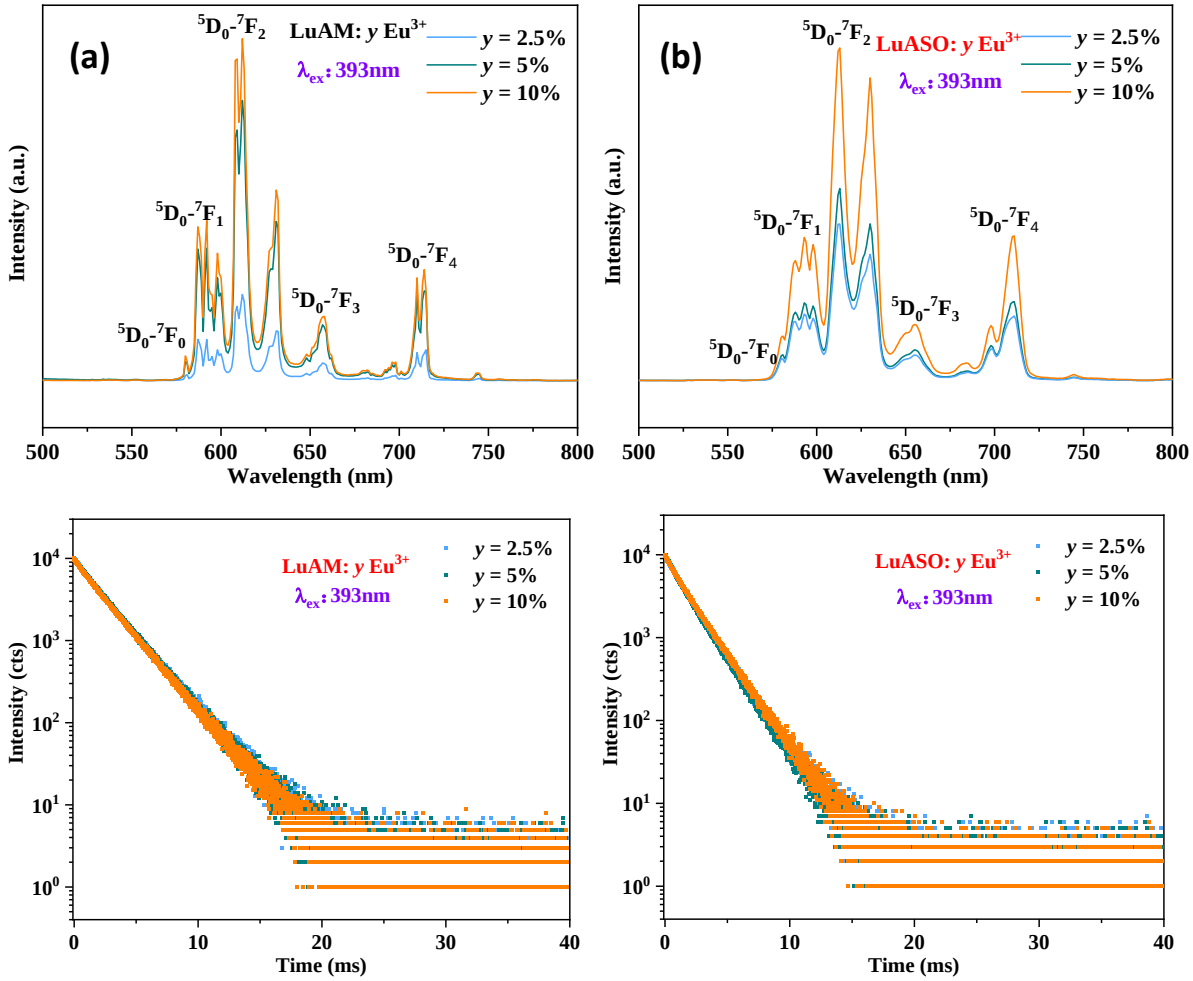

Fig 4.25 *PL emission spectra of* ***(a)*** *LuAM: yEu^{3+} and* ***(b)*** *LuASO: yEu^{3+}.* ***(c)*** *Decay curve of LuAM: yCe^{3+} and* ***(d)*** *LuASO: yCe^{3+}.*

Table 4.4 *Fitting parameters and lifetime obtained from LuAM: yEu^{3+} and LuASO: yEu^{3+} decay curves fitting results.*

Sample	Eu^{3+} %	A1%	t1(μs)	A2%	t2(μs)	T avg(μs)
LuAM	2.5%	88.21	2.47	11.79	1.06	2.40
	5%	90.33	2.44	9.67	0.71	2.27
	10%	89.78	2.39	10.22	0.82	2.23
LuASO	1%	71.13	2.02	28.86	1.10	1.85
	2%	84.00	1.83	16.00	0.71	1.65
	5%	86.32	1.90	13.68	0.50	1.70

4.5.3 Luminescence properties of LuAM and LuASO doped with 2%Er^{3+}/10%Yb^{3+}

Fig 4.26a shows the up-conversion emission spectra of LuAM: 2%Er^{3+}/10%Yb^{3+} (black curve) and LuAM: 2%Er^{3+}/10%Yb^{3+} (red curve) phosphors in the 500-700 nm range at an excitation wavelength of 980 nm. The spectra exhibit green emission centered around 526 nm and red emission centered around 661 nm at 564 nm, corresponding to the $^2H_{11/2}/^4S_{3/2}$-$^4I_{15/2}$ and $^4F_{9/2}$-$^4I_{15/2}$ transitions of the Er^{3+}, respectively[28]. Moreover, the broader contrast in the LuASO emission peak is attributed to the enhanced lattice symmetry, resulting in simplification of energy levels. This alteration in the emission spectrum consequently manifests as a change in emission color, as illustrated in ***Fig 4.25a*** inset CIE diagram. ***Fig 4.26b*** shows the decay curves of the red emission for LuAM (black curve) and LuASO (red curve), both curves are guaranteed to be a good fit using the double exponential equation. The fitted lifetimes displayed in **Table 4.5** show that LuASO exhibits a shorter lifetime, indicating a faster energy transfer capability in LuASO.

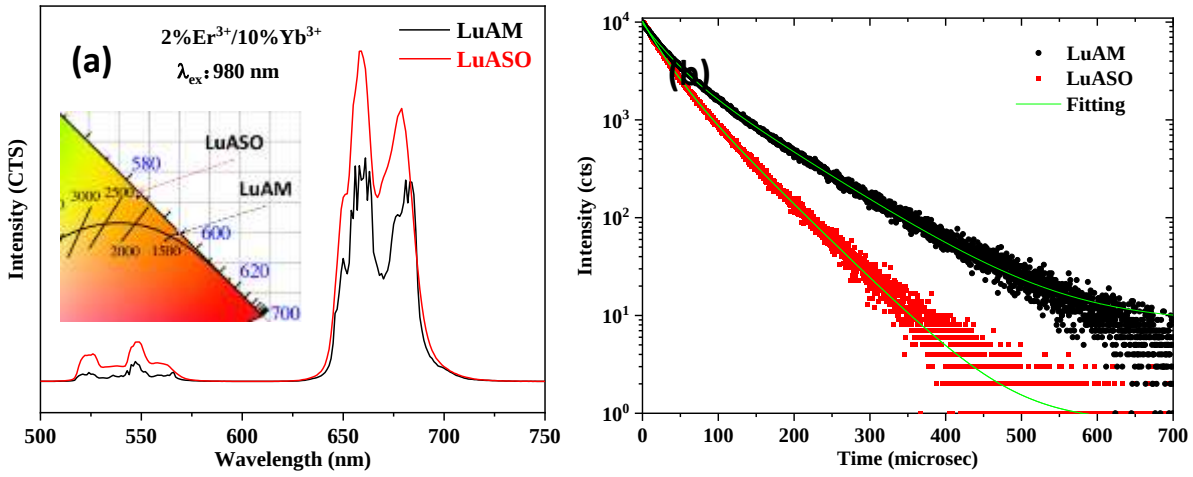

Fig 4.26 (a) *Up conversion spectrum of LuAM: 2%Er^{3+}/10%Yb^{3+} (black curve) and LuAM: 2%Er^{3+}/10%Yb^{3+} (red curve) under 980 nm excitation.* ***(b)*** *Decay curve of LuAM: 2%Er^{3+}/10%Yb^{3+} (black curve) and LuAM: 2%Er^{3+}/10%Yb^{3+} (red curve).*

Table 4.5 *Fitting parameters and lifetime obtained from LuAM: 2%Er^{3+}/10%Yb^{3+} and LuAM: 2%Er^{3+}/10%Yb^{3+}decay curves fitting results.*

Sample	A1%	t1(μs)	A2%	t2(μs)	T avg (μs)
LuAM	55.40%	29.5	44.60%	88.17	70.93
LuASO	56.20%	24.25	43.80%	57.19	45.57

4.6 Exploration on the synthesis of $Lu_{4-x}Mg_xAl_{2-x}Si_xO_9$.

In Feng's study[1], the authors reported the existence of a $(Lu/Mg)_4(Al/Si)_2O_9$. Furthermore, building upon our examination of $Lu_{4-\alpha}Al_{2-x}Si_xO_{9+\delta}$, it was suggested that the charge imbalance produced by the substitution of Si^{4+} for Al^{3+} may be compensated by the substitution of Mg^{2+} for Lu^{3+}. However, it could not be determined whether charge compensation is by Mg/Lu substitution or partial Mg/Lu and partial additional oxygen. Firstly, a series of $Lu_{3-x}Mg_xAl_{2-x}Si_xO_9$ composition were tried to synthesise. ***Fig 4.27a*** illustrates the PXRD pattern of the $Lu_{3-x}Mg_xAl_{2-x}Si_xO_9$ ($0 \le x \le 2$) solid solution, confirming the formation of single phase with $0 \le x \le 1.5$. Our observations indicate that as the substitution of Lu^{3+}-Al^{3+} by Mg^{2+}-Si^{4+}, the number of XRD diffraction peaks decreases, consistent with the $Lu_{4-\alpha}Al_{2-x}Si_xO_{9+\delta}$ solid solution.

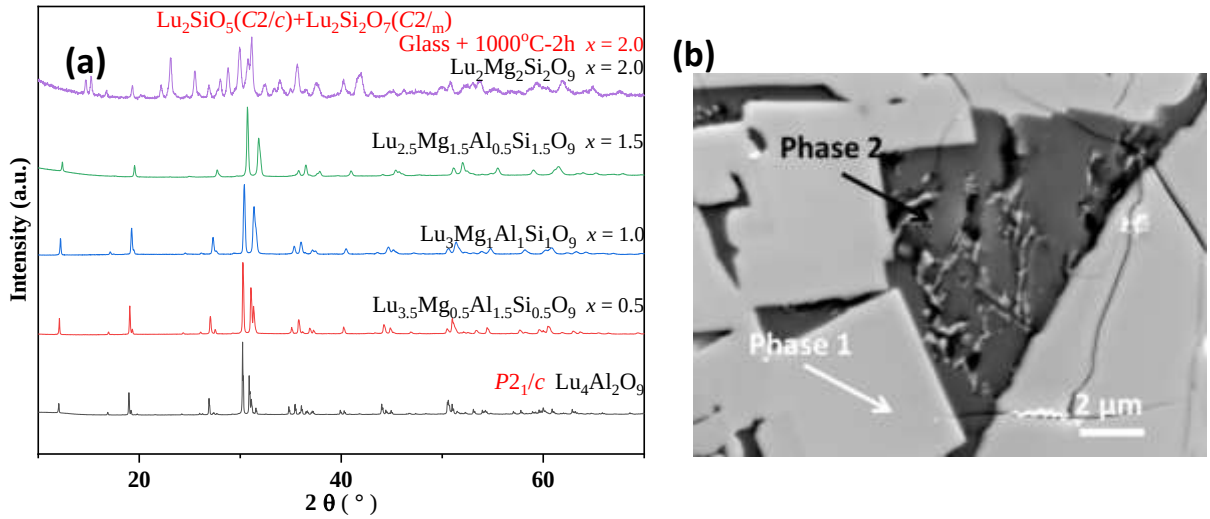

Fig 4.27 (a) *PXRD patterns of $Lu_{3-x}Mg_xAl_{2-x}Si_xO_9$ ($0 \le x \le 2$) and* ***(b)*** *SEM (BSE) image of $Lu_3MgAlSiO_9$*

However, upon analyzing the SEM image of $Lu_3MgAlSiO_9$, it becomes evident that the compound consists of a mixture of two phases (see ***Fig 4.27b***). The compositional analysis of these two phases determined by SEM-EDS, is presented in ***Table 4.6***. The $Lu_{3.48}Mg_{0.52}Al_{0.97}Si_{1.03}O_{9.26}$ compositions determined by EDS reminds us of the study of $Lu_{4-\alpha}Al_{2-x}Si_xO_{9+\delta}$. This tells us that the charge compensation of Si substitution for Al would be partially compensated by additional oxygen and the remainder by Mg substitution for Lu. Thus, it is evident that the introduction of Mg-Si substitution potentially leads to a more complex crystal structure within this solid solution, which will be further explored in future investigations.

Table 4.6 *Composition analysis of $Lu_3MgAlSiO_9$ by SEM-EDS.*

Sample	Phase	Lu (% at)	Al (% at)	Mg (% at)	Si (% at)	Experimental composition
(x = 1) $Lu_3MgAlSiO_9$	Phase 1	23.00	6.39	3.43	6.55	$Lu_{3.48}Mg_{0.52}Al_{0.97}Si_{1.03}O_{9.255}$
	Phase 2	6.27	7.43	21.51	7.58	$LuAl_{1.18}Mg_{3.43}Si_{1.21}O_{9.12}$

4.7 A new hexagonal $LuAlO_3$ perovskite

During the SEM observation and composition analysis of the $Lu_4Al_{0.5}Si_{1.5}O_{9.25}$ composition, the presence of a secondary phase was consistently observed with the composition $LuAl_3O_6$ within the solid solution (see ***Fig E.2.4a*** and ***Table E.2.3***). In order to clarify the structure of this secondary phase not matching any known compound, the synthesis of $LuAl_3O_6$ composition by ADL was attempted. Transparent beads, translucent beads as well as fully crystalline white beads (see photographs in ***Fig 4.28a)*** were obtained using oxygen and argon as the levitated gas to control the cooling rate, respectively. The PXRD pattern displayed in ***Fig 4.28b*** demonstrates that the pattern of the transparent beads can be indexed to the known hexagonal perovskite structure of $YAlO_3$ with a systematic peak shift towards higher angle. This phase is therefore assigned as hexagonal perovskite $LuAlO_3$ (LuAH) and is isomorphous to hexagonal $YAlO_3$ (YAH)[29] and $GdAlO_3$ (GdAH)[30]. The white crystalline bead is a mixture of LuAP and LuAG phases. And comparing the starting

composition, the extra Al_2O_3 here probably not easy detect by PXRD or in the form of glass. In order to figure out the composition of the beads, therefore SEM measurement was performed on the polished transparent beads

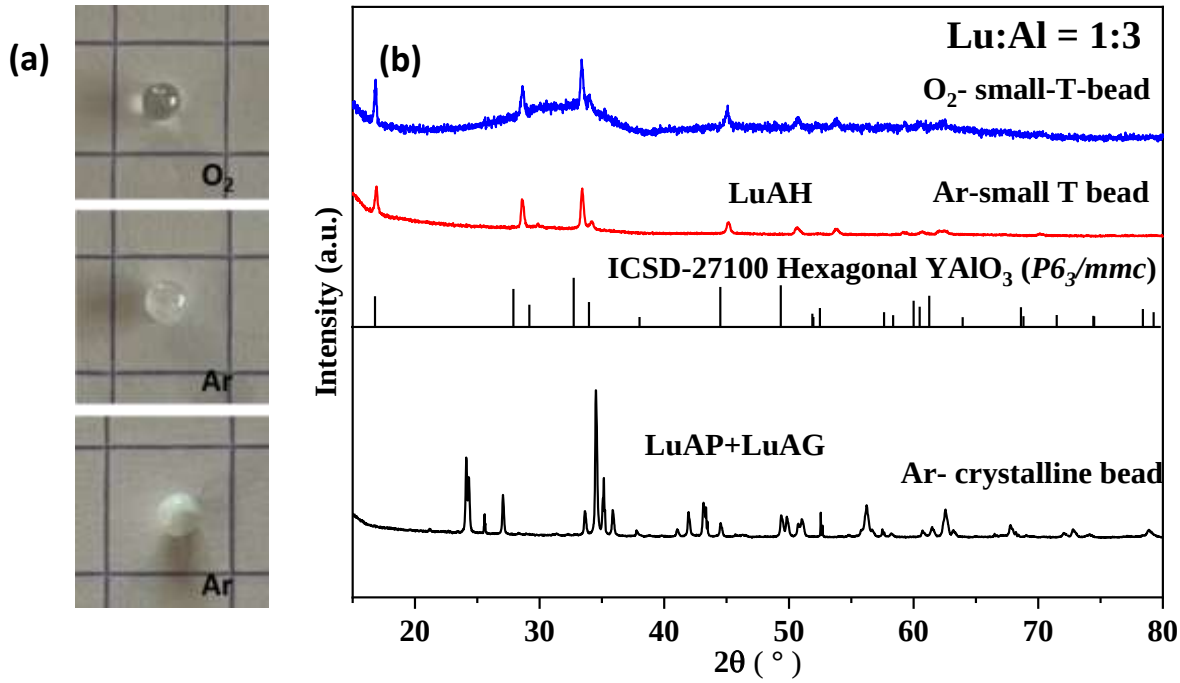

Fig 4.28 (a) *Photographs* ***(b)*** *PXRD pattern of the of* $LuAl_3O_6$ *samples obtained by synthesis using oxygen and argon gas by ADL.*

SEM measurements were carried out in order to further understand the micromorphology and composition of the transparent beads. The SEM image presented in ***Fig 4.29a*** provides an overall morphology of the polished bead surface, revealing two distinct regions with a glass component in the central part and an approximately 50 µm thick crystalline layer on the surface (see ***Fig 4.29b***). A closer observation of the BSE images shown in **Fig *4.29c*** and ***d*** indicates that the crystalline region consists of two distinct phases (black phase Al_2O_3 and white phase LuAH) and the morphology of the two phases is in the form of a long strip of approximately 300 nm in length and 50 nm in width. It is worth noting that these two phase are staggered with each other and their content ratio is approximately 1 : 1. This microscopic morphology is similar to that of the YAG glass reported in our group's work, which may become an excellent luminescent substrate material.

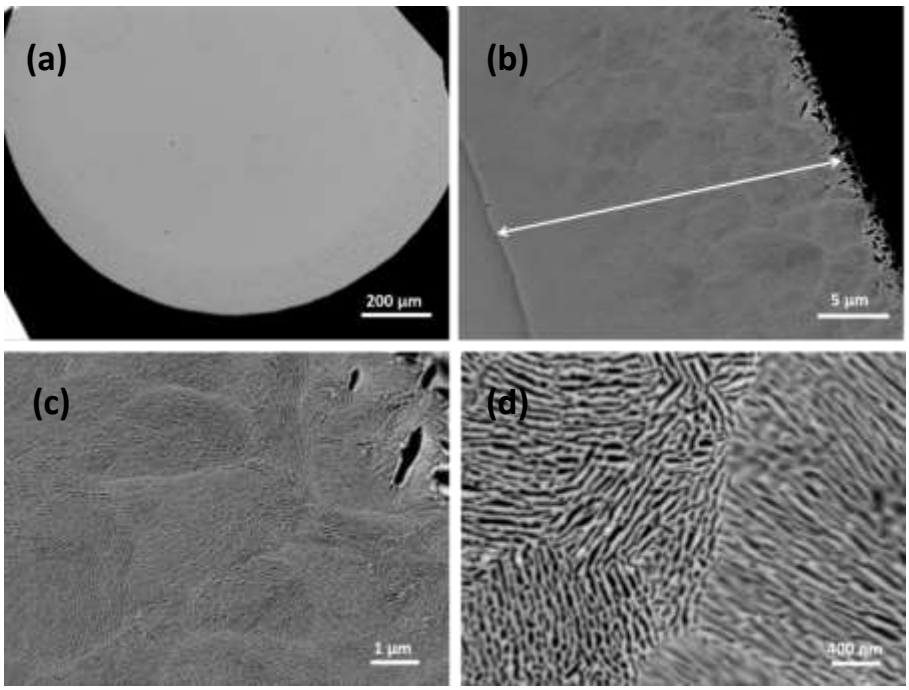

Fig 4.29 *SEM images of $LuAl_3O_6$ transparent beads.*

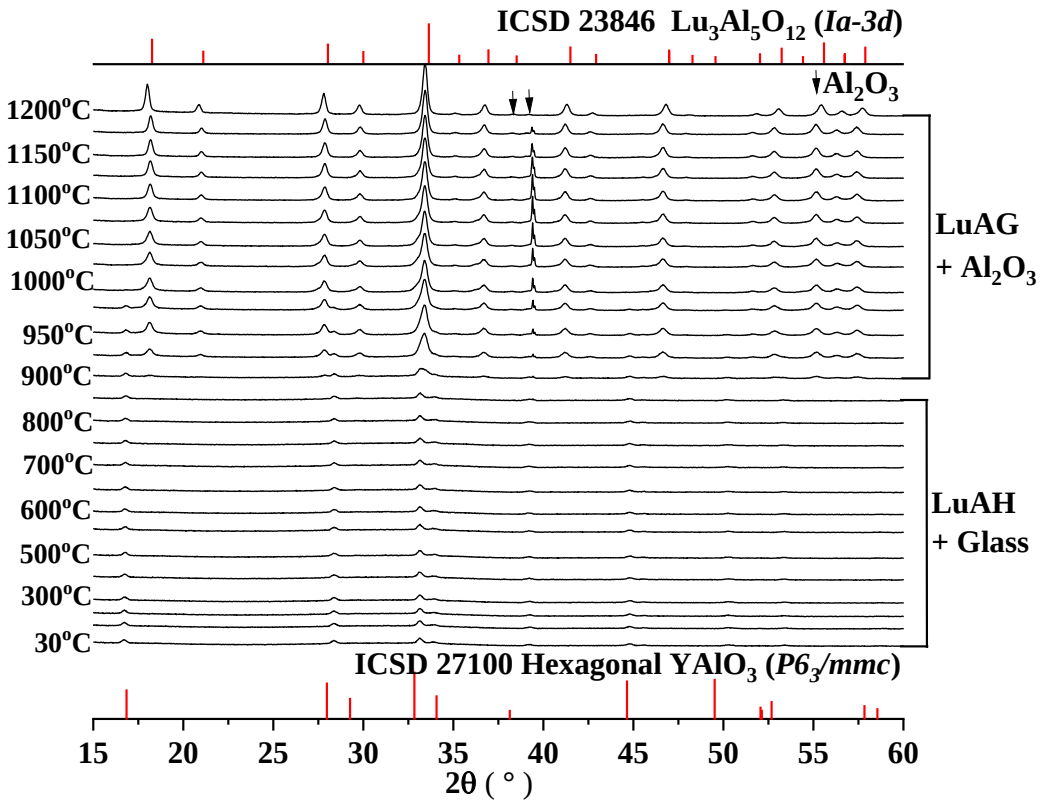

Fig 4.30 *VT-XRD pattern of $LuAl_3O_6$ transparent beads measured form room temperature to 1200°C. (black mark are Al_2O_3)*

To further explore the thermal stability of LuAH and the phase variation of the $LuAl_3O_6$

composition in the high temperature process, variable temperature XRD data were collected from room temperature to 1200°C, as shown in ***Fig 4.30***. It can be observed that the peak of LuAH does not exhibit sharpening as the temperature increases to 900°C, indicating that the the size of the coherent domains does not grow. In addition, the intensities of the peaks do not increase and no new peaks appeared, indicating that no grain growth and new crystal creation occurred below 900 °C. The LuAH phase gradually decomposes at 900°C and the whole composition eventually forms a mixture of LuAG and Al_2O_3 at high temperature.

In order to obtain fully nanocrystalline transparent ceramics for crystal structural analysis and luminescence applications[31-33], samples with different ratios of 1 Lu_2O_3 : 2.5 Al_2O_3, 1 Lu_2O_3 : 2 Al_2O_3 and 1 Lu_2O_3 : 1 Al_2O_3 composition were tried to prepared. The PXRD shown in ***Fig 4.31*** reveal that the $LuAl_{2.5}O_{5.25}$ and $LuAl_2O_{4.5}$ samples contain a higher proportion of glassy components compared to $LuAl_3O_6$. The glass samples could not be obtained using $LuAlO_3$ as the starting composition and crystallised as orthorhombic $LuAlO_3$. The splat quenching technique being developed in our laboratory may be an effective method for obtaining fully crystallised hexagonal LuAH nanograins. Otherwise, we would need to prepare very small beads to maximise the crystallinity of the hexagonal LuAH phase. The synthesis, structural analysis and optical applications of LuAH will be systematically explored in the near future, and this would be the first report about synthesis of LuAH.

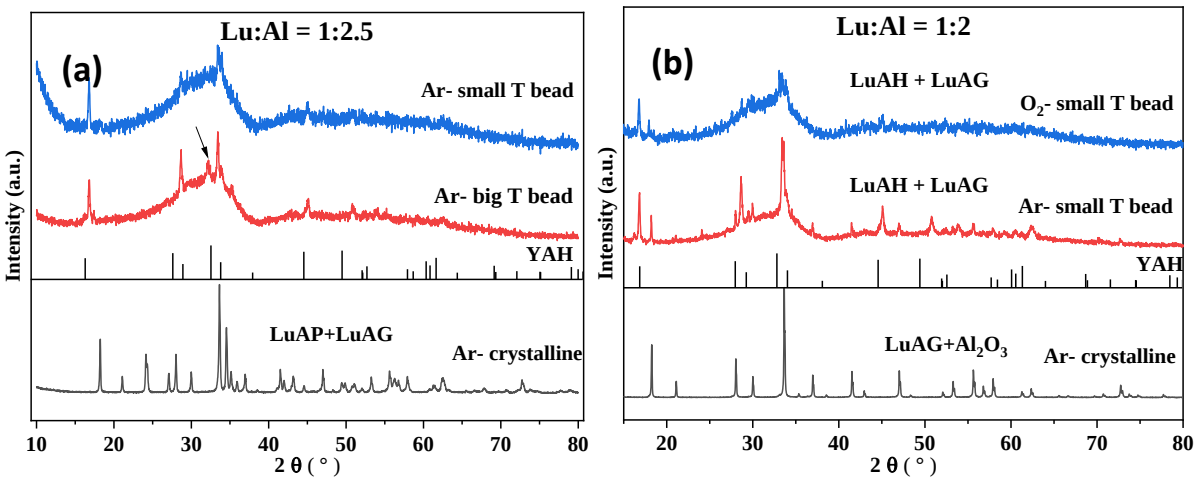

Fig 4.31 *PXRD of the* ***(a)*** *$LuAl_{2.5}O_{5.25}$ and* ***(b)*** *$LuAl_2O_{4.5}$ composition synthesized by ADL.*

4.8 Chapter conclusion and perspectives

In this chapter, single phases $Lu_4Al_2O_9$ and solid solution compounds of $Lu_{4-\alpha}Al_{2-x}Si_xO_{9+\delta}$ ($x = \alpha/3 + \delta/2$, $x = 0.5$, 1) were successfully synthesised for the firsttime using melt crystallisation method by the ADL. The substitution of Si^{4+} for Al^{3+} resulted in an elevation of crystal structure symmetry, transitioning from a monoclinic $P2_1/c$ phase to an orthorhombic *Pbnm* phase. PXRD, ^{27}Al and ^{29}Si NMR spectroscopic and SEM analysis revealed that the Si^{4+} substitution for Al^{3+} in LuAM results in the formation of solid solutions with the chemical formula $Lu_4Al_{2-x}Si_xO_{9+x/2}$. Beyond a Si content (x) of 0.6, solid solutions $Lu_{4-\alpha}Al_{2-x}Si_xO_{9+\delta}$ with Lu vacancies and extra oxygen coexisting were observed, within a solid solution range up to $x = 1$.

Different behaviors of photoluminescence response to the structural variation were verified between LuAM and LuASO. The phase transition from $P2_1/c$ to *Pbnm* resulted in $Ce^{3+}/Eu^{3+}/Er^{3+}$ occupying sites with different local symmetry, consequently leading to distinct luminescence properties. Novel solid solution phosphors were discovered, including the yellow LuAM: Ce^{3+} phosphor with blue excitation and blue LuASO: Ce^{3+} phosphor with UV excitation. In addition, the Eu^{3+} occupied different local symmetry sites in the two different hosts, leading to a more reddish emission colour in LuASO. Furthermore, the investigation of up conversion LuAM: Er^{3+}/Yb^{3+} and LuASO: Er^{3+}/Yb^{3+} revealed that changes in symmetry caused a shift in emission color from orange to yellow. These findings suggest that cation substitution can induce alterations in crystal symmetry and the introduction of defects and polyhedral distortion, which can affect the local environment of the dopant consequently affecting luminescence performance. Quantum efficiency is being investigated for two new phosphors. The phase transition induced by cation substitution offers a promising avenue for the exploration of new phosphors to fulfill the requirements of white LEDs.

Moreover, the potential of Mg-Si substituted Lu-Al in $Lu_4Al_2O_9$ solid solutions to yield new phosphors were explored. Additionally, during the investigation of $Lu_{4-\alpha}Al_{2-x}Si_xO_{9+\delta}$ solid solutions, hexagonal $LuAlO_3$ along with Al_2O_3 transparent glass-ceramics were discovered, holding promise as intriguing optical materials. These investigations will be further investigated in depth.

References

[1] S. Feng, Y. Guo, M. Allix et al., Cell Reports Physical Science. ***2022****, 3, 101044.*

[2] J. Li, J.-G. Li, J. Li et al., Journal of Solid State Chemistry. ***2013****, 206, 104-112.*

[3] B. Fetlinski, Z. Boruc, M. Kaczkan et al., Journal of Luminescence. ***2017****, 181, 133-137.*

[4] D. SinghS. Kadyan, Journal of Materials Science: Materials in Electronics. ***2017****, 28, 11142-11150.*

[5] G. Okada, M. Akatsuka, H. Kimura et al., Sensors and Materials. ***2018****, 30, 1547.*

[6] R. Simura, H. Yamane, Acta Crystallographica Section E. ***2020****, 76, 752-755.*

[7] A.G. Petrosyan, V.F. Popova, V.L. Ugolkov et al., Journal of Crystal Growth. ***2013****, 377, 178-183.*

[8] L. Kepinski, Journal of the American Ceramic Society. ***2018****, 101, 1356-1360.*

[9] L. Hennet, V. Cristiglio, J. Kozaily et al., The European Physical Journal Special Topics. ***2011****, 196, 151-165.*

[10] U. Kolitsch, H.J. Scifert, F. Aldinger, Journal of Phase Equilibria. ***1998****, 19, 426.*

[11] U. Kolitsch, H.J. Scifert, T.Ludwig et al., Journal of Materials Research. ***1999****, 14, 447–455.*

[12] J.P. Coutures, E.Antic, P. Caro, Materials Research Bulletin. ***1967****, 11, 699-706.*

[13] U. Kolitsch, H.J. Scifert, F. Aldinger, Journal of Alloys and Compounds. ***1999****, 257, 104-114.*

[14] A. Das, S. Saha, K. Panigrahi et al., CrystEngComm. ***2018****, 20, 2540-2552.*

[15] M. Kaczkan, Z. Boruc, S. Turczyński et al., Journal of Luminescence. ***2016****, 170, 330-335.*

[16] M. Kaczkan, S. Turczyński, D.A. Pawlak et al., Optical Materials. ***2016****, 58, 412-417.*

[17] M. Kaczkan, D.A. Pawlak, S. Turczynski et al., Journal of Alloys and Compounds. ***2017****, 728, 1009-1015.*

[18] V. Petříček, L. Palatinus, J. PlášilM. Dušek, ***2023****, 238, 271-282.*

[19] M.I. Aroyo, A. Kirov, C. Capillas et al., Acta Crystallogr A. ***2006****, 62, 115-128.*

[20] M. Shimada, H. Yamane, H.Takizawa et al., Key Engineering Materials. ***1997****, 132-136, 647-650.*

[21] H. Yamane, M.Omori, A. Okubo, The journal of the american ceramic society. ***1993****, 76, 2382-2384.*

[22] Z.G. Xia, A. Meijerink, Chemical Society Reviews. ***2017****, 46, 275-299.*

[23] Y. Wang, R. Hrubiak, S. Turczyński et al., Acta Materialia. ***2019****, 165, 346-361.*

[24] E.V. Bol'shakova, A.V. Malov, P.A. Ryabochkina et al., Optics and Spectroscopy. ***2011****, 110, 910-916.*

[25] Kai Li, M. Shang, H.Z. Lian et al., Inorganic Chemistry. ***2015****, 54, 7992–8002.*

[26] W. Ye, C. Zhao, X. Shen et al., ACS Applied Electronic Materials. ***2021****, 3, 1403-1412.*

[27] X. Zhang, T. Shen, D. Kan et al., Inorganic Chemistry. ***2020****, 59, 9927-9937.*

[28] W. You, F. Lai, H. Jiang et al., Physica B: Condensed Matter. ***2012****, 407, 1094-1098.*

[29] C.K. Cheng, L.B. Young, K.Y. Lin et al., Microelectronic Engineering. ***2017****, 178, 125-127.*

[30] L. Kepinski, R. Lisiecki, M. Ptak, Journal of Alloys and Compounds. ***2021****, 856, 158234.*

[31] X. Ma, X. Li, J. Li et al., Nature Communications. ***2018****, 9, 1175.*

[32] Y. Ji, J. Cao, Z. Zhu et al., Journal of Luminescence. ***2012****, 132, 702-706.*

[33] J. Li, A.E. Smith, P. Jiang et al., Inorganic Chemistry. ***2015****, 54, 837-844.*

General Conclusion

The aim of this thesis was to synthesise, characterise the structure and explore the properties of new materials to meet the needs of solid ceramic materials in various fields[1]. Non-equilibrium synthesis methods, involving the manipulation of kinetic pathways to create glass, metastable phases, amorphous structures that deviate from thermodynamic equilibrium by manipulating the processing conditions, are effective approaches for synthesizing new materials. ADL combined with laser heating is a setup developed at CEMHTI for the non-equilibrium synthesis of crystallization from melts or glass. This synthesis setup has been successfully used to synthesize various novel ceramic materials that cannot be synthesized using traditional solid-state reaction methods, and these materials have potential applications in optics, energy storage, and other fields[2-5]. The RE_2O_3-$(Al/Ga)_2O_3$ system is an important ceramic material system with compounds that have wide-ranging applications in multiple fields, such as electronics, catalysts, magnetism, and optics[6-8]. It is therefore promising to synthesise or search for unexplored of unreported materials in this system and to study their structure and applications. In these systems, highly non-stoichiometric YAG garnets[9] have recently been reported and demonstrate that the non-stoichiometry has unexpected effects on luminescent properties. Furthermore, a $(Lu/Mg)_4(Al/Si)_2O_9$ compound, with potential as a luminescent host material was found during the study of $(Lu/Mg)_3(Al/Si)_5O_{12}$ garnets[10]. Based on these two works, my PhD work focused on three systems: “structure and luminescence properties of non-stoichiometric $Gd_{3+x}Al_{5-x}O_{12}$ ($0 \leq x \leq 0.6$)”, “structure and persistent luminescence properties of non-stoichiometric $Gd_{3+x}Ga_{5-x}O_{12}$ and $Gd_{3+x}(Al_{0.4}Ga_{0.6})_{5-x}O_{12}$ ($0 \leq x \leq 0.6$)”, and “structure and luminescence properties of the $Lu_{4-\alpha}Al_{2-x}Si_xO_{9+\delta}$ ($0 \leq x \leq 1$) solid solution”. This summary gives the main conclusions of the three chapters.

Structure and luminescent properties of highly non-stoichiometric $Gd_{3+x}Al_{5-x}O_{12}$ ($0 \leq x \leq 0.6$)

This chapter aims to investigate the synthesis, structure and luminescence properties of

non-stoichiometric $Gd_{3+x}Al_{5-x}O_{12}$ based on the work on non-stoichiometric $Y_{3+x}Al_{5-x}O_{12}$ ($0 \leq x \leq 0.40$)[9]. As Gd^{3+} is larger than Y^{3+}, it may offer more possibilities for larger dopant ions to occupy the *B* octahedral sites, and therefore the trends in the distribution of dopant ions of different sizes in GAG were explored. Additionally, the dependence of luminescence properties on the new luminescent sites was investigated by luminescence spectroscopy study.

In this work, the $Gd_{3+x}Al_{5-x}O_{12}$ solid solutions were synthesized using the crystallization from glass method. PXRD Rietveld refinement reveals a linear increase in the lattice parameter *a* as x values increasing from 0 to 0.6, confirming the formation of highly nonstoichiometric GAG solid solutions. SPD refinement results suggest that in $Gd_{3.6}Al_{4.4}O_{12}$, up to 30% of Gd^{3+} occupies the six coordinated Al^{3+} site, which is 50% higher than 20% of octahedral Al^{3+} substituted by Y^{3+} in the nonstoichiometric $Y_{3.4}Al_{4.8}O_{12}$, despite the Gd^{3+} is larger than Y^{3+}. VT-PXRD data collected from room temperature to 1600^{o}C exhibits that the ns-GAG gradually decomposes into GAP and Al_2O_3 after 1150°C, which is much lower than the thermal stabilization temperature (1350°C) of ns-YAG due to Gd^{3+} is larger than Y^{3+}. SEM images revealed the grain morphology of GAG, appearing as irregular polygons of 2 to 3 microns in length and width, and displaying porosity that prevents the production of transparent ceramics. STEM-HAADF and STEM-EDS were used to characterize the location of octahedral Gd^{3+} at atomic scale, and the HADDF results suggest that octahedral Al was disordered substituted by Gd^{3+}. To probe the local environment around the Gd^{3+} ion, EXAFS measurements were successively performed on ns-GAG at the L_3 edge of Gd (7243 eV), and a comparison of experimental and simulation EXAFS spectrum confirmed the substitution of Al^{3+} ions at octahedron site by Gd^{3+} ions.

To gain insight into the distribution and location of dopant ions in the ns-GAG structure, the following experiments were performed. Firstly, microprobe mapping was carried out illustrating the homogeneity of the dopant ions distribution in the structure. Here STEM-EDS L-ray spectra at the atomic level were collected to directly observed the distribution of Tb^{3+} in the ns-$Gd_{3.2}Al_{4.8}O_{12}$:10% Tb^{3+} sample, and L-ray spectra extracted from Al_{16a} at *A* site and $2Gd_{24c}+2Al_{24d}$ at *A* + *B* site suggested that Tb is distributed not only at AO_8 but also at BO_6. EXAFS spectra at the L_3-eadge for rare earths (Yb^{3+} and Tm^{3+}) in ns-GAG were collected, and

fitting of different atomic substitution configurations generated by Supercell to the experimental spectra showed that the smaller size dopant ion Yb/Tm prefers to occupy the six coordination BO_6 site.

To understand the impact of non-stoichiometry on the luminescence properties, various dopant ions with different sizes and transition behaviors (eg. Ce^{3+}: f-d transition; Tb^{3+}, Er^{3+}, Tm^{3+}: f-f transition) were chosen to analyzed their luminescence properties. The photoluminescence study of Ce^{3+} shows that the non-stoichiometry affects the slight red shift of the emission band due to the environmental change of AO_8. However, there is no obvious change in emission color because Ce^{3+} is only located at the A site instead of two sites, consistent with ns-YAG: Ce^{3+}. Tb^{3+} was found to be distributed at different sites AO_8 and BO_6, however, the emission spectra of ns- GAG do not exhibit significant differences due to the insensitivity of the f–f transition of Tb^{3+} to the environment. In contrast, the emission spectra studies of GAG: Er^{3+}/Yb^{3+} and Tm^{3+}/Yb^{3+} up-conversion materials demonstrated a significant change in the emission color, which is due to the hypersensitive transitions of Er^{3+} and Tm^{3+} are sensitive to the new local BO_6 site in the ns-GAG.

Structure and luminescent properties of non-stoichiometric $Gd_{3+x}Ga_{5-x}O_{12}$ and $Gd_{3+x}(Al_{0.4}Ga_{0.6})_{5-x}O_{12}$ ($0 \le x \le 0.6$)

Garnet structure compounds are not only excellent host materials for up-conversion and down-conversion but also well-known host materials for persistent luminescence. Based on the ns-GAG work and previously reported work on GAGG persistent luminescence[11], adjusting the ratio of A/B ions (non-stoichiometric ratio) shifts the CB band and thus adjusts the depth of the electron trap as well as tuning the emission wavelength is theoretically considered to be feasible. In addition, it is noted that Ga^{3+} in larger than Al^{3+}, potentially creating a more favorable environment for Gd^{3+} ion occupation and leading to more significant perturbations in the luminescence ion's surroundings. Therefore, this chapter aims to investigate the effects of non-stoichiometry on the persistent luminescence properties of GGG and GAGG-based materials.

In this work, a series of $Gd_{3+x}Ga_{5-x}O_{12}$ materials have been synthesized using

crystallization from the melt method by ADL. PXRD Rietveld refinement reveals a linear increase in the lattice parameter *a* as x values increasing from 0 to 0.7, confirming the formation of highly nonstoichiometric GGG solid solutions. SPD refinement result shows that more than 30% of the six-coordinated Ga is occupied by Gd^{3+} in ns-GGG. A comparison of the solid solution ranges of GAG ($0 \le x \le 0.6$) and GGG ($0 \le x \le 0.7$) shows that larger *B*-site ions allowed a wider solid solution zone. The VT-XRD results demonstrate that the non-stoichiometric GGG is stable up to 1150 ^{o}C and then decomposes into the stoichiometric GGG, Gd_3GaO_6, and Gd_2O_3, consistent with the thermal stability of ns-GAG. In addition, the Gd L_3 edge EXAFS spectra of ns-GGG showed the same behavior as ns-GAG, explaining the local structure of the eight coordinated Gd^{3+} ion. $Gd_{3+x}(Ga_{0.6}Al_{0.4})_{5-x}O_{12}$ garnets were synthesized by crystallisation from glass. PXRD refinement result shown that the cell parameter *a* linear increase as the x value increases from 0 to 0.6 and up to 30% six coordinated Al/Ga site can substituted by Gd. The ratio of Ga/Al on the octahedron decreases with the occupation of Gd, which leads to cell parameter changes that are not strictly linear growing with increasing x values. SEM images showed that the ns-GAGG bead samples had short fiber nanostructures in the outer layer and irregular polygonal grains in the centre with lengths and widths ranging from 0.3 to 1 μm.

Based on the previous reports on GGG[12-13] and GAGG-based[14] persistent luminescent materials, GGG:Eu^{3+}/Cr^{3+}, GGG: Eu^{3+}/Tb^{3+} and GAGG:Ce^{3+}/Cr^{3+}, GAGG:Tb^{3+} persistent luminescence materials was chosen to study the effect of non-stoichiometric ratio on the emission color and persistent luminescence performance. The persistent luminescence exploration of GGG: Eu^{3+}/Cr^{3+} revealed that neither the stoichiometric GGG nor the non-stoichiometric GGG exhibited the persistent luminescence phenomenon similar to the reported. For ns-GGG: Eu^{3+}/Tb^{3+} persistent luminescence, the emission color remained unchanged, as the f–f transition of Tb^{3+} ions insensitive to new BO_6 sites. Persistent luminescence performance of ns-GAGG: Ce^{3+}/Cr^{3+} suggest that changes in the dodecahedral crystal field caused by the occupation of Al/Ga by Gd affect the emission colour and affect the trap depth thus changing the decay rate of the persistent luminescence.

In addition, the synthesis of a range of non-stoichiometric garnets and perovskite compounds were also explored. These non-stoichiometric garnets may yield new

applications in other areas that need to be further explored in the future.

Structure and luminescence properties of the $Lu_{4-\alpha}Al_{2-x}Si_xO_{9+\delta}$ ($0 \leq x \leq 1$) solid solution

Based the work on new unknown $(Lu/Mg)_4(Al/Si)_2O_9$ compounds discovered by our collaborative group in University of Science and Technology Beijing[10], the synthesis of $Lu_4Al_2O_9$, $Lu_4(Al/Si)_2O_9$ solid solution and the exploration of its optical properties are considered to be of great promise and significance. The substitution of Si^{4+} for Al^{3+} may introduce Lu vacancies or additional oxygen into the structure, leading to the formation of $Lu_{4-\alpha}(Al/Si)_2O_{9+\delta}$ with local defects and Al/Si disorder, which is respond to the luminescence performance. Thus, this chapter aims to investigate the synthesis, detailed crystal structures and luminescence properties of solid solutions with Si^{4+} substituted Al^{3+} in $Lu_4Al_2O_9$.

In this chapter, single phases $Lu_4Al_2O_9$ (LuAM) and solid solution compounds of $Lu_{4-\alpha}Al_{2-x}Si_xO_{9+\delta}$ ($x = \alpha/3 + \delta/2$, $x = 0.5$, 1) (LuASO) were successfully synthesised for the first time utilizing melt crystallisation method by the ADL. PXRD and SPD results suggested that the substitution of Si^{4+} for Al^{3+} resulted in an elevation of crystal structure symmetry, transitioning from a monoclinic $P2_1/c$ phase to an orthorhombic *Pbnm* phase. Average and local structural characterization though PXRD, SEM and ^{27}Al, ^{29}Si NMR revealed that the Si^{4+} substitution for Al^{3+} in LuAM lead to the formation of solid solutions with Lu vacancies and extra oxygen coexist at $x = 1$, which contains locally ordered chains of composite $(Al,Si)O_4$ and AlO_5 polyhedra, in contrast to the parent phase that had isolated AlO_4 tetrahedra.

The luminescence spectroscopic studies of the two compounds with different structures showed that the phase transition from $P2_1/c$ to *P*bnm leads to different luminescent properties as $Ce^{3+}/Eu^{3+}/Er^{3+}$ occupy sites with different local symmetries. As a result, two new solid solution phosphors were discovered, including the yellow LuAM: Ce^{3+} phosphor with blue excitation and blue LuASO: Ce^{3+} phosphor with UV excitation. In addition, the Eu^{3+} occupied different local symmetry sites in the two different hosts, leading to a more reddish emission colour in LuASO. Furthermore, the investigation of up conversion LuAM: Er^{3+}/Yb^{3+} and LuASO: Er^{3+}/Yb^{3+} revealed a shift in emission color from orange to yellow due

to changes in symmetry. These findings suggest that cation substitution can induce alterations in crystal symmetry and the introduction of defects and polyhedral distortion, which can affect the local environment of the dopant consequently affecting luminescence performance. The phase transition induced by cation substitution offers a promising avenue for the exploration of new phosphors to fulfill the requirements of white LEDs.

Moreover, the potential of Mg-Si substituted Lu-Al in $Lu_4Al_2O_9$ solid solutions were explored to yield new phosphors. Additionally, during the investigation of $Lu_{4-\alpha}Al_{2-x}Si_xO_{9+\delta}$ solid solutions, hexagonal $LuAlO_3$ along with Al_2O_3 transparent glass-ceramics were discovered, which hold promise as intriguing optical materials. These investigations will be further investigated in depth.

Résumé Générale

L'objectif de ma thèse était de synthétiser et caractériser la structure ainsi que d'explorer les propriétés de nouvelles céramiques solides pour répondre aux besoins dans divers domaines[1]. Les méthodes de synthèse hors-équilibre, impliquant l'utilisation de voies cinétiques pour élaborer du verre, des phases métastables, des structures amorphes éloignées de l'équilibre thermodynamique en optimisant les conditions de synthèse, sont des approches efficaces pour synthétiser de nouveaux matériaux. La lévitation aérodynamique (ADL) combinée au chauffage par laser est une technique développée au CEMHTI pour la synthèse hors-équilibre de nouveaux matériaux via la cristallisation directe depuis le liquide fondu à haute température ou du verre. Cette voie de synthèse a été utilisée avec succès pour synthétiser diverses nouvelles céramiques qui ne peuvent être élaborées par des méthodes traditionnelles de réaction à l'état solide. Ces matériaux ont des applications potentielles dans le domaine de l'optique, du stockage d'énergie et dans d'autres domaines [2-5].

Le système RE_2O_3-$(Al/Ga)_2O_3$ permet l'obtention de céramiques qui ont de nombreuses applications dans de multiples domaines, tels que l'électronique, les catalyseurs, le magnétisme et l'optique[6-8]. Il est donc prometteur de rechercher et de synthétiser de

nouveaux matériaux dans ce système et d'étudier leur structure et leurs applications. Dans ces systèmes, des grenats YAG hautement non-stœchiométriques[9] ont récemment été rapportés et il a été démontré que la non-stœchiométrique avait des effets inattendus sur les propriétés de luminescence. De plus, un composé $(Lu/Mg)_4(Al/Si)_2O_9$ a été trouvé lors de l'étude des grenats $(Lu/Mg)_3(Al/Si)_5O_{12}$[10] et a montré un potentiel intéressant en tant que matériau hôte pour la luminescence. Sur la base de ces deux études, ma thèse a porté sur trois systèmes : « structure et propriétés de luminescence de $Gd_{3+x}Al_{5-x}O_{12}$ non-stœchiométriques ($0 \leq x \leq 0.6$) », « structure et propriétés de luminescence persistante de $Gd_{3+x}Ga_{5-x}O_{12}$ et $Gd_{3+x}(Al_{0.4}Ga_{0.6})_{5-x}O_{12}$ ($0 \leq x \leq 0.6$) non-stœchiométriques ", et "structure et propriétés de luminescence de la solution solide $Lu_{4-\alpha}Al_{2-x}Si_xO_{9+\delta}$ ($0 \leq x \leq 1$)". Ce résumé donne les principales conclusions de ces trois chapitres.

Structure et propriétés de luminescence de $Gd_{3+x}Al_{5-x}O_{12}$ ($0 \leq x \leq 0.6$) fortement non-stœchiométriques

Ce chapitre vise à étudier la synthèse, la structure et les propriétés de luminescence des composés $Gd_{3+x}Al_{5-x}O_{12}$ non-stœchiométriques en se basant sur les travaux des composés $Y_{3+x}Al_{5-x}O_{12}$ non-stœchiométriques ($0 \leq x \leq 0{,}40$)[9]. Étant donné que l'ion Gd^{3+} est plus gros que l'ion Y^{3+}, il devrait offrir plus de possibilités pour insérer de larges ions dopants (terres rares) dans les sites octaédriques B de la structure grenat non-stœchiométrique. Dans ce but, les distributions des ions dopants de différentes tailles dans le GAG ont été explorées ainsi que la dépendance des propriétés de luminescence aux nouveaux sites luminescents grâce à la spectroscopie de luminescence.

Dans ce travail, la solution solide $Gd_{3+x}Al_{5-x}O_{12}$ a été synthétisée à partir de la cristallisation du verre. L'affinement Rietveld de données DRX sur poudre (PXRD) révèle une augmentation linéaire du paramètre de maille « a » lorsque les valeurs x augmentent de 0 à 0,6, confirmant la formation de solutions solides de GAG hautement non-stœchiométriques (ns-GAG). Les résultats de l'affinement de données de diffraction sur poudre au synchrotron (SPD) suggèrent que pour $Gd_{3.6}Al_{4.4}O_{12}$, jusqu'à 30 % de Gd^{3+} occupe les sites Al^{3+} de coordinance 6, ce qui est 50 % supérieur aux 20 % de substitution des sites octaédrique

d'Al^{3+} par Y^{3+} dans $Y_{3.4}Al_{4.8}O_{12}$ non-stœchiométrique, bien que Gd^{3+} soit plus grand que Y^{3+}. Les données VT-PXRD recueillies, depuis la température ambiante jusqu'à 1600°C, montrent que le ns-GAG se décompose progressivement en GAP et Al_2O_3 au-delà de 1150°C, ce qui est bien inférieur à la température de stabilisation thermique (1350°C) du ns-YAG, et ce à cause de la plus grande taille de Gd^{3+} comparé à Y^{3+}. Les images MEB ont révélé la morphologie des grains de GAG, qui apparaissent sous la forme de polygones irréguliers de 2 à 3 microns de largeur, et montrent une porosité qui empêche la production de céramiques transparentes. Les images STEM-HAADF à la résolution atomique ont été utilisées pour localiser l'emplacement du Gd^{3+} octaédrique et suggèrent un site Al octaédrique désordonné avec la substitution d'Al^{3+} par des Gd^{3+}. Pour sonder l'environnement local autour de l'ion Gd^{3+}, des mesures d'EXAFS ont été effectuées sur l'échantillon ns-GAG au niveau du seuil L_3 de Gd (7243 eV), et une comparaison entre les spectres d'EXAFS expérimentaux et simulés a confirmé la substitution sur le site octaédrique des ions Al^{3+} par des ions Gd^{3+}.

Pour mieux comprendre la distribution et l'emplacement des ions dopants dans la structure ns-GAG, diverses expériences ont été réalisées. Dans un premier temps, des cartographies par microsonde ont démontré l'homogénéité de la distribution des ions dopants dans la structure. Des cartographies STEM-EDS à la résolution atomique ont été collectées afin d'observer directement la distribution de Tb^{3+} dans l'échantillon ns-$Gd_{3.2}Al_{4.8}O_{12}$: 10% Tb^{3+}. Des spectres EDS localisés au niveau de Al_{16a} du site A et de $2Gd_{24c} + 2Al_{24d}$ du site A + B ont été extraits et suggèrent que Tb se situe non seulement sur AO_8 mais aussi sur BO_6. Les spectres EXAFS sur le seuil L_3 des terres rares (Yb^{3+} et Tm^{3+}) dans les échantillons de ns-GAG ont été collectés expérimentalement, et l'ajustement de différentes configurations de substitution atomique générées par Supercell comparé aux spectres expérimentaux a montré que les ions dopants de plus petite taille Yb/Tm préfèrent occuper le site BO_6 de coordinance 6.

Pour comprendre l'impact de la non-stœchiométrie sur les propriétés de luminescence, divers ions dopants de tailles et de comportements de transition différents (par exemple, Ce^{3+} : transition f-d ; Tb^{3+}, Er^{3+}, Tm^{3+} : transition f-f) ont été choisis pour analyser leurs

propriétés de luminescence. L'étude de photoluminescence de Ce^{3+} montre que la non-stœchiométrie affecte le léger décalage vers le rouge de la bande d'émission dû au changement environnemental de AO_8. Cependant, il n'y a pas de changement évident dans la couleur d'émission car Ce^{3+} n'est localisé qu'au niveau du site A et non pas sur les deux sites, ce qui est cohérent avec les échantillons ns-YAG : Ce^{3+}. Tb^{3+} s'est avéré être distribué sur les sites AO_8 et BO_6 ; cependant, les spectres d'émission de ns-GAG ne présentent pas de différence significative en raison de l'insensibilité de la transition f–f de Tb^{3+} à l'environnement. En revanche, les études de spectres d'émission de GAG : Er^{3+}/Yb^{3+} et Tm^{3+}/Yb^{3+}, matériaux pour la up-conversion, ont démontré un changement significatif de la couleur d'émission qui est dû à l'hypersensibilité des transitions de Er^{3+} et Tm^{3+} au nouveau site local BO_6 dans le ns-GAG.

Structure et propriétés de luminescence de $Gd_{3+x}Ga_{5-x}O_{12}$ et $Gd_{3+x}(Al_{0.4}Ga_{0.6})_{5-x}O_{12}$ ($0 \leq x \leq 0.6$) non-stœchiométriques

Les composés de structure grenat sont non seulement d'excellents matériaux hôtes pour des applications de up-conversion et de down-conversion, mais également des matériaux hôtes bien connus pour la luminescence persistante. Sur la base des travaux menés sur ns-GAG et des travaux précédemment rapportés sur la luminescence persistante de GAGG[11], il est théoriquement possible, via l'ajustement du rapport des ions A/B (rapport non-stœchiométrique), de permettre le déplacement de la bande CB et donc l'ajustement de la profondeur du piège à électrons ainsi que de la longueur d'onde d'émission. De plus, comme l'ion Ga^{3+} est plus gros que l'ion Al^{3+}, il est possible de créer un environnement plus favorable à l'occupation des ions Gd^{3+} et de conduire à des perturbations plus importantes de l'environnement de l'ion luminescent. Par conséquent, ce chapitre vise à étudier les effets de la non-stœchiométrie sur les propriétés de luminescence persistante des matériaux à base de GGG et GAGG.

Dans ce travail, une série de matériaux $Gd_{3+x}Ga_{5-x}O_{12}$ a été synthétisée par cristallisation directe du liquide fondu lors du refroidissement rapide (trempe) en utilisant le système ADL. L'affinement Rietveld de données PXRD révèle une augmentation linéaire du

paramètre de maille « a » lorsque les valeurs de x augmentent de 0 à 0,7, confirmant la formation de solutions solides GGG hautement non-stœchiométriques. Le résultat de l'affinement de données SPD montre que jusqu'à 30% du Ga en coordinance 6 est substitué par Gd^{3+} dans ns-GGG. Une comparaison des solutions solides de GAG ($0 \leq x \leq 0,6$) et GGG ($0 \leq x \leq 0,7$) montre que lorsque le site B est occupé par un plus large ion alors la zone de formation de solutions solides est plus étendue. Les résultats de VT-XRD démontrent que le GGG non-stœchiométrique est stable jusqu'à 1150°C, puis se décompose en GGG stœchiométrique, Gd_3GaO_6 et Gd_2O_3 à plus haute température, en accord avec la stabilité thermique du ns-GAG. De plus, les spectres EXAFS du seuil Gd-L_3 dans ns-GGG montrent un comportement similaire à ns-GAG, expliquant la structure locale de l'ion Gd^{3+} en coordinance 8. Les grenats $Gd_{3+x}(Ga_{0.6}Al_{0.4})_{5-x}O_{12}$ ont été synthétisés par cristallisation du verre. Le résultat de l'affinement Rietveld de données PXRD a montré que le paramètre de maille augmentait linéairement lorsque la valeur x augmentait de 0 à 0,6 et que jusqu'à 30 % des sites Al/Ga en coordinance 6 pouvaient être occupés par Gd. Le rapport Ga/Al sur l'octaèdre diminue avec le taux d'occupation de Gd, ce qui conduit à une croissance non-linéaire du paramètre de maille avec l'augmentation des valeurs de x. Les images MEB ont montré que les échantillons sous forme de bille de ns-GAGG avaient une couche externe composée de nanostructures sous forme de fibres courtes et des grains polygonaux irréguliers au centre avec des longueurs et des largeurs allant de 0,3 à 1 µm.

Sur la base de précédentes études sur les matériaux à luminescence persistante de type GGG[12-13] et GAGG[14], les matériaux à luminescence persistante GGG:Eu^{3+}/Cr^{3+}, GGG:Eu^{3+}/Tb^{3+} et GAGG:Ce^{3+}/Cr^{3+}, GAGG:Tb^{3+} ont été choisis pour étudier l'effet du taux de non-stœchiométrique sur la couleur d'émission et les performances de luminescence persistante. L'exploration de la luminescence persistante de GGG : Eu^{3+}/Cr^{3+} a révélé que ni le GGG stœchiométrique ni le GGG non-stœchiométrique ne présentaient le phénomène de luminescence persistante, contrairement à ce qui a été rapporté pour la composition stœchiométrique élaborée par solution solide. Concernant la luminescence persistante de ns-GGG : Eu^{3+}/Tb^{3+}, la couleur d'émission reste inchangée, car la transition f–f des ions Tb^{3+} est insensible aux nouveaux sites BO_6. Les performances de luminescence persistante de

ns-GAGG : Ce^{3+}/Cr^{3+} suggèrent que les changements du champ cristallin du site dodécaédrique causés par la substitution d'Al/Ga par Gd affectent la couleur d'émission et la profondeur de piège, modifiant ainsi le taux de décroissance de la luminescence persistante.

En outre, la synthèse d'une gamme de grenats non-stœchiométriques et de composés pérovskites a également été explorée. Ces grenats non-stœchiométriques pourrainet donner lieu à de nouvelles applications dans d'autres domaines qui doivent être explorés plus avant à l'avenir.

Structure et propriétés de luminescence de la solution solide $Lu_{4-\alpha}Al_{2-x}Si_xO_{9+\delta}$ ($0 \leq x \leq 1$)

Sur la base des travaux menés sur le nouveau composé $(Lu/Mg)_4(Al/Si)_2O_9$ découvert par notre groupe lors d'un récent travail de collaboration avec l'IPE à Pékin[10], la synthèse de la solution solide $Lu_4Al_2O_9$ - $Lu_4(Al/Si)_2O_9$ et l'exploration de ses propriétés optiques ont été envisagées. La substitution de Al^{3+} par Si^{4+} peut induire dans la structure des lacunes de Lu ou/et des oxygènes supplémentaires, conduisant à la formation de $Lu_{4-\alpha}(Al/Si)_2O_{9+\delta}$ avec des défauts locaux et un désordre Al/Si, qui répond aux performances de luminescence. Ainsi, ce chapitre vise à étudier la synthèse, les structures cristallines en détail et les propriétés de luminescence de solutions solides issues du composé $Lu_4Al_2O_9$ dans lequel Al^{3+} est substitué par Si^{4+}.

Dans ce chapitre, la phase stœchiométrique $Lu_4Al_2O_9$ (LuAM) et des composés issus de la solution solide $Lu_{4-\alpha}Al_{2-x}Si_xO_{9+\delta}$ ($x = \alpha/3 + \delta/2$, x = 0,5, 1) (LuASO) ont été synthétisés avec succès pour la première fois en utilisant la cristallisation du liquide fondu à haute température par ADL. Les résultats obtenus par PXRD et SPD suggèrent que la substitution d'Al^{3+} par Si^{4+} entraîne une élévation de la symétrie de la structure cristalline, passant d'une phase monoclinique $P2_1/c$ à une phase orthorhombique *Pbnm*. La caractérisation de la structure moyenne et locale par PXRD, MEB et RMN ^{27}Al et ^{29}Si a révélé que la substitution d'Al^{3+} par Si^{4+} dans LuAM conduit à la formation de solutions solides avec des lacunes de Lu et des oxygènes supplémentaires dont les deux coexistent pour x = 1, et qui contiennent des

chaînes composites localement ordonnées de $(Al,Si)O_4$ et de polyèdres AlO_5, contrairement à la phase mère dans laquelle on trouve des tétraèdres isolés d'AlO_4.

Les études de luminescence des deux composés avec des structures différentes ont montré que la transition de phase de $P2_1/c$ à *P*bnm conduit à des propriétés de luminescence différentes car $Ce^{3+}/Eu^{3+}/Er^{3+}$ occupent des sites avec différentes symétries locales. En conséquence, deux nouvelles solutions solides ont été découvertes, dont le luminophore jaune LuAM : Ce^{3+} excité par le bleu et le luminophore bleu LuASO : Ce^{3+} excité par UV. De plus, dans les deux structures hôtes l'Eu^{3+} occupe des sites de symétrie locale différents, conduisant à l'émission d'une couleur plus rouge dans LuASO. De plus, l'étude de l'up-conversion de LuAM : Er^{3+}/Yb^{3+} et LuASO : Er^{3+}/Yb^{3+} a révélé un changement de couleur d'émission de l'orange au jaune en raison de changements de symétrie. Ces résultats suggèrent que la substitution de cations peut induire des altérations de la symétrie cristalline et l'introduction de défauts et de distorsions polyédriques, qui peuvent affecter l'environnement local du dopant, affectant par conséquent les performances de luminescence. La transition de phase induite par la substitution cationique offre une voie pour l'exploration de nouveaux luminophores pour répondre aux exigences des LED blanches.

Le potentiel de la substitution de Lu-Al par Mg-Si dans des solutions solides de $Lu_4Al_2O_9$ a également été exploré pour produire de nouveaux luminophores. De plus, au cours de l'étude des solutions solides $Lu_{4-\alpha}Al_{2-x}Si_xO_{9+\delta}$, des vitrocéramiques transparentes de $LuAlO_3$ hexagonale et Al_2O_3 ont été découvertes et promettent des propriétés optiques intéressantes. Ces investigations feront l'objet d'un examen plus approfondi.

References

[1] C.N.R. Rao, Journal of Materials Chemistry C. ***1999****, 9, 1-14.*

[2] L. Hennet, V. Cristiglio, J. Kozaily et al., The European Physical Journal Special Topics. ***2011****, 196, 151-165.*

[3] M. Boyera, E. Verona, A. Isabel Becerro et al., CrystEngComm. ***2015****, 17, 6127-6135.*

[4] J. Fan, V. Sarou-Kanian, X. Yang et al., Chemistry of Materials. ***2020****, 32, 9016-9025.*

[5] M. Allix, S. Alahrache, F. Fayon et al., Advanced Materials. ***2012****, 24, 5570-5575.*

[6] X.Q. Yin, Y.L. Zhong, Y.M. Cao et al., Journal of Applied Crystallography. ***2021****, 54, 1641-1646.*

[7] M. Paddison, J.A. Jacobsen, H. Petrenko et al., Science. ***2015****, 350, 179-181.*

[8] G. Okada, M. Akatsuka, H. Kimura et al., Sensors and Materials. ***2018****, 30, 1547.*

[9] W.W Cao, A. Isabel Becerro, V. Castaing et al., Advanced Functional Materials. ***2023****, 33, 2213418.*

[10] S. Feng, Y. Guo, M. Allix et al., Cell Reports Physical Science. ***2022****, 3, 101044.*

[11] J. Ueda, K. Kuroishi, S. Tanabe, Applied Physics Express. ***2014****, 7, 062201.*

[12] J. Xu, J. Ueda, S. Tanabe, Optical Materials Express. ***2015****, 5, 963.*

[13] J. Ueda, S. Miyano, J. Xu et al., Advanced Photonics Research. ***2021****, 2, 2000102.*

[14] R. Tomala, K. Korkus, V. Boiko et al., Journal of Alloys and Compounds. ***2021****, 889, 161745.*

Appendix

Appendix A Samples preparation and characterisation techniques

Appendix A.1 Sample preparation method

Text A.1.1

The main synthetic methods were used in this work are crystallization from melt and crystallization from glass using ADL with laser heating. The process flow chart is shown in ***Fig A.1.1.*** The procedure was as follows: commercial staring materials (oxide purity and manufacturer information and are listed in ***Table A.1.1***) were weighed according to chemical formula (sample chemical formulas are listed in ***Table A.1.2***) and mixed well with ethanol in an agate mortar. The dried powder is pressed into a pellet with a diameter of 13 mm at a pressure of 555 MPa. Subsequently smaller fragments from the broken pellets are used to synthesize at ADL laser equipment (see ***Fig A.1.2***). O_2 or Ar was utilized to levitate the sample while a pair of CO_2 lasers heats the sample to completely melt it (approx. 1800°C-2400°C) for a few seconds until it is completely stable in the gas jet (no contact with the nozzle). Finally, the glass or crystal beads were obtained in a rapid cooling process, by switching off the lasers. Crystallized beads can be obtained directly from the melt by rapid cooling process, which is called the “crystallized from the melt” method. Alternatively, the glass beads are crystallized by a second heating step in a muffle furnace at crystallization temperature. Synthesis conditions for each sample are shown in ***Table A.1.3.***

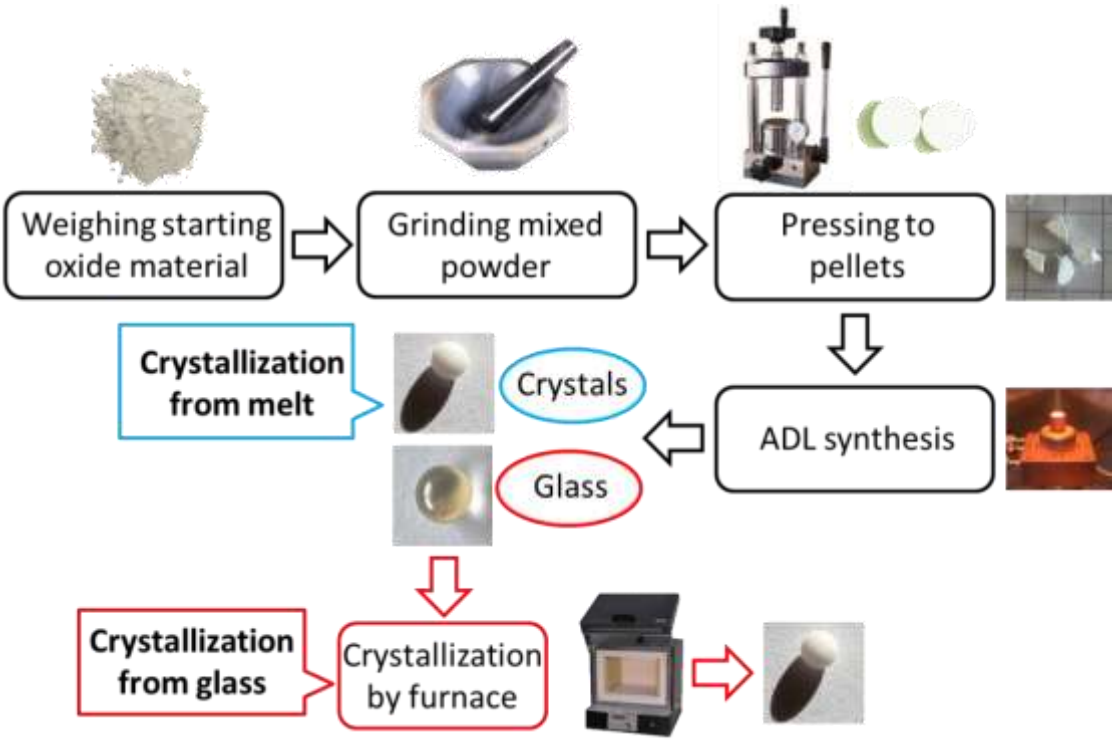

Fig A.1.1 *Flow chart of sample preparation.*

Table A.1.1 *Chemical information*

Commercial Chemical	Purity	ACS	Supplier
Y_2O_3	99.99%	1314-36-9	Alfa Aesar
Gd_2O_3	99.99%	12064-62-9	Strem Chemicals Inc
CeO_2	99.99%	1306-38-3	Alfa Aesar
Sm_2O_3	99.9%	12060-58-1	Strem Chemicals Inc
Eu_2O_3	99.99%	1308-96-6	Strem Chemicals Inc
Tb_2O_3	99.9%	1207-01-3	Strem Chemicals Inc
Ho_2O_3	99.99%	12056-62-8	Strem Chemicals Inc
Er_2O_3	99.995%	12061-16-4	Strem Chemicals Inc
Tm_2O_3	99.9%	12036-44-1	Strem Chemicals Inc
Yb_2O_3	99.99%	1314-37-0	Alfa Aesar
Lu_2O_3	99.9%	12032-20-1	Thermo scientific
Al_2O_3	99.997%	1344-28-1	Alfa Aesar
Ga_2O_3	99.998%	12024-21-4	Strem Chemicals Inc
SiO_2	99.999%	7631-86-9	Strem Chemicals Inc
MgO_2	99.95%	1309-48-4	Alfa Aesar
BN	99.5%	10043-11-5	Alfa Aesar
Cr_2O_3	99.97%	1308-38-9	Alfa Aesar

Table A.1.2 *Abbreviation and the full chemical formula of the sample*.

GAG system	Chemical formula (x = 0, 0.2, 0.4, 0.6)
GAG	$Gd_{3+x}Al_{5-x}O_{12}$
GAG: 2%Ce^{3+}	$(Gd_{0.98}Ce_{0.02})_{3+x}Al_{5-x}O_{12}$
GAGG:1%Tb^{3+}	$(Gd_{0.99}Tb_{0.01})_{3+x}(Ga_{0.2}Al_{0.8})_{5-x}O_{12}$
GAG: 10%Tb^{3+}	$(Gd_{0.9}Tb_{0.1})_{3+x}Al_{5-x}O_{12}$
GAG: 2%Er^{3+}/20%Yb^{3+}	$(Gd_{0.78}Er_{0.02}Yb_{0.2})_{3+x}Al_{5-x}O_{12}$
GAG: 1%Tm^{3+}/10%Yb^{3+}	$(Gd_{0.89}Tm_{0.01}Yb_{0.1})_{3+x}Al_{5-x}O_{12}$
GAG: 1%Ho^{3+}/10%Yb^{3+}	$(Gd_{0.89}Ho_{0.01}Yb_{0.1})_{3+x}Al_{5-x}O_{12}$
GGG system	Chemical formula (x = 0, 0.2, 0.4, 0.6)
GGG	$Gd_{3+x}Ga_{5-x}O_{12}$
GGG: 0.7%Eu^{3+}/0.05%Cr^{3+}	$(Gd_{0.993}Eu_{0.007})_{3+x}Ga_{4.999-x}Cr_{0.001}O_{12}$
GGG: 0.1%Eu^{3+}/0.1%Tb^{3+}	$(Gd_{0.997}Eu_{0.001})_{3+x}(Ga_{0.999}Tb_{0.001})_{5-x}O_{12}$
GAGG system	Chemical formula (x = 0, 0.2, 0.4, 0.6)
GAGG	$Gd_{3+x}(Al_{0.2}Ga_{0.3})_{5-x}O_{12}$
GAGG:0.5%Ce^{3+}/0.05%Cr^{3+}	$(Gd_{0.995}Ce_{0.005})_{5+x}(Al_{0.4}Ga_{0.6})_{4.999-x}Cr_{0.001}O_{12}$
GAGG:1%Tb	$(Gd_{0.99}Ce_{0.01})_{5+x}(Al_{0.8}Ga_{0.2})_{5-x}O_{12}$
$Lu_4Al_2O_9$-SiO_2 system	Chemical formula (x = 0, 0.5, 1, 1.25)
$Lu_4Al_2O_9$-SiO_2 (Lu vacancies)	$Lu_{4-x/3}Al_{2-x}Si_xO_9$
$Lu_4Al_2O_9$-SiO_2 (Lu vacancies and extra oxygen)	$Lu_{4-\alpha}Al_{2-x}Si_xO_{9+\delta}$

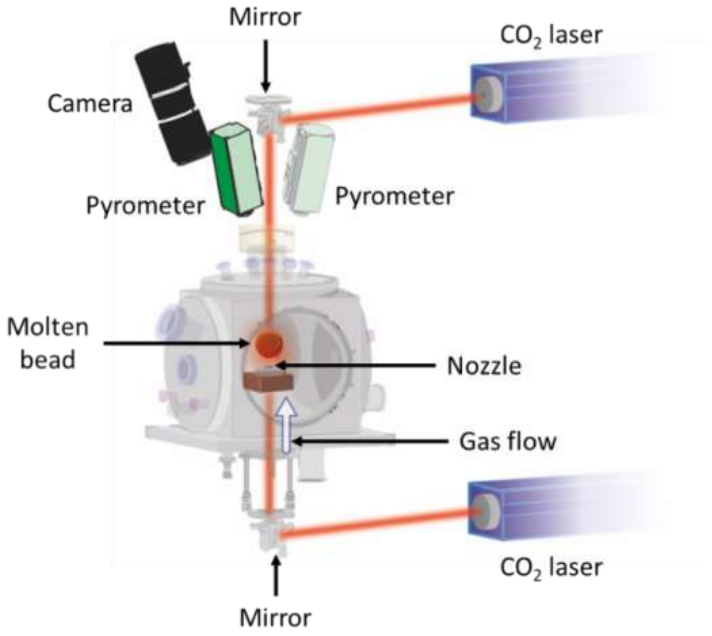

Fig A.1.2 *Schematic diagram of ADL combined with laser heating setup.*

Table A.1.3 *Sample synthesis methods and detailed synthesis conditions.*

GAG system	Synthesis method	Synthesis equipment	Synthesis condition
GAG	Crystallisation from glass	Glass: ADL Ceramic: Muffle furnace	Oxygen 950^{o}C-3h in air
GAG: 2%Ce^{3+}	Crystallisation from glass	Glass: ADL Ceramic: Muffle furnace	Oxygen 950^{o}C-3h in 95%Ar/5%H_2
GAG: 10%Tb^{3+} GAG: 2%Er^{3+}/20%Yb^{3+} GAG: 1%Tm^{3+}/10%Yb^{3+} GAG: 1%Ho^{3+}/10%Yb^{3+}	Crystallisation from glass	Glass: ADL Ceramic: Muffle furnace	Oxygen 950^{o}C-3h in air
GGG system			
GGG GGG: Eu^{3+}/Cr^{3+}	Crystallisation from glass	Glass: ADL Ceramic: Muffle furnace	Argon 950^{o}C-3h in air
GAGG system			
GAGG GAGG:Eu^{3+}/Cr^{3+} GAGG:Eu^{3+}/Tb^{3+} GAGG:Tb^{3+}/Cr^{3+}	Crystallisation from glass	Glass: ADL Ceramic: Muffle furnace	Oxygen 950^{o}C-3h in air
GAGG:Ce^{3+}/Cr^{3+}	Crystallisation from glass	Glass: ADL Ceramic: Muffle furnace	Oxygen 950^{o}C-3h in 95Ar/5%H_2
$Lu_4Al_2O_9$-SiO_2 system			
($Lu_{4-x/3}Al_{2-x}Si_xO_9$) (Lu4-Al2-xSixO9+) LAM: Eu^{3+}, LAM:Er^{3+}/Yb^{3+} and LuASO:1%Ce^{3+}, LASO:Er^{3+}/Yb^{3+}	Crystallisation from mel	ADL	Oxygen
LAM: Ce^{3+} and LuASO:Ce^{3+}	Crystallisation from melt	ADL	Argon

Appendix A.2 Material characterization method

Appendix A.2.1 Powder X-ray diffraction (PXRD), variable temperature X-ray diffraction (VT-XRD) and synchrotron powder diffraction (SPD)

When X-rays irradiate a sample, the scattering of X-rays by individual atoms within the crystal interferes, leading to the generation of intense X-ray diffraction in specific directions.

The Bragg equation represents the fundamental condition for X-ray diffraction in a crystal, given by 2dsinθ = nλ (where d is the interplanar spacing, θ is the Bragg angle, and λ is the X-ray wavelength) (see ***Fig A.2.1a)*** When X-rays illuminate the sample from different angles, diffraction occurs on different crystal planes. A detector captures the diffracted photons reflected from these planes, yielding a diffractogram that reveals the relationship between angles and intensities (see ***Fig A.2.1b***). Utilizing the Bragg equation, you can deduce the interplanar spacing (d) by employing X-rays with known wavelengths, thus obtaining crucial information about the crystal structure. The unit cell dimensions and internal symmetry (space group) by analysis of peak positions and systematic absences. In addition, information about the position and species of atoms can be obtained from the diffraction patterns intensity based on the structure factor (a parameter that quantitatively describes the pattern of influence of atomic arrangement and atomic species on the diffraction intensity). This detailed structural information and corrected crystal structures can be obtained by the Rietveld refinement method

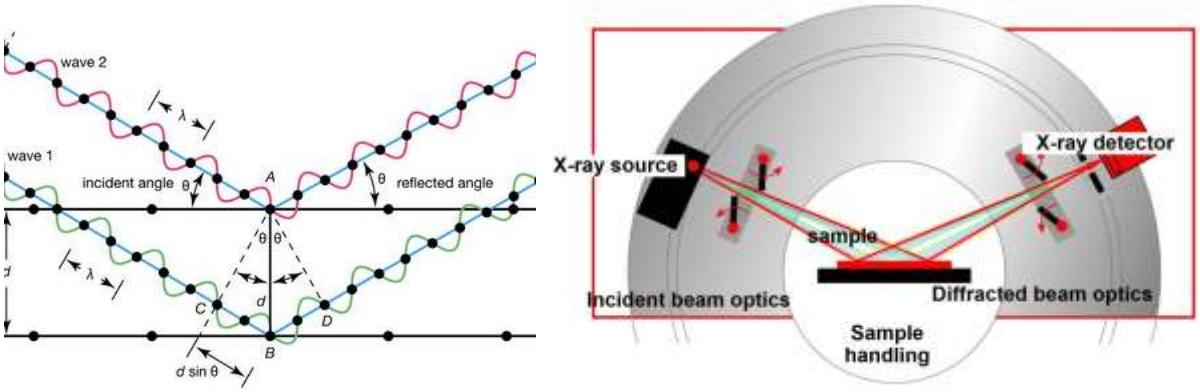

Fig A.2.1 (a) *Bragg law[1] and* ***(b)*** *schematic of the laboratory XRD diffractometer[2] in Bragg-Brentano geometry.*

The Rietveld refinement technique entails the computation of the polycrystalline diffraction profile, employing a specific peak shape function and utilizing an initial structural model with associated parameters. Concurrently, the iterative application of the least-squares method is employed to progressively optimize both the crystal's structural parameters and the parameters governing the peak shape. This iterative process aims to reconcile the calculated diffraction profile with the experimental diffraction data,

culminating in the acquisition of refined structural parameters that accurately reflect the crystal's characteristics. From these structural parameters, detailed average structural information can be obtained including cell parameters, atomic coordinates, bond lengths and angles, occupancy, multiple quantitative analyses, grain sizes, stress-strain analyses, etc.

Rietveld method uses the entire diffractogram data for its analysis, and a polycrystalline diffractogram can be viewed as a series of equally spaced columns of 2θ-y_{oi}data. If the structure of the crystal is known, then the theoretical intensity y_{ci} at each 2θ can be calculated using the crystal structure parameters as well as the peak shape parameters, and then the least squares method can be used to compare it with the measured intensity y_{oi}, and the various parameters can be continuously adjusted to minimise the difference M, i.e., the full spectrum is fitted.

$$M = \sum_{i=1}^{n} W_i(y_{oi} - y_{ci})$$

Where W_i is the statistical weight, y_{oi}, is observed intensity and y_{ci} is calculated intensity.

The theoretically calculated intensity (y_{ci}) can be calculated by integrating the intensity and the peak shape function. The theoretically calculated intensity y_{ci} for 2θ at a point on the diffraction pattern can be expressed as:

$$y_{ci} = y_{bi} + \sum_{k=1}^{m} I_k\, y_k(x_k)$$

Where $y_k(x_k)$ is the peak shape function, I_k is integrated intensity, y_{bi} is the background intensity.

In X-ray diffraction, examples of commonly used peak shape include the Pseudo-Voigt and Pearson Ⅶ function, which is in essence a combination of Gaussian and Lorentzian functions.

$$y(x) = n * G(x) + (1 - n) * L(x)$$

Where $G(x)$ is Gaussian function and $L(x)$ is Lorentzian function.

I_{hkl} can be calculated from the crystal structure and atomic composition, etc.; The integral intensity is calculated as:

$$I_{hkl} = S \times L_\theta \times P_\theta \times A_\theta \times T_{hkl} \times M_{hkl} \times E_{hkl} \times |F_{hkl}|^2$$

Where S is the scaling or proportionality factor, L_θ, P_θ and A_θ are Lorentz multiplier, polarization factor and absorption multiplier, respectively. T_{hkl} is the preferred orientation factor, M_{hkl} is the multiplicity factor, E_{hkl} is the extinction factorand $|F_{hkl}|$ is the structure factor.

Generally, the background is calculated as a Chebyshev polynomial.

As a result of its development, the Rietveld method can also be used for quantitative analysis of the physical phase, which is calculated by the formula:

$$W_i = \frac{S_i M_i V_i}{\sum_j S_j S_j V_j}$$

Where S_i, M_i and V_i are the scale factor, cell mass and cell volume, respectively.

Since refinement depends on finding the best fit between the computational and experimental models, it is important to have a numerical merit value that quantifies the quality of the fit. The quality factors commonly used to characterise the quality of the improvement are profile residual (R_p), weighted profile residual (R_{wp}), bragg residual (R_b), expected profile residual (R_{exp}) and goodness of fit (χ^2).

The diffractometer is equipped with a high-temperature furnace capable of heating the sample through a thermocouple-linked platinum sample holder. This equipment facilitates the acquisition of X-ray diffraction pattern of the sample at various temperatures. By analyzing the XRD pattern obtained at different temperatures, valuable insights into the sample's phase transitions and thermal behavior with temperature variation can be gleaned.

When free electrons in motion experience acceleration, they emit electromagnetic radiation, a phenomenon commonly referred to as radiation or luminescence. By employing a bending magnet to compel high-energy electron beams to circulate at velocities

approaching the speed of light within a circular synchrotron accelerator, electromagnetic waves are generated in the tangential direction due to the centripetal acceleration (***see Fig A.2.2***). This phenomenon is known as synchrotron radiation, exhibiting a broad wavelength range that includes X-rays. In conventional X-ray diffraction, the wavelength of incident X-rays is determined by the characteristic emissions of the target material's elements. Copper (Cu) is frequently chosen as the target material, yielding a preferred wavelength of 1.54 Å for X-ray generation at a single energy level. In the context of synchrotron XRD, the beamlines can provide higher X-ray energies (~100 keV). The 11BM beamline used in this work (Argonne National Laboratory, USA) provides an incident wavelength of ~0.4Å (31 keV). Synchrotron XRD employs double-crystal monochromators, offering an energy resolution (ΔE/E) typically around 2×10^{-4}, resulting in an X-ray wavelength bandwidth of approximately 0.0003 Å and a similar order of magnitude for errors in interplanar spacing. Consequently, synchrotron XRD affords exceedingly high-resolution spectra, facilitating the acquisition of more precise structural information.

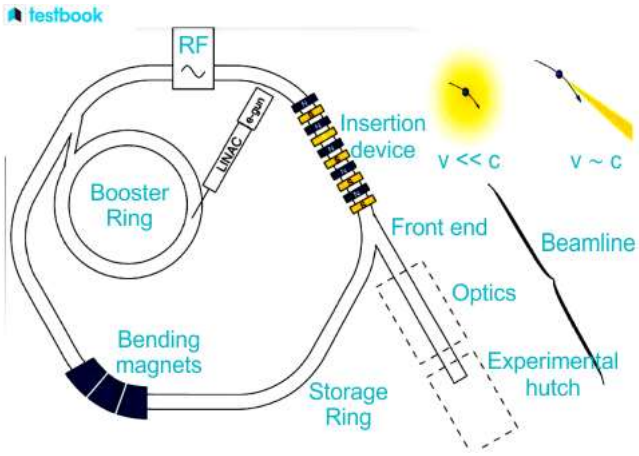

Fig A.2.2 *Schematic diagram of a synchrotron*[3]

In this work, laboratory powder X-ray diffraction (PXRD) patterns were recorded from 10 to 120° in 2θ and a step size of 0.02° with a scan time of 2s per step by a D8 Advance Bruker diffractometer with Cu $K\alpha_1/\alpha_2$ radiation (λ = 1.54056/1.54440 Å) at 40 Kv and 30 mA at room temperature. High variable temperature diffraction (VT-XRD) data for thermal stability measurement were collected from room temperature to 1600°C by every 100 °C and over 2θ range 10-120° with a step size of 0.02 for total 1h scanning using the

diffractometer equipped with an HTK1600N Anton Paar furnace in vacuum conditions. High-resolution data of synchrotron powder diffraction (SPD) data was recorded on 11-BM at Argonne National Laboratory, U.S.A. in the range of 2θ from 1 ^{o} to 50^{o} with a 0.0001^{o} step size using a wavelength of 0.4578 Å at room temperature (via their rapid access mail-in service)[4]. Generally, Rietveld refinement of powder diffraction patterns was fitted using TOPAS Academic version 6[5].

The samples for PXRD tested were ground powder dispersed on silicon wafers with ethanol. Similarly, powder samples mixed with ethanol were placed on a platinum ribbon for VT-XRD. Powders for SPD were prepared by crushing one bead for each composition and was loaded in glass capillaries with a diameter of 0.2 - 0.5mm that were held inside Kapton 11BM capillaries with a diameter of 0.8 mm. All glass capillary diameters are determined on the basis of the calculated absorption coefficient muR ≤ 1 using the "11BM X-ray Absorption Calculation"[6]

Appendix A.2.2 Extended X-ray Absorption Fine Structure (EXAFS)

X-ray Absorption Fine Structure (XAFS) is a spectroscopic analysis technique based on synchrotron X-ray sources. It can be further divided into X-ray Absorption Near Edge Structure (XANES) and Extended X-ray Absorption Fine Structure (EXAFS). XAFS provides valuable information about interatomic distances, coordination numbers, and atomic species surrounding the absorbing atom. As X-rays penetrate through matter, their intensity undergoes attenuation. If the incident X-ray intensity is denoted as I_0 and the material's linear absorption coefficient is represented as μ, with a sample thickness of x, the attenuated intensity I can be expressed as $I = I_0\, e^{(-\mu x)}$ (see ***Fig A.2.3a***) The absorption coefficient μ is dependent on factors such as atomic number, atomic mass, and sample density, in relation to the energy of the incident X-rays. When the X-ray energy matches the binding energies of inner shell K and L levels, a discontinuity in the absorption coefficient (μ) occurs, resulting in a sudden change. This phenomenon is attributed to the photoelectric absorption of X-ray photons, exciting inner shell electrons to higher unoccupied energy levels in the external continuum. This abrupt transition in the absorption coefficient is

known as an absorption edge (see ***Fig A.2.3b***). As the photoelectrons generated by atomic photoelectric absorption propagate outward, they encounter scattering by surrounding atoms. The interference between the emitted and scattered waves at certain energies leads to mutual reinforcement, resulting in peaks, and mutual attenuation, resulting in troughs. Consequently, the probability of photoelectric absorption is modulated, giving rise to oscillations in the absorption coefficient. This phenomenon gives birth to the phenomenon of Extended X-ray Absorption Fine Structure (EXAFS) spectra.

The oscillations within EXAFS encompass a range of frequencies, each corresponding to a distinct coordination shell with varying interatomic distances from the absorbing atom. Given its capacity for frequency-to-space domain transformation, the Fourier transform plays a pivotal role in the analysis of EXAFS. The generation of EXAFS is intimately tied to the scattering of the absorbing atom and its surrounding atoms, inherently linked to the structural arrangement. Therefore, the measurement of EXAFS provides a means to investigate the neighboring structural arrangement around the absorbing atom, enabling the determination of parameters such as interatomic distances, coordination numbers, and atomic mean-square displacements.

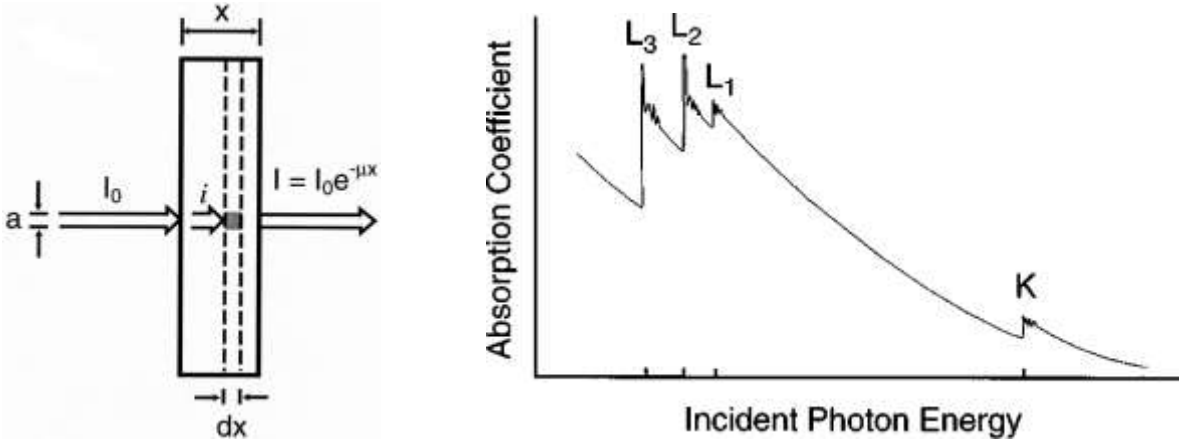

Fig A.2.3 (a) *Schematic view of x-ray absorption and* ***(b)*** *schematic view of x-ray absorption coefficient as a function of incident photon energy* [7]

X-ray absorption fine structure (EXAFS) spectra measurement at Gd L_3-edge (7243 eV), Tm L_3-edge (8648 eV) and Yb L_3-edge (8944 eV) was carried out on SAMBA beamline at the SOLEIL synchrotron, France. The experiments were carried out in transmission mode at room

temperature using a monochromator consisting of 2 Si (220) crystals and ionisation chambers filled with N_2 gas or a N_2/He mixture to collect the X-ray photons before and after the samples have passed through. To avoid possible problems of inhomogeneity due to the sample, we chose to work with a beam width of 3 mm and a height of 250 µm. During the experiment 3 series of samples were measured in addition to reference oxides (Gd_2O_3, Yb_2O_3 and Tm_2O_3).

The measured pellets of 10 or 13 mm diameter were pressed mixture of powder sample and boron nitride BN powders. The amount of sample powder (100 mg) was optimised with the XAFS mass software[8] so that for any threshold considered in our study, the edge jump was between 0.1 and 1.5 and the total absorption was less than 2.5.

To support the EXAFS analysis, theoretical structural models with different compositions and defect configurations were derived from a single garnet unit cell (1 x 1 x 1) with 160 atoms in space group *P*1, substituted with 0, 1 or 2 Gd^{3+} ions on the *B* sublattice and 0, 1 or 2 RE^{3+} ions (Tm or Yb) on the *A* and/or *B* sublattices. For each composition, all symmetrically-inequivalent configurations were generated using Supercell[9]. Certain configurations were relaxed using VASP via plane-wave based DFT calculations. Finally theoretical EXAFS spectra were calculated for the L_3-edge using the FEFF8 code [10-11].

Note that EXAFS experiments were conducted and analysed with the assistance of Dr. Emiliano Fonda (SAMBA beamline, SOLEIL) and Dr. Didier Zanghi (CEMHTI).

Appendix A.2.3 Scanning electron microscopy (SEM) and microprobe

Scanning Electron Microscopy (SEM) is a powerful imaging technique that uses focused electron beams to investigate the surface morphology and composition of materials at high magnifications. Energy Dispersive X-ray Spectroscopy (EDS) and Backscattered Electron (BSE) imaging are two common analytical techniques often used in conjunction with SEM to provide additional information about the elemental composition and material contrast.

When a sample is bombarded with high-energy electrons from the SEM's electron beam, inner-shell electrons of atoms in the sample may be ejected. This creates electron vacancies in the inner shells. To fill these vacancies, electrons from higher energy shells drop

down, releasing energy in the form of X-ray photons. The energy of these X-rays is characteristic of the elements present in the sample. The detector sorts the X-rays based on their energies, creating an X-ray spectrum. This spectrum provides information about the elements present in the sample and their relative abundance. By comparing the intensities of the characteristic X-ray peaks to known standards, EDS can provide semi-quantitative or quantitative information about the elemental composition of the sample.

When the high-energy electron beam interacts with the sample, some electrons are scattered back (backscattered electrons) due to interactions with the sample's atomic nuclei. The energy and number of backscattered electrons depend on the sample's atomic number (Z) and density. The intensity of backscattered electrons depends on the sample's composition. Elements with higher atomic numbers (heavier elements) tend to produce more backscattered electrons and appear brighter in BSE images, while elements with lower atomic numbers (lighter elements) appear darker. By detecting and collecting the backscattered electrons, a BSE image is formed. This image provides information about the surface morphology and compositional variations, grain orientation of the sample.

The electron microprobe generates a finely focused electron beam with energy levels ranging from 5 to 50 keV, which is directed onto the surface of the sample. Due to the small area of electron beam irradiation, the corresponding characteristic X-ray spectral lines' wavelengths and intensities reflect the elemental composition and content within this minute region. The sensitivity and resolution of microprobe significantly exceed the standard EDS by an order of magnitude which provides notably more precise data. Additionally, it enables accurate quantitative analysis of light elements such as B, C, N, O, and F.

Microstructural analysis was conducted using an IT800SHL JEOL scanning electron microscope (FEG SEM) that was equipped with an SSD Ultim Max 100mm2 detector (EDS Oxford system). The elemental analysis was performed using a Cameca SX Five electron microprobe (EMP) at the joint BRGM-CNRS facility in Orleans, which provided high precision measurements. The EMP analyses were conducted using an acceleration voltage of 15 kV, a sample current of 20 NA, a focused beam of 1 µm, and a counting time of 10 s for each element on each of the 40 spots per sample.

All of the samples for SEM imaging and microprobe measurement were obtained from

randomly selected crystallized beads that were embedded in epoxy resin, polished, and carbon coated under vacuum conditions. In order to standardize the measurements, a stoichiometric $Gd_3Al_5O_{12}$, $Lu_4Al_2O_9$, $Lu_{3.889}AlSiO_{9.333}$ sample was used as a reference.

These experiments were carried out with the help of Dr. Emmanuel Veron (CEMHTI).

Appendix A.2.4 Scanning transmission electron microscopy (STEM)

Scanning Transmission Electron Microscopy (STEM) is a development of Transmission Electron Microscopy (TEM). In recent years, with the introduction of spherical aberration correctors, STEM's spatial resolution has reached the sub-angstrom level, enabling imaging and observation of individual atomic columns. Besides imaging through the reception of scattered signals by annular detectors, STEM is also capable of acquiring Electron Energy Loss Spectroscopy (EELS) and Energy-Dispersive X-ray Spectroscopy (EDS) results through post-specimen electron energy loss and X-ray signal detection. This allows for obtaining chemical composition and electronic structure information of the sample[12-14].

A typical imaging mode in STEM is High-Angle Annular Dark-Field Imaging (HAADF-STEM), where scattered electrons are received from higher angles to achieve non-coherent imaging. In dark-field imaging, phase contrast is nearly eliminated, and the image intensity I is approximately proportional to the square of the atomic number Z. Consequently, the brightness of spots in the image reflects the atomic number of the real atomic columns, achieving Z-contrast imaging. In a specimen of constant composition, the intensity of HAADF-STEM images is roughly proportional to the number of atoms in the atomic column. Thus, compositional information at atomic resolution can be obtained[15].

As the electron beam penetrates the specimen, a fraction of incident electrons undergoes inelastic collisions with the atoms in the sample, leading to processes such as ionization of surface electrons, excitation of valence electrons, and oscillations, resulting in energy loss. By collecting information from these inelastically scattered electrons, Electron Energy Loss Spectroscopy (EELS) can be acquired, providing insights into the sample's chemical composition, electronic structure, chemical bonding, and other related information[16].

Incorporating an Energy-Dispersive Spectroscopy (EDS) detector on the sample allows for STEM-EDS analysis. This setup collects and detects characteristic X-rays generated by the interaction of the sample with the electron beam, enabling elemental mapping and semi-quantitative compositional analysis based on the intensity and wavelength distribution of X-rays[17].

High-resolution scanning transmission electron microscopy - high angle annular dark field (STEM-HAADF) imaging and energy dispersive X-ray spectroscopy (EDS) elemental mapping were carried out on a JEOL ARM200F (JEOL Ltd.) Cold FEG transmission electron microscope (TEM) operating at 200 kV, equipped with a double spherical aberration corrector and fitted with a JEOL SDD CENTURIO EDS system and a GIF Quantum. The thickness of the samples was estimated using Energy Filtered Transmission Electron Microscopy (EFTEM). The cation arrangements were imaged at the atomic scale by STEM-EDS elemental mapping and in STEM-HAADF imaging mode with a 68-174.5 mrad inner-outer collection angles and a probe size of 0.1nm.

The samples measured were first polished using a tripod and inlaid diamond discs on individual beads until a thickness of approximately 40µm was obtained. Thin foils of 8 - 15nm thickness were then obtained by argon ion milling (Gatan PIPS), by gradually reducing the incident beam voltage to remove beam-induced amorphization.

TEM data collection was carried out by Dr. Cécile Genevois (CEMHTI).

Appendix A.2.5 Solid state nuclear magnetic resonance spectroscopy (NMR)

Solid-state nuclear magnetic resonance spectroscopy (NMR) is a non-destructive technique employed for localized probing of material structures. The NMR phenomenon arises from the interaction between radiofrequency waves of a specific frequency and atomic nuclei with non-zero spin quantum number I, situated within a static magnetic field. When the nuclear spin quantum number I is non-zero, the nucleus develops a magnetic moment μ. Placing nuclei with magnetic moments within an external magnetic field B_o results in an interaction between the magnetic field and the nuclear magnetic moment, leading to different orientations and energy level splittings of the nuclear magnetic

moments, a phenomenon known as Zeeman splitting. Applying a specific radiofrequency wave along a direction perpendicular to the static magnetic field B_o induces resonant transitions between the Zeeman energy levels, giving rise to nuclear magnetic resonance. The relationship between the Larmor frequency (ν_o) and the magnetic field strength (B_o) is given by $\omega_o = 2\pi\nu_o = \gamma B_o$, where γ is the gyromagnetic ratio constant[18-19].

Due to the orbital angular momentum of electrons, atomic nuclei in molecules generate magnetic fields influenced by the nearby electronic distribution, leading to the origin of chemical shifts. Solid-state NMR technology investigates diverse local environments around nuclei, corresponding to short-to-medium range interactions. This approach provides rich and detailed structural information, suitable for analyzing the structures of both highly crystalline solid materials and those with lower crystallinity, including amorphous substances. It reveals molecular structural aspects such as bond lengths, bond angles, hydrogen bond formation, intramolecular, and intermolecular interactions. It serves as a complementary method to X-ray diffraction and other techniques focused on long-range interactions in studying overall solid-state structures[19-20].

A Bruker Avance 750 MHz (17.6 T magnetic field) spectrometer was applied to collect ^{27}Al NMR spectra. The instrument is equipped with a high-speed MAS probe and operated with a 2.5 mm diameter aluminum-free zirconia rotor spinning at 30 kHz. π/18 pulses and 1s cycle times were used to obtain quantitative signals. ^{29}Si NMR spectra were collected on Bruker Avance WB 300 MHz (7 T magnetic field) equipped with MAS probe. This experiment operates at 59.63 MHz and spinning at 20 kHz using 4mm ZrO_2 rotor. Full relaxation of the magnetization was ensured by accumulating 137 scans after a π/2 excitation pulse of 4.6 μs and using a cycle time of 200s.

The samples for NMR measurement were powder. The deconvolution of the resulting NMR spectra was performed using DM-fit software[21]. Czsimple model lines deduced form Gaussian Isotropic Model [22]was used to fitting ^{27}Al MAS NMR spectra.

NMR data were collected by Dr. Vincent Sarou-Kanian (CEMHTI).

Appendix A.2.6 Differential scanning calorimetry (DSC)

Differential Scanning Calorimetry (DSC) is a widely used thermal analysis technique that measures the heat flow associated with physical and chemical changes in a material as a function of temperature or time. DSC provides valuable insights into various processes, such as phase transitions, reactions, melting, and crystallization.

Differential scanning calorimetry (DSC) data was performed using a Perkin Elmer Setaram MULTI HTC 1600 Thermal Analyzer with a heating rate of 10 ºC min^{-1} from 30 ºC to 1100 ºC (GAG glass), 1400 ºC and 1600 ºC (LuAM and LuASO) under airflow. All samples measured were randomly selected samples of beads crushed into powder contained in a platinum crucible.

Data were collected with the assistance of Sandra Ory (CEMHTI).

Appendix B.2.7 Luminescence performance characterization

Photoluminescence (PL) measurement is a spectroscopic technique used to study the emission of light (photons) from a material after it has absorbed photons and undergone electronic transitions. It provides insights into the electronic structure, energy levels, and optical properties of materials. Peaks in the photoluminescence spectrum correspond to specific electronic transitions and energy levels in the material. The position (wavelength) and intensity of these peaks provide information about the band structure, electronic states, and impurity levels. The quantum efficiency of photoluminescence refers to the ratio of emitted photons to absorbed photons. It provides insights into the efficiency of radiative recombination. Additionally, the photoluminescence lifetime measures the average time an excited electron remains in an excited state before returning to a lower energy state.

Up-conversion and down conversion photoluminescence (PL) and photoluminescence excitation (PLE) spectra of samples at room temperature were recorded using an FLS1000 photoluminescence spectrometer (Edinburgh Instruments) equipped with a 980 nm pulsed laser and a Xe-lamp as excitation source, respectively. The luminescence decay curves of phosphor were also measured by a FLS1000 instrument at room temperature under excitation. The PL emissions and excitation spectra were recorded over the temperature

range of 80 - 280K on a photoluminescence spectrometer FLS1000 instrument with a sample holder capable of controlling sample temperature. The dependence of emission intensity of the up conversion luminescence was recorded by varying the pump power of the 980 nm laser using an iris filter.

Persistent luminescence excitation (PersLE) and photoluminescence (PersPL) spectra were measured using a FLS1000 fluorescence spectrophotometer (Edinburgh Instruments). Samples were place in the quartz sample holder. For every point of the spectra the sample was excited at λ_{exc} = 450 nm during 1 min (slits exc/em = 8/5). Then, PersL decay was recorded during 2 min. Every point of the spectra represent integration of decays that were recorded at different wavelengths. Between each measurement the samples were removed from the spectrofluorometer and heated using hair drier (to keep sample at the same place in the sample holder) during 1 min and then kept cooled down to RT (cooling time of 4 min approx.). All these steps were carried out in the dark to prevent from charging with ambient light.

All samples tested were place in the quartz sample holder. The bead samples used for the down-conversion and up-conversion measurements for GAG system are randomly selected beads that have been polished on both sides. Optical data for all LuAM systems and GAGG persistent materials were collected using mixed with homogeneous powder samples from several crushed beads.

Luminescence data were collected and analysed with the assistance of Dr. Victor Castaing and Dr. Ana Becerro (CSIC, Seville, Spain).

Appendix B Supporting information for Chapter 2

Appendix B.1 PXRD and SPD refinement

Text B.1.1

The processing steps and sequence for refining each dataset were identical. The Rietveld fitting procedure for the 11BM data entailed the import of SPD xye files and GAG structure information. The background signal was initially smoothed by a 15-term background Chebyshev polynomial and corrected for sample displacement and axial divergence. The TCHZ peak type was utilized for peak shape simulations. The lattice parameter *a* was freely refined, followed by the oxygen atom coordinates and thermal vibration factors for each site. The occupancies of Gd1, Al2, and O were constrained to 1. The occupancy number of Al16 was defined as 1 and was augmented with the same atomic coordinates as Al16a defined as Gd2, with an occupancy of 1-occAl16a and free refinement. The Al_{16a} occupancy was refined independently until the R_{wp} value no longer varied. If secondary and impurity phases were present, their peak shapes and refinement of cell parameters were incorporated.

The distribution of doped rare earth cations (e.g., Ce^{3+}, Tb^{3+}, Yb^{3+}, Tm^{3+}, Er^{3+}, Ho^{3+}) cannot be detected by Rietveld refinement due to the weak X-ray scattering contrast with Gd^{3+}. Therefore, the laboratory PXRD data here can only provide the evolution of the cell parameters with the x value.

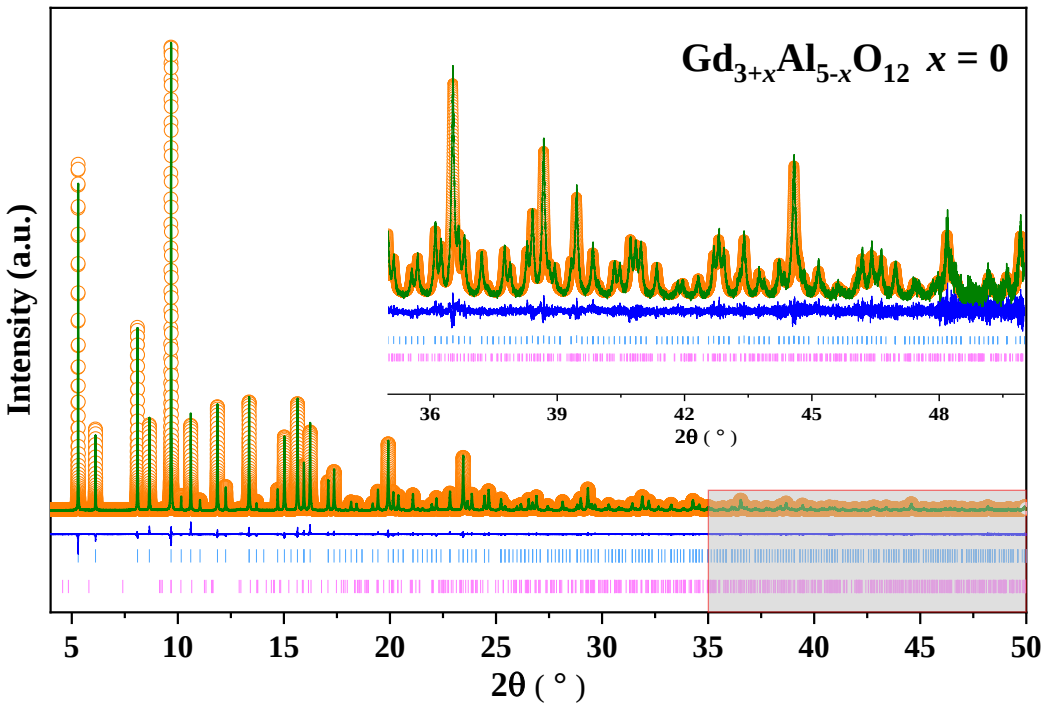

Fig B.1.1 *SPD Rietveld refinement profiles of $Gd_3Al_5O_{12}$ (R_{wp} = 7.41%, Gof = 1.76) (light blue ticks marks are GAG garnet reflections, pink tick marks correspond to 2.36(1) wt% Al_2O_3)*

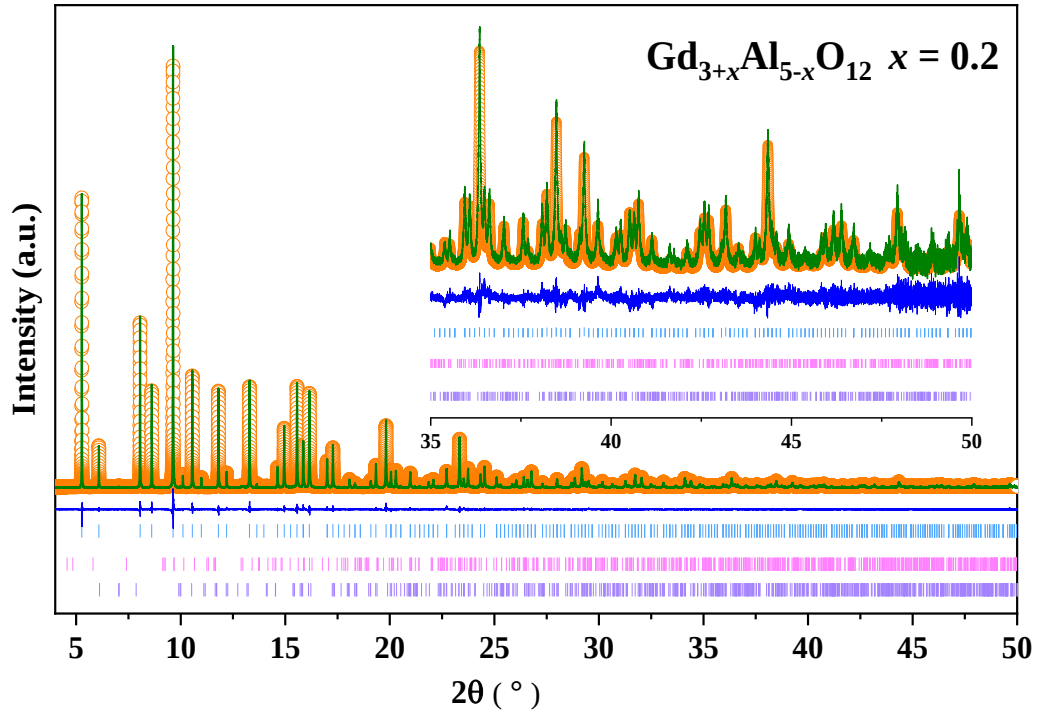

Fig B.1.2 *SPD Rietveld refinement profiles of $Gd_{3.2}Al_{4.8}O_{12}$ (R_{wp} = 9.17%, Gof = 1.89) (light blue ticks marks are ns-GAG garnet reflections, pink tick marks correspond to 1.35(1) wt% Al_2O_3, purple ticks marks correspond to 0.35(1) wt% $GdAlO_3$ (GAP) perovskite)*

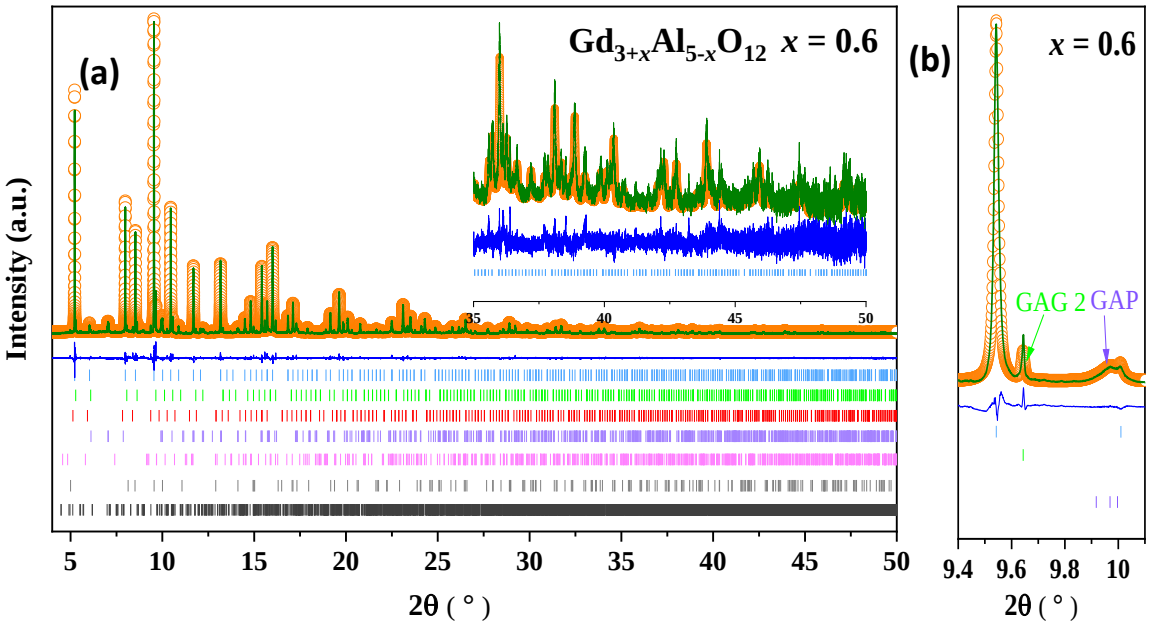

Fig B.1.3 *SPD Rietveld refinement profiles of* ***(a)*** *$Gd_{3.6}Al_{4.4}O_{12}$ (R_{wp} = 10.38%, Gof = 1.99)* ***(b)*** *Zoomed main peaks of $Gd_{3.6}Al_{4.4}O_{12}$ (light blue ticks marks correspond to 83.7(9) wt% ns-GAG garnet reflections, pink tick marks are Al_2O_3 reflections, purple ticks marks are $GdAlO_3$ (GAP) perovskite reflections, green tick marks correspond to secondary GAG garnet reflections, red tick marks are third GAG garnet reflections, blank tick marks are $Gd_4Al_2O_9$ reflections, gray tick marks are $GdAlO_3$ reflections).See also the Table 2.1.*

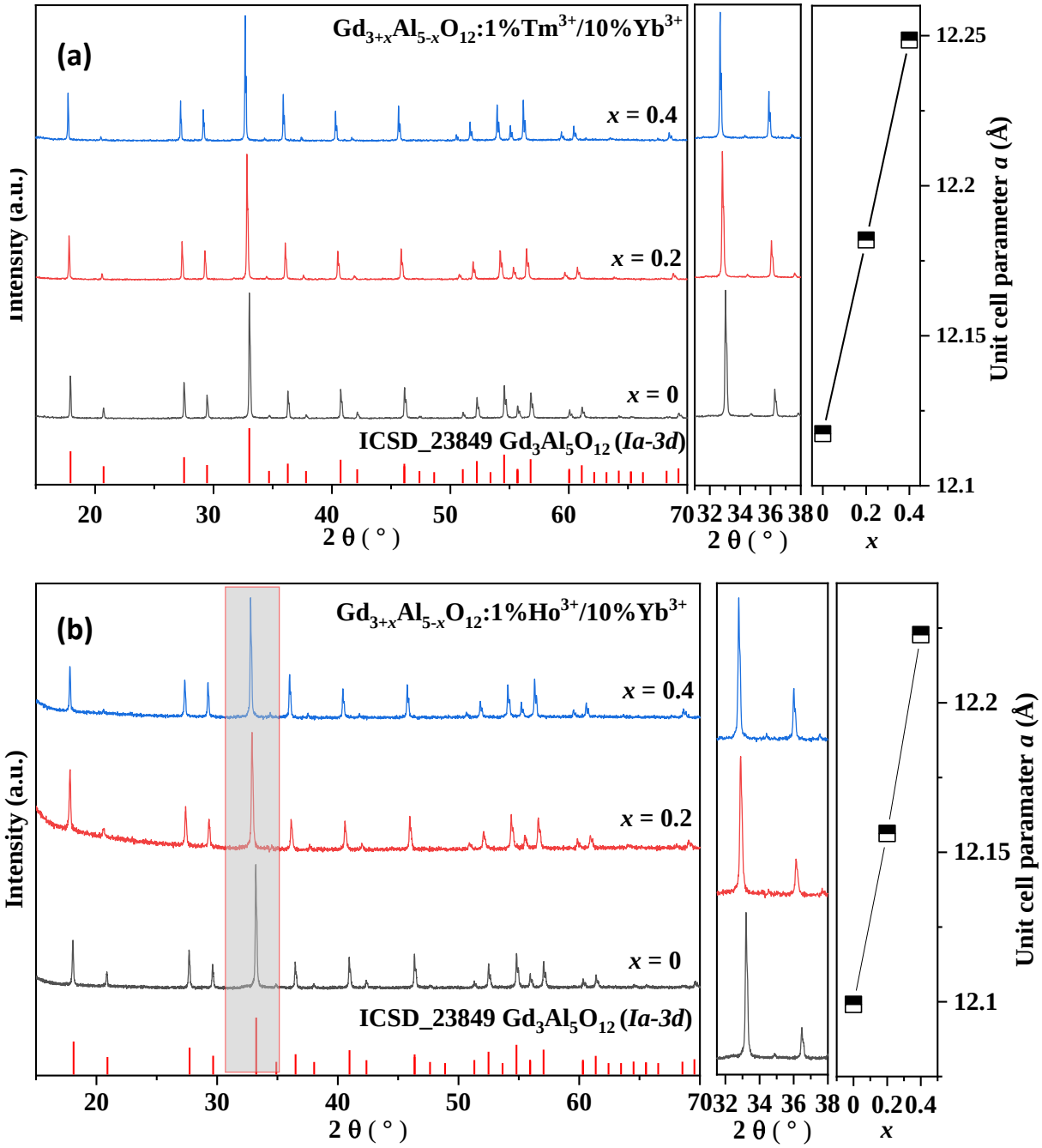

Fig B.1.4 *XRD pattern of GAG doped sample $Gd_{3+x}Al_{5-x}O_{12}$ (x = 0, 0.2, 0.4):* ***(a)*** *1% Tm^{3+}/10% Yb^{3+},* ***(b)*** *1% Ho^{3+}/10% Yb^{3+}.*

Table B.1.1 *PXRD refinement result of $Gd_{3+x}Al_{5-x}O_{12}$ doped with RE^{3+} (RE = Ce, Tb, Er/Yb, Tm/Yb, Ho/Yb).*

Sample	x = 0	x = 0.2	x = 0.4
$Gd_{3+x}Al_{5-x}O_{12}$: 2%Ce^{3+}	*a* = 12.1672(2) Å R_{wp} = 9.2%, Gof = 1.70	*a* = 12.2110(1) Å R_{wp} = 7.32%, Gof = 1.15	*a* = 12.2548(1) Å 1.4(1) wt% $GdAlO_3$ R_{wp} = 9.6%, Gof = 1.19%
$Gd_{3+x}Al_{5-x}O_{12}$: 10%Tb^{3+}	*a* = 12.1288(1) Å R_{wp} = 11.2%, Gof = 1.35	*a* = 12.1872(3) Å R_{wp} = 7.90%, Gof = 1.32	*a* = 12.2570(1) Å R_{wp} = 7.68%, Gof = 1.65
$Gd_{3+x}Al_{5-x}O_{12}$: 2%Er^{3+}/20%Yb^{3+}	*a* = 12.0999(1) Å R_{wp} = 10.30%, Gof = 1.14	*a* = 12.19837(2) Å R_{wp} = 9.17%, Gof = 1.89	*a* = 12.2258(2) Å R_{wp} = 7.86%, Gof = 1.18
$Gd_{3+x}Al_{5-x}O_{12}$: 1%Tm^{3+}/10%Yb^{3+}	*a* = 12.1177(1) Å R_{wp} = 6.98%, Gof = 1.61	*a* = 12.1819(1) Å R_{wp} = 8.35%, Gof = 1.60	*a* = 12.2485(1) Å R_{wp} = 9.38%, Gof = 1.08
$Gd_{3+x}Al_{5-x}O_{12}$: 1%Ho^{3+}/10%Yb^{3+}	*a* = 12.0999(1) Å R_{wp} = 4.40%, Gof = 1.32	*a* = 12.1563(5) Å R_{wp} = 4.50%, Gof = 1.16	*a* = 12.2228(2) Å R_{wp} = 4.42%, Gof = 1.34

Appendix B.2 Microprobe results

Text B.2.1

Fig B.2.1 and ***Fig B.2.2*** illustrates the electron microprobe elemental mapping of the GAG: 2%Er^{3+}/20%Yb^{3+} (x = 0, 0.2, 0.4) and GAG: 1%Tm^{3+}/10%Yb^{3+} (x = 0, 0.2, 0.4) beads sample. It can be seen that the sample contains porosity, and the Gd, Al and lower concentration doped Er/Yb and Tm/Yb elements are uniformly distributed in the grains with no obvious aggregation. A total of 40 collection points were used for the compositional analysis, spaced at 20 μm intervals from the centre to the edge of the bead. The average compositions listed in ***Table B.2.1*** and ***Table B.2.2*** are in good agreement with the theoretical compositions.

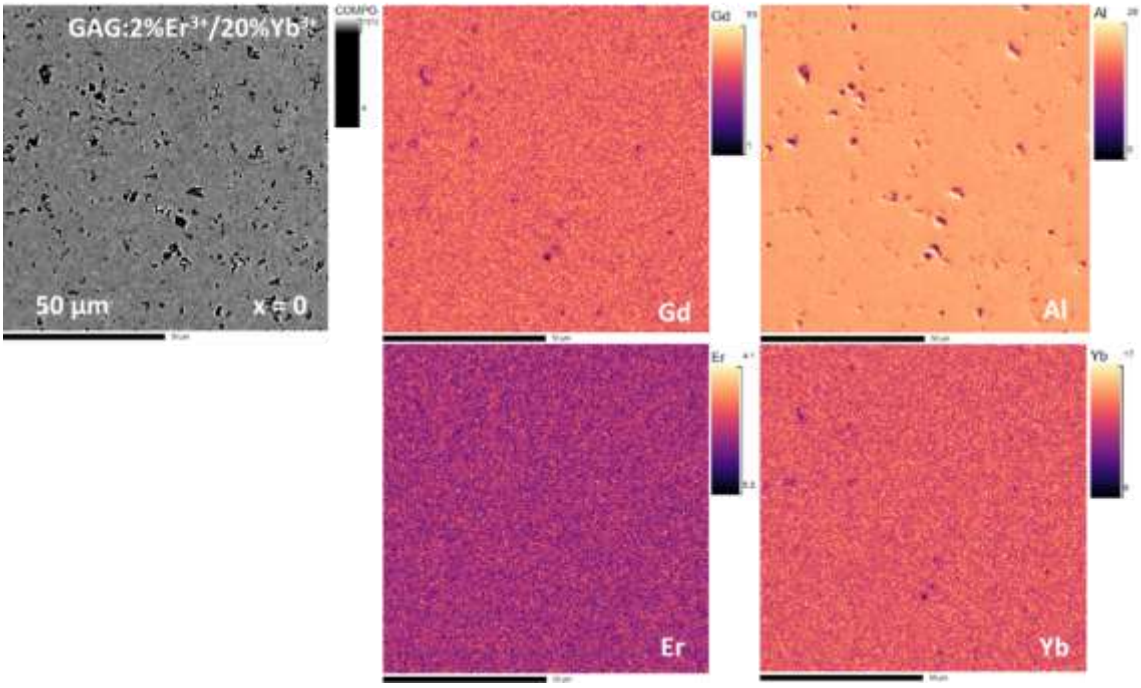
GAG:2%Er3+/20%Yb3+
50 µm
x = 0
COMPO
Gd
Al
Er
Yb

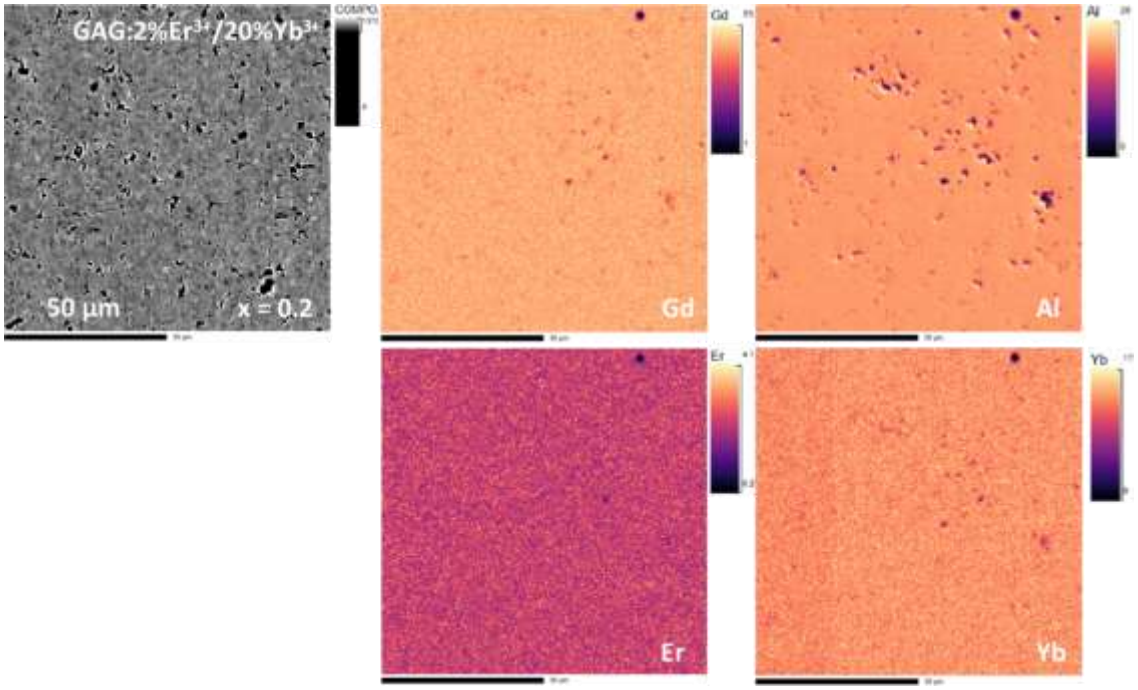
GAG:2%Er3+/20%Yb3+
50 µm
x = 0.2
COMPO
Gd
Al
Er
Yb

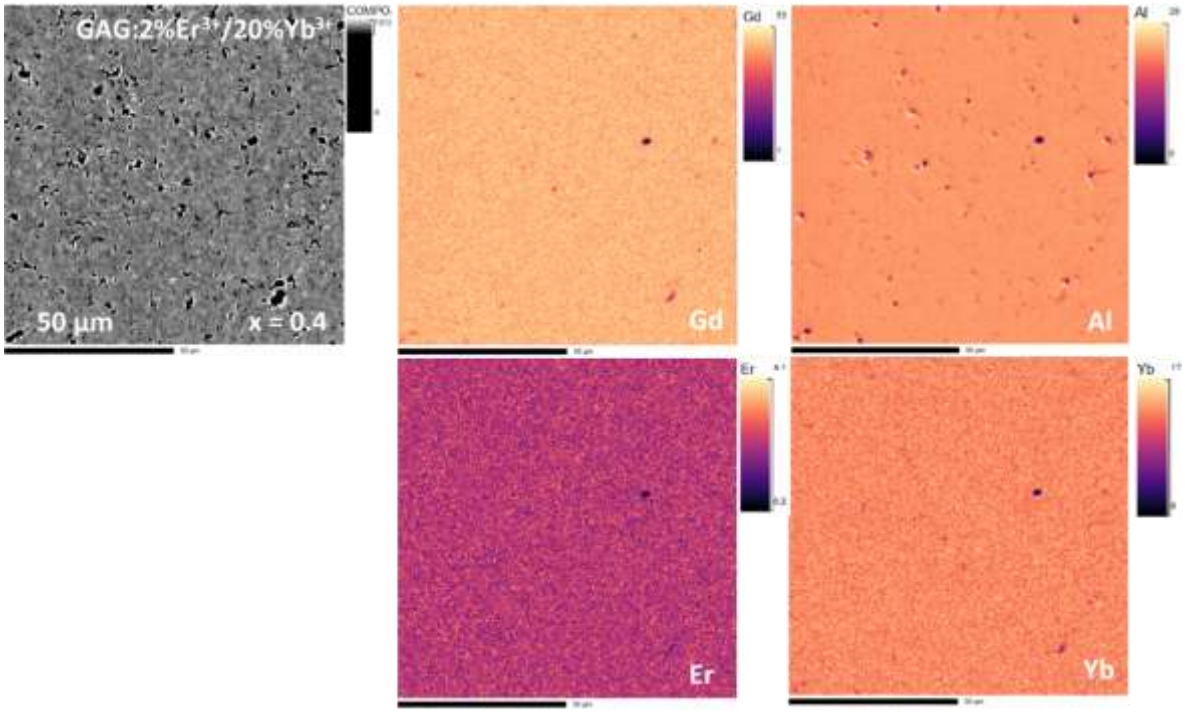

Fig B.2.1 *Electron microprobe elemental mapping of GAG: 2%Er^{3+}/20%Yb^{3+} (x = 0, 0.2, 0.4).*

Table B.2.1 *Microprobe composition analysis of GAG: 2%Er^{3+}/20%Yb^{3+}(x = 0, 0.2, 0.4).*

$(Gd_{0.78}Er_{0.02}Yb_{0.2})_{3+x}Al_{5-x}O_{12}$	Experimental composition	Theoretical composition
x = 0	$Gd_{2.28(3)}Er_{0.063(2)}Yb_{0.61(1)}Al_{5.05(3)}O_{12}$	$Gd_{2.34}Er_{0.06}Yb_{0.6}Al_5O_{12}$
x = 0.2	$Gd_{2.38(3)}Er_{0.067(3)}Yb_{0.64(1)}Al_{4.92(3)}O_{12}$	$Gd_{2.496}Er_{0.064}Yb_{0.64}Al_{4.8}O_{12}$
x = 0.4	$Gd_{2.68(2)}Er_{0.070(3)}Yb_{0.68(1)}Al_{4.58(3)}O_{12}$	$Gd_{2.652}Er_{0.068}Yb_{0.68}Al_{4.6}O_{12}$

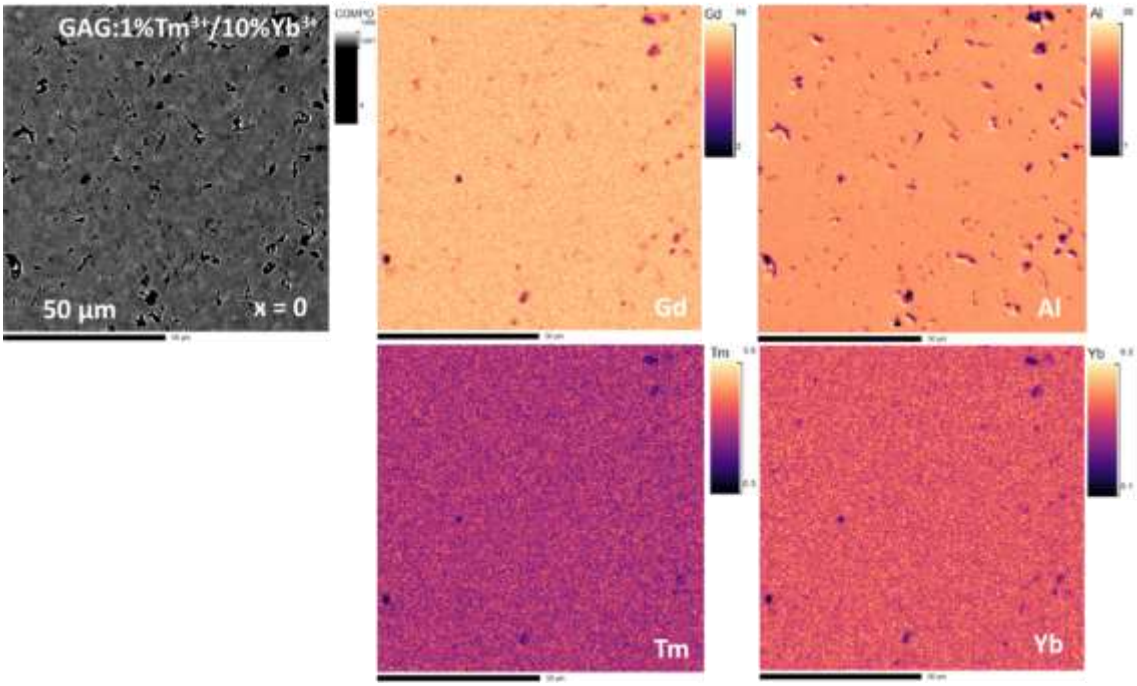
GAG:1%Tm3+/10%Yb3+
50 µm
x = 0
Gd
Al
Tm
Yb

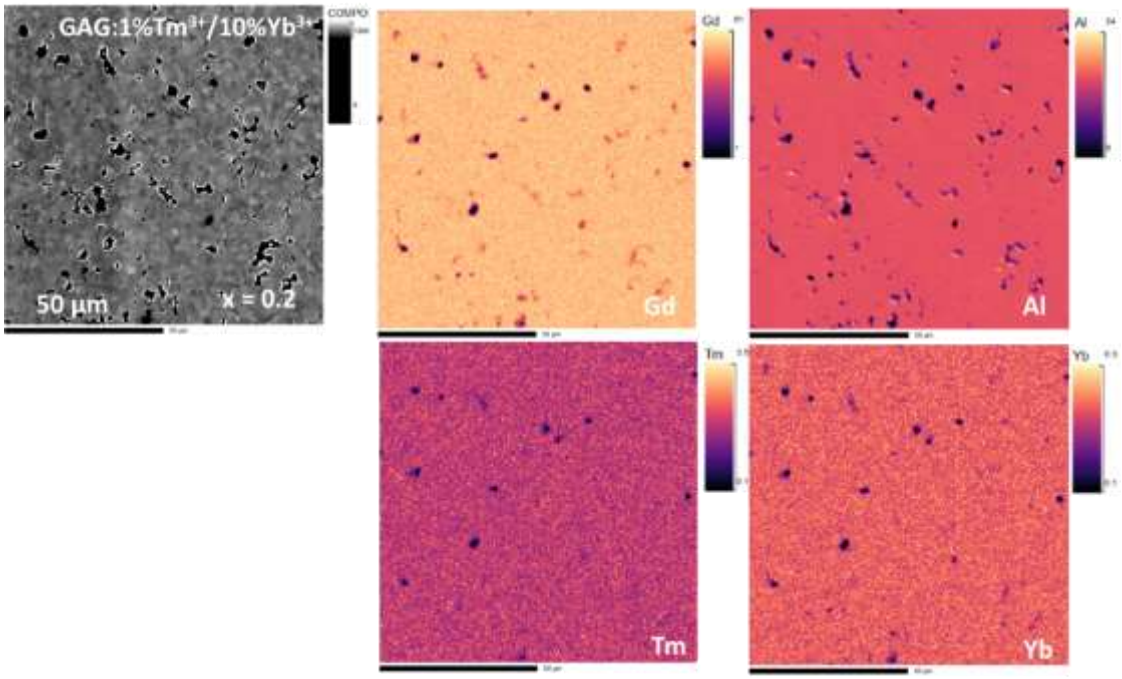
GAG:1%Tm3+/10%Yb3+
50 µm
x = 0.2
Gd
Al
Tm
Yb

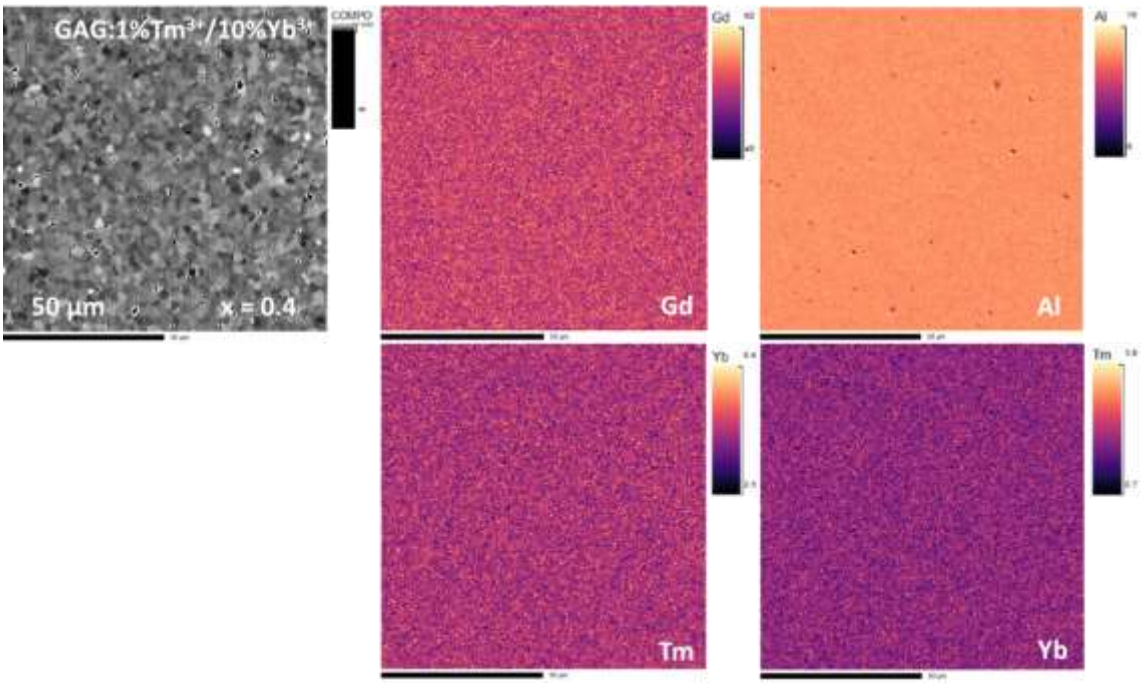

Fig B.2.2 *Electron microprobe elemental mapping of GAG: 1%Tm^{3+}/10%Yb^{3+} (x = 0, 0.2, 0.4).*

Table B.2.2 *Microprobe composition analysis of GAG: 1%Tm^{3+}/10%Yb^{3+}(x = 0, 0.2, 0.4).*

$(Gd_{0.89}Tm_{0.01}Yb_{0.1})_{3+x}Al_{5-x}O_{12}$	Experimental composition	Theoretical composition
x = 0	$Gd_{2.72(4)}Tm_{0.035(3)}Yb_{0.145(4)}Al_{5.10(4)}O_{12}$	$Gd_{2.67}Tm_{0.03}Yb_{0.3}Al_5O_{12}$
x = 0.2	$Gd_{2.89(4)}Tm_{0.038(3)}Yb_{0.155(6)}Al_{4.92(4)}O_{12}$	$Gd_{2.848}Tm_{0.032}Yb_{0.32}Al_{4.8}O_{12}$
x = 0.4	$Gd_{3.06(5)}Tm_{0.040(3)}Yb_{0.164(5)}Al_{4.74(6)}O_{12}$	$Gd_{3.026}Tm_{0.034}Yb_{0.34}Al_{4.6}O_{12}$

Appendix B.3 EXAFS results

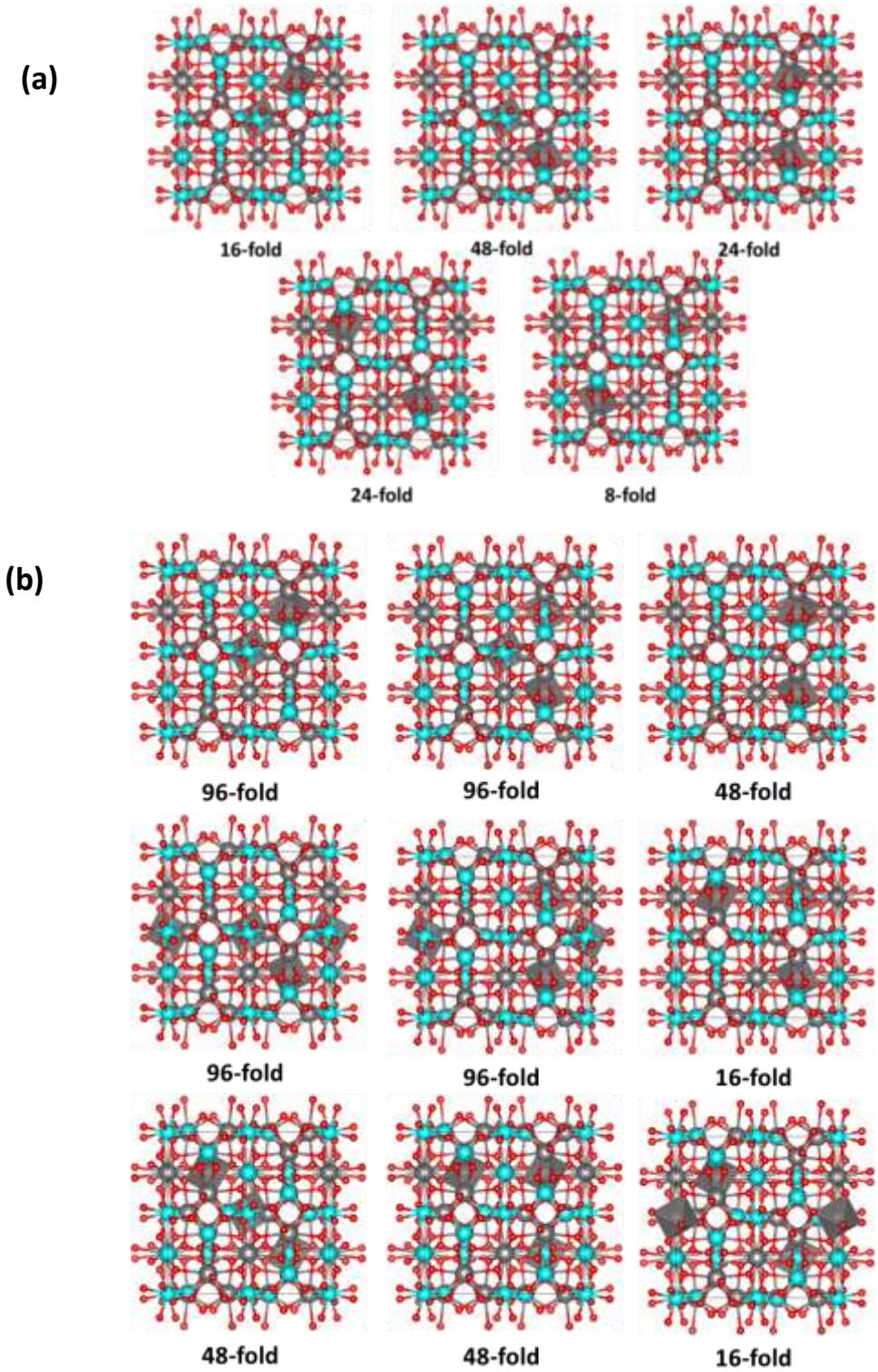

Fig B.3.1 (a) *The five symmetrically inequivalent* $Gd_{3.25}Al_{4.75}O_{12}$ *unit cells (1 x 1 x 1, space group P1) containing two* GdO_6 *substituted units* ***(b)*** *The nine symmetrically inequivalent* $Gd_{3.375}Al_{4.625}O_{12}$ *unit cells (1 x 1 x 1, space group P1) containing three* GdO_6 *substituted units.*

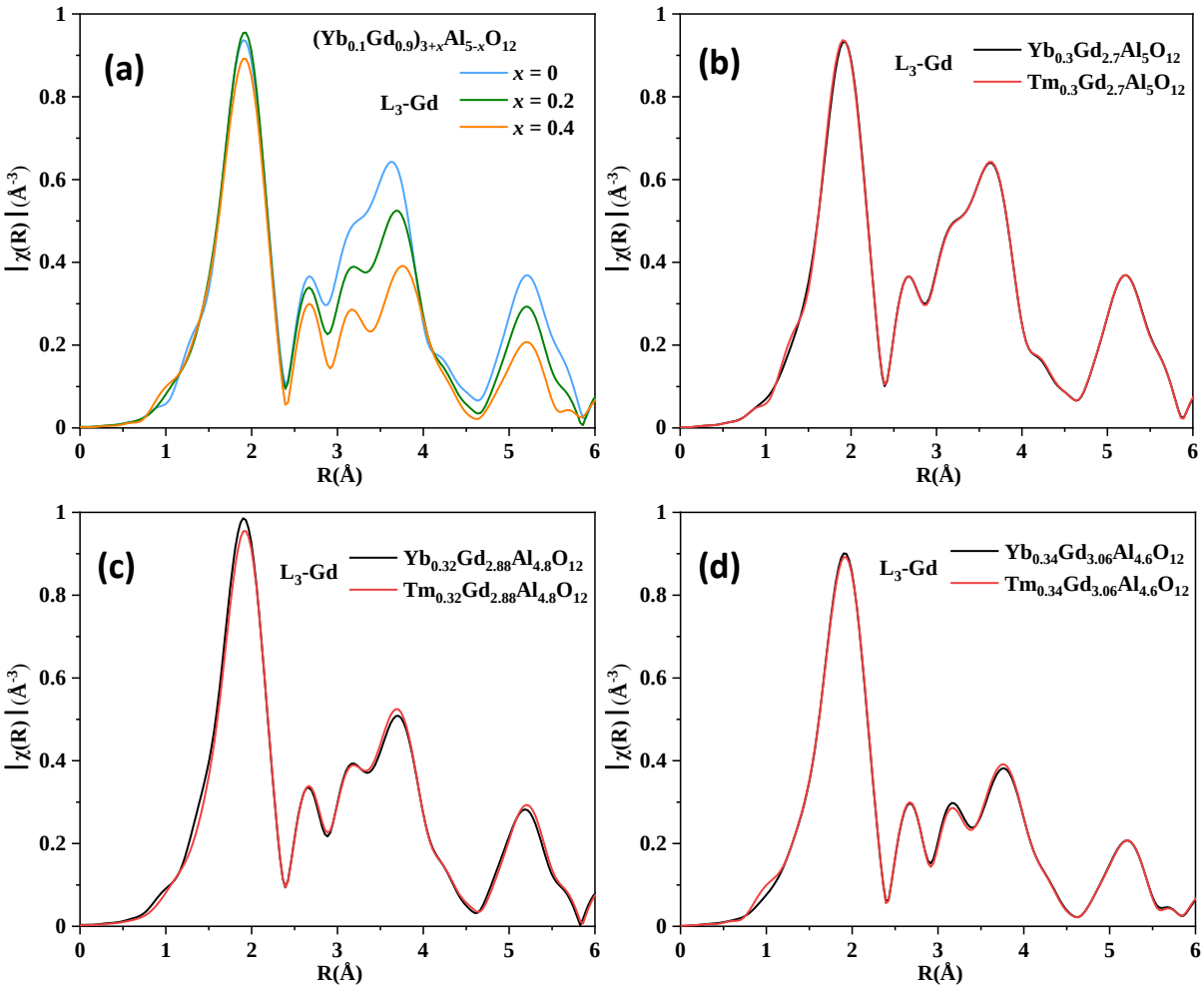

Fig B.3.2 *Experimental Fourier transforms of the EXAFS spectra extracted from the linear absorption coefficient measured at the Gd L_3-edge of* ***(a)*** *$(Yb_{0.1}Gd_{0.9})_{3+x}Al_{5-x}O_{12}$ (x = 0, 0.2, 0.4),* ***(b)*** *$Yb_{0.3}Gd_{2.7}Al_5O_{12}$ (black line) and $Tm_{0.3}Gd_{2.7}Al_5O_{12}$,* ***(c)*** *$Yb_{0.32}Gd_{2.88}Al_{4.8}O_{12}$ (black line) and $Tm_{0.32}Gd_{2.88}Al_{4.8}O_{12}$, and* ***(d)*** *$Yb_{0.34}Gd_{3.06}Al_{4.6}O_{12}$ (black line) and $Tm_{0.34}Gd_{3.06}Al_{4.6}O_{12}$.*

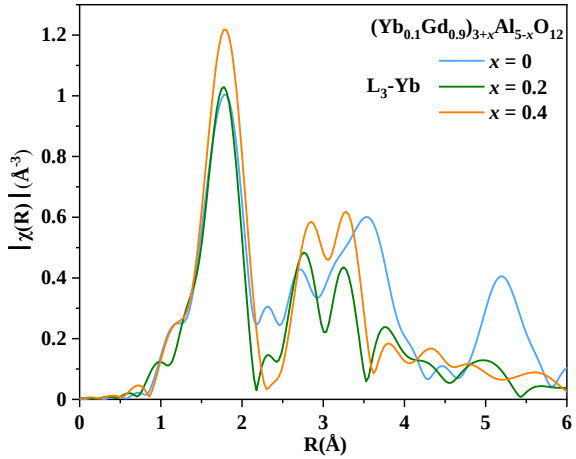

Fig B.3.3 *Experimental Fourier transforms of the EXAFS spectra extracted from the linear absorption coefficient measured at the Yb L_3-edge of $(Yb_{0.1}Gd_{0.9})_{3+x}Al_{5-x}O_{12}$ (x = 0, 0.2, 0.4)*

Appendix B.4 Luminescence properties results

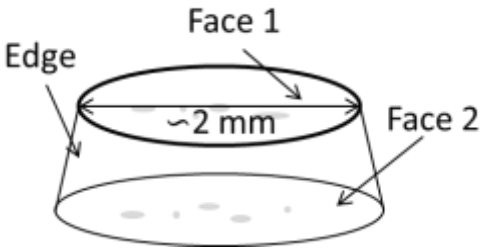

Fig B.4 *Schematic of polished beads for upconversion luminescence performance measurement.*

Appendix B.4.1 Luminescence properties of down-conversion $Gd_{3+x}Al_{5-x}O_{12}$(x = 0, 0.2, 0.4): 10%Tb^{3+}

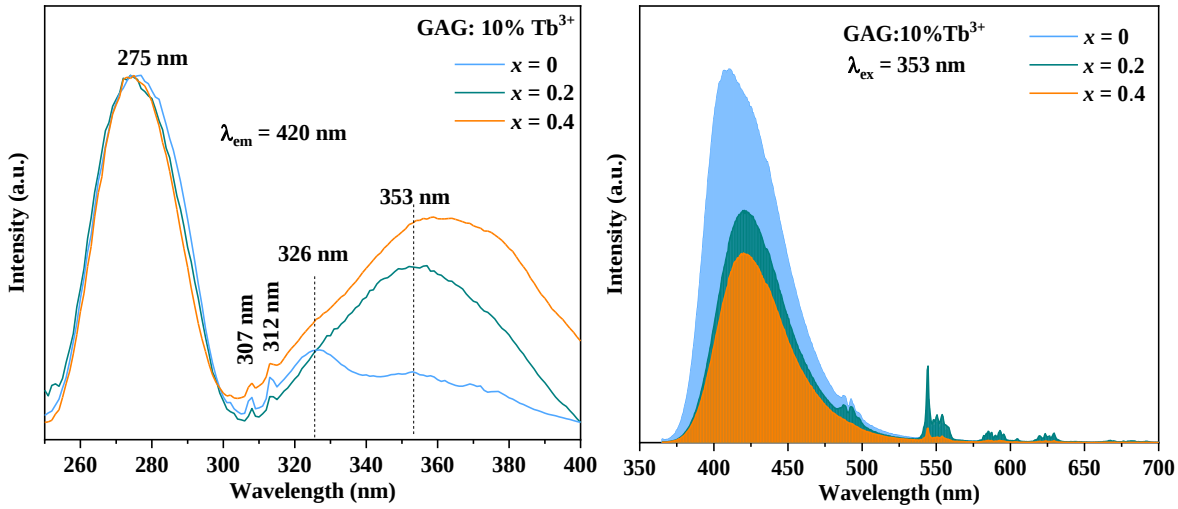

Fig B.4.1 *(a) PLE spectra under 420 nm emission (b) PL spectra under 353 nm excitation. (e) Decay curves of Tb^{3+} with 544 nm emission peak monitored at 270 nm.*

Text B.4.1

The excitation band corresponding to the f-d transition of Tb^{3+} exhibits a clear blue shift with increasing of x value, indicating a change in the crystal field environment in which Tb^{3+} is located. However, the emission peaks structure of the f-f transition do not differ between GAG and ns-GAG excited at 353nm, which suggests that the f-f transition of Tb^{3+} is insensitive to new local BO_6 sites.

Appendix B.4.2 Luminescence properties of up-conversion $Gd_{3+x}Al_{5-x}O_{12}$ (x = 0, 0.2, 0.4): 2%Er^{3+}/20%Yb^{3+}

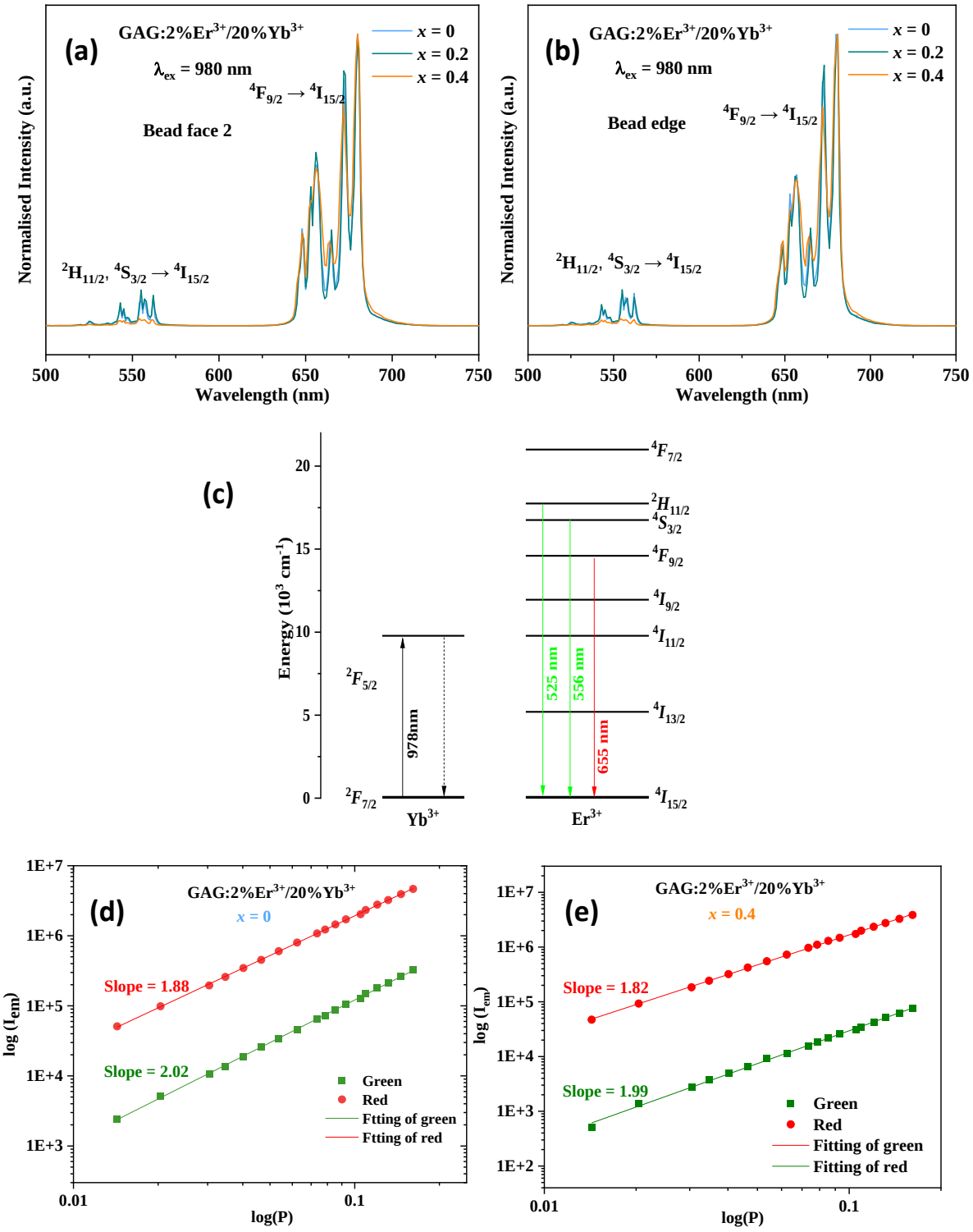

Fig B.4.2 *Up-conversion emission spectra under excitation at 980 nm of bead* ***(a)*** *second face and* ***(b)*** *edge.* ***(c)*** *Scheme of the successive energy transfers process, the relationship between log(I) and log(P) of red and green emission for the* ***(d)*** *x = 0 and (e) x = 0.4 of GAG: Er^{3+}/Yb^{3+} up conversion system.*

Appendix B.4.3 Luminescence properties of up-conversion $Gd_{3+x}Al_{5-x}O_{12}$ (x = 0, 0.2, 0.4): 1%Tm^{3+}/10%Yb^{3+}

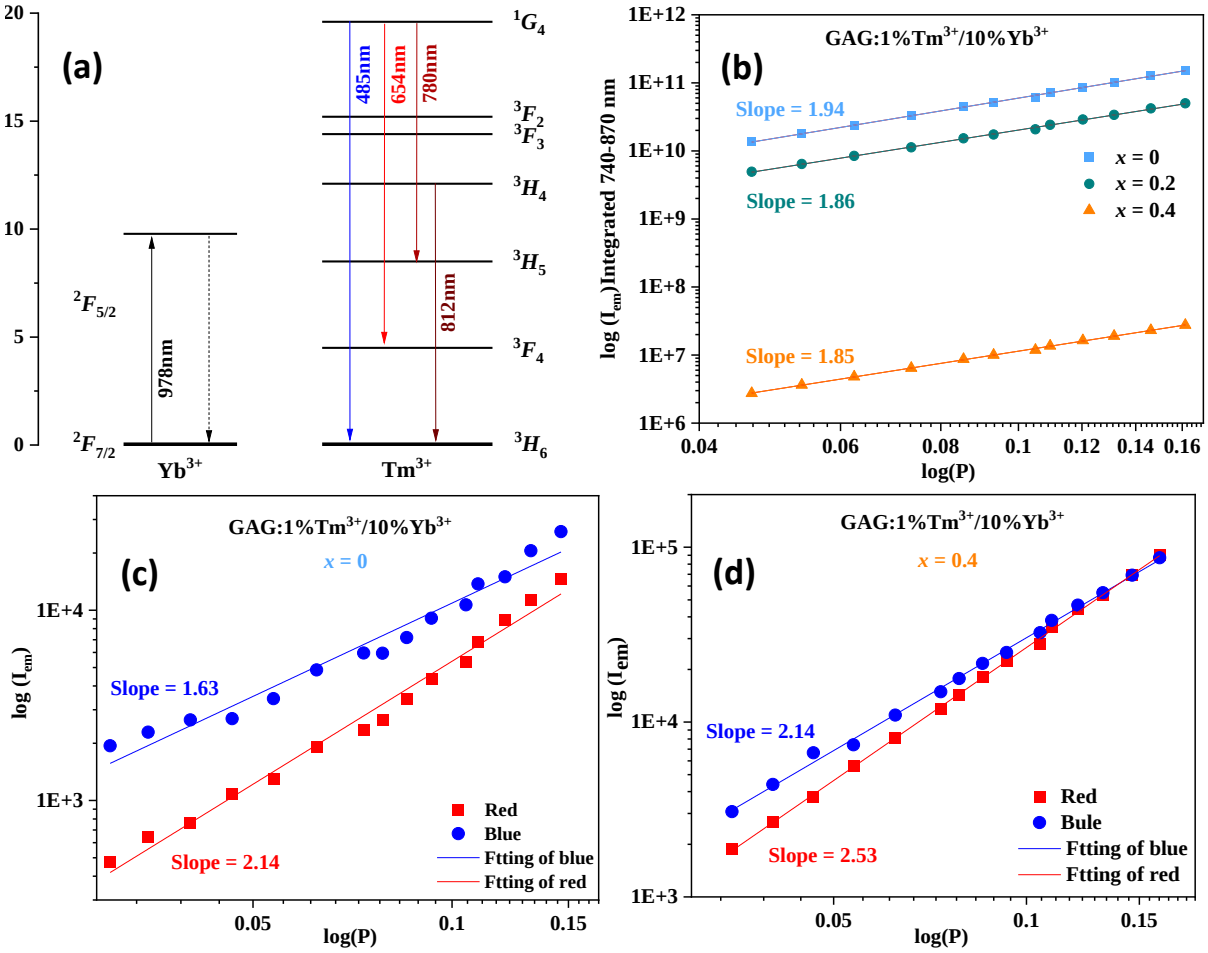

Fig B.4.3 (a) *Scheme of the successive energy transfers process, the relationship between log(I) and log(P) of* ***(b)*** *infrared emission, red and green emission for the* ***(c)*** *x = 0 and* ***(d)*** *x = 0.4 of GAG:Tm $^{3+}$/Yb^{3+} up conversion system.*

Appendix B.4.4 Luminescence properties of up-conversion $Gd_{3+x}Al_{5-x}O_{12}$ (x = 0, 0.2, 0.4): 1%Ho^{3+}/10%Yb^{3+}

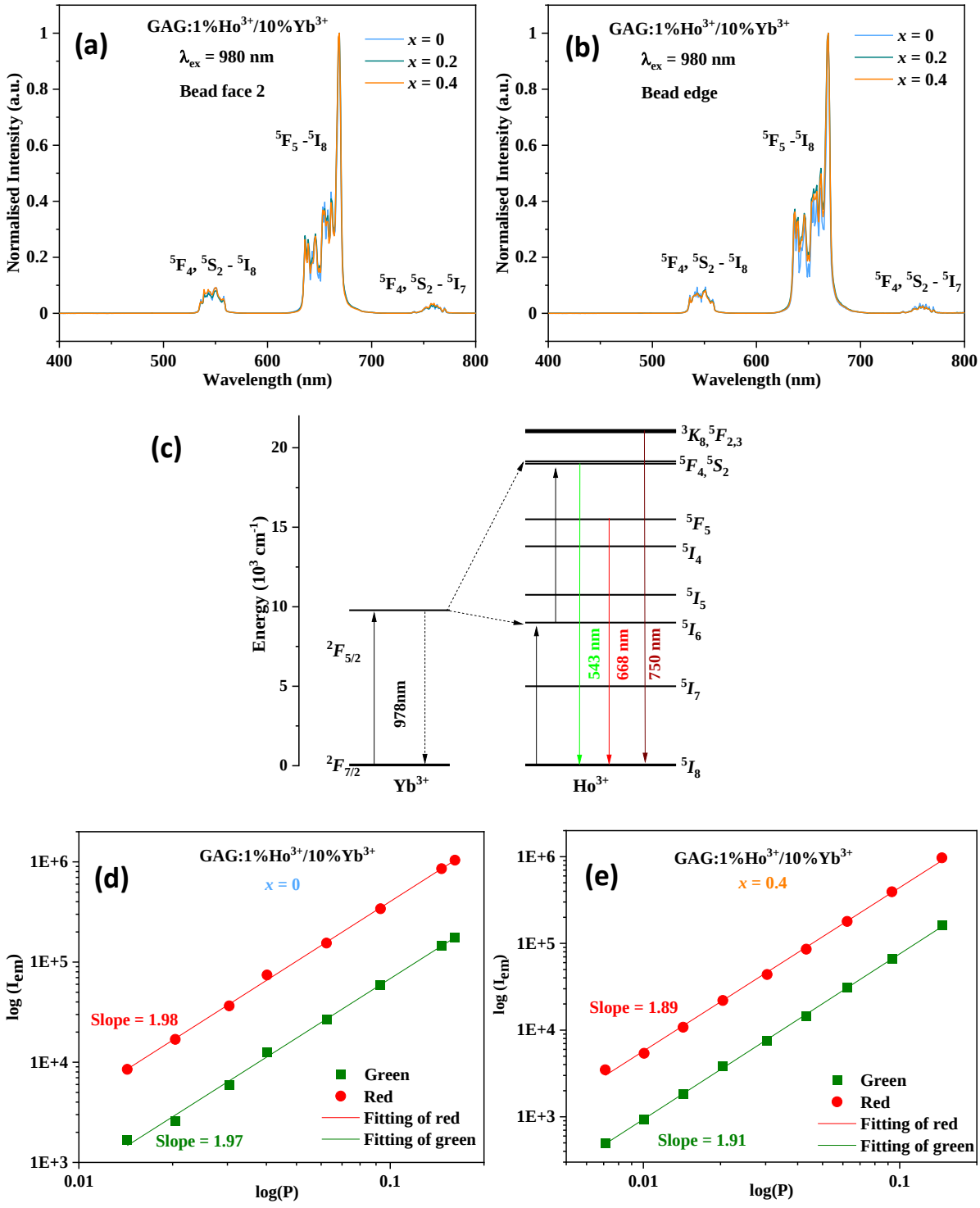

Fig B.4.4 *Up-conversion emission spectra under excitation at 980 nm of bead* ***(a)*** *second face and* ***(b)*** *edge,* ***(c)*** *Scheme of the successive energy transfers process, the relationship between log(I) and log(P) of red and green emission for the* ***(d)*** *x = 0 and* ***(e)*** *x = 0.4 of GAG:Ho $^{3+}$/Yb^{3+} up conversion system.*

Appendix C Supporting information for Chapter 3

Appendix C.1 PXRD, SPD refinement information of GGG

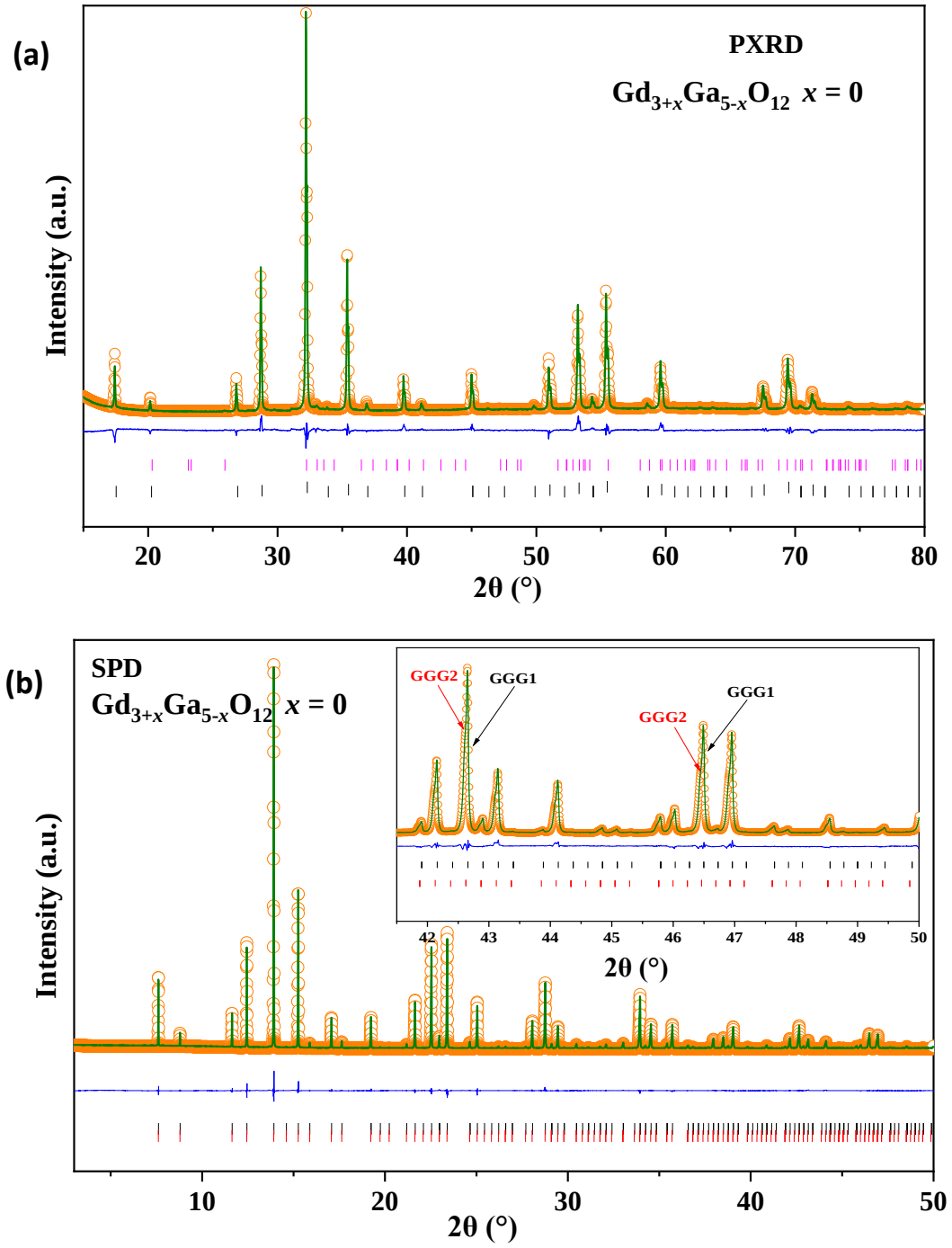

Fig C.1.1 (a) *PXRD (R_{wp} = 3.85% Gof = 1.97) and* ***(b)*** *SPD Rietveld refinement profiles of $Gd_3Ga_5O_{12}$ with 28.7(5) wt% ns-GGG2 (black rick marks are GGG reflections, red tick marks are GGG2 reflections, pink tick marks are $GdGaO_3$ reflections).*

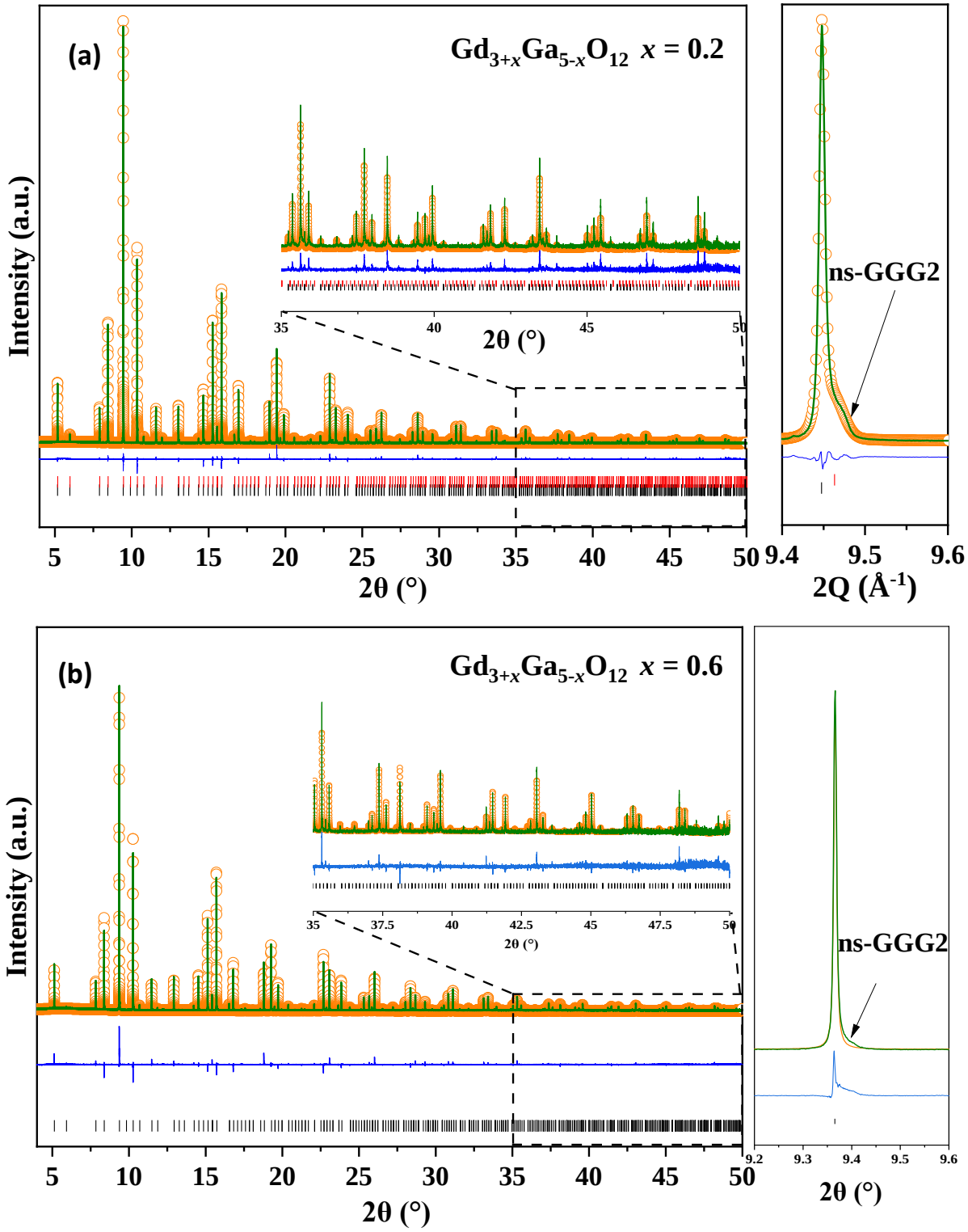

Fig C.1.2 *SPD Rietveld refinement profiles of* ***(a)*** $Gd_{3.2}Ga_{4.8}O_{12}$ (R_{wp} = 10.41%, Gof = 1.23) ***(b)*** $Gd_{3.6}Ga_{4.4}O_{12}$ (R_{wp} = 13.10%, Gof = 1.25) *Zoomed main peaks of at right (black rick marks are ns-GGG reflections, red rick marks are ns-GGG2)*

Table C.1.1 *Bond lengths of $Gd_{3+x}Ga_{5-x}O_{12}$ (x = 0, 0.2, 0.4, 0.6) from SPD refinement.*

x	Band Gd-O	Band length (Å)	Band Ga-O	Band length (Å)
x = 0	$Gd1\text{-}O^S$	2.466(6)	Ga1-O	1.941 (7)
	$Gd1\text{-}O^L$	2.539(6)	Ga2-O	1.767(6)
x = 0.2	$Gd1\text{-}O^S$	2.452(4)	Ga1/Gd2-O	1.977(5)
	$Gd1\text{-}O^L$	2.511(4)	Ga2-O	1.763(5)
x = 0.4	$Gd1\text{-}O^S$	2.442(5)	Ga1/Gd2-O	2.033(6)
	$Gd1\text{-}O^L$	2.518(5)	Ga 2-O	1.762(6)
x = 0.6	$Gd1\text{-}O^S$	2.465(4)	Ga1/Gd2-O	2.078(5)
	$Gd1\text{-}O^L$	2.474(4)	Ga2-O	1.765(5)

Table C.1.2 *PXRD refinement result of $Gd_{3+x}Ga_{5-x}O_{12}$ doped with RE^{3+} (RE = Eu/Cr, Eu/Tb)*

Sample	x = 0	x = 0.2	x = 0.4
$Gd_{3+x}Ga_{5-x}O_{12}$: *0.7%Eu^{3+}/0.05%Cr^{3+}*	*a* = 12.3902(5) Å R_{wp} = 6.39%, Gof = 1.14	*a* = 12.4366(1) Å 31.0(7) wt% GGG2 *a* = 12.3967(6) Å R_{wp} = 11.84%, Gof = 1.24	*a* = 12.5643(2) Å 40.1(1) wt% GGG2 *a* = 12.536(1) Å R_{wp} =11.3%, Gof = 1.5%
$Gd_{3+x}Al_{5-x}O_{12}$: 10%Tb^{3+}	*a* = 12.4019(6) Å R_{wp} = 12.09%, Gof = 1.65	*a* = 12.4342(3) Å R_{wp} = 12.01%, Gof = 1.13	*a* = 12.4787(2) Å 35.6(1) wt% GGG2 *a* = 12.435(1) Å R_{wp} = 8.55%, Gof = 1.91

Appendix C.2 EXAFS results of GGG

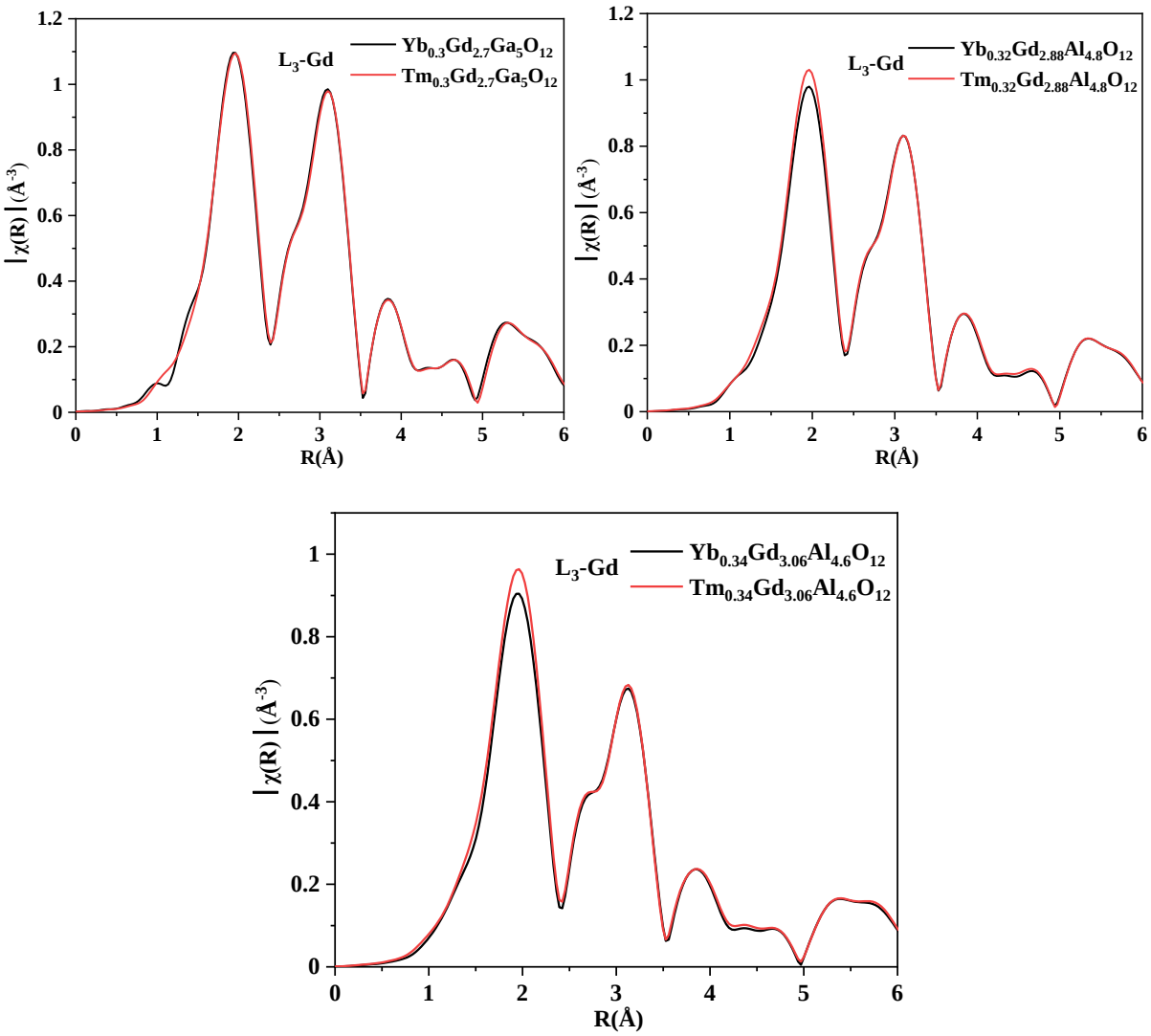

Fig C.2.1 *Experimental Fourier transforms of the EXAFS spectra extracted from the linear absorption coefficient measured at the Gd L_3-edge of* ***(a)*** *$Yb_{0.3}Gd_{2.7}Ga_5O_{12}$ (black line) and $Tm_{0.3}Gd_{2.7}Ga_5O_{12}$,* ***(b)*** *$Yb_{0.32}Gd_{2.88}Ga_{4.8}O_{12}$ (black line) and $Tm_{0.32}Gd_{2.88}Ga_{4.8}O_{12}$, and* ***(c)*** *$Yb_{0.34}Gd_{3.06}Ga_{4.6}O_{12}$ (black line) and $Tm_{0.34}Gd_{3.06}Ga_{4.6}O_{12}$.*

Appendix C.3 PXRD refinement information of GAGG

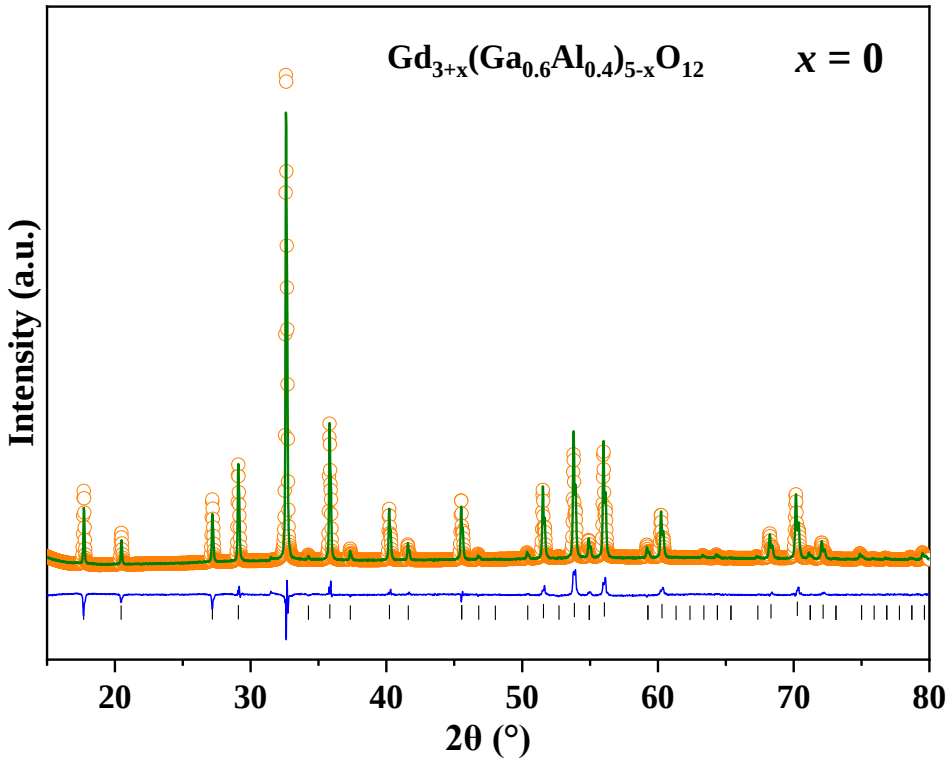

Fig C.3.1 *PXRD Rietveld refinement profiles of $Gd_3Al_2Ga_3O_{12}$ (x = 0)(R_{wp} = 8.09% Gof = 1.18)*

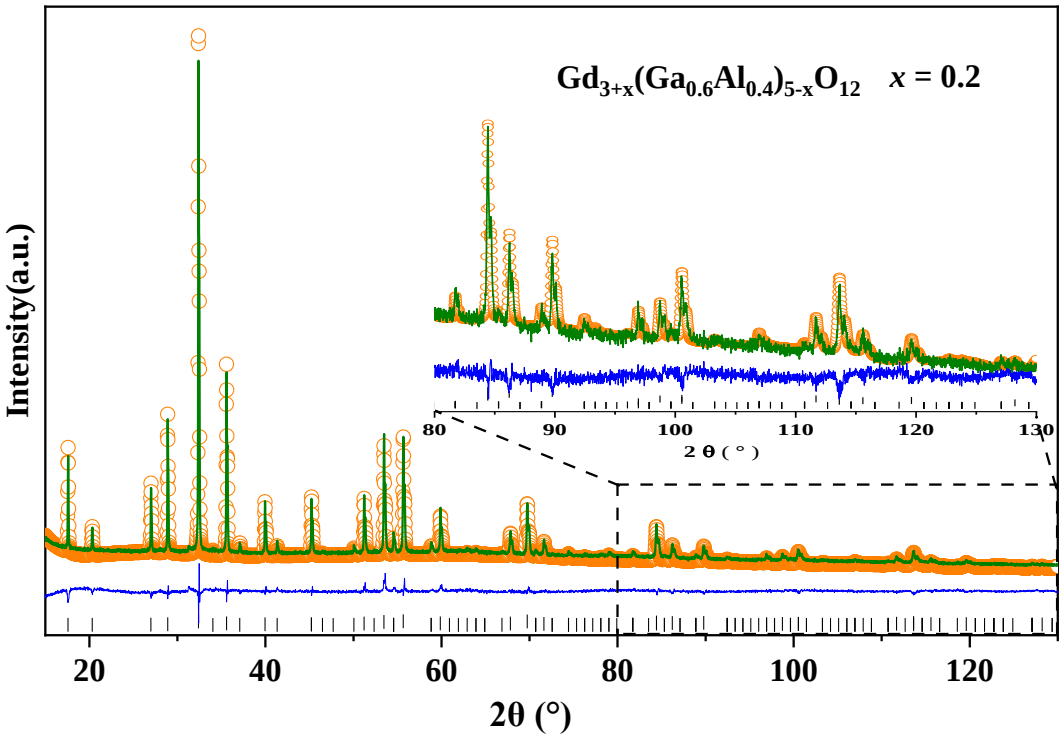

Fig C.3.2 *PXRD Rietveld refinement profiles of $Gd_{3.2}(Al_{0.4}Ga_{0.6})_{4.8}O_{12}$ (x = 0.2) (R_{wp} = 3.48%, Gof = 1.85)*

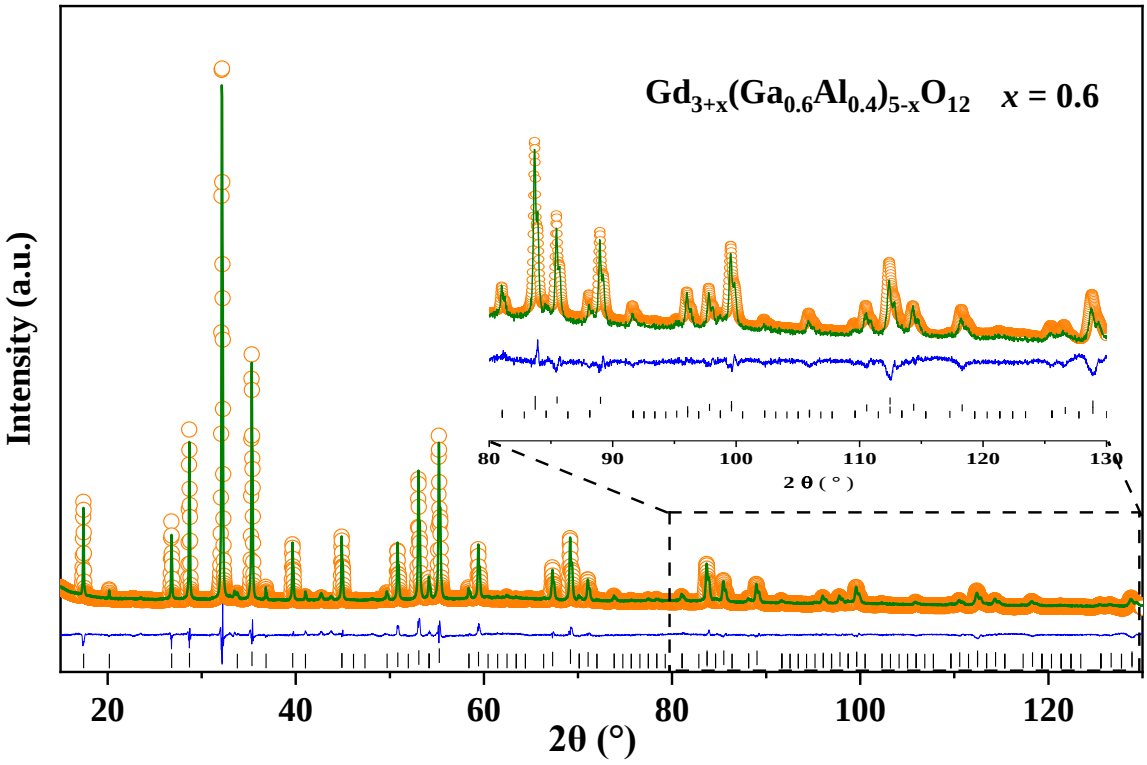

Fig C.3.3 *PXRD Rietveld refinement profiles of* $Gd_{3.6}(Al_{0.4}Ga_{0.6})Ga_{4.4}O_{12}$ *(x = 0.6) (*R_{wp} *= 5.84%, Gof = 1.65)*

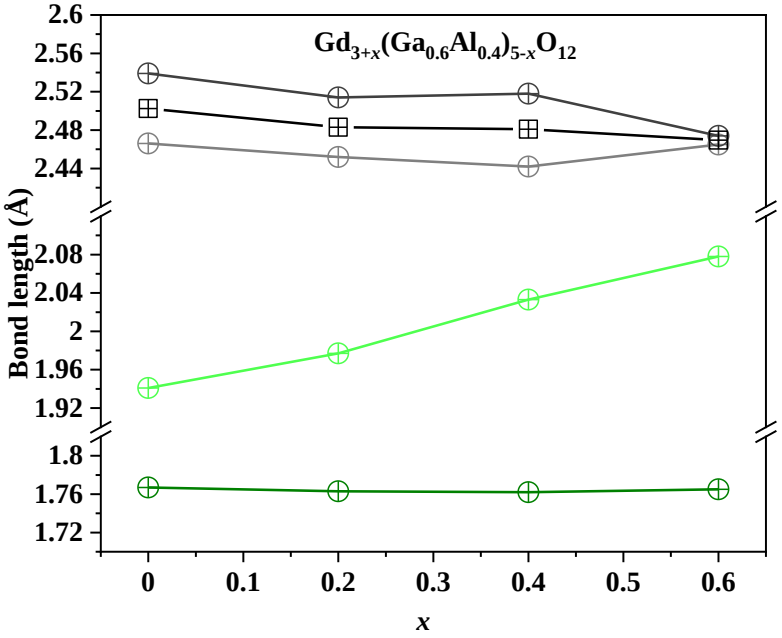

Fig C.3.4 *XRD refined metal-oxygen distances of* $Gd_{3+x}(Ga_{0.6}Al_{0.4})_{5-x}O_{12}$ *(x = 0, 0.2, 0.4, 0.6). Gray lines are Gd1-O bonds, pale blue is Gd2/Al1/Ga1-O bond, and deep blue is Ga2/Al2-O bond.*

Table C.3.1 *Bond lengths of $Gd_{3+x}(Al_{0.4}Ga_{0.6})_{5-x}O_{12}$ (x = 0, 0.2, 0.4, 0.6) from PXRD refinement.*

x	Bond Gd-O	Bond length (Å)	Ga-O	Bond length (Å)
x = 0	Gd1-O^S	2.466(6)	Ga/Al1-O	1.971(6)
	Gd1-O^L	2.539(6)	Ga/Al2-O	1.799(6)
x = 0.2	Gd1-O^S	2.443(4)	Ga1/Al1/Gd2-O	2.010(4)
	Gd1-O^L	2.522(5)	Ga2/Al2-O	1.763(4)
x = 0.4	Gd1-O^S	2.437(6)	Ga1/Gd2-O	2.047(8)
	Gd1-O^L	2.516(5)	Ga2/Al2-O	1.753(7)
x = 0.6	Gd1-O^S	2.461(4)	Ga1/Al1/Gd2-O	2.086(5)
	Gd1-O^L	2.474(4)	Ga2/Al2-O	1.765(4)

Table C.3.2 *Refined cell parameters of GAGG: 0.5%Ce^{3+}/0.05%Cr^{3+} and fitting results obtained from PXRD data.*

$Gd_{3+x}(Ga_{0.6}Al_{0.4})_{5-x}O_{12}$	atom	site	x	y	z	occupancy	U_{iso}*100
x = 0	Gd1	24c	0.125	0	0.25	1	0.67(1)
	Ga1	16a	0	0	0	0.66(1)	0.34 (3)
	Al1	16a	0	0	0	0.34(1)	0.34(3)
	Ga2	24d	0.375	0	0.25	0.563(8)	0.14(1)
	Al2	24d	0.375	0	0.25	0.437(8)	0.14(1)
	O1	96h	0.9499(8)	0.0419(9)	0.151(1)	1	0.56(4)
Lattice parameter： *a* = 12.301(3) Å					*Fitting parameters: R_{wp} = 7.33% Gof = 1.13*		
x = 0.2	Gd1	24c	0.125	0	0.25	1	0.98(1)
	Gd2	16a	0	0	0	0.1	0.43(2)
	Ga1	16a	0	0	0	0.54(1)	0.43(2)
	Al1	16a	0	0	0	0.36(1)	0.43(2)
	Ga2	24d	0.375	0	0.25	0.600(8)	0.33(2)
	Al2	24d	0.375	0	0.25	0.400(7)	0.33(2)
	O1	96h	0.9626(2)	0.0516(3)	0.1498(3)	1	0.56(3)
Lattice parameter： *a* = 12.3684(2) Å					*Fitting parameters: R_{wp} = 7.82%, Gof = 1.05*		
x = 0.4	Gd1	24c	0.125	0	0.25	1	0.42(2)
	Gd2	16a	0	0	0	0.2	0.10(1)
	Ga1	16a	0	0	0	0.51(1)	0.10(1)
	Al1	16a	0	0	0	0.29(1)	0.10(1)
	Ga2	24d	0.375	0	0.25	0.58(1)	0.52(2)
	Al2	24d	0.375	0	0.25	0.42(1)	0.52(2)
	O1	96h	0.9628(3)	0.0520(4)	0.1507(4)	1	1.09(1)
Lattice parameter： *a* = 12.4099(7) Å			*Secondary phases: 4.4(3)% $GdAlO_3$*		*Fitting parameters: R_{wp} = 11.07%, Gof = 1.45*		

Appendix D Exploration of the other non-stoichiometric garnets and perovskite by ADL

The studies presented in Chapters 2 and 3 indicate that non-stoichiometry has an impact on the luminescence performance of garnet materials such as GAG, GGG, and GAGG. Garnet structured materials have a wide range of applications in various fields, it is then important to explore other types of non-stoichiometric garnet. LuAG is an exceptional candidate for scintillator host material[23], LuAGG: Ce^{3+}/Cr^{3+} [24], LuAGG: Pr^{3+} [25], YAGG: Ce^{3+}/Cr^{3+} [26] are also excellent persistent luminescence material, and YIG and YSG are excellent magnetic materials[27]. Consequently, synthesizing a range of non-stoichiometric garnets is necessary to explore and develop new optical and magnetic materials. Finally, despite not being optimal choices for optical host materials, the synthesis of SmAG and EAG facilitates understanding of the maximum ionic radius at which non-stoichiometric REAG can form, which enables the creation of novel materials for diverse applications. In turn, this synthetic exploration contributes to our understanding of the relationship between the ion sizes at the A and B sites of non-stoichiometric garnet formation

Appendix D.1 Synthesis of non-stoichiometric garnets $Sm_3Al_5O_{12}$/$Eu_3Al_5O_{12}$/$Eu_3Ga_5O_{12}$ /$Lu_3Al_5O_{12}$

Text D.1.1 $Sm_3Al_5O_{12}$ (SmAG)

Glass samples of $Sm_{3+x}Al_{5-x}O_{12}$ composition with x = 0 - 0.5 can be synthesized by ADL using O_2 as a gas carrier. A crystallisation temperature of 895°C was determined by DSC test using $Sm_{3.5}Al_{4.5}O_{12}$ glass powder, as shown in ***Fig D.1.1a***. ***Fig D.1.1b*** shows the XRD diffraction patterns of glass samples $Sm_{3+x}Al_{5-x}O_{12}$ with x = 0 and 0.2 after thermal treatment at 900°C for 3h to fully crystallisation, which demonstrate that the SmAG (x = 0) composition crystallises into the perovskite $SmAlO_3$ phase, while the ns-SmAG (x = 0.2) composition is a mixture of several different phases (SmAP, SmAG, SmAM and Al_2O_3).

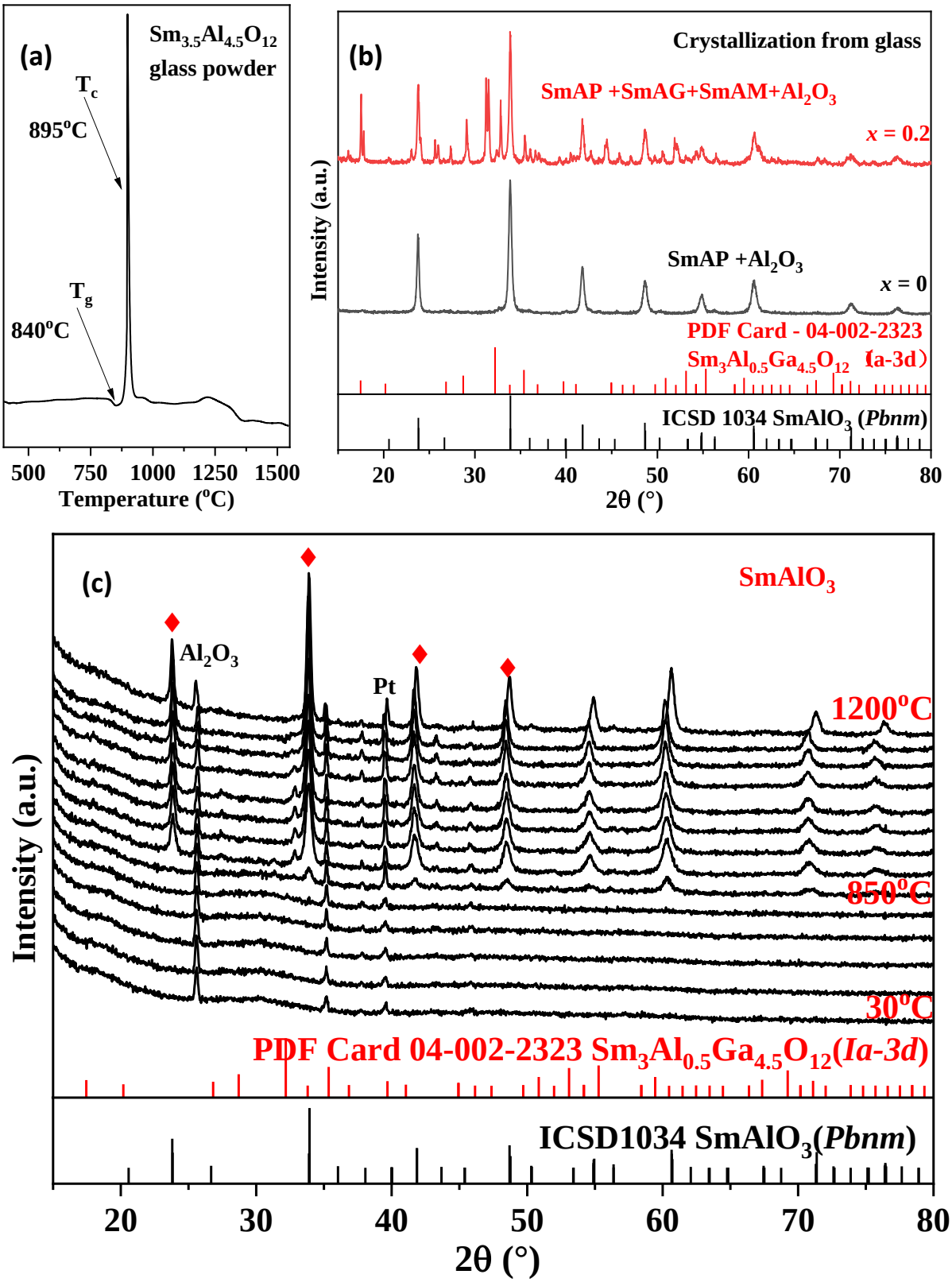

Fig D.1.1 (a) *DSC curve of $Sm_{3.5}Al_{4.5}O_{12}$ glass powder.* ***(b)*** *Lab-XRD pattern of $Sm_{3+x}Al_{5-x}O_{12}$ (x = 0, 0.2) sample synthesized by crystallization from glass.* ***(c)*** *VT-XRD pattern of $Sm_3Al_5O_{12}$ glass powder from 30 to 1200°C.*

To accurately determine the crystallisation temperature to obtain the garnet phase, VT-XRD measurements of SmAG (x = 0) glass samples were conducted. The VT-XRD patterns, as illustrated in ***Fig D.1.1c***, indicate that the "glass" transparent bead obtained by ADL contained Al_2O_3 crystals and the glass composition gradually crystallised into a $SmAlO_3$ phase when the temperature reached 850°C. After several attempts at synthesis, it was not possible to obtain a pure glass sample, so ultimately pure SmAG garnet could not be formed. Alternatively, direct crystallisation from melt has been attempted for synthesis, but a mixture of perovskite $SmAlO_3$ and Al_2O_3 phase was obtained. There are only a few reports of finding small amounts of SmAG as an impurity phase[28-29]. The non-equilibrium synthesis i.e. crystallisation from glass/melt are very efficient synthetic methods to obtain the metastable phase, however here we could not get pure glass samples or garnet sample. In addition, controlling the mass of the beads or the type of carrier gas (He, mixture O_2/He) may yield a completely glassy sample. In crystallising from lass it may be possible to obtain pure SmAG. This requires further attempts to synthesise. Alternatively, replacing Sm^{3+} with a small amount of Y[28] or Gd may give the $(Sm_{1-x}Gd_x)_3Al_5O_{12}$ phase.

Text D.1.2 $Eu_3Al_5O_{12}$ (EuAG)

Non-stoichiometric EuAG was considered for synthesis using ADL, as the ionic radius of Eu^{3+} (0.95 Å) is similar to that of Gd^{3+} (0.94 Å). The glass precursors with $Eu_{3+x}Al_{5-x}O_{12}$ (x = 0 - 0.6) composition were successfully obtained using oxygen as a gas carrier. However, $Eu_{3.7}Al_{4.3}O_{12}$ (x = 0.7) composition cannot form glass. The glass sample crystallised into the garnet phase after a 3 hours heat treatment at 900°C (see crystallisation temperature 887°C shown in ***Fig D.1.2a***), as evidenced by the XRD pattern in ***Fig D.1.2b***.

The compounds at x = 0 and 0.2 are single garnet phases, the compound at x = 0.4 is a mixture of ns-EuAG garnet, 35% perovskite $EuAlO_3$ and Al_2O_3 phases, while the primary phase of the composition at x = 0.6 is a perovskite $EuAlO_3$ phase with 5 wt% secondary ns-EuAG garnet phase. The (211) peak of garnet, shown on the right side of the ***Fig D.1.2b,*** shifts towards the lower value 2θ as x increase from 0 to 0.6. ***Fig D.1.2c*** shows the refined cell parameters a from the XRD data, which display a linear expansion of the cell parameters as x increases to 0.6. The cell parameters begin to deviate from linear increase at x = 0.6

indicating that the solid solution range of the non-stoichiometric EuAG is between 0.6 and 0.7. As indicated by the SPD refinement results in ***Fig D.1.2d*** (detailed refinement structure information is listed in ***Table D.1***), the cell parameters gradually expand as x increases, and the excess Eu^{3+} occupies the Al sites. SPD refinement profiles of $Eu_{3+x}Al_{5-x}O_{12}$ (x = 0, 0.2, 0.4) are shown in ***Fig D.1.3-D.1.5.***

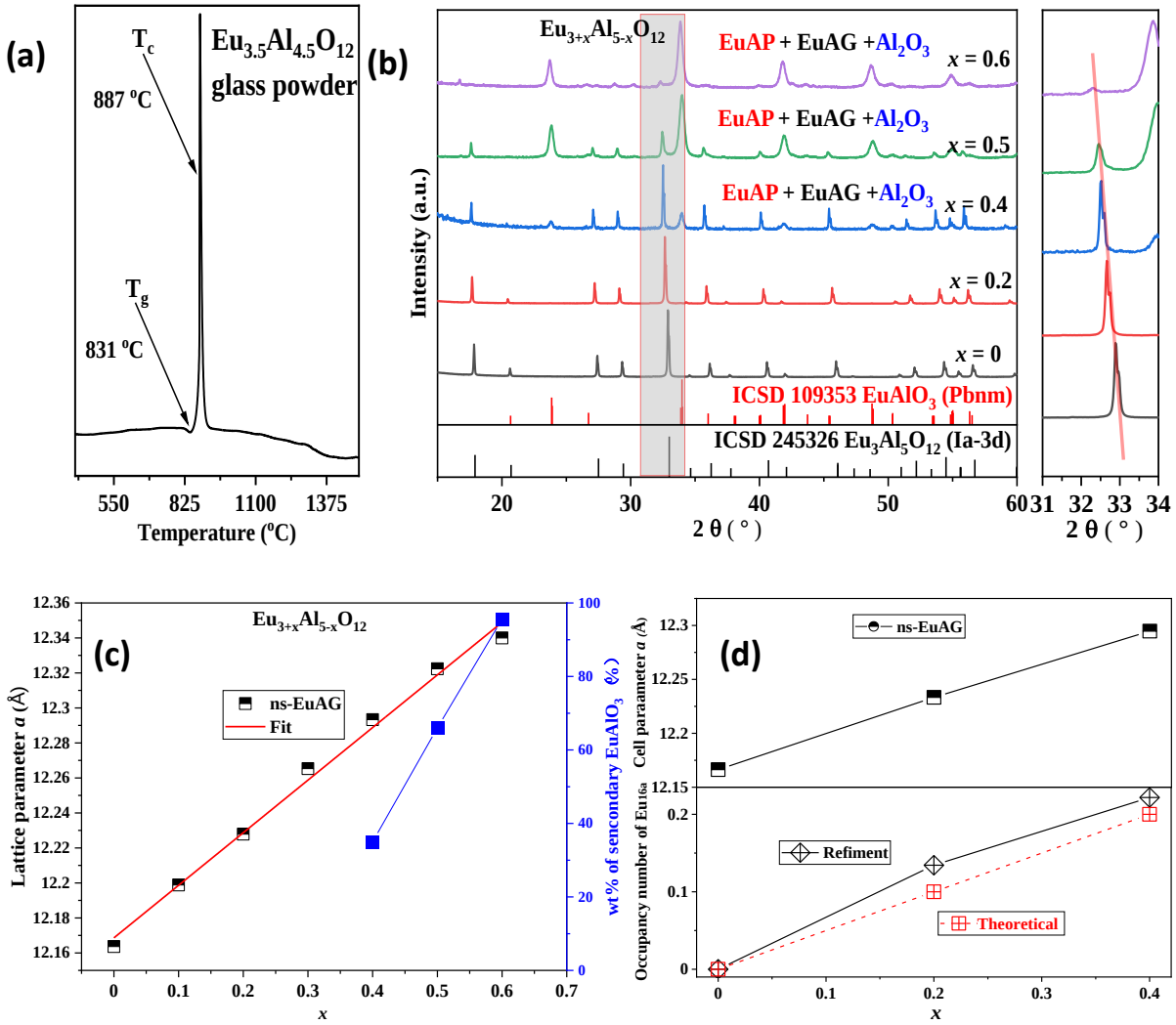

Fig D.1.2 (a) *DSC curve of $Eu_{3.5}Al_{4.5}O_{12}$ glass powder.* ***(b)*** *Laboratory XRD pattern of $Eu_{3+x}Al_{5-x}O_{12}$ (x = 0 -0.6) sample.* ***(c)*** *Laboratory XRD data refined lattice parameter a of ns-EuAG (blank line) and the wt% of the secondary EuAP is on the right axis.* ***(d)*** *Refined lattice parameter a of ns-EuAG (blank line) with different x value (upper), plots of refined occupancy of the AlO_6 octahedral site by Eu^{3+} (blank line) and theoretical occupancy (red line) vs x value (lower).*

Table D.1 *Refined cell parameters of EuAG and fitting results obtained from SPD data.*

$Eu_{3+x}Al_{5-x}O_{12}$	atom	site	x	y	z	occupancy	U_{iso}*100
	Eu1	24c	0.125	0	0.25	1	0.432(2)
	Eu2	16a	0	0	0	0.9567(7)	0.34(1)
x = 0	Al1	16a	0	0	0	0.0343(7)	0.34(1)
	Al2	24d	0.375	0	0.25	1	0.35(9)
	O1	96h	0.46800(7)	0.04825(7)	0.35220(7)	1	0.50(1)
Lattice parameter: *a = 12.166322(2)*			*Secondary phases:* *0.40(1)wt% EuAG2*			*Fitting parameters:* *R_{wp} = 8.73% Gof = 2.00*	
	Eu1	24c	0.125	0	0.25	1	0.837(3)
	Eu2	16a	0	0	0	0.1344(5)	0.58(1)
x = 0.2	Al1	16a	0	0	0	0.86551(2)	0.58(1)
	Al2	24d	0.375	0	0.25	1	0.65(1)
	O1	96h	0.45711(7)	0.05036(8)	0.35018(1)	1	1.03(1)
Lattice parameter: *a = 12.233364(1)*			*Secondary phases:* *4.09(2)wt% EuAG2 and 1.02(2) wt%EuAP*			*Fitting parameters:* *R_{wp} = 8.46%, Gof = 1.78*	
	Eu1	24c	0.125	0	0.25	1	1.015(6)
	Eu2	16a	0	0	0	0.2218(9)	0.46(1)
x = 0.4	Al1	16a	0	0	0	0.7781(9)	0.46(1)
	Al2	24d	0.375	0	0.25	1	0.83(1)
	O1	96h	0.4660(1)	0.0512(1)	0.3495(1)	1	1.16(3)
Lattice parameter: *a = 12.29471(1)*			*Secondary phases:* *24.2(2) wt%EuAP, 2.57 (2) wt%EuAM and 3.4(2) wt%Al_2O_3*			*Fitting parameters:* *R_{wp} = 9.88%, Gof = 2.20*	

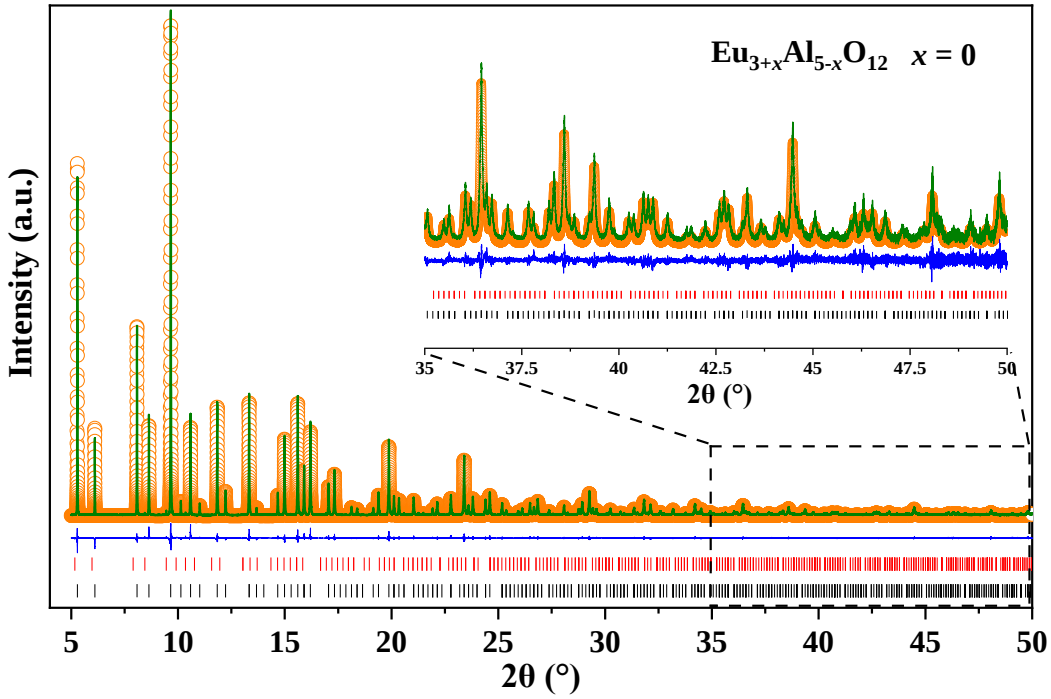

Fig D.1.3 *SPD Rietveld refinement profiles of $Eu_3Al_5O_{12}$ (R_{wp} = 8.73% Gof = 2.00) (black ticks marks are EuAG garnet reflections, red ticks marks are 0.40(1)wt% ns-EuAG2 garnet reflections)*

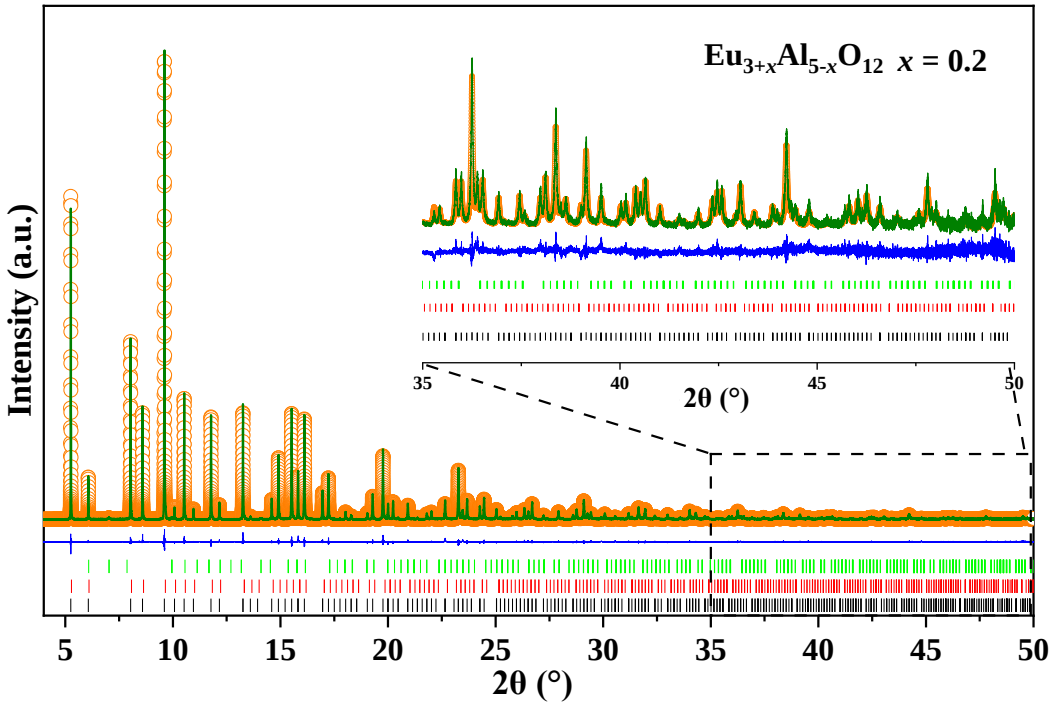

Fig D.1.4 *SPD Rietveld refinement profiles of $Eu_{3.2}Al_{4.8}O_{12}$ (R_{wp} = 8.46%, Gof = 1.78) (black ticks marks are ns-EuAG garnet reflections, red ticks marks are 4.09(2)wt% ns-EuAG2 garnet reflections, green ticks marks correspond to 1.02(2) wt% EuAP perovskite reflections)*

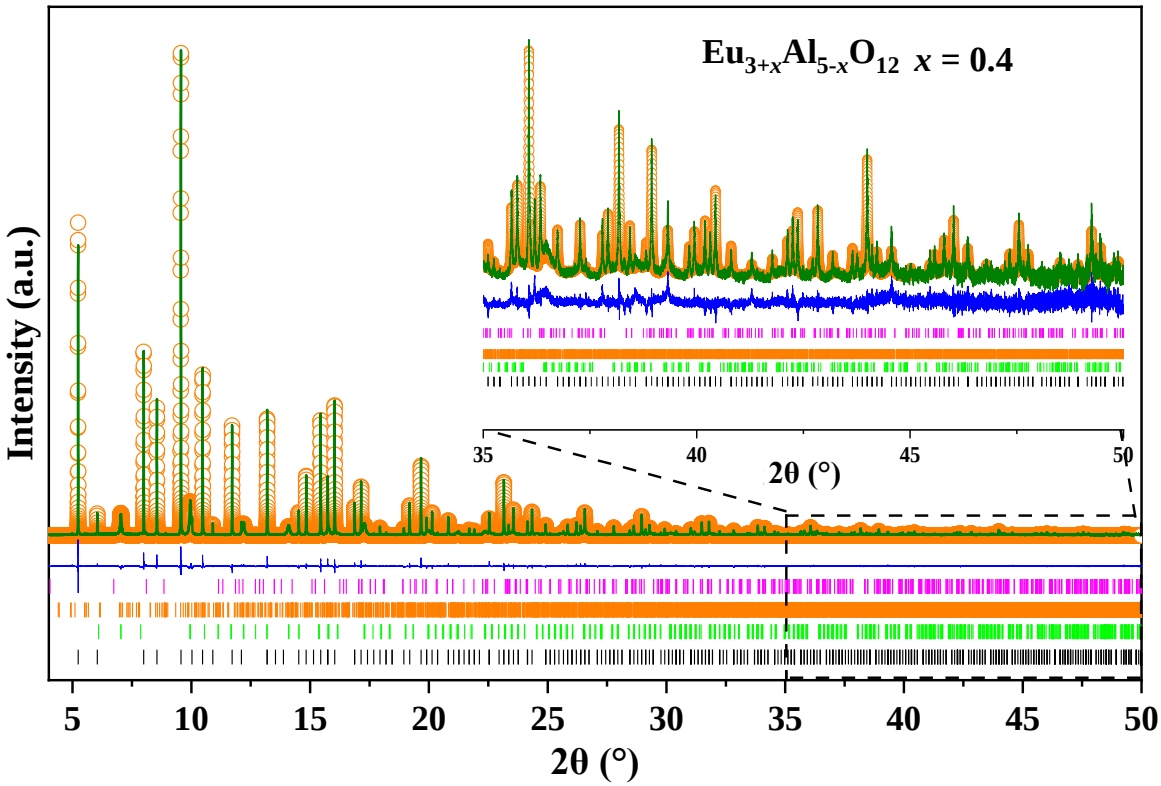

Fig D.1.5 *SPD Rietveld refinement profiles of $Eu_{3.4}Al_{4.4}O_{12}$ (R_{wp} = 9.88%, Gof = 2.20) (black ticks marks are ns-EuAG1 garnet reflections, green ticks marks are 24.2(2) wt% EuAP perovskite reflections, pink tick marks correspond to 2.57(2) wt% EuAM $Eu_4Al_2O_9$ reflections, orange tick marks are 3.4(2) wt% Al_2O_3 reflections)*

Text D.1.3 $Eu_3Ga_5O_{12}$ (EuGG)

An attempt was made to synthesize non-stoichiometric $Eu_{3+x}Ga_{5-x}O_{12}$ (x = 0 - 0.6) solid solutions via melt crystallization method by ADL. The XRD pattern in ***Fig D.1.6*** reveal a single garnet phase for compositions with x = 0 - 0.4, with a second phase starting to appear for compositions at x = 0.5. The enlarged image of the main peak on the right side displays that the peak shifts to a lower value 2θ as x increases, indicating a unit lattice expansion. The refined lattice parameter demonstrates *a* linear increase with x from 0 - 0.6, implying a solid solution range of x = 0 - 0.7 for the non-stoichiometric EuGG.

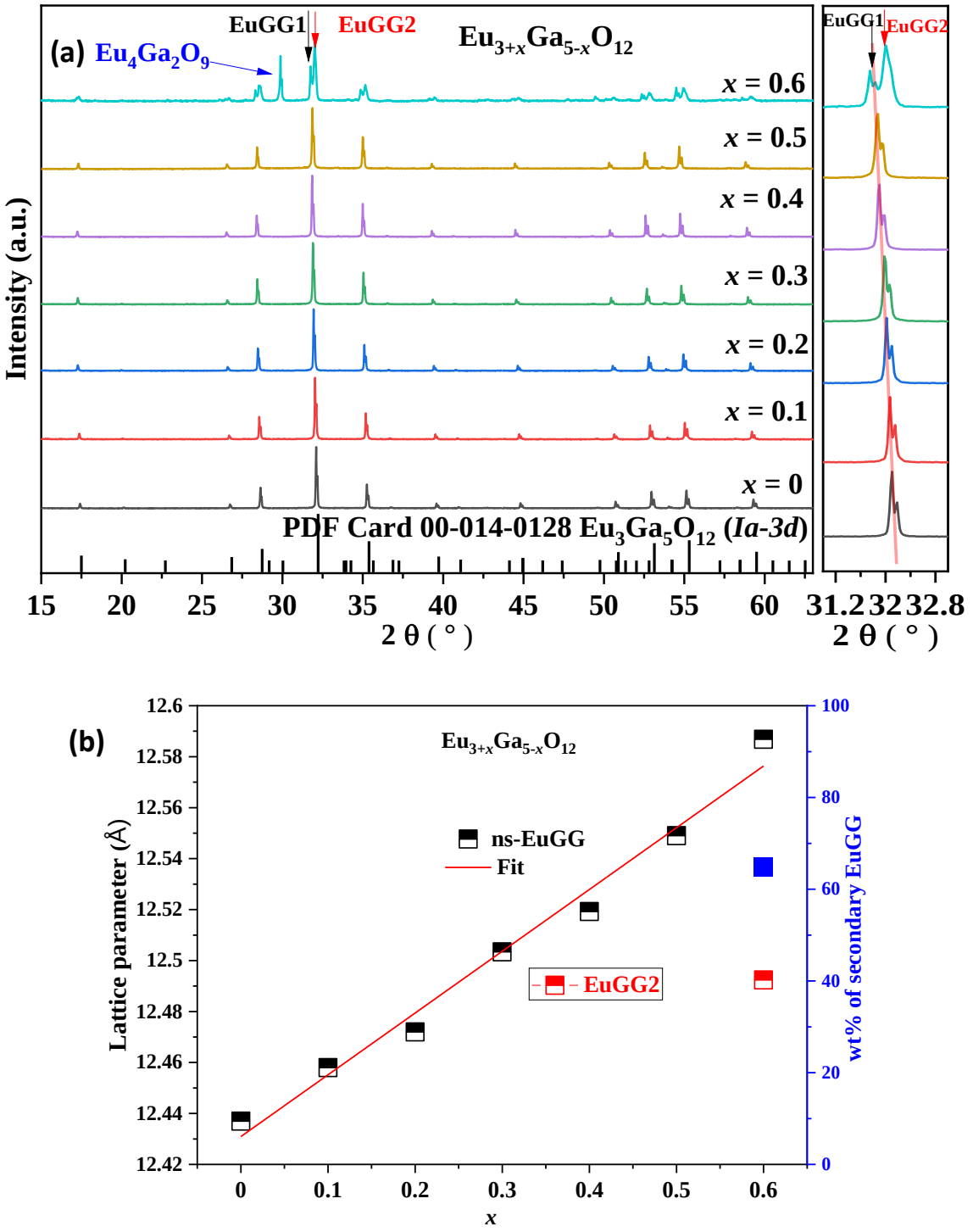

Fig D.1.6 (a) *Laboratory XRD pattern of $Eu_{3+x}Ga_{5-x}O_{12}$ (x = 0 -0.6) sample synthesized by crystallization from melt.* ***(b)*** *Laboratory XRD data refined lattice parameter a of ns-EuGG (blank line) and secondary EuGG (red line) with different x value, and the wt% of the secondary EuGG2 is on the right axis.*

Text D.1.4 $Lu_3Al_5O_{12}$ (LuAG)

The XRD patterns of $Lu_{3+x}Al_{5-x}O_{12}$ (x = 0, 0.1) compositions synthesised through the crystallisation from melt using ADL, as shown in ***Fig D.1.7***, reveal that the composition with x = 0.1 is a mixed phase of $LuAlO_3$ and Al_2O_3. We were unable to synthesise the glass samples in many attempts. Consequently, it can be inferred that obtaining a high non-stoichiometric ratio LuAG sample via the synthetic method of ADL is not feasible.

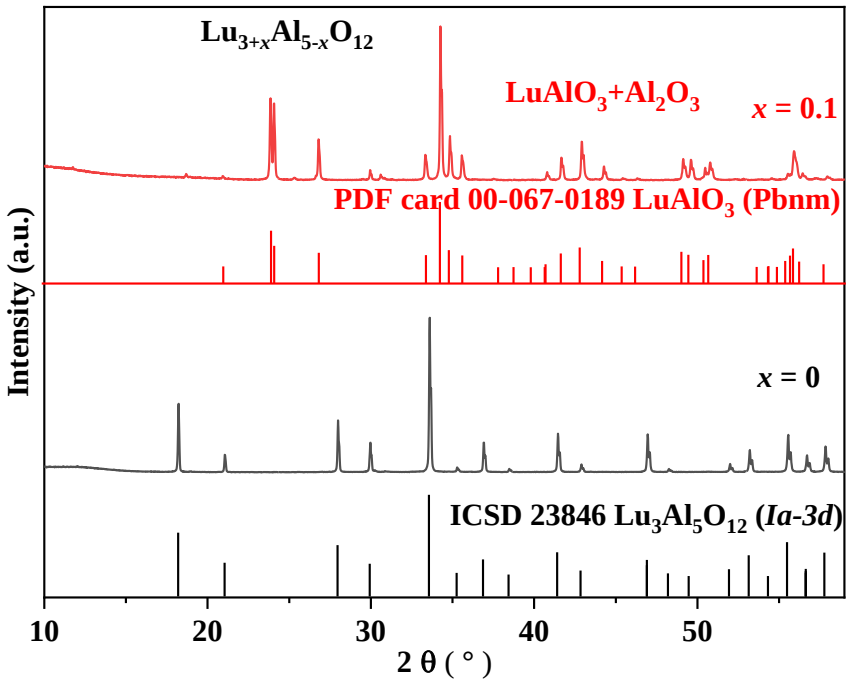

Fig D.1.7 *Laboratory XRD pattern of $Lu_{3+x}Al_{5-x}O_{12}$ (x = 0, 0.1) synthesized by crystallization from melt.*

Appendix D.2 Synthesis of non-stoichiometric garnets $Y_3Sc_5O_{12}$/ $Y_3Fe_5O_{12}$/ $Y_3Al_2Ga_3O_{12}$.

Text D.2

In addition to the synthesis of non-stoichiometric REAlG and REGaG, alternative types of garnet have been considered for the synthesis of non-stoichiometric solid solutions due to their good optical and magnetic properties. Unfortunately, not only non-stoichiometric but stoichiometric YScG, YIG, YAGG garnets cannot be obtained by the ADL synthesis method (see the XRD pattern shown in ***Fig C.4.1-3***).

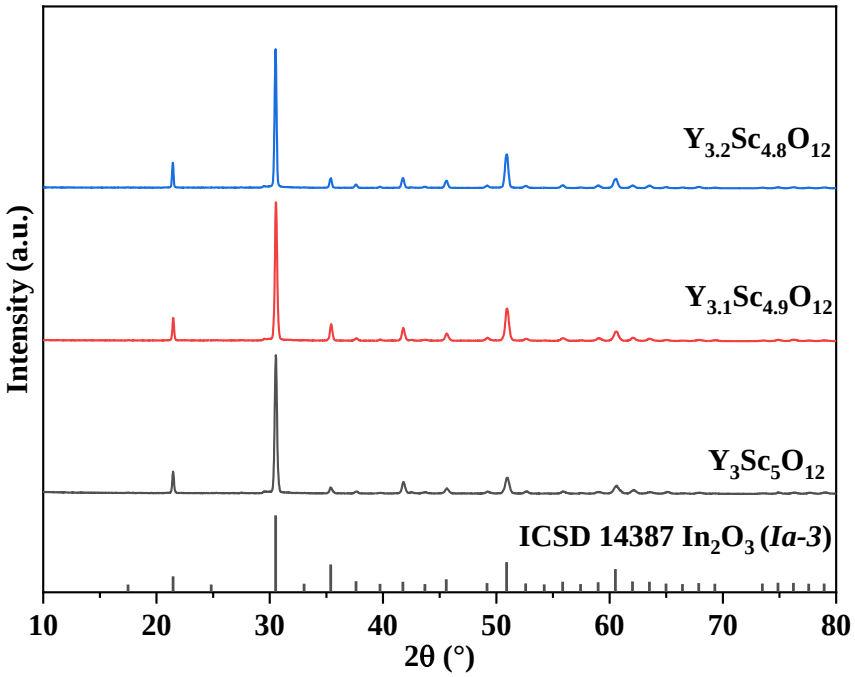

Fig D.2.1 *Laboratory XRD pattern of $Y_{3+x}Sc_{5-x}O_{12}$ (x = 0, 0.2) synthesized by crystallization from melt.*

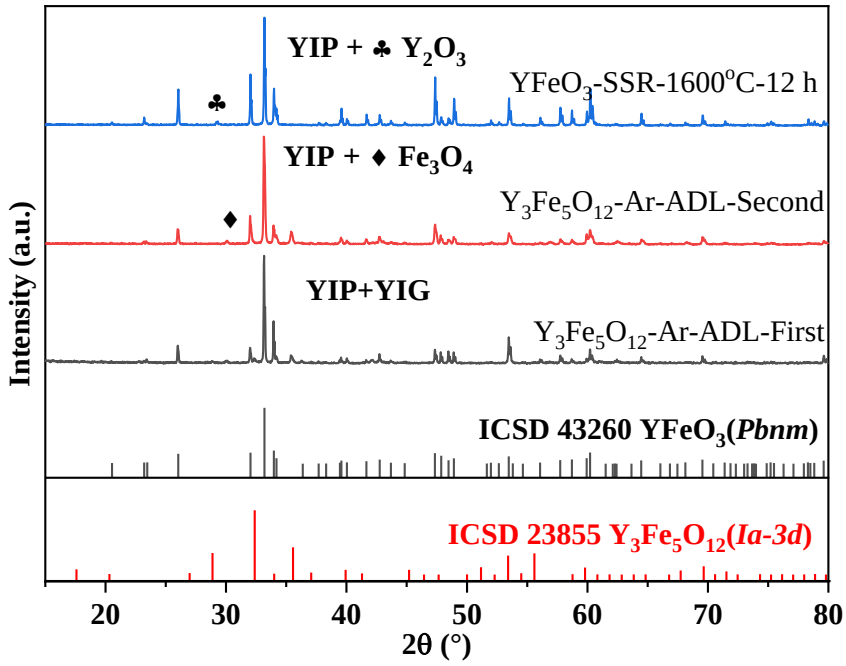

Fig D.2.2 *Laboratory XRD pattern of $Y_{3+x}Fe_{5-x}O_{12}$ (x = 0) compositions synthesized by crystallization from melt and SSR.*

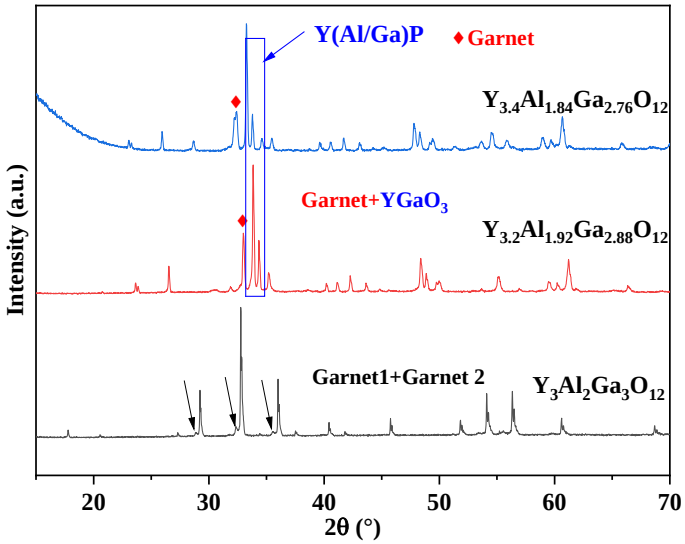

Fig D.2.3 *Laboratory XRD pattern of $Y_{3+x}(Ga_{0.6}Al_{0.4})_{5-x}O_{12}$ (x = 0, 0.2, 0.4) compositions synthesized by crystallization from melt.*

Appendix D.3 Synthesis of non-stoichiometric perovskite.

Text D.3

Here we have attempted to synthesize three different types of non-stoichiometric perovskite compositions. The XRD pattern shown in ***Fig D.3.1-3*** indicates that a single phase of non-stoichiometric perovskite could not be obtained by ADL.

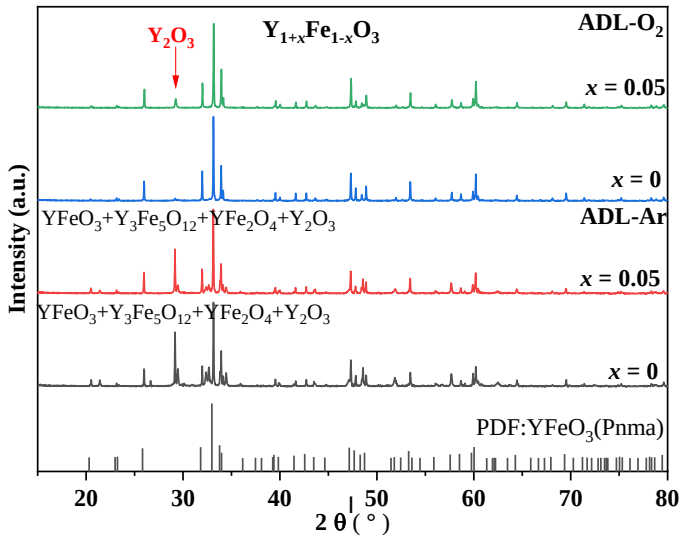

Fig D.3.1 *Laboratory XRD pattern of $Y_{1+x}Fe_{1-x}O_3$ (x = 0, 0.05) compositions synthesized by crystallization from melt using ADL.*

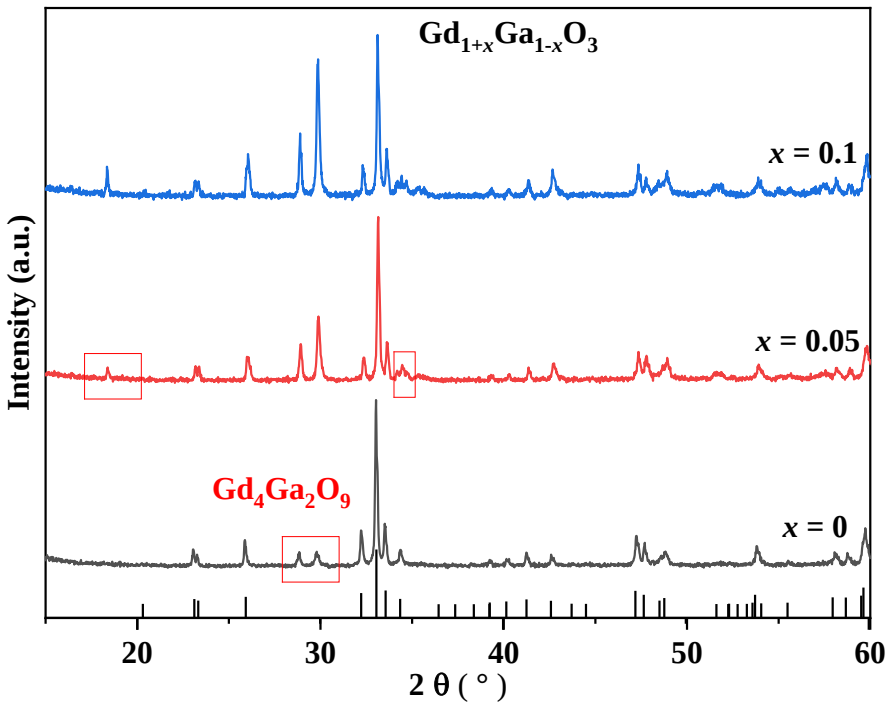

Fig D.3.2 *Laboratory XRD pattern of* $Gd_{1+x}Al_{1-x}O_3$ *(x = 0, 0.05, 0.1) compositions synthesized by crystallization from melt using ADL.*

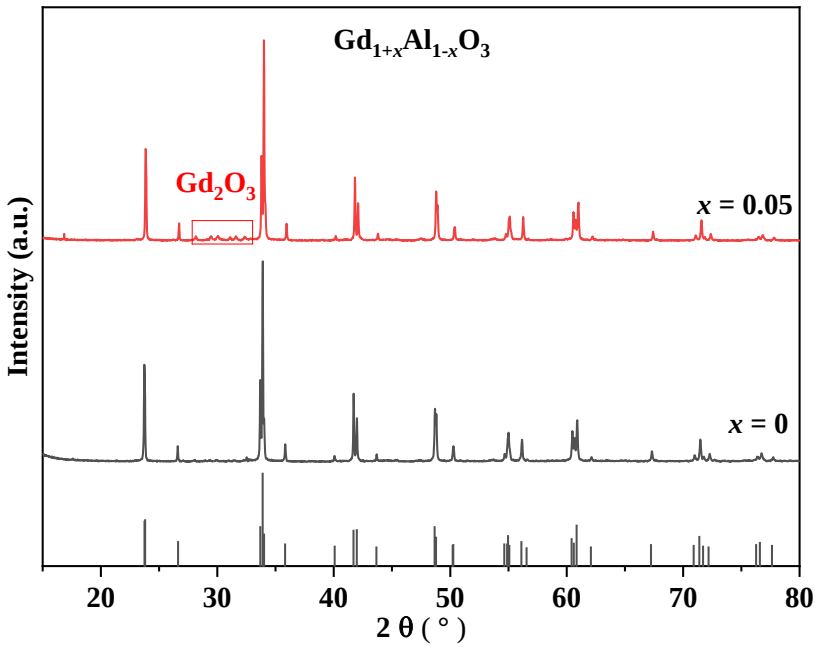

Fig D.3.3 *Laboratory XRD pattern of*$Gd_{1+x}Ga_{1-x}O_3$ *(x = 0, 0.05) compositions synthesized by crystallization from melt using ADL.*

Text D Conclusion

By attempting to synthesise a series of non-stoichiometric garnets (SmAG, EuAG, GAG,

LuAG), we conclude that the formation of non-stoichiometric garnet $RE_3Al_5O_{12}$ is not only related to the radius of the RE^{3+} ion, but also to synthesis method. The ionic radius of Lu^{3+} is smaller than that of Gd/Y, but no non-stoichiometric LuAG can be obtained, which we attribute to the lack of glass-forming ability of the LuAG composition. Comparing the synthesis and solid solution intervals of REAlG and REGaG, we find that the larger B-site ions may be able to accommodate more A, and that the endpoints of the solid solution range of GGG ($0 \leq x \leq 0.7$) are wider than that of GAG ($0 \leq x \leq 0.6$).

In addition to $RE_3Al_5O_{12}$ garnet, we have tried to synthesise other types of garnet YIG, etc., and tried to synthesise non-stoichiometric perovskite, but we have not found any other types of non-stoichiometric garnet and non-stoichiometric perovskite. This also suggests that the formation of non-stoichiometric ratio garnets is not only related to the ionic radius of *A*/*B*. ***Table D.2*** lists the attempted syntheses of non-stoichiometric garnet and perovskite

Table D.2 Synthesis method and solid solution of non-stoichiometric garnet and perovskite.

Garnet	Composition	Non-stoichiometric	Solid solution	ADL (Crystallisation from glass/melt)
REAG	$Sm_{3+x}Al_{5-x}O_{12}$	**No**	-	glass
	$Eu_{3+x}Al_{5-x}O_{12}$	**Yes**	0 - 0.4	glass
	$Gd_{3+x}Al_{5-x}O_{12}$	**Yes**	0 - 0.6	glass
	$Y_{3+x}Al_{5-x}O_{12}$	**Yes**	0 - 0.4	glass/melt
	$Lu_{3+x}Al_{5-x}O_{12}$	**No**	0	melt
REGG	$Sm_{3+x}Ga_{5-x}O_{12}$	?	?	?
	$Eu_{3+x}Ga_{5-x}O_{12}$	**Yes**	0 - 0.5	melt
	$Gd_{3+x}Ga_{5-x}O_{12}$	**Yes**	0 - 0.7	melt
	$Y_{3+x}Ga_{5-x}O_{12}$	?	?	?
	$Lu_{3+x}Ga_{5-x}O_{12}$	?	?	?
YSG/YIG	$Y_{3+x}Sc_{5-x}O_{12}$	**No**	-	melt
	$Y_{3+x}Fe_{5-x}O_{12}$	**No**	-	melt
GAGG/YAGG	$Y_{3+x}(Ga_{0.6}Al_{0.4})_{5-x}O_{12}$	**×**	-	melt
	$Gd_{3+x}(Ga_{0.6}Al_{0.4})_{5-x}O_{12}$	**Yes**	0 - 0.6	glass
YIP/GAP/GGP	$Y_{1+x}Fe_{1-x}O_3$	**No**	-	melt
	$Gd_{1+x}Al_{1-x}O_3$	**No**	-	melt
	$Gd_{1+x}Ga_{1-x}O_3$	**No**	-	melt

Appendix E Supporting information for Chapter 4

Appendix E.1 XRD and SPD refinement

Table E.1.1 *Structural information from SPD Rietveld refinement result $Lu_{3.67}AlSiO_9$ (Pbnm)*

Atom	Site	x	y	z	Occupancy	U_{iso}*100(Å^2)
Lu1	4e	0.20791(5)	0.39741(5)	0.25	0.948(5)	1.61(1)
Lu2	4e	0.42743(4)	0.62492(5)	0.75	0.952(5)	1.48(1)
Al1	4e	0.3842(2)	0.1685(2)	0.75	0.5	0.55(6)
Si1	4e	0.3842(2)	0.1685(2)	0.75	0.5	0.55(6)
O1	4e	0.3921(6)	0.4955(5)	0.25	1	3.01(9)*
O2	4e	0.609(1)	0.798(1)	0.75	0.5	3.01(9)*
O3	4e	0.2410(5)	0.2630(1)	0.75	1	3.01(9)*
O4	4e	0.3343(5)	0.0335(6)	0.75	1	3.01(9)*
O5	4e	0.5245(6)	0.2274(6)	0.75	1	3.01(9)*
						*Constrained to the same value
	Lattice parameter： *a* = 10.43294(4) *b* = 10.17436(5) *c* = 3.64122(1)				*Fitting parameters:* *R_{wp} = 11.39%, Gof = 1.55*	

Table E.1.2 *Structural information from SPD Rietveld refinement result $Lu_{3.89}AlSiO_{9.33}$ (Pbnm)*

Atom	Site	x	y	z	Occupancy	U_{iso}*100(Å^2)
Lu1	4e	0.20861(7)	0.39512(7)	0.25	0.976(9)	1.00(1)
Lu2	4e	0.42555(6)	0.62364(6)	0.75	0.968(9)	0.67(1)
Al1	4e	0.3866(4)	0.1626(3)	0.75	0.5	0.15(6)
Si1	4e	0.3866(4)	0.1626(3)	0.75	0.5	0.15(6)
O1	4e	0.3967(9)	0.4944(7)	0.25	1	2.33(8)*
O2	4e	0.607(1)	0.785(1)	0.75	0.667	2.33(8)*
O3	4e	0.2386(8)	0.2662(8)	0.75	1	2.33(8)*
O4	4e	0.3318(8)	0.019(7)	0.75	1	2.33(8)*
O5	4e	0.498(1)	0.2202()	0.75	1	2.33(8)*
						*Constrained to the same value
	Lattice parameter： *a* = 10.45455(7) Å *b* = 10.19952(5) Å *c* = 3.63902(1) Å				*Fitting parameters:* *R_{wp} = 11.82%, Gof = 1.49*	

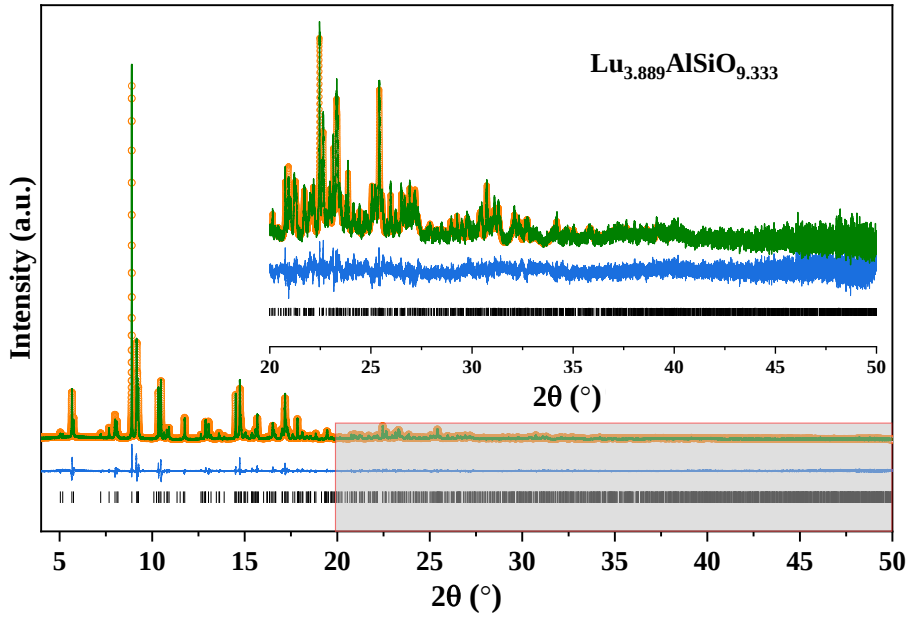

Fig E.1.1 *SPD Rietveld refinement profiles of $Lu_{3.889}AlSiO_{9.333}$ (R_{wp} = 11.82%, Gof = 1.49)*

Table E.1.3 *Lu-O bond length and bond valence sums (BVS) value in LuAM obtain from SPD refinement data. (Calculated by structure prediction diagnostic software[30])*

Bond Lu1-O ($Lu1O_7$)	**Length(Å)**	**Bond Lu3-O ($Lu3O_7$)**	**Length (Å)**
Lu1-O6	2.148(10)	Lu3-O9	2.147(15)
Lu1-O3	2.154(13)	Lu3-O2	2.150(10)
Lu1-O9	2.181(12)	Lu3-O5	2.261(11)
Lu1-O5	2.293(10)	Lu3-O9	2.302(12)
Lu1-O7	2.376(15)	Lu3-O8	2.350(14)
Lu1-O2	2.439(11)	Lu3-O6	2.564(11)
Lu1-O1	2.579(12)	Lu3-O4	2.700(12)
Average bond length	2.31	**Average bond length**	2.35
BVS	3.03	**BVS**	2.80
Bond Lu2-O ($Lu2O_6$)	**Length/Å**	**Bond Lu4-O ($Lu4O_6$)**	**Length/Å**
Lu1-O1	2.096(11)	Lu4-O2	2.198(11)
Lu1-O7	2.182(13)	Lu4-O8	2.201(16)
Lu1-O8	2.267(13)	Lu4-O4	2.263(11)
Lu1-O2	2.267(11)	Lu4-O8	2.324(13)
Lu1-O3	2.280(14)	Lu4-O9	2.346(14)
Lu1-O4	2.323(11)	Lu4-O6	2.384(11)
Average bond length	2.24	**Average bond length**	2.29
BVS	3.19	**BVS**	2.31

Table E.1.4 *Lu-O bond length and bond valence sums (BVS) value in LuASO obtain from SPD refinement data. (Calculated by structure prediction diagnostic software[30])*

Bond Lu1-O ($Lu1O_6$)	**Length(Å)**	**Bond Lu2-O ($Lu2O_7$)**	**Length (Å)**
Lu1-O1	2.212(10)	Lu2-O2	2.198(11)
Lu1-O4	2.256(5)	Lu2-O8	2.201(16)
Lu1-O4	2.256(5)	Lu2-O4	2.263(11)
Lu1-O3	2.267(5)	Lu2-O8	2.324(13)
Lu1-O3	2.267(5)	Lu2-O9	2.346(14)
Lu1-O5	2.496(10)	Lu2-O6	2.384(11)
		Lu2-O2	2.198(11)
Average bond length	2.29	**Average bond length**	2.37
BVS	2.59	**BVS**	2.54

Appendix E.2 Composition analysis by NMR and SEM

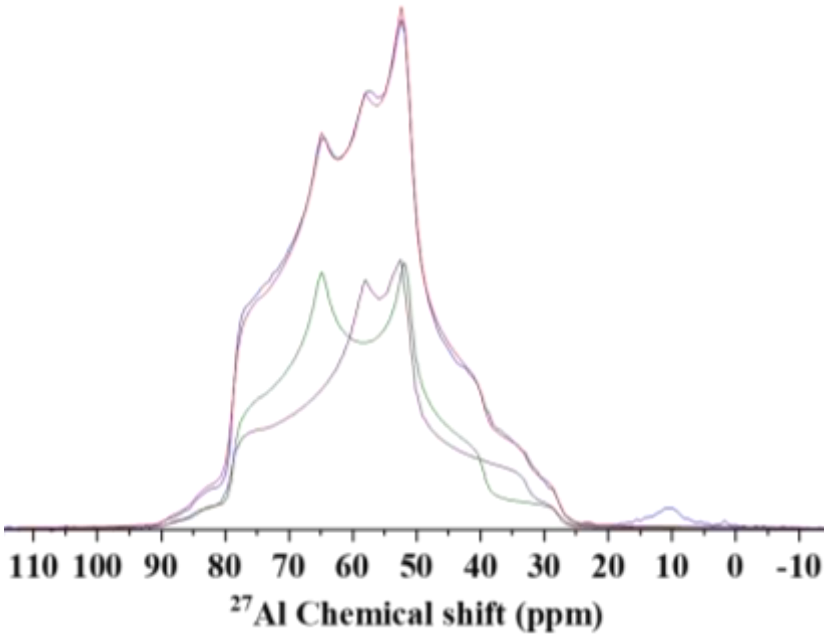

Fig E.2.1 *Quantitative fitted ^{27}Al NMR spectrum for $Lu_4Al_2O_9$.*

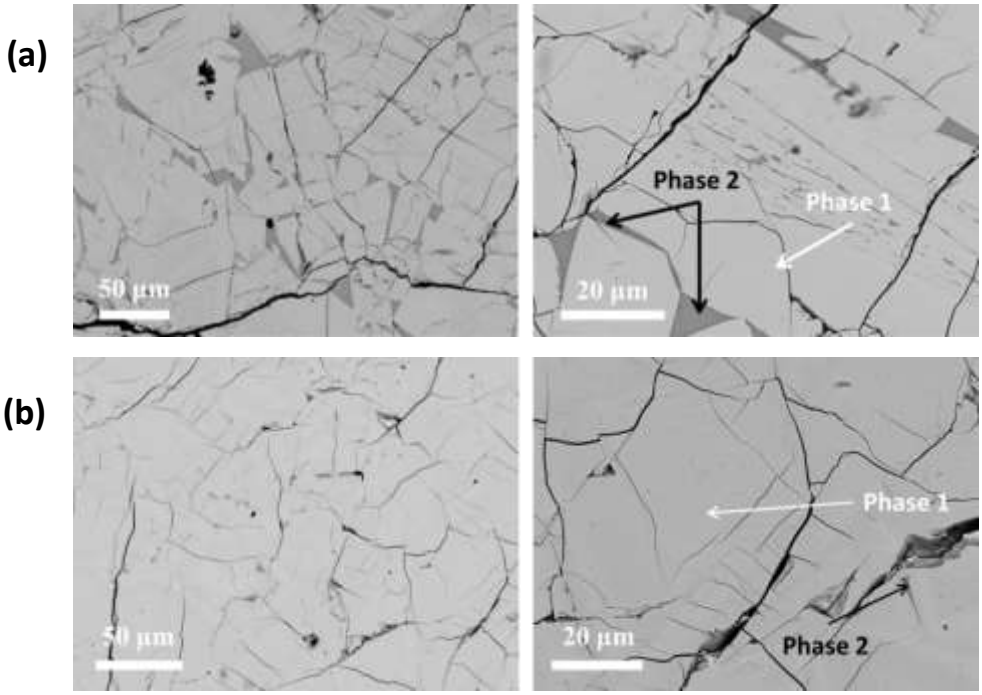

Fig E.2.2 *SEM (BSE) images of* ***(a)*** $Lu_{3.67}AlSiO_9$, ***(b)*** $Lu_{3.89}AlSiO_{9.33.}$

Table E.2.1 *Composition analysis of* $Lu_{3.667}AlSiO_9$ *and* $Lu_{3.889}AlSiO_{9.33}$ *using SEM-EDS.*

Composition	Phase	Lu (At. %)	Al (At. %)	Si (At. %)	Experimental composition
$Lu_{3.667}AlSiO_9$	Phase 1	25.21	7.02	6.48	$Lu_{3.74(2)}Al_{1.0(2)}Si_{0.96(2)}O_{9.08(5)}$
	Phase 2	15.06	9.19	13.12	$Lu_{1.64(2)}Al_{1.00(1)}Si_{1.4(1)}O_{6.75(2)}$
$Lu_{3.889}AlSiO_{9.33}$	Phase 1	25.64	6.62	6.45	$Lu_{3.9(3)}Al_{1.0(1)}Si_{0.99(3)}O_{9.38(1)}$
	Phase 2	14.72	7.85	14.5	$Lu_{2.2(4)}Al_{1.00(9)}Si_{2.23(2)}O_{9.38(6)}$

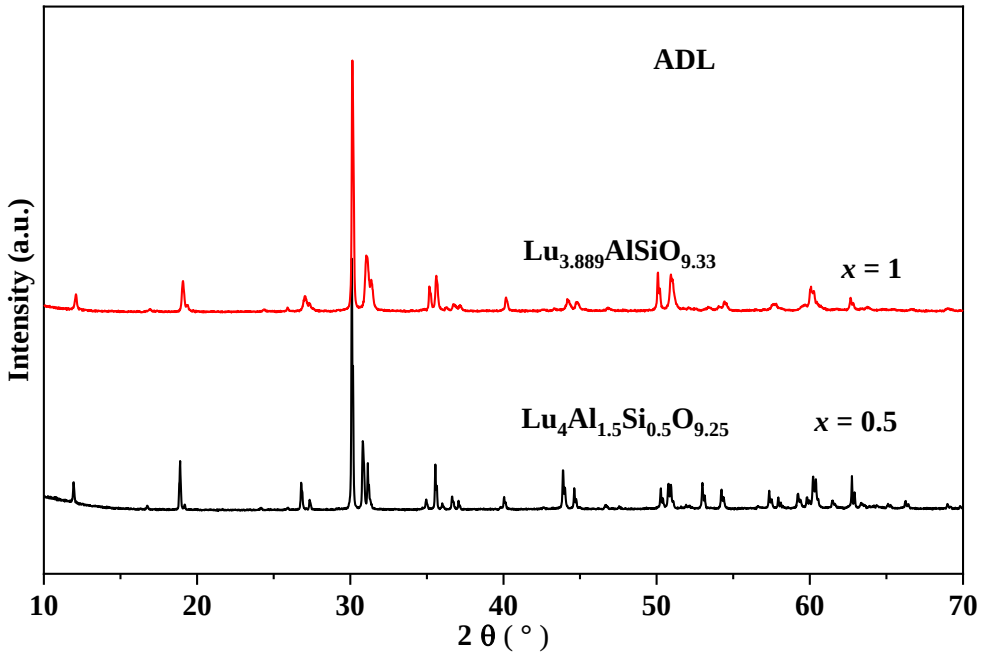

Fig E.2.3 *PXRD pattern of $Lu_4Al_{1.5}Si_{0.5}O_{9.25}$ (x = 0.5) and $Lu_{3.889}AlSiO_{9.33}$ (x = 1)*

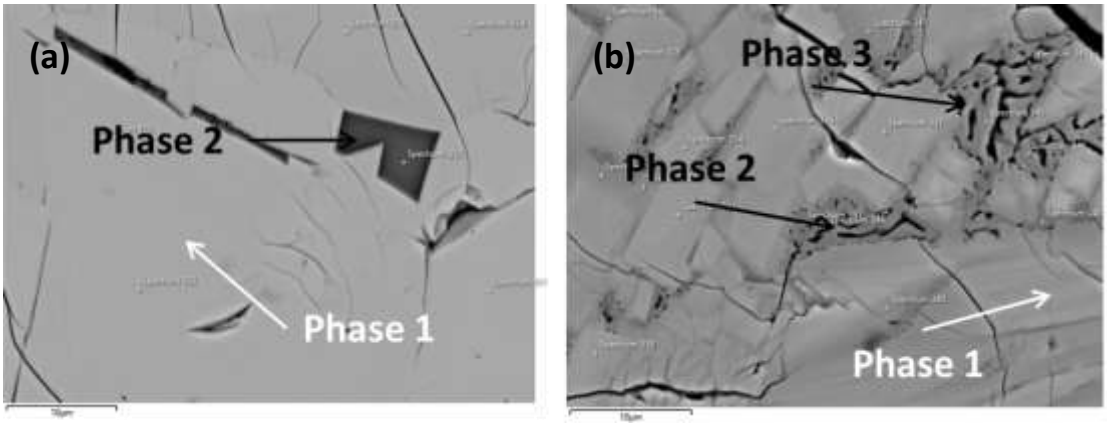

Fig E.2.4 *SEM (BSE) images of* ***(a)*** *$Lu_4Al_{1.5}Si_{0.5}O_{9.25}$,* ***(b)*** *$Lu_{3.89}AlSiO_{9.33}$.*

Table E.2.3 *SEM-EDS analysis of $Lu_4Al_{1.5}Si_{0.5}O_{9.25}$ and $Lu_{3.89}AlSiO_{9.33}$.*

Solid solution	Phase	Lu (At. %)	Al (At. %)	Si (Si. %)	Experimental composition
(x = 0.5) $Lu_4Al_{1.5}Si_{0.5}O_{9.25}$	Phase 1	25.91	10.1	3.33	$Lu_{4.0(2)}Al_{1.5(4)}Si_{0.5(3)}O_{9.25}$
	Phase 2	10.45	28.18	1.14	$LuAl_{2.7}Si_{0.11}O_{5.715}$
(x =1.25) $Lu_{3.86}Al_{0.75}Si_{1.25}O_{9.415}$	Phase 1	26.83	5.35	6.25	$Lu_{3.76(2)}Al_{0.75(9)}Si_{0.88(1)}O$
	Phase 2	25.64	5.54	7.35	$Lu_{3.47(2)}Al_{0.75(1)}Si_{0.96(1)}O$
	Phase 3	23.42	2.5	11.73	$Lu_{7.0\,(3)}Al_{0.75(4)}Si_{3.5(6)}O$

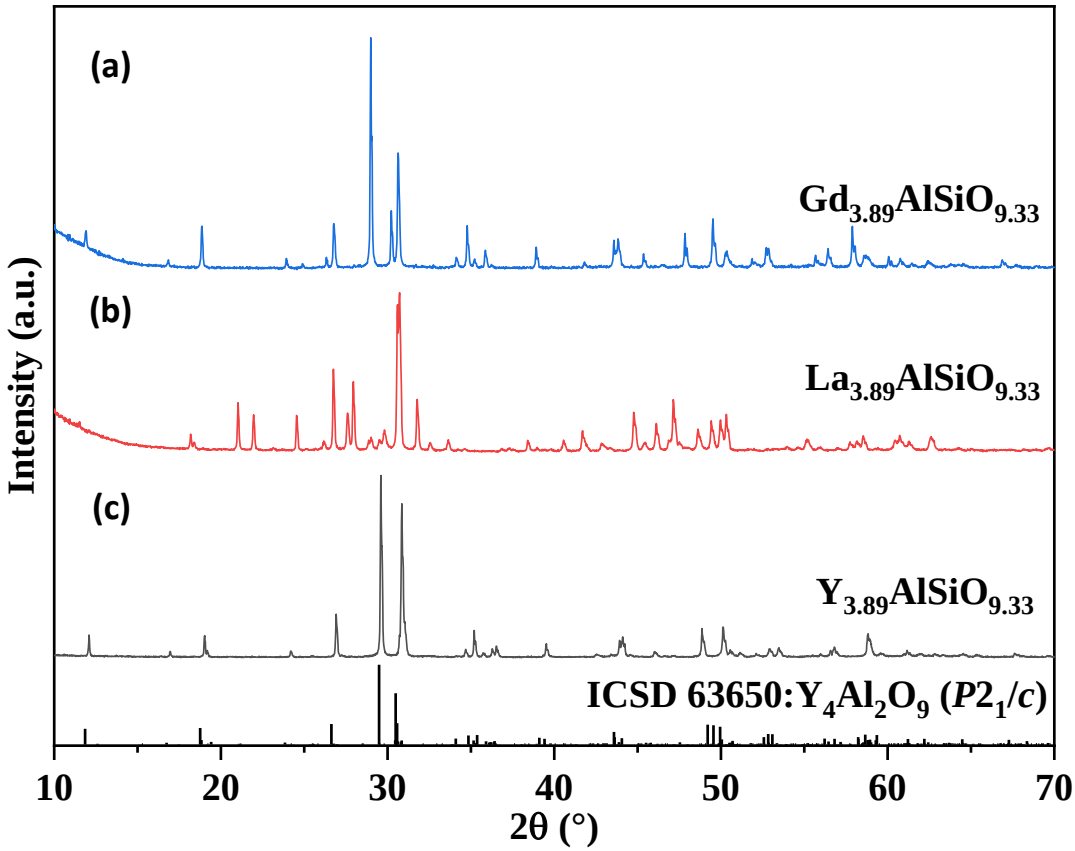

Fig E.2.5 *PXRD pattern of* ***(a)*** $Gd_{3.89}AlSiO_{9.33}$, ***(b)*** $La_{3.89}AlSiO_{9.33}$, ***(c)*** $Y_{3.89}AlSiO_{9.33}$.

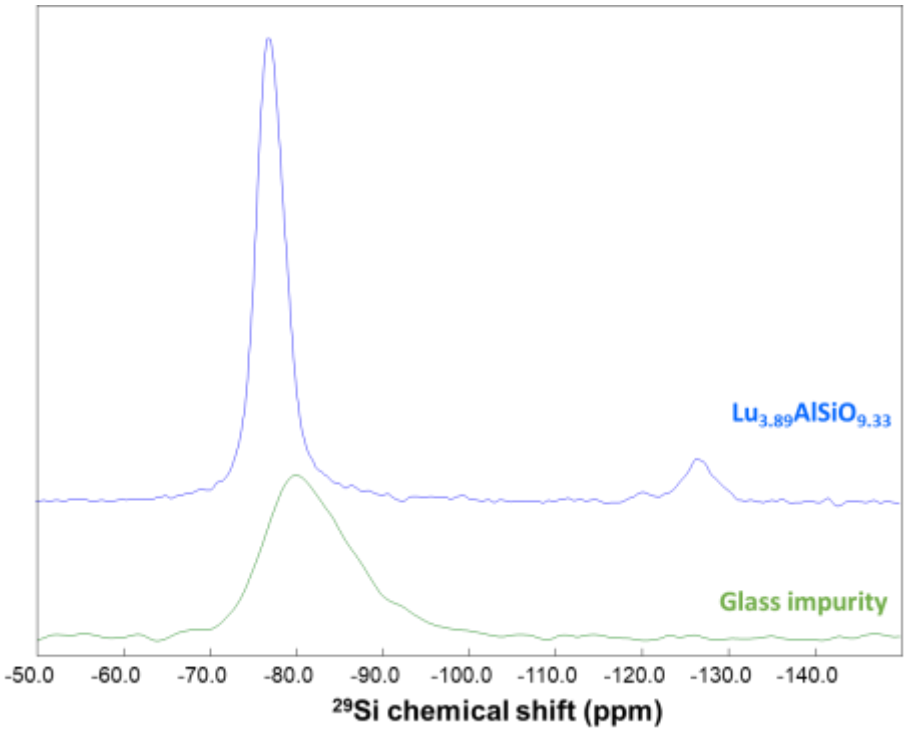

Fig E.2.6 *Comparison of* ^{29}Si *NMR spectra of glass impurity phases (green curve) and* $Lu_{3.89}AlSiO_{9.33}$ *(blue curve)*

Appendix E.3 Luminescence properties

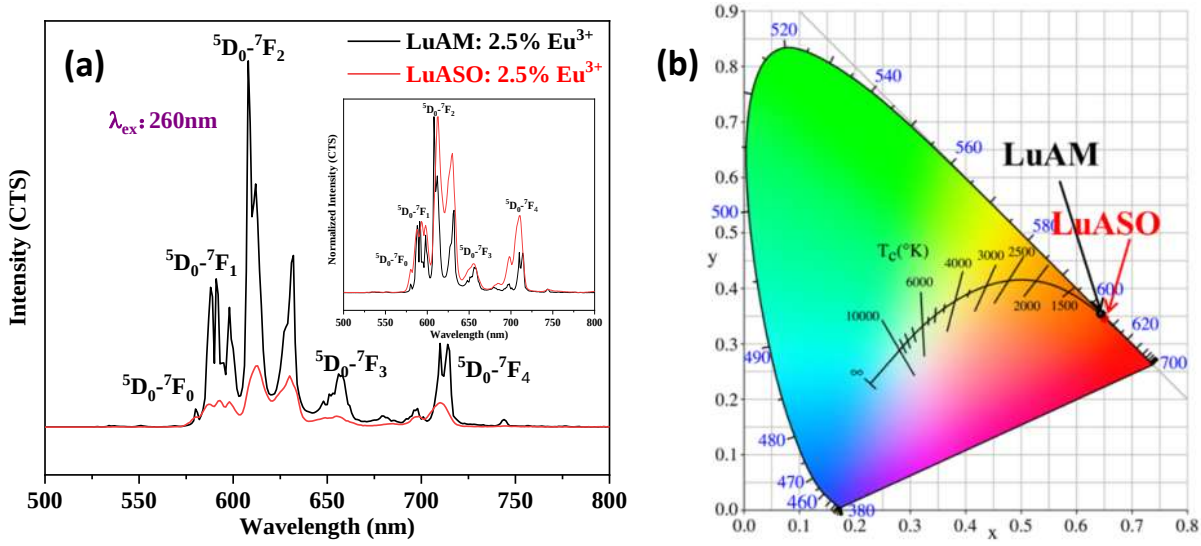

Fig E.3.1 *Luminescence properties of LuAM: 2.5%Eu^{3+} and LuASO: 2.5%Eu^{3+} under 260nm excitation.*

(a) *Emission spectrum.* ***(b)*** *CIE chromaticity coordinates diagram.*

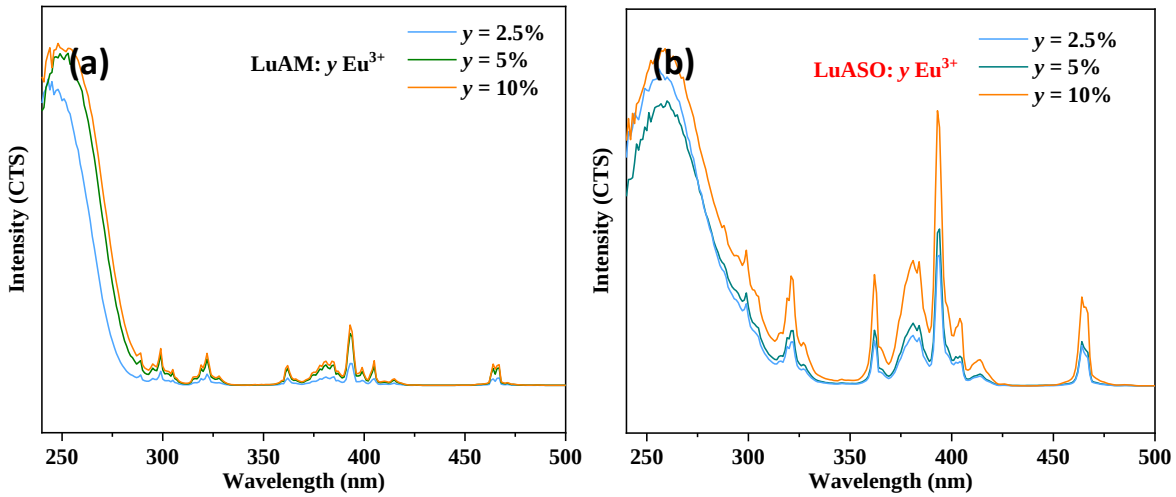

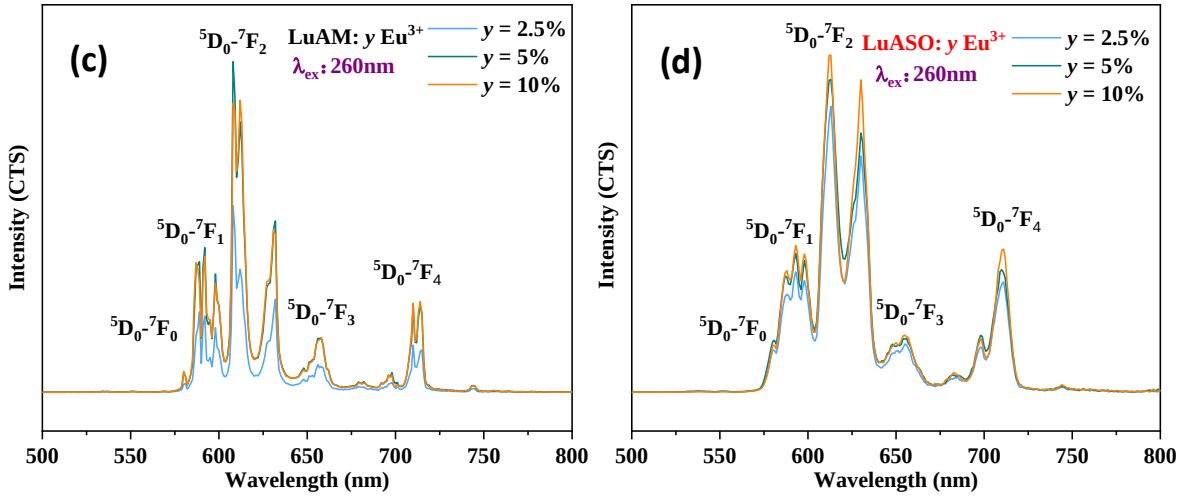

Fig E.3.2 *Luminescence properties of LuAM: yEu^{3+} and LuASO: yEu^{3+}. PLE spectrum under emission 500 nm of* ***(a)*** *LuAM: yEu^{3+} and* ***(b)*** *LuASO: yEu^{3+}. PL spectrum under excitation 260 nm of* ***(c)*** *LuAM: yEu^{3+} and* ***(d)*** *LuASO: yEu^{3+}.*

References

[1] Britannica, The Editors of Encyclopaedia. "Bragg law". Encyclopedia Britannica, 15 Mar. 2022, https://www.britannica.com/science/Bragg-law..

[2] S.N. Bose, National Centre for Basic Sciences, 14-15/12/2011, Advanced X-ray Workshop.

[3] https://testbook.com/physics/synchrotron

[4] https://www.aps.anl.gov/Beamlines/Directory/Details?beamline_id=90

[5] A.A. Coelho, Journal of Applied Crystallography. ***2018****, 51, 210-218.*

[6] B. Robert, V. Dreele, R. Matthew et al., https://11bm.xray.aps.anl.gov/absorption.html

[7] J.J. Rehr, R.C. Albers, Reviews of Modern Physics. ***2000****, 72, 621-654.*

[8] M. Alain, M. Jacques, M.-B. Diane, et al., Journal of Physics: Conference Series. ***2009****, 190, 012034.*

[9] M.D. Segall, J.D.L. Philip, M.J. Probert et al., Journal of Physics: Condensed Matter. ***2002****, 14, 2717.*

[10] A. L. Ankudinov,B. Ravel, J. J. Rehr et al.,Physical Review B. ***1998****, 58B, 7565.*

[11] B. Ravel, M. Newville, J Synchrotron Radiat. ***2005****, 12, 537-541.*

[12] A.V. Crewe, Journal of Microscopy. ***1974****, 100, 247-259.*

[13] A.V. Crewe, J. Wall, L.M. Welter, Journal of Applied Physics. ***2003****, 39, 5861-5868.*

[14] J.M. LeBeau, S.D. Findlay, L.J. Allen et al., Phys Rev Lett. ***2008****, 100, 206101.*

[15] J.Y. Zhang, J. Hwang, B.J. Isaac et al., Scientific Reports. ***2015****, 5, 12419.*

[16] S. Muto, Y. Yamamoto, M. Sakakura et al., ACS Applied Energy Materials. ***2022****, 5, 98-107.*

[17] S. Iijima, I. Ohnishi, Z. Liu, Scientific Reports. ***2021****, 11, 18022.*

[18] D.D. Laws, H.-M.L. Bitter, A.Jerschow, Angewandte Chemie International Edition. ***2002****,41(17), 3096-3129.*

[19] B. Reif, S.E. Ashbrook, L. Emsley, M. Hong, Nature Reviews Methods Primers. ***2021****, 1, 2.*

[20] T. Polenova, R. Gupta, A. Goldbourt, Analytical Chemistry. ***2015****, 87, 5458-5469.*

[21] S. Abu-Baker, G.A. Lorigan, Open Journal of Biophysics. ***2012****, 02, 109-116.*

[22] G. Czjzek, J. Fink, F. Götz et al., Physical Review B. ***1981****, 23, 2513-2530.*

[23] M. Nikl, A. Yoshikawa, K. Kamada et al., Progress in Crystal Growth and Characterization of Materials. ***2013****, 59, 47-72.*

[24] J. Kim, S.Oh. Y.J. Kim, Journal of Materials Chemistry. C. ***2016****, 4, 11457-11464.*

[25] L. Feng, Z. Wang, C. Cao et al., Journal of Rare Earths. ***2017****, 35, 47-52.*

[26] J. Xu, J.Ueda, S.Tababe, Journal of Materials Chemistry. C. ***2016****, 4, 4380-4386.*

[27] Y. Rao, D. Zhang, L. Jin et al., Journal of Magnetism and Magnetic Materials. ***2020****, 497, 165817.*

[28] R. Skaudzius, S. Sakirzanovas, A. Kareiva, Journal of Electronic Materials. ***2018****, 47, 3951-3956.*

[29] M. Inoue, H. Otsu, H. Kominami et al. , Journal of Alloys and Compounds. ***1995****, 226, 146-151.*

[30] M.W. Lufaso, P.M. Woodward, Acta Crystallographica Section B. ***2001****, 57, 725-738.*

Xue FANG

Structures et propriétés de luminescence de nouveaux aluminates et gallates de terres rares obtenus par synthèse hors équilibre

La synthèse de nouveaux oxydes cristallins est cruciale pour développer de nouveaux matériaux fonctionnels. Dans cette thèse, la lévitation aérodynamique (ADL) combinée à un chauffage laser CO_2 tel que développé au CEMHTI permet la synthèse de nouveaux oxydes cristallins hors équilibre, via la cristallisation à partir du verre ou directement à partir du liquide fondu à haute température lors d'un refroidissement rapide. Nous présentons ici de nouveaux aluminates et gallates de terres rares synthétisés par une méthode hors équilibre et explorons leur structure qui sont ensuite discutées et corrélées avec leurs propriétés de luminescence.

Dans une première partie, de nouvelles solutions solides $Gd_{3+x}Al_{5-x}O_{12}$, $Gd_{3+x}Ga_{5-x}O_{12}$, $Gd_{3+x}(Ga_{0.6}Al_{0.4})_{5-x}O_{12}$ ($0 \leq x \leq 0.6$) hautement non stœchiométriques ont été synthétisées par cristallisation à partir du verre et du liquide fondu à haute température. En combinant des analyses de diffraction sur poudre avec des résultats de microscopie électronique à transmission et de mesures EXAFS, nous montrons que jusqu'à 30 % des cations B à hexacoordonnés sont remplacés de manière désordonnée par des cations A dans la structure grenat $A_3B_2C_3O_{12}$ non stœchiométrique, ce qui permet au dopant de plus petite taille RE^{3+} (Tb^{3+}, Er^{3+}, Tm^{3+}, Yb^{3+}) d'occuper partiellement le site BO_6, formant ainsi un polyèdre REO_6 hexacoordonné. Les études de photoluminescence et de luminescence persistante prouvent que les sites de luminescence AO8 et BO6 non équivalents sont responsables de la régulation de la couleur de la luminescence et de la durée de vie de la luminescence persistante.

Dans une deuxième partie, les phases $Lu_4Al_2O_9$ (LuAM) et $Lu_{4-\alpha}Al_{2-x}Si_xO_{9+\delta}$ ($x = \alpha/3 + \delta/2$, $x = 0{,}5$, 1) (LuASO) issues d'une solution solide originale ont été synthétisées avec succès pour la première fois en utilisant la cristallisation par refroidissement rapide à partir du liquide fondu à haute température. La substitution de Al^{3+} par Si^{4+} a entraîné une augmentation de la symétrie de la structure cristalline, passant d'une structure monoclinique $P2_1/c$ à une structure orthorhombique *Pbnm*. Dans la solution solide $Lu_{4-\alpha}Al_{2-x}Si_xO_{9+\delta}$, la substitution d'$Al^{3+}$ par Si^{4+} est de manière très originale compensée par des lacunes de Lu et des oxygènes supplémentaires. Une étude par diffraction sur poudre a permis de déterminer la structure cristalline moyenne, tandis que l'étude par RMN du solide a permis de sonder le désordre induit par la substitution de Al^{3+} par Si^{4+} à l'échelle locale. L'étude de la photoluminescence de LuAM et LuASO dopés RE^{3+} (Ce^{3+}, Eu^{3+}, Er/Yb^{3+}) a révélé que la substitution cationique induit un changement de symétrie cristalline et introduit des défauts et une distorsion polyédrique, qui affectent l'environnement local du dopant et les propriétés de luminescence.

Mots clés : Lévitation aérodynamique, Aluminates et gallates de terres rares, Luminescence

Structures and luminescence properties of some new rare-earth aluminates and gallates obtained by non-equilibrium synthesis

The synthesis of new materials is crucial to develop novel functional materials. In this thesis, aerodynamic levitation (ADL) combined with laser heating setup as developed at CEMHTI enables non-equilibrium synthesis of new crystalline oxides, via crystallisation from glass or directly from the melt during rapid cooling. Here we report some new rare-earth aluminates and gallates synthesized by non-equilibrium method and explore their structures which are correlated with their luminescence properties.

In a first part, new highly non-stoichiometric $Gd_{3+x}Al_{5-x}O_{12}$, $Gd_{3+x}Ga_{5-x}O_{12}$, $Gd_{3+x}(Ga_{0.6}Al_{0.4})_{5-x}O_{12}$ ($0 \leq x \leq 0.6$) solid solution were synthesized using crystallisation from the glass and the melt. Using a combination of powder diffraction, transmission electron microscopy, and EXAFS measurements, we show that up to 30 % of six-coordinated B ions are disorderly replaced by A in non-stoichiometric $A_3B_2C_3O_{12}$, which allow the smaller size dopant RE^{3+} (Tb^{3+}, Er^{3+}, Tm^{3+}, Yb^{3+}) to partially occupy the BO_6 site, forming six coordinated REO_6. Photoluminescence and persistent luminescence studies prove that inequivalent AO_8 and BO_6 luminescence sites are responsible for the regulation of luminescence colour and persistent luminescence lifetime.

In a second part, single phases $Lu_4Al_2O_9$ (LuAM) and $Lu_{4-\alpha}Al_{2-x}Si_xO_{9+\delta}$ ($x = \alpha/3 + \delta/2$, $x = 0.5$, 1) (LuASO) solid solution were successfully synthesised for the first time using crystallisation from the melt. The substitution of Si^{4+} for Al^{3+} resulted in an increase of crystal structure symmetry, transitioning from a monoclinic $P2_1/c$ to an orthorhombic *Pbnm*. In the solid solution $Lu_{4-\alpha}Al_{2-x}Si_xO_{9+\delta}$, the substitution of Al3+ by Si^{4+} is originally compensated by Lu vacancies and extra oxygens. Using powder diffraction, the average structure was determined, then solid state NMR enabled to probe the disorder induced by the substitution of Si^{4+} for Al^{3+} at local scale. Photoluminescence study of RE^{3+} (Ce^{3+}, Eu^{3+}, Er/Yb^{3+}) doped LuAM and LuASO revealed that cation substitution induce crystal symmetry change and introduce defects and polyhedral distortion, which affect the local environment of the dopant and affect the luminescence performance.

Keywords : Aerodynamic levitation, Rare-earth aluminates and gallates, Luminescence

CEMHTI-CNRS UPR3079
1D Avenue de la Recherche Scientifique
45071 Orléans Cedex 2